Analysis of Composite Materials with Random Microstructure

by

Jan Zeman

A treatise submitted in partial fulfillment
of the requirements for the degree of

Doctor of Philosophy

Czech Technical University in Prague
Klokner Institute

2003

Date

TABLE OF CONTENTS

LIST OF FIGURES

LIST OF TABLES

ACKNOWLEDGMENTS

First of all, I would like to express my gratitude to my thesis advisor, Ing. Miroslav Černý, CSc., for his support and patience during the whole course of the work on this thesis. I am deeply indebted to my friend and colleague Doc. Ing. Michal Šejnoha, Ph.D. whose unfailing enthusiasm and encouragement provided continuous inspiration throughout my research. I also thank Prof. Ing. Jiří Šejnoha, DrSc. for his interest and numerous interesting discussions on the topic of this thesis. In addition, special gratitude is to Prof. RNDr. Ivo Marek, DrSc., Prof. RNDr. Karel Rektroys, DrSc. and Doc. Ing. Tomáš Roubíček, DrSc. whose inspiring lectures and great personalities made an invaluable contribution to my education. In this connection, I also want to thank organizers of the Ph.D. courses "Advanced Topics in Structural Optimization", held at the Danish Technical University in 2001, and "Homogenization on Multiple Scales", held in Politechnico di Torino in 2002, for their hospitality and funding during my stays. Finally, I would like to express my thanks to Dr. Milan Jirásek for hospitality and support during my stay at EPLF in 2003 and to Prof. Marc Geers for making numerous suggestions which helped to improve the clarity of the text.

I would also like to mention my friends and colleagues with whom I had numerous fruitful and inspiring discussions on topics addressed in this thesis. In particular, I would like to thank Ms. Anička Kučerová, Ing. Matěj Lepš and Ing. Ondřej Hrstka for pleasant cooperation on problems of evolutionary computation; the aid of Doc. Dr. Ing. Daniel Rypl was indispensable for solving the problems of three-dimensional mesh generation. Moreover, I greatly benefited from discussions with Mr. Richard Valenta on the problems of non-linear viscoelasticity and with Mgr. Ing. Martin Wierer on modelling of woven composites.

Most importantly, I would like to thank my parents and my sister Barbora for their endless encouragement and support that gave me confidence to attain the goal I have set and the opportunity to fully concentrate on my study.

Last but not least, the financial support of this work provided by the research project MSM 210000015 and the GAČR 106/99/0096 grant is gratefully acknowledged.

Czech Technical University in Prague
Klokner Institute

Abstract

Analysis of Composite Materials with Random Microstructure

by Jan Zeman

In this thesis, a comprehensive approach to the modelling of composite materials with a microstructure exhibiting various types of disorder is proposed. In particular, a fibrous graphite-epoxy composites with fibers randomly distributed within a transverse plane section and plain weave fabric composites are addressed as representatives of such material systems. Two different modelling strategies are examined. The first one assumes a well defined geometry of the microstructure arrangement and specific boundary conditions. In this framework, the complicated real microstructure is replaced by a substantially simpler periodic unit cell, which statistically resembles the real microstructure in a suitable sense. Periodic distribution of such unit cells is explored and the finite element method is called to carry out the numerical computation. The theoretical basis for the second approach are the Hashin-Shtrikman variational principles. The random character of the fiber distribution is incorporated directly into the variational formulation employing certain statistical descriptors.

A number of statistical descriptors suitable for the microstructure characterization of a random medium is examined first. Several methods for their determination are proposed and tested for a simple theoretical model of a microstructure. Additionally, a validity of various statistical hypotheses usually accepted for a random heterogenous medium is checked for the real microstructure represented here by the graphite fiber tow embedded into the polymer matrix. Next, a stochastic optimization algorithm based on efficient combination of genetic algorithm essentials with basic concepts of the simulated annealing method is introduced.

Suitable optimization procedure formulated in terms of the selected statistical descriptors is proposed to derive the desired unit cell. Several numerical experiments are performed to demonstrate the applicability of the selected optimization method to this complicated optimization problem. A number of numerical studies is performed to quantify individual unit cells. The objective is to identify a number of particles required for specific problems to provide a sufficiently accurate representation of the behavior of real composites. A standard problem of deriving the effective mechanical properties is considered first. A general approach permitting either strain or stress control is pursued. It is observed that the unit cell consisting of five fibers only provides reasonably accurate estimates of the macroscopic properties. Similar conclusions apply to the thermal, linear and non-linear viscoelastic problems considered next.

In certain applications the finite element approach used with the unit cell analysis may prove to be unnecessary expensive. In such a case, one may appreciate well-known effective medium theories where applicable. Here, the most widely used variational principles of Hashin and Shtrikman extended to account for the presence of various transformation fields defined as local eigenstrain or eigenstress distributions in the phases are revisited.

Random character of fibers arrangement is described here by the two-point probability function. When used with the Hashin-Shtrikman variational principles this function provides sufficient information for obtaining bounds or estimates on the effective material properties of real composites with statistically homogeneous microstructures. The Fourier transform-based approach is successfully implemented when solving the resulting equations. An extensive comparison with the finite element-based methodology is presented to investigate the applicability and limitations of this modelling strategy.

The extension of principles proposed for the determination of statistically optimized periodic unit cell to the modelling of plain-weave composites is proposed. Again, the parameters of the idealized periodic unit cell are found by matching appropriate statistical descriptors related to the target microstructure and two-dimensional cross-section of the geometry model. In particular, the ability to incorporate a longitudinal shift of individual layers of the composite system into the model of the periodic unit cell is examined. Geometrical parameters derived from the optimization procedure are then used to generate an equivalent periodic unit cell, which is then combined with the finite element method analysis to provide the desired effective material properties. Finally, an example of application of Hashin-Shtrikman based homogenization to study the prestress effects on failure behavior of a braided weave composite system is presented.

České vysoké učení technické v Praze
Kloknerův ústav

Abstrakt

Analýza kompozitních materiálů s náhodnou mikrostrukturou

Jan Zeman

Tématem prezentované práce je problematika modelování kompozitních materiálů s nepravidelnou mikrostrukturou. V práci jsou využity dva různé přístupy k analýze těchto materiálových systémů. V prvním případě uvažujeme heterogenní materiály s jasně definovanou geometrií, kdy skutečnou komplikovanou mikrostrukturu nahrazujeme podstatně jednodušší periodickou jednotkovou buňkou, která nicméně do jisté míry reprezentuje původní materiál ve smyslu zvoleného statistického deskriptoru. Periodicita jednotkové buňky je následně využita pro efektivní numerickou simulaci metodou konečných prvků. Teoretickým základem druhého přístupu jsou rozšířené Hashin-Shtrikmanovy variační principy. V tomto případě je náhodnost mikrostruktury přímo zahrnuta do variační formulace ve formě vhodných statistických deskriptorů.

Nejprve jsou popsány statistické deskriptory vhodné pro popis mikrostruktury náhodných heterogenních materiálů spolu s algoritmy vhodnými pro určení těchto deskriptorů pro digitalizované obrazy skutečných kompozitů. Důraz je přitom kladen na případnou anizotropii mikrostruktury. Přesnost a efektivita těchto metod jsou demonstrovány jak pro teoretický model mikrostruktury, tak i pro digitalizované obrazy skutečných materiálů. Následně je detailně popsána globální stochastická optimalizační metoda, kombinující principy genetických algoritmů, rozšířeného simulovaného žíhání a diferenciální evoluce, která je užita pro řešení optimalizačních problémů uvažovaných v této práci.

Parametry ekvivalentní periodické jednotkové buňky na mikroúrovni plynou z řešení optimalizačního problému, formulovaného na základě porovnání statistických deskriptorů vztažených k ekvivalentní jednotkové buňce a cílové mikrostruktuře. Vhodnost zvolené optimalizační metody je demonstrována na několika testovacích příkladech. Kvalita výsledných jednotkových buněk je následně zkoumána z hlediska celkové odezvy daného kompozitního materiálu. Jako první uvažujeme problém určení efektivních lineárně pružných vlastností kompozitu. Je podána obecná formulace tohoto problému s uvážením možnosti zatížení celkovou deformací nebo napětím. Uvedené výsledky ukazují, že jednotková buňka obsahující pět až deset vláken reprezentuje celkovou odezvu s dostatečnou přesností. Obdobné závěry plynou i pro efektivní součinitele tepelné roztažnosti a pro lineární i nelineární vazkopružnost.

Pro některé aplikace (například simulace rozsáhlých kompozitních konstrukcí) se může analýza založená na metodě konečných prvků ukázat příliš časově i výpočetně náročnou. V tomto případě lze efektivně využít jednodušších přístupů mechaniky kompozitních materiálů. Příkladem těchto metod jsou Hashin-Shtrikmanovy variační principy, rozšířené o případný vliv transformačních polí, uvažovaných v této práci. Náhodný charakter uspořádání vláken kompozitu je v tomto případě zohledněn dvojbodovou pravděpodobnostní funkcí. Kombinace této informace s Hashin-Shtrikmanovými variačními principy následně umožňuje získat meze nebo odhady efektivních vlastností kompozitů se statisticky homogenní mikrostrukturou. Získané výsledky jsou porovnány s aproximací

metodou konečných prvků. Pro daný materiálový systém se přístup založený na Hashin-Shtrikmanových variačních principech velmi dobře shoduje pro problémy lineární pružnosti, součinitele tepelné roztažnosti a lineární vazkopružnosti; rozdíl mezi oběma přístupy je nicméně dosti značný pro kompozit s nelineárně vazkopružnou matricí.

Dále je studována možnost aplikace principů použitých pro definici statisticky optimalizované mikroskopické periodické jednotkové buňky na modelování kompozitů vyztužených tkaninou plátnové vazby. Důraz je kladen na možnost zohlednění vzájemného posunu a různých tlouštěk jednotlivých vrstev kompozitu. Geometrické parametry jednotkové buňky na mezoúrovni, získané z obdobného optimalizačního problému jako v původním případě, jsou následně použity pro vytvoření konečněprvkového modelu jednotkové buňky a získání koeficientů efektivní elastické matice tuhosti. Výsledky této analýzy ukazují, že navržená metoda je vhodná pro vícevrstvé kompozity s různou výškou jednotlivých lamin za předpokladu, že posun jednotlivých vrstev není příliš velký nebo je roven přibližně polovině šířky buňky. V opačném případě se zdá být nevyhnutelné uvažovat komplikovanější dvojvrstvou jednotkovou buňku. Na závěr této práce je prezentováno užití homogenizace kombinující metodu konečných prvků a Hashin-Shtrikmanovovy variační principy pro analýzu vlivu předpnutí výztuže na porušení kompozitní trubky s komplikovanou mikro i mezostrukturou.

NOTATION

General notation

$\mathbf{a}$	Vector
$\boldsymbol{a}$	Second-order tensor
$\mathbf{A}$	Fourth-order tensor
$a_{ij}b_i$	Summation with respect to i, i.e. $\sum_i a_{ij}g_i$
$\boldsymbol{a}\cdot\mathbf{b}$	Simple contraction, i.e., $\sum_j a_{ij}b_j = a_{ij}b_j$
$\mathbf{A}:\boldsymbol{a}$	Double contraction, i.e $\sum_{kl} A_{ijkl}a_{kl} = A_{ijkl}a_{kl}$
$\operatorname{Tr}\boldsymbol{a}$	Trace of a second order tensor $\boldsymbol{a}$
$\{\mathsf{a}\}$	Column vector or vectorial representation of symmetric second-order tensor
$[\mathsf{A}]$	Matrix or matrix representation of symmetric fourth-order tensor
$\{\mathsf{a}\}^{\mathsf{T}}, [\mathsf{A}]^{\mathsf{T}}$	Transpose of vector or matrix
$[\mathsf{A}]^{-1}, \boldsymbol{a}^{-1}, \mathbf{A}^{-1}$	Inverse of matrix, second or fourth-order tensors
$\|\mathbf{a}\|$	Eucleidian norm of $\mathbf{a}$
$\|A\|$	Volume/area of domain A
∂A	Boundary of domain A
d	Problem dimension, $d = 2, 3$
$\mathrm{DFT}\{f\}(\boldsymbol{\xi})$	Discrete Fourier transform of data f
$f_{,i}$	Partial derivative $\partial f/\partial x_i$
$\widetilde{f}(\boldsymbol{\xi}), \mathcal{F}(f)(\boldsymbol{\xi})$	Fourier transform of function f
$\mathcal{F}^{-1}(f)(\mathbf{x})$	Inverse Fourier transform of function f
$\mathrm{IDFT}\{f\}$	Inverse discrete Fourier transform of the data
O	Order of growth
δ	Dirac's delta function
δ_{ij}	Kronecker's delta

Constitutive models

a_σ	Stress shift function
A	Material parameter of Leonov's model
$\boldsymbol{e}$	Deviatoric part of strain tensor
E_μ	Young's modulus of the μ-th Maxwell unit
$\widehat{E}$	Time-dependent Young's modulus of generalized Maxwell's model
G_μ	Shear modulus of the μ-th Maxwell unit
$\widehat{G}$	Time-dependent shear modulus of Leonov's model
K	Bulk modulus
$\mathbf{L}$	Fourth-order material stiffness tensor
$\{\mathsf{m}\}$	Vector of coefficients of thermal expansion
M	Number of units in generalized Maxwell models

Constitutive models

M	Fourth-order material compliance tensor
$\boldsymbol{s}$	Deviatoric part of stress tensor
$[\mathsf{T}^{\varepsilon}]$	Strain transformation matrix
$[\mathsf{T}^{\sigma}]$	Stress transformation matrix
y_{μ}	Viscous resistance coefficients of the μ-th Maxwell unit
Y_{ij}	Strength value with respect to stress state σ_{ij}
α_i	Coefficient of thermal expansion in direction i
$\boldsymbol{\varepsilon}$	Second-order tensor of small deformations
η_0	Zero shear viscosity
η_{μ}	Shear viscosity of the μ-th Maxwell unit
θ	Temperature
Θ_{μ}	Retardation time
$\boldsymbol{\lambda}$	Second-order eigenstress tensor
$\boldsymbol{\mu}$	Second-order eigenstrain tensor
ν	Poisson's ratio
$\boldsymbol{\sigma}$	Second-order stress tensor
σ_m	Mean stress
σ_{μ}	Stress in the μ-th Maxwell unit
τ_0	Material parameter of Leonov's model
τ_{eq}	Equivalent shear stress

Quantification of microstructure morphology

$\overline{f(\mathbf{x})}$	Ensemble average of function $f(\mathbf{x}, \alpha)$
$\langle f(\mathbf{x}, \alpha) \rangle$	Spatial average of function $f(\mathbf{x}, \alpha)$
c_r	Volume fraction of phase r
$D_r(\alpha)$	Domain occupied by phase r in sample α
f	Fiber phase
H	Number of bitmap rows (bitmap height)
$L_r(\mathbf{x}_1, \mathbf{x}_2)$	Lineal path function for phase r
m	Matrix phase
n	Number of phases
N_d	Number of rays of sampling template
$N_{\ell}(i)$	Number of pixels in the i-th sampling ray
r_{ij}	Length of vector $\mathbf{x}_{ij}$
R	Fiber diameter
$\mathcal{S}$	Set of material samples
$S_{rs}(\mathbf{x}_1, \mathbf{x}_2)$	Two-point probability function for phases r and s
T_H	Height of sampling template
T_W	Width of sampling template
W	Number of bitmap columns (bitmap width)
$\mathbf{x}_{ij}$	Difference $\mathbf{x}_j - \mathbf{x}_i$
Y	Periodic unit cell

Quantification of microstructure morphology

α	Index of sample
Δ_H, Δ_W	Sampling template steps
$\chi_r(\mathbf{x}, \alpha)$	Characteristic function for phase r and sample α

Stochastic optimization

F	Objective function
$ch_{ij}(t)$	Gene j of $CH_i(t)$
$CH_i(t)$	Chromozome i of generation t
$I(t)$	Individual of generation t
L	Lower bound on optimized variables
N	Dimension of optimization problem
t	Number of generations
T	Algorithmic temperature
$u(a, b)$	Real random variable with uniform distribution on closed interval $\langle a; b \rangle$
$u[a, b]$	Integer random variable with uniform distribution on closed interval $\langle a; b \rangle$
U	Upper bound on optimized variables
`b`	Shape parameter of non-uniform mutation
`num_counter_max`	Maximal number of function calls for one cooling step
`num_dif_max`	Maximal number of differential crossover applications
`num_success_max`	Maximal number of replaced individuals for one cooling step
`p_bnd_mut`	Probability of selection of boundary mutation operator
`p_dif_crs`	Probability of selection of differential crossover operator
`p_mnu_mut`	Probability of selection of multi non-uniform mutation operator
`p_nun_mut`	Probability of selection of non-uniform mutation operator
`p_sar_crs`	Probability of selection of simple arithmetic crossover operator
`p_smp_crs`	Probability of selection of simple crossover operator
`p_uni_mut`	Probability of selection of uniform mutation operator
`p_war_crs`	Probability of selection of whole arithmetic crossover operator
`pop_size`	Size of population
`q`	Probability of selection of best individual
`T_frac`	Ratio determining initial temperature
`T_frac_min`	Ratio determining minimal temperature
`T_mult`	Temperature ratio of cooling schedule

Microscale modelling via periodic fields

$\{\mathsf{b}_\mathsf{r}\}$	Thermal stress concentration vector of phase r
$\mathcal{B}$	Set of admissible vectors $\mathbf{x}^N$
$[\mathsf{B}]$	Strain-displacement matrix
$[\mathsf{B}_\mathsf{r}]$	Mechanical stress concentration matrix of phase r
$\boldsymbol{E}$	Overall strain tensor (with respect to Y)
$\{\mathsf{f}\}$	Vector of generalized nodal forces

Microscale modelling via periodic fields

$\{\mathsf{f_e}\}$	Vector of generalized element nodal forces
F_D	Objective function related to statistical descriptor D
H_1, H_2	Dimensions of periodic unit cell
$i_{\max}, j_{\max}$	Matching range of S_{mm}-based objective function
$[\mathsf{K}]$	Stiffness matrix
$[\mathsf{K_e}]$	Element stiffness matrix
$\left[\mathsf{L}^{\mathsf{fem}}\right]$	Finite element approximation to homogenized stiffness matrix
$\mathbf{L}^{\mathbf{hom}}$	Effective (homogenized) stiffness tensor
$\left[\mathsf{M}^{\mathsf{fem}}\right]$	Finite element approximation to homogenized compliance matrix
$\mathbf{M}^{\mathbf{hom}}$	Effective (homogenized) compliance tensor
N	Number of particles in periodic unit cell
$[\mathsf{N}]$	Matrix of finite element shape functions
N_e	Number of elements
$\{\mathsf{r}\}$	Vector of nodal values of fluctuating displacement
$\mathbf{u}^*$	Fluctuating displacement in Y
V	Heterogeneous body
$\mathbf{x}^N$	Vector storing position of particles in periodic unit cell
Y	Microscale periodic unit cell
$\boldsymbol{\nabla}^S$	Symmetric part of gradient
$\boldsymbol{\varepsilon}^*$	Fluctuating strain in Y
η	Ratio H_1/H_2
$\boldsymbol{\Sigma}$	Overall stress tensor (with respect to Y)
$\{\Lambda^{\mathsf{fem}}\}$	Finite element approximation to overall eigenstress vector
$\{\Upsilon^{\mathsf{fem}}\}$	Finite element approximation to overall eigenstrain vector

Microscale modeling via extended Hashin-Shtrikman variational principles

$[\mathsf{A_{rs}}]$	Microstructure-dependent matrices for primary principle
$[\mathsf{B_{rs}}]$	Microstructure-dependent matrices for dual principle
$\mathbf{L}_0$	Stiffness tensor of a reference medium
$\left[\mathsf{L}^{\mathsf{HS}}\right]$	Hashin-Shtrikman approximation to homogenized stiffness matrix
$\mathbf{M}_0$	Compliance tensor of a reference medium
$\left[\mathsf{M}^{\mathsf{HS}}\right]$	Hashin-Shtrikman approximation to homogenized compliance matrix
$U(\cdot,\cdot)$	Primary Hashin-Shtrikman functional
V	Representative volume
$V(\cdot,\cdot)$	Dual Hashin-Shtrikman functional
$\boldsymbol{\epsilon}_{\mathbf{0}}^*$	Strain Green's function
$\boldsymbol{\gamma}$	Strain polarization tensor
$\{\Lambda^{\mathsf{HS}}\}$	Hashin-Shtrikman approximation to overall eigenstress vector
$\boldsymbol{\sigma}_{\mathbf{0}}^*$	Stress Green's function
$\boldsymbol{\tau}$	Stress polarization tensor
$\{\Upsilon^{\mathsf{HS}}\}$	Hashin-Shtrikman approximation to overall eigenstrain vector

Mesoscale modeling via periodic fields

a	Mesoscale unit cell half-width
a^{ℓ}	Quantity in local coordinate system
a^{g}	Quantity in global coordinate system
b	Bundle height in mesoscale unit cell
$\left[\widehat{\mathsf{B}}\right]$	Rotated displacement-strain matrix
$\boldsymbol{E}_{\mathrm{meso}}$	Overall strain tensor (with respect to Y_{meso})
F_D	Objective function related to statistical descriptor D
g	Gap between bundles in mesoscale unit cell
$[\mathsf{G}]$	Matrix of periodic boundary conditions
h	Mesoscale unit cell height
H	Number of bitmap rows (bitmap height)
$[\mathsf{P}]$	Matrix relating displacements on opposite unit cell faces
$\{\mathsf{r}\}_{\mathrm{meso}}$	Vector of nodal values of fluctuating displacement
s_{tow}	Tow surface function
s_{warp}	Warp surface function
$\mathbf{u}^*_{\mathrm{meso}}$	Fluctuating mesoscale displacement in Y_{meso}
W	Number of bitmap columns (bitmap width)
Y_{meso}	Mesoscale periodic unit cell
$\boldsymbol{\varepsilon}^*_{\mathrm{meso}}$	Fluctuating mesoscale strain in Y_{meso}
ρ	Penalization parameter
$\boldsymbol{\Sigma}_{\mathrm{meso}}$	Overall stress tensor (with respect to Y_{meso})
θ_y^{fill}	Angle of fill bundle rotation
θ_y^{warp}	Angle of warp bundle rotation
χ_f	Bundle characteristic function
$\psi,\, \vartheta, \varphi$	Euler angles

Chapter 1

INTRODUCTION AND STATE OF THE ART

The doubtless benefits offered by composite materials such as a high strength, light weight, non-corrosive properties and design flexibility resulted in an extensive use of these materials in diverse applications in aerospace, aircraft and automobile industry in last decades. Recently, these materials have drawn an attention in Civil Engineering industry primarily in conjunction with rehabilitation and repair of concrete and masonry structures. An endless search for reliable and low cost structural and material systems resulted in inexpensive fabrication methods, such as, e.g., resin transfer moulding allowing production of complex shapes and large components, which have made composites affordable to other applications such as facade and structural parts of both commercial and industrial buildings and even bridges.

It is a well-understood and widely accepted fact that an overall response of such structures is highly influenced by both the material behavior and geometrical arrangement of distinct phases of the composite system and, as suggested by Fig. 1.1, such a research venture inevitably involves analyses on different length scales. However, each scale of modeling is typically several orders of magnitude smaller that the preceding one, which makes the direct "brute force" approach, relying on detailed description of the whole structure with all details present, practically intractable even on modern powerful computers. Therefore, to obtain a realistic prediction of the behavior of the whole structure, we need suitable solution strategies which efficiently combine the analysis on individual scales of the structure together with a reliable transfer of the appropriate information between various modeling levels. This calls for hierarchical or adaptive multi-scale modeling starting with analysis on the *macroscale*, represented by a large structural element, having certain effective or macroscopic properties derived for the analysis on the *mesoscale*, e.g., on the level on individual tows of a textile composite, which, of course, depend on the distribution of local fields on the level of individual constituents, referred to as *micro scale*.

Another complication comes from the fact that the microstructural configuration on individual levels is apparently disordered and does not comply with idealized geometries frequently encountered in the literature. Formally, this difficulty can be resolved by analyzing the so-called *representative volume elements* (RVEs) on each scale which, loosely speaking, are samples of a microstructure large enough to suitably reflect the stochastic fluctuations of material properties on the pertinent scale. The requirement of computational feasibility, on the other hand, calls for as small sizes of the RVE as possible. During the last forty years, several definitions have been proposed to quantify more rigorously the size of the RVE:

Hill (1963)[94] This phrase (the RVE) will be used when referring to a sample that (a) is structurally entirely typical of the whole structure on average, and (b) contains sufficient number of inclusions for the apparent overall moduli to be effectively

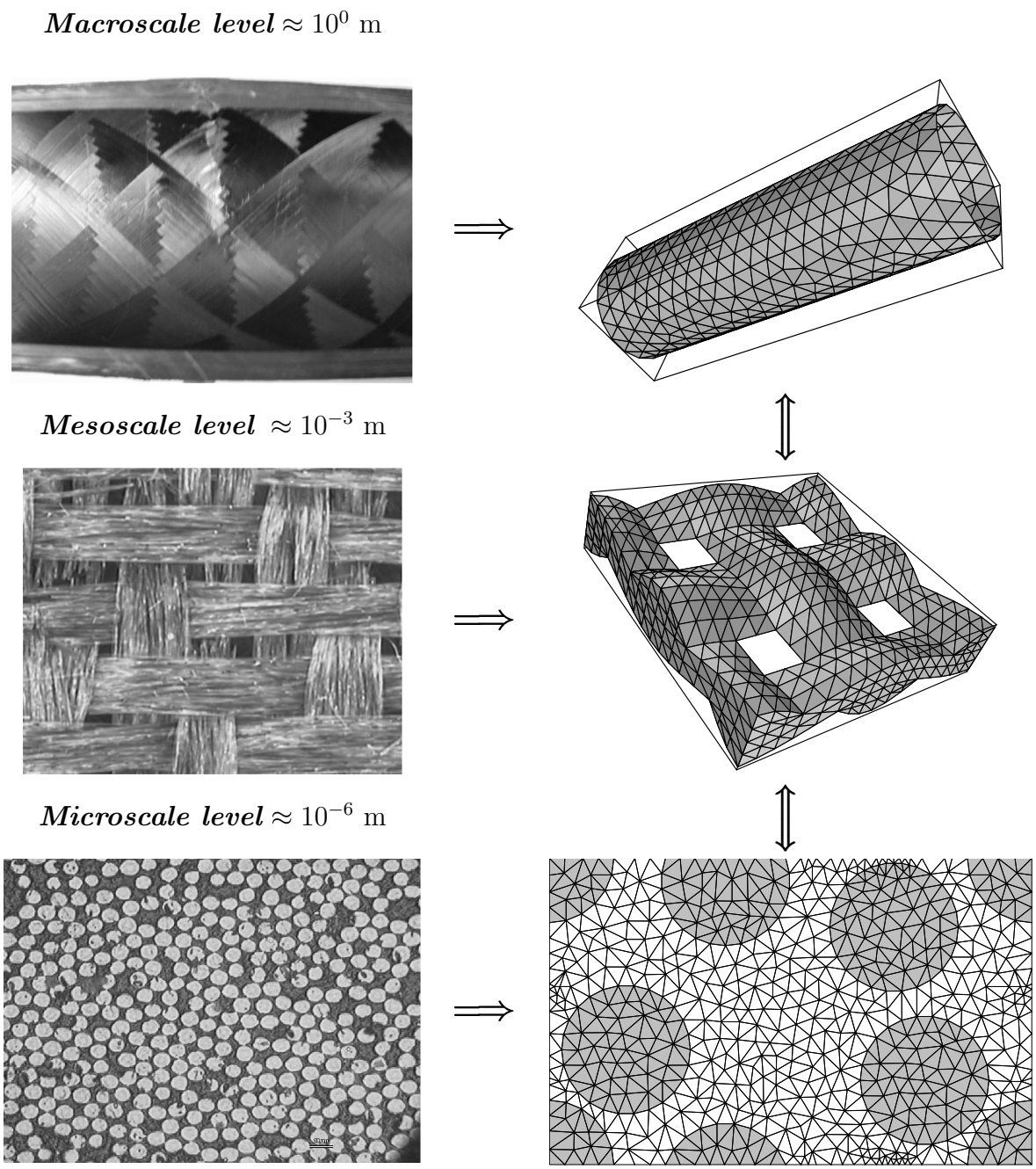

Figure 1.1: A scheme of three-scale modeling

independent of the surface value of traction and displacement, so long as these values are "macroscopically uniform".

Hashin (1983)[88] The RVE is a model of the material to be used to determine the corresponding effective properties of the homogenized macroscopic model. The RVE should be large enough to contain sufficient information about the microstructure in order to be representative, however it should be much smaller than the macroscopic body.

Drugan and Willis (1996)[49] The RVE is the smallest material volume element of the composite for which the usual spatially constant "overall modulus" macroscopic constitutive representation is a sufficiently accurate model to represent the mean constitutive response.

Ostoja-Starzewski (2001)[188] The RVE is very clearly defined in two situations only: (i) it is a unit cell of a periodic microstructure, and (ii) volume containing a very large set of microscale elements, possessing statistically homogeneous and ergodic properties.

Stroeven, Askes and Sluis (2002)[239] The determination of the RVE size is by no means straightforward. It depends on the material under consideration, but also on the structure sensitivity of the physical quantity that is measured. Normally, elastic moduli are taken as the governing parameter, however, other quantities can also be taken, such as energy dissipation in case of microstructural cracking.

The main goal of the present thesis is to introduce and justify an alternative approach to the RVE definition, which essentially relies on microstructural statistics. In particular, the original microstructure configuration is characterized by suitable statistical descriptors and then a simplified *periodic unit cell* is found such that it approximates the target microstructure as close as possible in terms of selected statistical descriptors. There are definitely several interesting features, supporting this notion of the RVE: (i) it leads to a natural sequence of periodic unit cells with increasing complexity, (ii) it exploits the well-known relationship between effective behavior of composite materials and microstructural statistics (a topic addressed in in this thesis as well, see Chapter 4), (iii) resulting periodic unit cells have well-defined geometry, can be directly used for numerical homogenization techniques without the need of stochastic simulations, (iv) the numerical assesment can be performed for a selected quantity of interest to choose an appropriate size of the representative volume, (v) since the microstructure of the periodic unit cells is optimized, a quick convergence of the quantity of interest can be expected. The assumption of microstructure periodicity, on the contrary, may appear to be rather artificial and inappropriate for real materials; the recent numerical studies of Terada et al. [251] as well as theoretical analyses of Sab [221] and Ohwadi [189] revealed that the periodicity conditions are surprisingly well suited for the analysis of materials with disordered microstructure.

To successfully implement and verify the present definition of the RVE, a variety of tools and ideas coming from different branches of science needs to be explored: namely, the quantification of microstructure morphology, stochastic optimization algorithms, homogenization of heterogenous materials, variational principles for composites with disordered

microstructure and the numerical methods for the modeling of textile composites will be combined to attain the goal we set. In the following, we introduce and discuss each of these topics in more details.

1.1 RVE definition and analysis of microstructure morphology

Since a rather detailed overview and discussion of the RVE definition was given in the introductory part, we start this section by giving only a few clarifying remarks. The concept of the Representative Volume Element was first established by Hill in one of his fundamental works [94]. Much later, the ideas present in Hill's definition were generalized by Huet [106], who extended these results for bodies which are smaller than the Representative Volume by introducing a notion of *apparent overall properties*. He also derived several useful relations for apparent elastic properties of samples with varying size. The work was further extended to incorporate boundary condition effects by Hazanov and Huet [91] for elastic bodies, by Huet [107] for the case of viscoelasticity and by Jiang et al. [116] for elasto-plastic composites. The numerical assesment complementing the theoretical analysis can be, e.g., found in works [187, 196]. The analysis of the "goal-dependent" minimum RVE size, initiated by Drugan and Willis [49], received a considerable attention in the last few years. On the theoretical level, it was further refined by Drugan [48], who incorporated higher order effects neglected in the original work. The numerical validation was performed by Gusev [85] for three-dimensional linear elasticity and by Rend and Zheng [209] for polycrystalline materials, the extension to nonlinear material behavior was studied by Stroeven et al. [239]. The idea of incorporating the microstructural information into the definition of the RVE was, to author's best knowledge, first proposed in the work of Povirk [202] for a rather artificial material system and further extended by Zeman and Šejnoha [298] for analysis of real materials described by isotropic microstructural function. Somehow related approach, relying on computer generation of hard-core model with varying particle sizes mimicking real microstructures, was independently proposed by Shan and Gokhale [225].

There is an enormous amount of literature on description and quantitative analysis of the morphology of random heterogenous media. Apart from obvious goal of simulating disordered microstructures experimentally observed in real materials, this research has been fueled by the fact that these statistical descriptors arise in rigorous bounds of diverse physical quantities, see, e.g., the pioneering work of Beran [18, and references therein]. Due to such a wide range of topics, it is almost impossible to review the subject adequately; instead of this, we focus on problems touched in the present work and refer an interested reader to book of Stoyan et al. [238] and recent Torquato's monograph [257] or the overview article [255] for further discussion.

In particular, the approach followed in the discussion of the n-point probability function is due to Torquato and Stell [258]; the notion of the lineal path function was introduced by Lu and Torquato [147]. The pioneering work devoted to determination of n-point probability functions for micrographs of real media is attributed to Corson [39]. Despite the fact that his procedure was rather cumbersome (it was based on manual evaluation of photographs taken from samples of the real material) the principle itself (evaluation of the characteristic function on some sampling grid and then averaging the corresponding values) was used and extended in following works. Berryman [19] auto-

mated the Corson's procedure by image processing techniques, simple simulation method for the determination of functions S_n, suitable for non-digitized media as well, was proposed by Smith and Torquato [232]. Note that a similar approach is employed in this work for the determination of the lineal path function.

In the last decade, an increasing attention is paid to combination of microstructure quantification with stochastic or deterministic numerical simulation to capture, at least quantitatively, deformation processes, such as plasticity or damage, in real materials. Pyrz [205] investigated relation between radial distribution function and stress distribution in fiber reinforced composites, Axelsen in his Ph.D. thesis [7] proposed a classification scheme of different microstructural configuration together with an efficient method for the evaluation of stress fields, Babuška et al. [10] presented detailed microstructural analysis of fiber-reinforced composites combined with extensive numerical simulation to obtain statistics of peak stresses to predict the damage propagation in fibrous composites, Li et al. [145] used the lineal path function characterization together with the radial distribution function and the Voronroi tessellation method to characterize three-dimensional particle reinforced metal matrix composites, Buryachenko et al. [29] compared the statistical parameters and overall response of numerically simulated and real microstructures, and the list is by no means complete.

The subject of the present thesis is also closely related to the problem of reconstructing random media with the specified microstructural function. In particular, Rintoul and Torquato [211] proposed a method for reconstruction of particulate systems based on the radial distribution function and the Simulated Annealing method. This work was further extended by Yeong and Torquato [291], where the isotropized lineal path and the two-point probability functions were used in the reconstruction process; the problems of three-dimensional microstructures reconstruction from two-dimensional cross-sections [292] and real-world materials [152, 247] were also considered. The importance of using non-isotropized descriptors was recognized and addressed in [41] and further extended in [226], where the hexagonal grid sampling was advocated. Finally, the recent work of Rozman and Utz [216, 217] revealed that the non-uniqueness problems, reported in previous studies, can be, to a great extent, attributed to the artificial isotropy of optimized function and to convergence of the selected optimization method to a local minimum.

1.2 Stochastic optimization methods

In general, the optimization algorithms can be divided into two large groups: local optimization methods, that operate on a single potential solution and look for some improvements in its neighborhood, and global optimization techniques – represented here by so called *evolutionary methods* – that maintain large sets of potential solutions and apply recombination and selection operators to obtain better solution. During the last decades, evolutionary methods have received a considerable attention and experienced a rapid development, mainly due to their simplicity, versatility and remarkable robustness. Namely, the *Genetic Algorithms*, *Simulated Annealing* and the *Differential Evolution* established themselves as the most prominent representatives of stochastic optimization algorithms.

Genetic Algorithms (GAs). This class of evolutionary methods is formulated on the basis of analogy with the real-world genetic processes of biological organisms – the evolution and self-organization of natural systems over many generation according to the principle of natural selection and "survival of the fittest" paradigm. In reality, individuals of one population compete with each other for limited natural resources and for attracting a mate. Those which succeed in obtaining resources and attracting mates will have a large number of offsprings, while individuals performing poorly will produce smaller number of descendants and eventually die out. As a result of this process, the abilities of successful individuals are more likely to be passed to following generations and result in better adaption to the environment. GAs closely mimic all these natural processes – they work with a whole *population* of individuals, each representing a solution to a given problem. A *score* or *fitness* is assigned to each individual depending on how good solution it presents. The individuals with higher fitness are more likely to be reproduced by *crossover* and to pass their characteristics to their offsprings. Moreover, an individual can also undergo a *mutation* if appropriate. In this way, over a number of successive populations, the good characteristic of individuals are mixed and spread over all population, so that it converges to the optimal solution.

The earliest work on this subject was in fact Darwin's *Origin of Species* where the fundamental role of aforementioned principles was first revealed. The basic ideas of GAs were first rigorously laid down by Holland [99], the detailed discussion on these methods can be found, e.g., in [14, 81, 138, 159, 164]. Note that in their classical formulation, GAs work with the binary representation of optimized variables, which is not always very well suited for real-world problems. To overcome this difficulty, Michalewicz in [160] proposed a variant of GAs, which uses the floating-point representation of searched variables and demonstrated the superiority of the real-encoded operators for a wide range of constrained and unconstrained optimization problems.

Simulated Annealing (SA). The motivation of the Simulated Annealing method comes from physical rather than biological principles; it effectively explores the analogy between optimization problem and the annealing process of solid bodies. In the physical process of annealing the temperature of a solid is kept rather high initially and then decreases sufficiently slowly so that the individual particles have the possibility to attain the state with the minimal energy for a given constant temperature. As the temperature gradually decreases the energy of the whole body decreases as well and finally reaches the minimum value. SA algorithm works on the same principle - initial solution is created randomly, some artificial parameter called *temperature* is set to a starting value and new solutions are randomly generated. If the new solution is better than the preceding one in terms of fitness, it is accepted automatically and replaces the original solution. However, even if the new solution is worse, it still has a chance to replace the original solution (the probability depends on the difference of objective function and the actual temperature), which enables the solution to escape from a local minimum. This procedure is repeated a number of times for a constant temperature and then the temperature is decreased until it reaches certain prescribed minimal value. This version of algorithm was first proposed by Kirkpatrick et al. [120] and independently by Černý [265]. Detailed discussion of basic principles and further aspects of the Simulated Annealing method can be found, e.g., in [108, 109, 138].

To solve complex optimization problems, Mahfoud and Goldberg [150, 151] introduced the efficient combination of GAs and SA methods. This algorithm exploits the essentials of GAs (a population of chromozomes, rather than a single point in space is optimized) together with the basic concept guiding the search towards minimal energy states. Some additional suggestions and implementation issues of this method are also given in [138, Chapter 6].

Differential Evolution (DE). This evolutionary algorithm has been recently proposed as an efficient solution method for the Chebychev trial polynomial problem by Storn and Price [237]. It can be generally described as a simplified real-encoded genetic algorithm – this method operates directly on real valued chromozomes and uses the so-called differential operator, which replaces the role of the cross-over in the standard genetic algorithm. In particular, it generates a new individual by adding the weighted difference between two randomly chosen individuals in a population to a third vector. The mutation operator as well as selection mechanism are completely neglected. The main advantage of this method is its conceptual simplicity and good convergence properties for objective functions with relatively small number of parameters. The numerical experiments reported by Hrstka and Kučerová [103] revealed, however, that performance of the Differential Evolution method experiences a substantial deterioration for optimization problems with a large number of variables. On the other hand, the remarkable performance of the differential crossover operator was fully confirmed. More details together with the description of further modification of this evolutionary optimizer can be found in [236, 237].

1.3 Multiscale modeling

The multiscale computational strategies can be divided into two basic categories: the *uncoupled approach*, where the problems on individual scales are solved separately and the output from one scale, e.g., the average stress or strain, is used as the input for the analysis on the second one and the *coupled approach*, where the whole structure with all significant details is modeled.

As already mentioned in the introduction, the fully coupled approach in not computationally feasible except for simple geometries (including problems with periodic microstructure) or for structures with not very different lengthscales. A variety of efficient and sophisticated solution techniques, exploiting the multiscale nature of the problem, were proposed in the last decade. The multiresolution analysis was employed by Brewster and Beylkin [26] and Dorobantu and Engquist [47] to obtain hierarchical representation of solution on individual levels of a structure, the application of multigrid methods for numerical homogenization is discussed, e.g., in the work of Neuss et al. [179] while the aggregation-based multilevel solver was implemented by Fish and Belsky [65] and Fish et al. [71]. Hackbusch and Sauter [87] introduced the notion of composite finite element to study problems on domains containing small geometrical details. Finally, Hou and Wu discuss in [101] a general multiscale finite element method, where the basis functions are constructed to directly accommodate the local distribution of material parameters.

The rigorous analysis of a coupled problems with periodic microstructure based on the Fourier transform techniques was presented in the work of Morgan and Babuška [170,

171]; their theoretical results were recently successfully implemented within the framework of the generalized finite element method by Matache et al. [155] and Matache and Schwab [156]. Similar principles were employed in several physically motivated finite element definitions fitted to a special microstructure, see, e.g, the works of Meguid and Hu [158] and Haan et al. [86]. Employing the ideas of uncoupled modeling approach, Fish and Belsky proposed an efficient multigrid procedure for the multiscale analysis of problems with periodic microstructure [63, 64].

The enormous computational burden of fully coupled approach can be, of course, reduced by exploiting the adaptive modeling, i.e., only the most critical parts of the analyzed structure are modeled in very details. If the location of such regions is known a priori, as, for example, in the case of sharp corners or notches, the mesh overlay techniques can be advantageously used, see, e.g., extensive overview of Fish and Shek [69] and the work of Takano et al. [244] for an application to problems similar to those encountered in this thesis. Ghosh and coworkers [77] used heuristic microstructural-based error indicator for automated adaptive modeling. Finally, a rigorous framework of goal-oriented modeling employing a posteriori error estimation has recently been introduced by Oden and coworkers [183, 185] and applied to the hierarchical analysis of heterogeneous materials [184, 266].

The uncoupled multiscale approach, on the other hand, implicitly relies on the periodicity of the microstructure and the multiple scale expansion method (see fundamental works of Babuška [8], Bensoussan et al. [16] and Sanchez-Palencia [222, 223] for more detailed discussion). Loosely speaking, this method is based on expansion of the searched solution in powers of ε, a small parameter related to a ratio of different length scales, which is plugged into the governing equations of the problem. The terms corresponding to a different powers of ε yield a hierarchy of equations to be solved on each scale. The solution procedure starts from the lowest scale, then proceeds to higher scales, where the averaged quantities from the lower scale are supplemented as the input to the upper one. This allows rather natural physical interpretation of, for example, the averaged stress-strain relationship as a general form of constitutive equations for heterogenous materials. Moreover, this formalism is especially well-suited for numerical implementation in the common framework of the finite element method, and, as such, it is also employed in this work. The uncoupled modeling approach was studied in diverse works, we briefly mention just a few of them. Fish and coworkers in a formidable collection of papers applied this strategy to various problems of computational solid mechanics, starting from small strain [70] and finite deformation [68] plasticity, viscoplasticity [67], damage mechanics [72, 74], wave propagation [66] and fatigue problems [73]. An excellent discussion on physical aspects of uncoupled approach can be found, e.g., in the work of Kouznetsova et al. [124] with the extension to gradient continuum theories considered in [125]; Sluis et al. [262] examined the effect on microstructural modeling on overall response of nonlinear materials. A general framework for uncoupled multiscale computational inelasticity was provided in recent works of Terada et al. [252] and Miehe [163].

1.4 Microscale modeling

With respect to the topic of the present work and the discussion above, we focus our attention on the three-scale uncoupled modeling approach, i.e., we assume that the analysis

is now decomposed into three different problems on microscale, mesoscale and macroscale, respectively and, in addition, the geometry on macroscale and microscale levels is periodic. This section focuses on the aspects of the microscale modeling, while the mesoscale strategies are postponed to Section 1.5[1].

In contrary to the discussion on the general multi-scale analysis, which was concerned solely with numerical aspects of the modeling, the overall behavior on microstructural level can be estimated either by analytical methods, based, e.g., on equivalent inclusion method, series expansion or variational principles, or by numerical methods typically relying on the microstructure periodicity. A variety of analytical methods for the microstructural modeling stems from the famous Eshelby's finding [61] that the stress field in an ellipsoidal inclusion in a medium subjected to a far-field stress is also uniform. This result led to a variety of approximate techniques exploring the presence of uniform fields within the composite improving the dilute approximation [58] such as the self-consistent method of Budiansky [27] and Hill [96] and the Mori-Tanaka theory [172], respectively its reformulation by Benveniste [17]. See, e.g., reviews by Laws [140] and Walpole [274] for more detailed discussion. These ideas were later generalized to inelastic composite materials by Dvorak and Benveniste in the framework of the Transformation Field Analysis [51, 52].

The second category of the effective medium theories is based on variational principles for composite media, starting from the well-known result of Hill [93] who showed that the Voight [267] and Reuss [210] estimates for polycrystals yield rigorous bounds on the effective stiffness tensor. Hashin and Shtrikman in their famous article [89] proposed new variational principles and applied them to obtain bounds on bulk and shear moduli for binary isotropic composites with well-ordered phases. Subsequently, their discovery was extended by numerous authors; Walpole [273] removed rather technical assumption on well-ordered phases considered in the original work. Kröner [133] and Willis [285] provided statistical interpretation of the Hashin-Shtrikman bounds and showed that they actually explicitly incorporate information about the microstructure morphology (see also overview articles [134, 286] for more detailed discussion on these topics). Willis [287] extended these principles for modeling of wave propagation in heterogenous media, an alternative interpretation of Hashin-Shtrikman variational principles in the framework of translation method was provided by Milton [166] and Milton and Kohn [168]. The extension of Hashin-Shtrikman variational principles to non-linear composites based on introduction of a linear comparison medium was proposed by Ponte Castañeda [198] and Talbot and Willis [246] (see the overview by Ponte Castañeda and Suquet [200] and the most recent work of Ponte Castañeda [199] for more detailed discussion and an inventory of applications). Nesi et al. [178] presented the comparison of non-linear variational principles and the translation method. We conclude this brief list of applications of Hashin-Shtrikman variational principles by mentioning the recent work on relaxation of non-convex variational problems by Smyshlyaev and Willis [233, 234].

Kröner [133] and Willis [286], among others, derived the series expansion of the effective moduli and local fields. Moreover, Kröner showed that the truncated series can be advantageously used as trial fields in classical variational principles to obtain bounds incorporating higher-order correlation functions. These results were further extended by

[1] Note that this terminology is rather formal as some methods described in this section can be applied to mesoscale modeling with only minor changes. We adopted this nomenclature to follow the scheme displayed in Fig. 1.1 and to distinguish the methods specialized to the analysis of woven composites.

Torquato [256] who proposed an alternative series expansion incorporating n-point probability functions; see also Ph.D. thesis of Derr [45] for implementation of this theory for real-world materials. Finally note that more details and exhaustive discussion on the topics merely outlined here can be found in outstanding recent monographs by Milton [167] and Torquato [257].

Apart from a variety of tools coming from analytical modeling many numerical techniques have been explored for the solution of microscale problems. We begin with the most common finite element method employed for the solution of the unit cell problem, pioneered by Bourgat [22] and further extended, for example, by Guedes and Kichuki [84], Holmbom et al. [100], Suquet [241] and Michel et al. [161]. An alternative homogenization method based on Bloch decomposition method [38], originally devised for the study of wave propagation in periodic materials, has been recently proposed by Conca and Natesan [37]. In addition, the boundary element techniques were used by Eischen and Torquato [59] and Okada et al. [186], Ghosh et al. [78] employ the Voronroi cell method to efficiently solve unit cells with multiple inclusions. Motivated by the analysis of problems with a complicated microstructure, obtained typically from the image analysis of real materials, the digital image-based method was introduced by Terada et al. [253] (see, e.g., the work of Nagai et al. [176] for application of this method for analysis of three dimensional concrete microstructures), while Moulinec and Suquet [173] and Michel et al. [162] use the iterative method based on the fast Fourier Transform. Finally note the work of Greengard and Helsing [83] where an efficient method for the analysis of planar isotropic composites based on fast multipole method was used to compute the effective elastic moduli of complex microstructures with ten digit accuracy.

1.5 Analysis of woven fabric composites

Similarly to the microstructural modeling, the overall properties of woven fabric composites can be obtained either by numerical simulation methods or simplified engineering analytic approaches. The complex three-dimensional structure of woven fabric composites results in rather extensive computational problems, therefore a variety of heuristic homogenization procedures based on various simplifying assumptions has been proposed. Moreover, to author's best knowledge, all works dealing with the numerical analysis of woven fabric composites rely on the finite element method approaches[2], a situation totally different from microstructural modeling, where a variety of different routes can be pursued. Note that, due to their manufacturing process, the structure of woven composites can be, at least theoretically, fully described by one periodic unit cell, which makes asymptotic homogenization techniques rather attractive for the analysis of these materials.

The analytical methods for woven fabric composites start either from modified classical laminate theories (CLT) or basic energy principles. The CLT-based approach was pioneered in the series of works by Ishikawa and Chou, who used the the one-dimensional fiber undulation model [112], two-dimensional mosaic model [110] relying on piecewise constant geometry and the bridging model [111] combining features of the two previous approaches to analyze elastic behavior of a variety of woven fabric composites. The

[2] The fast Fourier transform based analysis was examined in the work of Wierer [283]. Unfortunately, the complex structure of woven fabric composites causes serious convergence problems which has not been satisfactory resolved yet.

experimental validation of these methods can be found, e.g, in Ishikawa et al. [113]. Naik and Shembekar in [177] extended these results by considering a more refined version of the woven composite geometry. See, e.g., the overviews by Cox and Flanagan [40], Raju and Wang [207] and Tan et al. [248] for more detailed discussion on these methods. Note that although modeling strategies based on classical laminate theory show a reasonably good correspondence with experiments for special types of loading, the numerical study of Whitcomb and Tang [280] demonstrated that their success can be attributed to error cancellation rather that to sound physical justification of simplifying assumptions.

The alternative approach to analytical modeling of woven composites is based on the classical energy principles; starting either from the simplest assumption on constant strain or stresses within a fabric composite resulting in stiffness/compliance averaging techniques, see, e.g., works of Kregers and Malbardis [130], Pastore and Gowayed [192], Weissenbach et al. [275] and Sheng and Hoa [228], or considering more refined version based on decomposition of the woven composite basic unit cell into several sub-cells and subsequent minimization of given energy functional assuming piecewise constant variation of fields within sub-cells (note that conceptually similar method was introduced by Aboudi [3] for general composite materials), see, e.g. the works of Pastore et al. [191], Vandeurzen et al. [263, 264] and Tabiei and Yi [243] for implementation of this methodology. The mixed variational principles were explored by Roy and Sihn to obtain reliable stress distribution in woven composites [215]. Kuhn et al. [136] employed the Ritz method to get a trigonometric series expansion of the displacement field for the in-plane loading conditions for a particular geometrical model of woven composite; this technique was further extented by Marvalová [154] by introducing the "brick method", which is free of any geometry assumptions. The Mori-Tanaka method has also been employed for the determination of overall elastic properties of composite materials by Gommers et al. [82].

In the last decade, the finite element-based methods has been employed for the analysis of woven fabric composites. It originated from the pioneering works of Zhang and Harding [300] for a simplified two-dimensional model and by Paumelle at al. [194, 195] for a fully three-dimensional behavior. These studies were further followed by Dasgupta and Bhandarkar [44, 43], Chapman and Whitcomb [34] and Whitcomb and Sriregan [279]. The automated CAD-based finite element procedures for the modeling of woven composites are discussed in the work by Wentorf et al. [277], Takano et al. [244] employed the mesh overlay technique to study composite structures with small geometrical details; the effect of woven architecture on overall permeability was recently addressed in [245] by the same authors. To reduce the computational work associated with modeling of woven fabric composites, the local-global finite element method based on static condensation was proposed by Whitcomb et al. [282, 281]. This technique was further employed by Woo and Whitcomb for studies on failure behavior [288], reinforcement imperfection [288] and reliable recovery of local stress distribution [290]. Recently, efficient mesh generation procedures, tailored to the needs of adaptive analysis of woven composites, were proposed by Kim and Swan [118, 119]. In last few years, a number of comparative studies emerged in the literature, an excellent discussion and overview of various topic associated with engineering analysis of textile composites can be found in the report of Cox and Flanagan [40] and an extensive numerical comparison of various methods is presented in the works of Byström et al. [30], Chung and Tamma [36], Tabei and Yi [243] and Whitcomb et al. [278].

Although all the above analyses are based on the idealized geometry of woven fabric

composites, it is well-understood that the overall behavior is to a great extent influenced by imperfections appearing during the fabrication process. On the experimental level, these effects were qualitatively investigated in several works, see, e.g., Breiling and Adams [25], Košek and Košková [128], Roy [214] and Yurgartis et al. [294]; the systematic classification and discussion of sources of individual types of imperfection was proposed by Pastore [190]. The theoretical studies of this phenomenon were addressed in the framework of laminate theories by Shembekar and Naik [227] who incorporated a possible shift of individual layers in their model and in the excellent work of Yushanov and Bogdanovich [295, 296], who considered a general random imperfections to the tow path and used the stiffness averaging method to obtain statistics on the overall elastic moduli. For numerical studies of this phenomenon see the works of Woo and Whitcomb [289] for the three-dimensional geometry of the woven fabric composite and Byström et al. [30, 115] for a simplified two-dimensional model.

1.6 Present work

The topics addressed in the present work are confined to the problem of unit cell definition on the meso and microscale levels based on microstructural statistics and to an efficient alternative method incorporating the appropriate statistical descriptors on the microscale level. Various novel approaches and ideas discussed so far are introduced here in very details and applied to composite materials with elastic, thermoelastic and linear and non-linear viscoelastic phases. An attention is paid to unified representation of all these constitutive models in the framework of eigenstress and eigenstrain fields and incorporation of both the overall stress and strain driven response, which allows to present a rather extensive comparison and discussion of similarities and differences between individual modeling strategies.

The work is organized as follows. Chapter 2 reviews basic statistical descriptors for the two-phase random medium. First, the concept of an ensemble is briefly discussed and the principle of *ensemble averaging* is outlined. Then, microstructural descriptors suitable for the characterization of the two-phase two-dimensional media are introduced together with methods for their evaluation with emphasis put on reflecting possible anisotropy of the media. Example results illustrate their applicability for the selected types of theoretical as well as real-world microstructures. The chapter ends with description of the stochastic optimization algorithm used for the solution of various minimization problems encountered in the following chapters.

Chapter 3 deals with the micromechanical analysis of periodic microstructures by means of the finite element method. It takes the reader through a complex optimization process, which provides a unit cell with the sub-optimal material statistics as the real composite. The resulting periodic unit cell is then subjected to a set of thermomechanical loading conditions leading to uniform overall stress and strain fields. Applications to material systems prone to viscoelastic deformation are visited in conjunction with the generalized viscoelastic models of the Maxwell type.

Micromechanical analysis of random composites combined with the Hashin-Shtrikman variational principles is the subject of Chapter 4. Both the primary and dual principles, extended to account for the presence of initial strains, are revisited in a systematic way. The main objective are macroscopic constitutive equations incorporating the random

nature of the microstructure. The Fourier transform based approach is suggested to derive various microstructure dependent tensors or matrices entering the overall constitutive law.

The extension of principles employed in Chapter 3 to the modeling of woven fabric composites is presented in Chapter 5 to incorporate the longitudinal shift of individual tows into the model of the periodic unit cell proposed by Kuhn and Charalambides [135]. In particular, the parameters of the idealized periodic unit cell are found by matching appropriate statistical descriptors related to the target microstructure and two-dimensional cross-section of the geometry model. Geometrical parameters derived from the optimization procedure are then used to generate an equivalent periodic unit cell, which is then combined with the finite element method analysis to provide the desired effective material properties of a composite. The chapter ends with an example of application of Hashin-Shtrikman based homogenization to study the prestress effects on failure behavior of braided weave composite systems.

Theoretical background and technicalities related to previous chapters are exposed in associated appendices. Appendix A lists the constitutive models used in this work, technical details related to the Hashin-Shtrikman variational principles are gathered in Appendix B. Finally, a mathematically rigorous analysis of the uncoupled modeling is presented in Appendix C to justify the intuitive engineering approaches used in this text.

Chapter 2

QUANTIFICATION OF MICROSTRUCTURE MORPHOLOGY

Traditional micromechanical analysis of composite media with disordered microstructure is typically based on very limited microstructural information such as volume fraction of individual phases[1]. However, when a certain additional knowledge of the real microstructure is available, the estimates of local fields can be improved by treating random composites (see, e.g., [131, 133, 134, 255, 257, 285, 286] and references herein). Such a modeling framework is considered throughout this text.

This opening chapter outlines evaluation of various statistical descriptors, which arise in the analysis of binary microstructures with random arrangement of individual phases. With regard to specific applications discussed in the following chapters (analysis of the graphite fiber tow embedded in the polymer matrix and two-dimensional sections of plain weave composites), the background introduced in this chapter is quite general and can be applied to any two-phase random heterogeneous medium of arbitrary phase geometry[2]. The chapter ends with the description of stochastic optimization algorithm used for solving various minimization problems encountered in Chapters 3 and 5.

Section 2.1 reviews basic concepts and hypotheses associated with quantification of microstructure morphology. Individual statistical descriptors used in the present work are introduced in Sections 2.2. The methods of their numerical evaluation are presented in Section 2.3 together with numerical examples for a theoretical model of microstructure. Then, extension to real-world composite systems is provided in Section 2.4. Finally, a stochastic optimization algorithm is discussed in Section 2.5.

2.1 Basic concepts and hypotheses

Motivation. To introduce the subject, imagine a collection of a large number of micrographs describing the geometry of a two phase fibrous composite. An example of such a micrograph is displayed in Fig. 2.1. Fig. 2.1a represents a portion of a graphite–fiber tow containing approximately twelve thousand fibers. A random cut consisting of about three hundred fibers is shown in Fig. 2.1b. Although having a large number of fibers, one can hardly assume that such a representative can completely describe the morphology of the whole composite. Simply taking similar micrographs from other parts of the fiber tow indicates visual difference in the microstructure from sample to sample. At this point, we

[1] Namely, stiffness and compliance averaging method [94, 210, 267], dilute approximation [58], self-consistent method [27, 96], differential scheme [182] and Mori-Tanaka method [17, 172] fall into this category.

[2] In the case of *particulate* composites, a variety of specialized microstructural descriptors can be used for microstructure characterization, see, e.g, [205, 212, 238, 255, 257, 271] and improved estimates of local fields [153, 201, 255]. Moreover, we refer a more theoretically oriented reader to [238] for mathematically rigorous discussion related to subjects of this chapter.

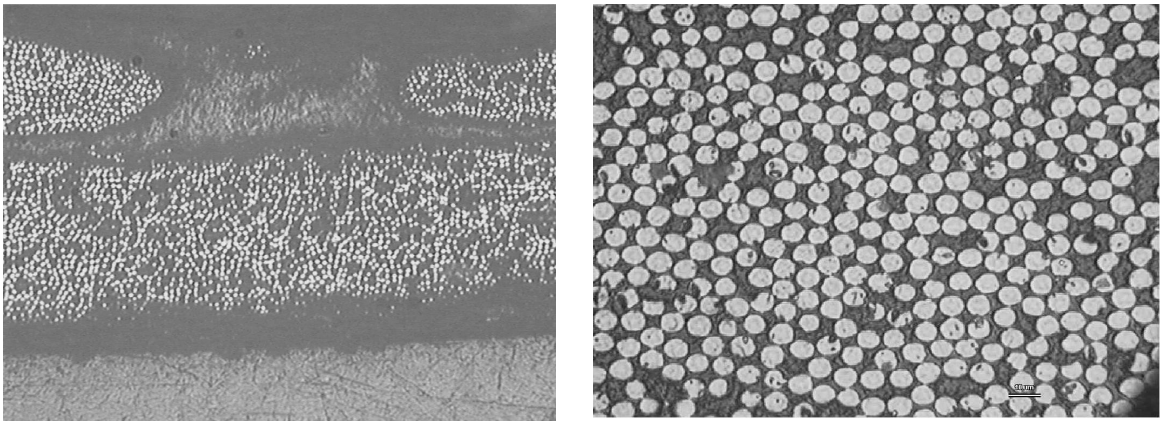

(a) (b)

Figure 2.1: A real micrograph of a transverse plane section of the fiber tow

should perhaps ask ourself whether there is a reliable approach in modeling of composite materials, which permits in some way incorporating elements of real microstructure into the analysis. The answer is affirmative once we recognize the *random nature* of geometrical arrangements of phases and treat random composites – it means that the particular microstructure of a given part of a fiber tow yields only one possible arrangement of phases. Therefore, instead of determining the exact value of some quantity at a given point (which is sample dependent), attention is given to its *expected* or *averaged* or *macroscopic* value, which incorporates information from all samples taken from a material.

2.1.1 Concept of an ensemble

To reflect a random character of a heterogeneous medium it is convenient to introduce the concept of an *ensemble* – a set of a large number of systems which are different in their microscopical details but they are entirely identical within a point of view of macroscopic scale (see, e.g., [18, 88, 131, 133, 137, 286]). Random nature of such material systems further suggests that individual members of the ensemble, to be statistically representative of the composite, should be sufficiently large compared to the microstructural length scale (e.g., fiber diameter).

To begin, consider a sample space $\mathcal{S}$ defined here as a collection of material samples similar to one of Fig. 2.1b. Formation of $\mathcal{S}$ then opens a way to provide an estimate for effective or expected value of some quantity, say stress or strain field, through the process of its averaging over all systems in the ensemble. To proceed, identify individual members of this space by α and define $p(\alpha)$ as the probability density of α in $\mathcal{S}$ (see [122, 131, 134, 286] for further reference). Then, the *ensemble average* of function $F(\mathbf{x}, \alpha)$ at a point $\mathbf{x}$ is provided by

$$\overline{F(\mathbf{x}, \alpha)} = \int_{\mathcal{S}} F(\mathbf{x}, \alpha) p(\alpha) \, \mathrm{d}\alpha. \tag{2.1}$$

Following the above definition would require experimental determination of the ensemble average of function $F(\mathbf{x}, \alpha)$ for a given point $\mathbf{x}$ through the cumbersome procedure of manufacturing a large number of samples (which form the ensemble space $\mathcal{S}$), measuring $F(\mathbf{x}, \alpha)$ for every sample and then its averaging for all samples. Therefore, it appears

meaningful to introduce certain hypotheses regarding the ensemble average, which substantially simplify this task.

2.1.2 Ergodic hypothesis

This hypothesis demands all states available to an ensemble of the systems to be available to every member of the system in the ensemble as well [18, 131, 137, 221, 238]. Once this hypothesis is adopted, *spatial* or *volume average* of function $F(\mathbf{x}, \alpha)$ given by

$$\langle F(\mathbf{x}, \alpha) \rangle = \frac{1}{|V|} \int_V F(\mathbf{x} + \mathbf{y}, \alpha) \, \mathrm{d}\mathbf{y}, \tag{2.2}$$

is independent of α and identical to the *ensemble average* for $|V| \to \infty$, i.e.,

$$\langle F(\mathbf{x}, \alpha) \rangle = \overline{F(\mathbf{x}, \alpha)}, \tag{2.3}$$

for all $\alpha \in \mathcal{S}$. This hypothesis allows an examination of only one arbitrary member of the sample space, provided that the sample is "sufficiently large". A possible way to fulfill this condition is to assume a periodic composite described by a unit cell Y. Then [221],

$$\lim_{|V| \to \infty} \frac{1}{|V|} \int_V F(\mathbf{x} + \mathbf{y}, \alpha) \, \mathrm{d}\mathbf{y} = \frac{1}{|Y|} \int_Y F(\mathbf{x} + \mathbf{y}, \alpha) \, \mathrm{d}\mathbf{y}, \tag{2.4}$$

so for the ergodic periodic composite medium, the ensemble average of $F(\mathbf{x}, \alpha)$ is equal to the volume average taken over the unit cell.

2.1.3 Statistical homogeneity

Suppose that function F depends on n vectors $\mathbf{x}_1, \ldots, \mathbf{x}_n$. If the material is *statistically homogeneous* the ensemble average of F is invariant with respect to translation [18, 238, 258], so the relation

$$\overline{F(\mathbf{x}_1, \ldots, \mathbf{x}_n)} = \overline{F(\mathbf{x}_1 - \mathbf{y}, \ldots, \mathbf{x}_n - \mathbf{y})}, \tag{2.5}$$

holds for an arbitrary value of $\mathbf{y}$. The most common choice is to set $\mathbf{y} = \mathbf{x}_1$, so

$$\overline{F(\mathbf{x}_1, \ldots, \mathbf{x}_n)} = \overline{F(\mathbf{0}, \mathbf{x}_2 - \mathbf{x}_1, \ldots, \mathbf{x}_n - \mathbf{x}_1)} = \overline{F(\mathbf{x}_{12}, \ldots, \mathbf{x}_{1n})}, \tag{2.6}$$

where $\mathbf{x}_{ij} = \mathbf{x}_j - \mathbf{x}_i$.

2.1.4 Statistical isotropy

Further simplification arises when assuming the material to be *statistically isotropic* [18, 238, 258]. In such a case, the ensemble average is not only independent of the position of the coordinate system origin but also of the coordinate system rotation. Under this hypothesis, the ensemble average depends on the absolute value of vectors $\mathbf{x}_{12}, \ldots, \mathbf{x}_{1n}$ only:

$$\overline{F(\mathbf{x}_{12}, \ldots, \mathbf{x}_{1n})} = \overline{F(r_{ij})}, \tag{2.7}$$

where $r_{ij} = \|\mathbf{x}_{ij}\|, i = 1, \ldots, n, j = (i+1), \ldots, n$.

2.2 Microstructure description

A number of statistical descriptors is available to characterize the microstructure of a two-phase random medium. This section describes two specific sets of descriptors which proved to be useful in the present work. First, a set of general n-point probability functions, applicable to an arbitrary two-phase composite, is introduced. A different statistical function deserves attention when phase connectivity information are to be captured in more detail. The lineal path function is discussed as an example of such a descriptor.

Both types of functions are introduced through a fundamental random function relevant to the microstructure configuration. Then, statistical moments of this function are identified as descriptors of the microstructure morphology. Finally, similarities and differences between individual types of statistical descriptors are discussed.

2.2.1 n-point probability functions

Fundamental function and statistical moments. Consider an ensemble of a two-phase random medium. To provide a general statistical description of such a system it proves useful to characterize each member of the ensemble by a stochastic function–*characteristic* function $\chi_r(\mathbf{x}, \alpha)$, which is equal to one when point $\mathbf{x}$ lies in the phase r in the sample α and equal to zero otherwise [18, 258, 238],

$$\chi_r(\mathbf{x}, \alpha) = \begin{cases} 1, & \text{if } \mathbf{x} \in D_r(\alpha), \\ 0, & \text{otherwise,} \end{cases} \tag{2.8}$$

where $D_r(\alpha)$ denotes the domain occupied by the r-th phase. Except where noted, composites consisting of clearly distinguishable continuous matrix phase are considered. Therefore, $r = m, f$ is further assumed to take values m for the matrix phase while symbol f is reserved for the second phase. For such a system the characteristic functions $\chi_f(\mathbf{x}, \alpha)$ and $\chi_m(\mathbf{x}, \alpha)$ are related by

$$\chi_m(\mathbf{x}, \alpha) + \chi_f(\mathbf{x}, \alpha) = 1. \tag{2.9}$$

Following [18, 238, 258, 286], we write the ensemble average of the product of characteristic functions

$$S_{r_1,\ldots,r_n}(\mathbf{x}_1, \ldots, \mathbf{x}_n) = \overline{\chi_{r_1}(\mathbf{x}_1, \alpha) \cdots \chi_{r_n}(\mathbf{x}_n, \alpha)}, \tag{2.10}$$

where function $S_{r_1,\ldots,r_n}$ referred to as the *general n-point probability* gives the probability of finding n points $\mathbf{x}_1, \ldots, \mathbf{x}_n$ randomly thrown into a medium located in the phases $r_1, \ldots, r_n$.

Functions of the first and second order. Hereafter, we limit our attention to functions of the order of one and two, since higher-order functions are quite difficult to determine in practice[3]. Therefore, description of a random medium will be provided by the *one-point probability* function $S_r(\mathbf{x})$

$$S_r(\mathbf{x}) = \overline{\chi_r(\mathbf{x}, \alpha)}, \tag{2.11}$$

[3] Note, however, that relatively efficient procedures for approximation of higher-order probability functions for ergodic and statistically isotropic media were recently proposed in [45] and [46].

which simply gives the probability of finding the phase r at $\mathbf{x}$ and by the *two-point probability* function $S_{rs}(\mathbf{x}_1, \mathbf{x}_2)$

$$S_{rs}(\mathbf{x}_1, \mathbf{x}_2) = \overline{\chi_r(\mathbf{x}_1, \alpha)\chi_s(\mathbf{x}_2, \alpha)}, \tag{2.12}$$

which denotes the probability of finding simultaneously the phase r at $\mathbf{x}_1$ and the phase s at $\mathbf{x}_2$. In general, evaluation of these characteristics may prove to be prohibitively difficult. Fortunately, a simple method of attack can be adopted when accepting an assumption regarding the material as statistically homogeneous, so that (compare with Eq. (2.5))

$$S_r(\mathbf{x}) = S_r, \tag{2.13}$$

$$S_{rs}(\mathbf{x}_1, \mathbf{x}_2) = S_{rs}(\mathbf{x}_1 - \mathbf{x}_2). \tag{2.14}$$

Further simplification arises when assuming the medium to be *statistically isotropic*. Then $S_{rs}(\mathbf{x} - \mathbf{x}_2)$ reduces to (see also Eq. (2.7))

$$S_{rs}(\mathbf{x}_1 - \mathbf{x}_2) = S_{rs}(\|\mathbf{x}_1 - \mathbf{x}_2\|). \tag{2.15}$$

Finally, making an ergodic assumption allows a substitution of the one-point correlation function by its volume average, i.e., *volume concentration* or *volume fraction* of the r-th phase c_r,

$$S_r = c_r. \tag{2.16}$$

Limiting values. In addition, the two-point probability function S_{rs} depends on the one-point probability function S_r for certain values of its arguments such that

$$\text{for } \mathbf{x}_1 = \mathbf{x}_2 \;:\; S_{rs}(\mathbf{x}_1, \mathbf{x}_2) = \delta_{rs} S_r(\mathbf{x}_1), \tag{2.17}$$

$$\text{for } \|\mathbf{x}_1 - \mathbf{x}_2\| \to \infty \;:\; \lim_{\|\mathbf{x}_1 - \mathbf{x}_2\| \to \infty} S_{rs}(\mathbf{x}_1, \mathbf{x}_2) = S_r(\mathbf{x}_1) S_s(\mathbf{x}_2), \tag{2.18}$$

where symbol δ_{rs} stands for Kronecker's delta. Relation (2.17) states that the probability of finding two different phases at a single point is equal to 0 (see also Eq. (2.9)) or is given by the one-point probability function if phases are identical. Equation (2.18) manifests that for large distances points $\mathbf{x}_1$ and $\mathbf{x}_2$ are statistically independent. This relation is often denoted as the *no-long range orders* hypothesis (see e.g. [153, 285]).

Finally, according to Eq. (2.9), we may determine one and two-point probability functions for all phases provided that these functions are given for one arbitrary phase. For one-point probability function of statistically homogeneous and ergodic medium, this relation assumes a trivial form

$$c_m = 1 - c_f. \tag{2.19}$$

Relations for the two-point probability functions of statistically uniform and ergodic medium are summarized in Table 2.1[4].

[4] Note that, by definition (2.12) and assumption of statistical homogeneity, $S_{rs}(\mathbf{x}) = S_{sr}(\mathbf{x})$.

	Known function		
	$S_{mm}(\mathbf{x})$	$S_{mf}(\mathbf{x})$	$S_{ff}(\mathbf{x})$
$S_{mm}(\mathbf{x})$	$S_{mm}(\mathbf{x})$	$c_m - S_{mf}(\mathbf{x})$	$c_m - c_f + S_{ff}(\mathbf{x})$
$S_{mf}(\mathbf{x})$	$c_m - S_{mm}(\mathbf{x})$	$S_{mf}(\mathbf{x})$	$c_f - S_{ff}(\mathbf{x})$
$S_{ff}(\mathbf{x})$	$c_f - c_m + S_{mm}(\mathbf{x})$	$c_f - S_{mf}(\mathbf{x})$	$S_{ff}(\mathbf{x})$

Table 2.1: Relations between two-point probability functions

2.2.2 Lineal path function

As already noted in the previous section, the determination of probability functions of order higher than two encounters serious difficulties, both analytical and numerical[5]. However, the importance of these functions for the characterization of morphology and overall properties of heterogeneous materials is substantial (see, e.g., [45, 165, 169, 255] and references therein). To overcome this difficulty, one can study low-order microstructural descriptors based on a more complex fundamental function which contains more detailed information about phase connectedness and hence certain information about long-range orders. The lineal path function [147], described in this section, is a representative of such indicators.

Fundamental function and statistical moments. To maintain a formal similarity with the discussion of the n-point probability functions, we introduce a random function $\lambda_r(\mathbf{x}_1, \mathbf{x}_2, \alpha)$ as

$$\lambda_r(\mathbf{x}_1, \mathbf{x}_2, \alpha) = \begin{cases} 1, & \text{if } \mathbf{x}_1\mathbf{x}_2 \subset D_r(\alpha), \\ 0, & \text{otherwise,} \end{cases} \tag{2.20}$$

i.e., a function which equals to 1 when the segment $\mathbf{x}_1\mathbf{x}_2$ is contained in the phase r for the sample α and zero otherwise. The *lineal path function*[6], denoting the probability that the $\mathbf{x}_1\mathbf{x}_2$ segment lies in the phase r, then follows directly from the ensemble averaging of this function [147]

$$L_r(\mathbf{x}_1, \mathbf{x}_2) = \overline{\lambda_r(\mathbf{x}_1, \mathbf{x}_2, \alpha)}. \tag{2.21}$$

Under the assumptions of statistical homogeneity and isotropy, the function simplifies equivalently to relations (2.5) and (2.7)

$$L_r(\mathbf{x}_1, \mathbf{x}_2) = L_r(\mathbf{x}_1 - \mathbf{x}_2), \tag{2.22}$$

$$L_r(\mathbf{x}_1 - \mathbf{x}_2) = L_r(\|\mathbf{x}_1 - \mathbf{x}_2\|). \tag{2.23}$$

Limiting values. Obviously, if the points $\mathbf{x}_1$ and $\mathbf{x}_2$ coincide, the lineal path function is nothing else but the one-point probability function; for points $\mathbf{x}_1$ and $\mathbf{x}_2$ that are far

[5] See, e.g., [19, 39, 45] for discussion of procedures for determination of third-order probability functions for statistically isotropic ergodic media.

[6] The lineal path function can be related to the lineal contact distribution function $H_r^\ell(u)$ introduced in [238]. Indeed, the lineal contact distribution function for a line ℓ starting at the origin and the r-th phase is defined by relation $H_r^\ell(u) = 1 - P(\{D_r \cap u\ell\} = \emptyset)/(1 - c_r)$. Then, e.g., for $r = m$, we get $H_f^\ell(u) = 1 - L_m(u\ell)/(1 - c_f)$ and finally $L_m(u\ell) = c_m(1 - H_f^\ell)$. See also [152, 247].

apart the lineal path function vanishes,

$$\text{for } \mathbf{x}_1 = \mathbf{x}_2 \quad : \quad L_r(\mathbf{x}_1, \mathbf{x}_2) = S_r(\mathbf{x}_1), \tag{2.24}$$

$$\text{for } \|\mathbf{x}_1 - \mathbf{x}_2\| \to \infty \quad : \quad \lim_{\|\mathbf{x}_1 - \mathbf{x}_2\| \to \infty} L_r(\mathbf{x}_1, \mathbf{x}_2) = 0. \tag{2.25}$$

The substantial difference between the lineal path function and n-point probability function is that the functions related to different phases cannot be, in general, uniquely determined by relations similar to Table 2.1. This is just another confirmation of the fact that this function contains additional information which needn't be captured by low-order probability functions[7].

2.3 Numerical evaluation of microstructural statistics

Numerical evaluation of microstructural statistics introduced in the previous sections proceeds as follows. We begin with the n-point probability functions assuming an ergodic medium. An approach suitable for digitized media is explored. Then, a procedure for the determination of lineal path function is proposed. Both descriptors are evaluated for a selected representative of theoretical microstructural models[8].

2.3.1 n-point probability functions

To determine $S_{r_1,\ldots,r_n}$ we recall that the *general n-point probability* gives the probability of finding n points $\mathbf{x}_1, \ldots, \mathbf{x}_n$ randomly thrown into a medium located in the phases $r_1, \ldots, r_n$. Among all functions, the one–point and two–point probability functions deserve a special attention as they arise in the formulation of macroscopic constitutive equations of random composites discussed in Chapter 4. In view of Table 2.1 we further consider only the matrix probability functions.

To follow the above definition, the one–point matrix probability function S_m gives the chance of finding a randomly placed point located in the matrix phase. To determine this quantity, a simple Monte-Carlo like simulation can be utilized – we throw randomly point into the microstructure and count successful "hits" into the matrix phase. Then, the value of function S_m can be estimated as

$$S_m \approx \frac{n'}{n}, \tag{2.26}$$

where n' is the number of successful hits and n denotes the total number of throws. Entirely similar procedure can be employed to determine values of $S_{mm}(\mathbf{x})$[9].

[7] For various deterministic periodic microstructures with smooth boundaries between phases, however, the extensive numerical studies reported in [217] led the authors to the conjecture that the two-point probability functions are sufficient to *uniquely* reconstruct the given microstructure (up to the translation and possible inversion of the image).

[8] An interested reader may consult the overview article [255] or the books [238, 257] for exhaustive and systematic discussion of various microstructural models.

[9] For statistically isotropic microstructure, Smith and Torquato [232] proposed more efficient procedure for the determination of $S_{mm}(\|\mathbf{x}_{12}\|)$. Instead of tossing a line corresponding to $\mathbf{x}$ into a medium, a sampling template is used for the determination of two-point probability function. See also [271] for comparison of this method with approaches presented hereafter.

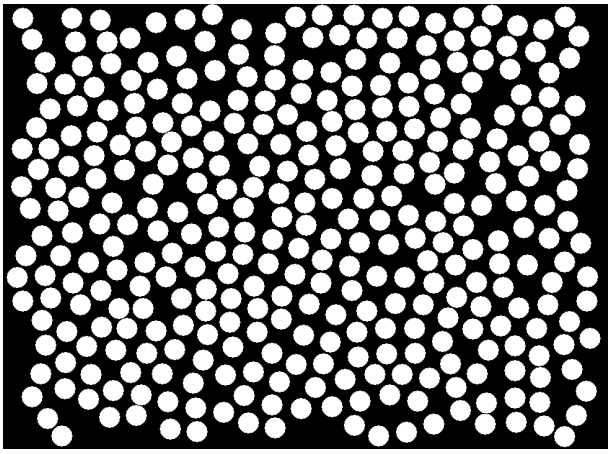

Figure 2.2: Idealized binary image of Fig. 2.1b. Bitmap resolution is 976 × 716 pixels

Another, more attractive, approach is available when the real microstructure is replaced by its binary image. A binary version of Fig. 2.1b is shown in Fig. 2.2. Such a digitized micrograph can be imagined as a discretization of the characteristic function $\chi_r(\mathbf{x}, \alpha)$, usually presented in terms of a $W \times H$ bitmap. Denoting the value of χ_r for the pixel located in the i-th row and j-th column as $\chi_r(i, j)$ allows writing the first two moments of function S_n for an ergodic and statistically homogeneous as medium in the form[10]

$$S_r = \frac{1}{WH} \sum_{i=0}^{W-1} \sum_{j=0}^{H-1} \chi_r(i, j), \tag{2.27}$$

$$S_{rs}(m, n) = \frac{1}{(i_M - i_m)(j_N - j_n)} \sum_{i=i_m}^{i_M-1} \sum_{j=j_n}^{j_N-1} \chi_r(i, j)\chi_s(i + m, j + n), \tag{2.28}$$

where $i_m = \max(0, -m)$, $i_M = \min(W, W-m)$ and $j_n = \max(0, -n)$, $j_N = \min(H, H-n)$. Observe that to compute function S_r requires $O(WH)$ operations, while $O((WH)^2)$ operations are needed for function S_{rs}. This might be computationally demanding, particularly for a large micrograph, and does not seem to bring any advantages over simulation techniques.

The required number of operations, however, can be reduced when writing the two–point probability function S_{rs} for a *periodic* ergodic medium as a *correlation* of functions χ_r and χ_s, recall Eq. (2.4),

$$S_{rs}(\mathbf{x}) = \frac{1}{|Y|} \int_Y \chi_r(\mathbf{y})\chi_s(\mathbf{x} + \mathbf{y}) \, \mathrm{d}\mathbf{y}. \tag{2.29}$$

Then, using relation (B.3), the Fourier transform of S_{rs} is provided by

$$\widetilde{S}_{rs}(\boldsymbol{\xi}) = \frac{1}{|Y|} \widetilde{\chi}_r(\boldsymbol{\xi}) \overline{\widetilde{\chi}_s(\boldsymbol{\xi})}, \tag{2.30}$$

[10] Throughout the text, the C-language type of array indexing is consistently used, i.e., we denote the first element of an array a as a_0 and the last element of the array as a_{L-1}, where L is the array length.

where $\bar{\cdot}$ now stands for the complex conjugate. Taking advantage of the periodicity of function χ_r one may implement the Discrete Fourier Transform (DFT) [28] when evaluating Eq. (2.30). To shed a light on this subject we first write the discrete version of Eq. (2.29) in the form

$$S_{rs}(m,n) = \frac{1}{WH}\sum_{i=0}^{W-1}\sum_{j=0}^{H-1}\chi_r(i,j)\chi_s((i+m)\%W,(j+n)\%H), \tag{2.31}$$

where symbol "%" stands for modulo. The above equation, usually termed the cyclic correlation [28], readily implies periodicity of function S_{rs}. Note that the correlation property of DFT holds for cyclic correlation. Referring to Eq. (2.30) it is given by the following relation

$$\mathrm{DFT}\{S_{rs}(m,n)\} = \mathrm{DFT}\{\chi_r(m,n)\}\overline{\mathrm{DFT}\{\chi_s(m,n)\}}. \tag{2.32}$$

The inverse DFT denoted as IDFT then serves to derive function S_{rs} at the final set of discrete points as [19]

$$S_{rs}(m,n) = \frac{1}{WH}\mathrm{IDFT}\{\mathrm{DFT}\{\chi_r(m,n)\}\overline{\mathrm{DFT}\{\chi_s(m,n)\}}\}. \tag{2.33}$$

This method is very economical and its accuracy depends only on the selected resolution of the digitized medium. See also Appendix B for further discussion. Usually, the Fast Fourier Transform, which needs only $O(WH\log(WH)+WH)$ operations, is called to carry out the numerical computation[11].

2.3.2 Lineal path function

Following the definition of the lineal path function as a probability of finding a segment randomly thrown into a medium contained in a given phase, Eq. (2.21), an elementary Monte Carlo-based procedure can be again used for its evaluation, i.e., we randomly throw segments into a medium and count the cases when the segment meets the given condition. Computationally more intensive approach, however, can be employed following the idea of sampling template introduced in [232].

To that end, we form a sampling template with dimensions $T_W \times T_H$ pixels. Then, we draw a set of segments from the center of a template to the points on the template boundary separated by given discrete steps Δ_W and Δ_H (see Figure 2.3). If the DDA algorithm (see, e.g., [105]) is used for a construction of segments, the template can be rapidly assembled using only integer operations. Moreover, this algorithm can be effectively combined with the bitmap representation of the microstructure. Once a template is formed, the values of the lineal path function for a given direction starts with placing the template center at a given point found, say, in phase r and then marking the pixel at which the segment corresponding to the selected direction meets the other phase, say s[12]. Then, counters corresponding to pixels of a given segment which are closer to the center than the marked pixel are increased by one while remaining counters are left unchanged. The value

[11] The public-domain package **FFTW** version 2.1.3 [60] was used for the evaluation of (2.33).

[12] In particular, the matrix phase is checked when L_f function is determined while the fiber phase represents the "stop condition" for the L_m function.

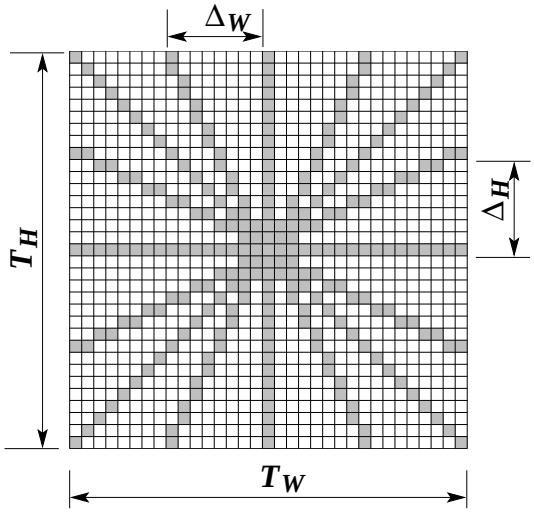

Figure 2.3: An example of sampling template

of the lineal path function then can be obtained either by stochastic sampling (randomly throwing template center in a medium) or deterministic sampling (template center is successively placed in all pixels of a bitmap) and averaging the obtained results. Moreover, the latter method allows us to actually use only a half of the sampling template, provided that the analyzed microstructure is statistically homogeneous. Note that even though this procedure basically needs only integer-based operations, it is still substantially slower than the FFT-based approach. Hence, a relatively sparse sampling template is unavoidable if one wishes to keep the efficiency of this procedure comparable to the determination of the two-point probability function (see Section 2.3.4 for a concrete example).

2.3.3 Microstructural statistics for fully overlapping discs

The purpose of this section is to test the proposed evaluation techniques for an example of statistically isotropic models of microstructure – the model of equal-sized fully penetrable discs. Selection of this (rather simple) microstructural model is rather intentional as the closed form of the functions $S_{mm}(r)$ and $L_m(r)$ are readily available in the literature, see e.g., [147, 238, 255].

Two-point probability function. Recall that $S_{mm}(\mathbf{x}_1, \mathbf{x}_2)$ represents the probability of finding two points $\mathbf{x}_1$ and $\mathbf{x}_2$ randomly thrown into the medium both in the matrix. For fully penetrable discs this function corresponds to the probability that union of two discs with radius R and centers located in points $\mathbf{x}_1$ and $\mathbf{x}_2$ is not occupied by any other particle center. Denoting ρ as a number of discs per unit area, such an event can be described by the Poisson probability distribution (see, e.g., [238]) with the intensity $\rho\,\Omega_u(\mathbf{x}_1, \mathbf{x}_2)$,

$$S_{mm}(\mathbf{x}_1, \mathbf{x}_2) = \exp(-\rho\,\Omega_u(\mathbf{x}_1, \mathbf{x}_2)), \tag{2.34}$$

where $\Omega_u(\mathbf{x}_1, \mathbf{x}_2)$ is area of the union of two identical discs with radius R and centers located at points $\mathbf{x}_1$ and $\mathbf{x}_2$ (see Fig. 2.4a). By the statistical isotropy of the present

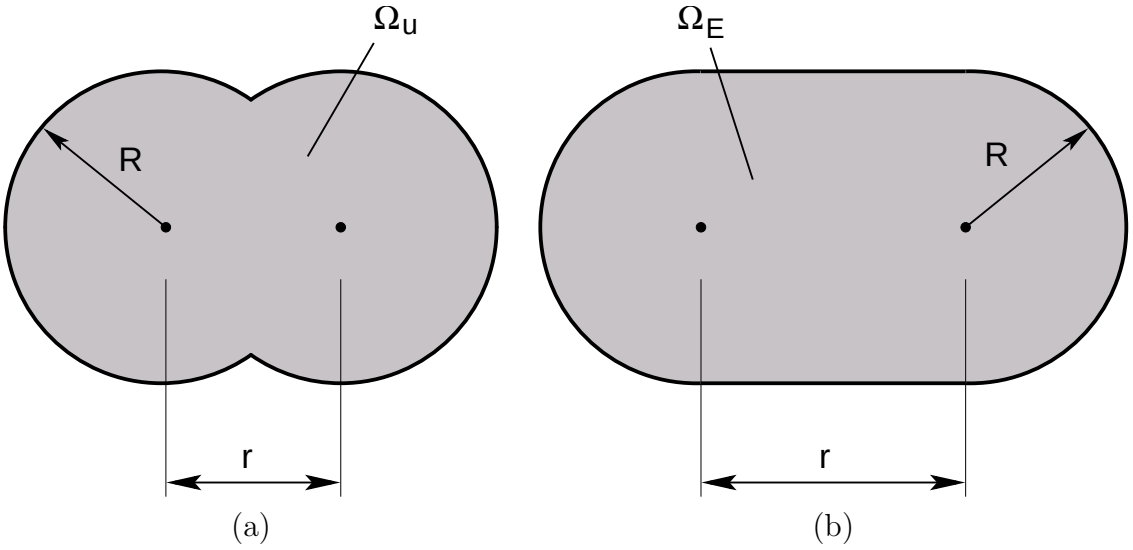

Figure 2.4: Fully penetrable discs model: (a) set $\Omega_u(r)$, (b) set $\Omega_E(r)$

model, this function depends only on the distance of these two points $r = \|\mathbf{x}_1 - \mathbf{x}_2\|$, i.e.,

$$\Omega_u(r) = \begin{cases} 2R^2 \left[\pi - \arccos(r/2R) + r/2R\sqrt{1-(r/2R)^2}\right], & r < 2R, \\ 2\pi R^2, & r \geq 2R. \end{cases} \tag{2.35}$$

Thus, the two-point matrix probability function is isotropic and provided by expression [238, 255]

$$S_{mm}(r) = \exp(-\rho\,\Omega_u(r)). \tag{2.36}$$

Lineal path function. Similar reasoning can be used to obtain the matrix lineal path function for the current model. The function represents the probability that a set of points with the distance from the segment $\mathbf{x}_1\mathbf{x}_2$ smaller than R is not occupied by any particle center. Denoting the area of this set as $\Omega_E(r)$ we arrive at the expression [147, 206]

$$L_m(r) = \exp(-\rho\,\Omega_E(r)), \tag{2.37}$$

where $\Omega_E(r)$ is provided by (see also Fig. 2.4b)

$$\Omega_E(r) = \pi R^2 + 2Rr. \tag{2.38}$$

Finally, to arrive at the number of particles ρ per unit area (volume) we combine Eqs. (2.17) and (2.36) (or, equivalently, Eqs. (2.24) and (2.37)) to write the matrix volume fraction in the form

$$S_{mm}(r=0) = L_m(r=0) = c_m = \exp(-\rho\,\pi R^2). \tag{2.39}$$

Therefore, for a given matrix volume fraction c_m, the above relation readily provides the corresponding value of ρ.

2.3.4 Numerical experiments

Numerical experiments were performed for 50 different configurations containing 100 circular particles having common radius $R = 16$ pixels. Each configuration was generated purely randomly keeping the matrix volume fraction c_m fixed. The value of S_{mm} was found by the Fast Fourier Transform (2.33), while the sampling template with parameters $T_W = T_H = 161$ pixels and discrete steps $\Delta_W = \Delta_H = 20$ pixels was used for the determination of values of L_m function[13]. The solid dots appearing in Fig. 2.5 were obtained by averaging the resulting values from all fifty configurations and by isotropising the data for selected distances[14], while the horizontal lines indicate the scatter of the averaged data. The individual curves in Fig. 2.5 are the theoretical values obtained by relations (2.36) and (2.37). It is evident that a very satisfactory match between theoretical and simulation results was obtained and that the sampling procedures introduce no artificial anisotropy in computed statistics. Also note that the function L_m contains substantial long-range information for higher values of c_m compared to the two-point matrix probability function S_{mm}.

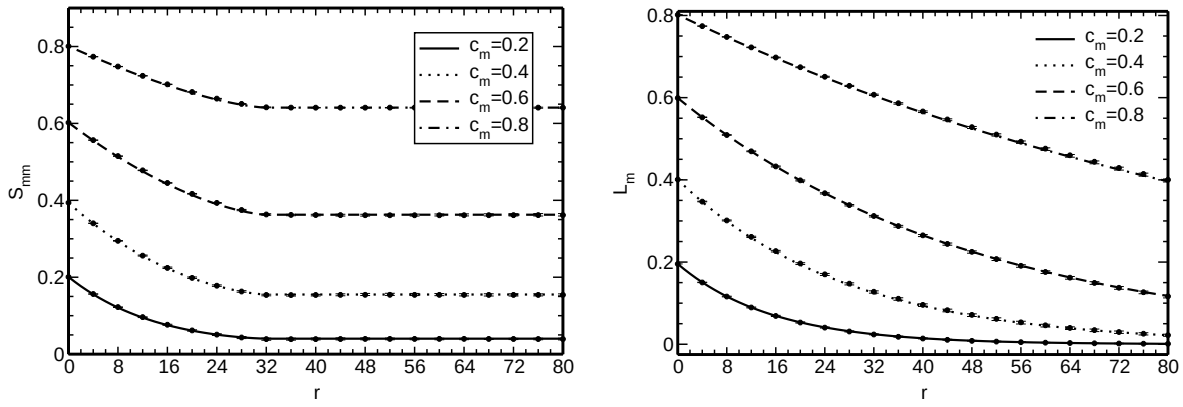

(a) (b)

Figure 2.5: Fully penetrable discs model: (a) Two-point matrix probability function, (b) Matrix lineal path function

Table 2.2 stores the computational time needed for individual tests[15]. Clearly, the FFT-based approach outperforms the sampling template method by an order of magnitude from the point of view of computational efficiency, mainly due to the remarkable performance of **FFTW** library [60]. Therefore, to keep the computational time reasonable, one should inevitable turn to rather sparse sampling templates and relatively low

[13] The results for the direct approach, see Eq. (2.28), are not presented here as the computation is very time-consuming and delivers similar results as the FFT-based approach. An interested reader may, however, consult the work [271] for numerical comparison of these two approaches.

[14] Following [19], we compute statistics of the isotropized $S_{rs}(\mathbf{x})$ function for the length of a vector $\mathbf{x}$ equal to r by sampling values at positions $(r\cos\phi, r\sin\phi)$ with regular angular step $\Delta\phi = \pi/(4r)$. Values for non-integer positions are obtained by bilinear interpolation of the data given on a regular grid.

[15] The tests were run on a computer with Intel Celeron 700 MHz processor and 256MB RAM under the Linux operating system. The C++ code was compiled by **gcc 2.96** GNU complier with `-O3` optimization switch.

resolutions of analyzed bitmaps. Fortunately, these conditions are met in applications presented in Chapters 3 and 5, so the performance of the implemented algorithms is satisfactory.

Volume fraction	**0.2**	**0.4**	**0.6**	**0.8**
S_{mm}	4.98	8.97	16.0	21.52
L_m	20.24	127.97	528.58	2453.27
$W \times H$	228×228	304×304	408×408	616×616

Table 2.2: Fully penetrable discs model: Overall CPU times in seconds for 50 configurations in seconds

2.4 Analysis of unidirectional fiber composite

In this section, the preceding procedures are applied to the real microstructure represented here by the micrograph of Fig. 2.1b taken from the bundle of graphite fibers bonded to the polymer matrix. For numerical analysis, the real microstructure is replaced by its idealized binary image, Fig. 2.2, which offers rather concise yet more useful notion about the actual arrangement of fibers within a sample[16].

At present, the periodicity of microstructure is invoked so the micrograph is assumed to be surrounded by periodic replicas of itself, which directly implies statistical homogeneity of the medium. Moreover, the validity of the ergodic assumption is checked to some extent, see Section 2.4.1. A number of results derived for the selected statistical descriptors are referenced in Section 2.4.2–2.4.3.

2.4.1 Testing ergodic hypothesis

To test the ergodic hypothesis it is necessary to form the ensemble space $\mathcal{S}$. When sampling individual members of $\mathcal{S}$ we started from three micrographs of the fiber tow taken from three specimens at approximately the same location. Each member of the ensemble was then found through a random cut of a part of a given micrograph subjected to condition of the "same" fiber volume fraction. This condition actually supplements the lack of infinity of our composite medium. Fig. 2.6 shows six such individuals generated from the micrograph displayed in Fig. 2.2. In view of the above comments we shall only require that

$$c_r = \frac{1}{N} \sum_{i=0}^{N-1} S_r^i, \qquad r = f, m, \tag{2.40}$$

where N is the number of members in the ensemble. Functions S_r^i can be derived by randomly placing a point in the member i in a certain number of times while counting

[16] The **LUCIE** software was used for the enhancement and binary conversion of original image and to provide for the basic geometrical information such as the fiber radius, position of all particles in the sample and the fiber volume fraction. The detailed description of this procedure can be found in work [76]. General discussion of necessary steps and operations can be found, e.g., in [10, 19, 20, 29, 253, 277] and references therein.

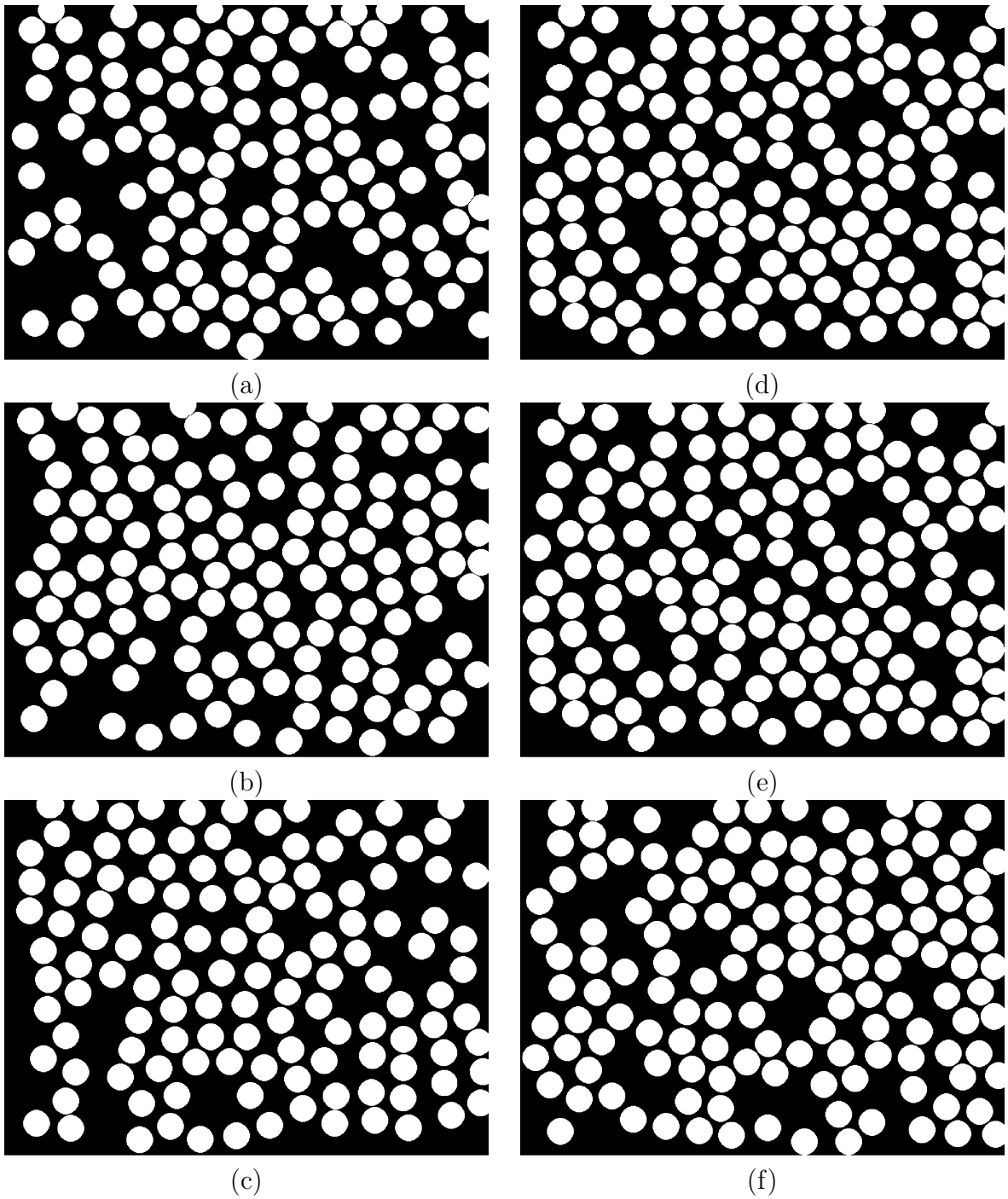

Figure 2.6: Selected members of the sample space

the number of hits in the phase r and then dividing by the total number of throws. When setting the number of throws equal to 500 we found $\overline{S_f} = 0.42$, which agrees well with the average fiber volume fraction $\overline{c_f} = 0.435$. A better agreement can be expected for larger N. Although an ultimate justification of an ergodic assumption would require to prove equality of higher moments as well, we argue that the presented results are sufficient for the medium to be considered as ergodic, providing the medium is indeed statistically homogeneous. In the sense of an ergodic assumption we suggest that a single micrograph can be used hereafter for evaluation of the required statistical descriptors.

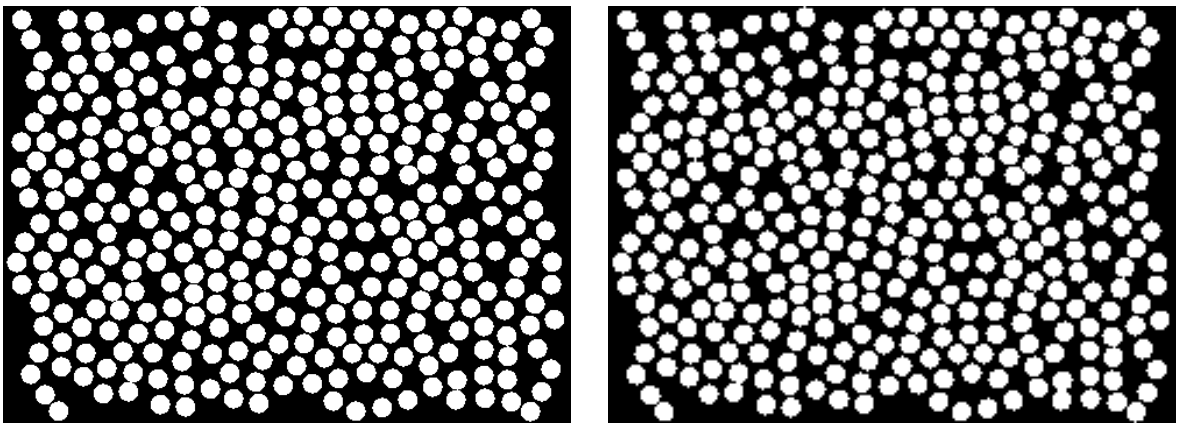

(a) (b)

Figure 2.7: Idealized binary images of Fig. 2.1b; (a) resolution 488×358 pixels, (b) resolution 244×179 pixels

2.4.2 Two-point probability function

The two-point probability function was determined by the FFT-based approach for several different bitmap resolutions to test the sensitivity of resulting microstructural descriptors with respect to the size of the bitmap. In particular, three different resolutions of the idealized binary images were explored: 976×716 pixels (radius of a fiber $R = 16$ pixels, Fig. 2.2), 488×358 ($R = 8$ pixels, Fig. 2.7a) and 244×179 ($R = 4$ pixels, Fig. 2.7b). Resulting isotropized values together with coefficient of variation appear in Fig. 2.8. Note that the r coordinate was scaled for lower resolutions to keep results comparable.

It is evident that the obtained values are nearly independent of the bitmap resolution so we can safely use the bitmap with dimensions 488×358 in further analyses. Further, it can be observed that the matrix two-point probability function is nearly isotropic; the maximal coefficient of variation $\approx 5\%$, Fig. 2.8b, can be accepted as a reasonable violation of the assumption. Finally, for the sake of clarity, three-dimensional picture of the two-point probability function is drawn in Fig. 2.9[17].

[17] All three-dimensional pictures appearing in this thesis were created with the public-domain application **OpendDX 4.1.3** [2] by IBM corporation and postprocessing visual program obtained by the courtesy of Mr. Martin Wierer.

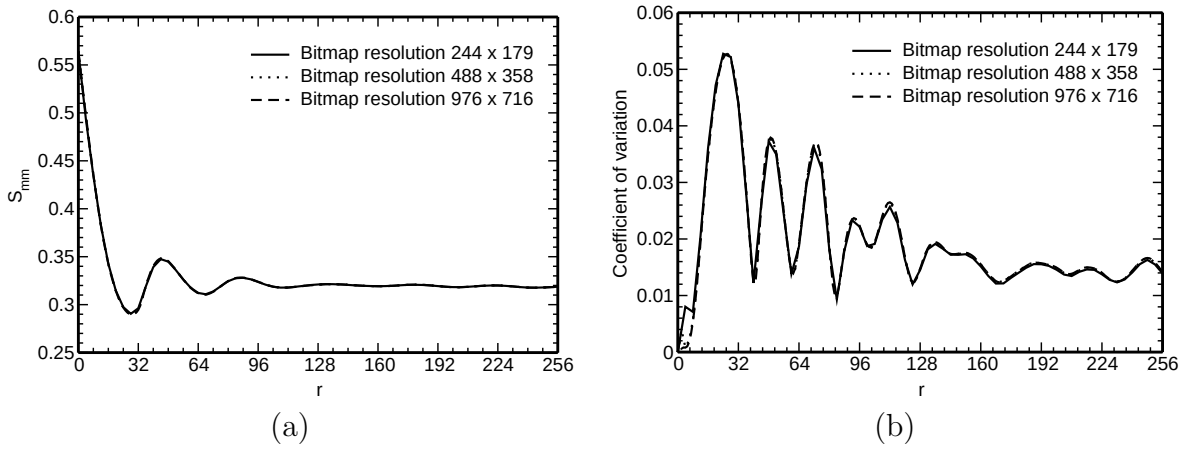

(a) (b)

Figure 2.8: Isotropized two-point probability function and variation coefficient for unidirectional fiber composite

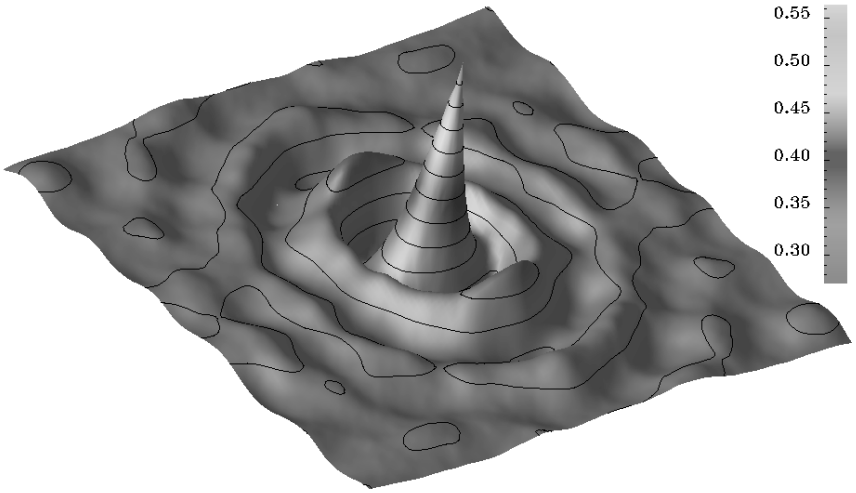

Figure 2.9: Two-point matrix probability function of unidirectional fiber composite. Bitmap resolution is 488×358 pixels.

2.4.3 Lineal path function

A similar set of tests was performed for the matrix lineal path function. The sampling template with $T_W = T_H = 257$ pixels and steps $\Delta_W = \Delta_H = 4$ pixels was formed and deterministic sampling procedure was executed to obtain the values of matrix lineal path function from the bitmap displayed in Fig. 2.2. The procedure was repeated for bitmaps in Figs. 2.7a and 2.7b with suitably rescaled sampling template. The resulting isotropized lineal-path functions and coefficients of variations are shown in Fig. 2.10. The presented results again indicate the insensitivity of computed statistics with respect to bitmap (un)refinement. Similarly to the fully penetrable cylinders model, see Section 2.3.4, the lineal path function carries information of substantially longer range than the two-point probability function. Also note quite high scatter of the values for larger distances r, Fig 2.10b, which is not captured by the two-point probability function. Finally, the three-dimensional plot of the lineal path function is presented in Fig. 2.11.

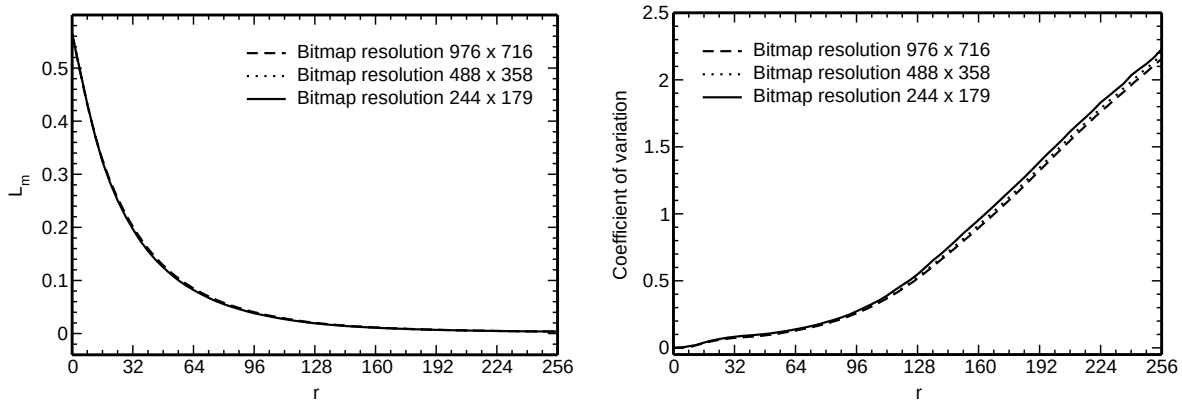

Figure 2.10: Isotropized matrix lineal path function and variation coefficient for unidirectional fiber composite

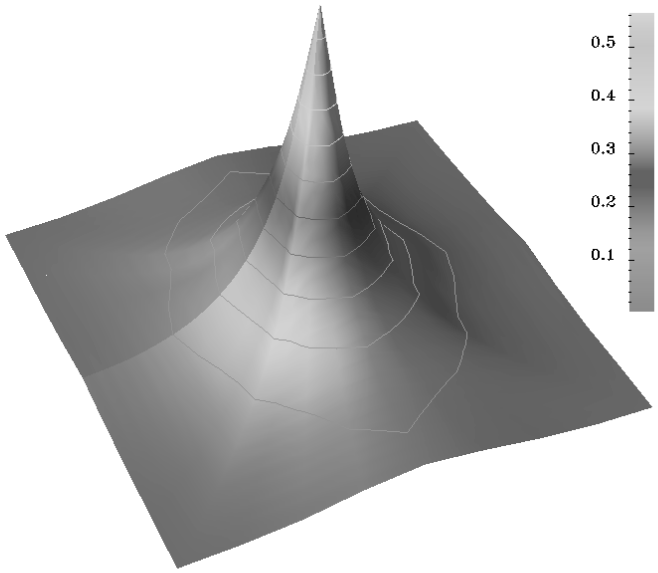

Figure 2.11: Matrix lineal path function of unidirectional fiber composite. Bitmap resolution is 488×358 pixels.

2.5 Optimization algorithm

Motivation. As already stated in the introductory Chapter 1, a substantial part of the presented work deals with definition of periodic unit cells, which represent a real microstructure as close as possible. If we characterize the original microstructure by certain statistical descriptors, this requirement can be easily recasted as a bound-constrained minimization of an objective function defined in terms of selected statistical descriptors (see Chapters 3 and 5 for explicit examples). Unfortunately, a careful inspection reveals that the function to be minimized is non-convex, multi-modal and discontinuous due to

finite resolution of binary representation of a microstructure[18]. This type of problems calls for *global optimization* techniques[19] with a variety of *stochastic optimization* methods as important representatives of these methods. Based on rather extensive numerical experiments reported in [104, 157], a stochastic algorithm employing a combination of principles of the Parallel Simulated Annealing [150, 151], the Differential Evolution method [236, 237] and real-encoded Genetic Algorithms [102, 160] was implemented. A brief description of this method, denoted hereafter as Real-encoded Augmented Simulated Annealing (**RASA**), is given in following sections.

2.5.1 Algorithm description

```
   AugmentedSimulatedAnnealing
1  T = T_max, t = 0
2  generate P_0, evaluate P_0
3  While (TerminationCondition == false)
4     counter = success = 0
5     While ((counter < counter_max) ∧ (success < success_max))
6        counter++, t++
7        Select operator O
8        Select individual(s) I_t from P_t
9        Modify I_t by O
10       Select individual(s) I'_t from P_t
11       p = exp((F(I'_t) − F(I_t))/T)
12       If (u(0,1) ≤ p)
13          success++
14          Insert I_t into P_t instead of parents
15          Evaluate P_t
16    Decrease T
```

Table 2.3: Augmented Simulated Annealing algorithm

The Augmented Simulated Annealing method is basically the combination of two stochastic optimization techniques – a Genetic Algorithm and a Simulated Annealing. It uses basic principles of genetic algorithms (selection, recombination by genetic operators, whole set of possible solutions instead of only one is optimized), but controls replacement of parents by the Metropolis criterion (2.42). This increases the robustness of the method, since we allow a worse child to replace its parent and thus escape from local minima, which is in contrary to classical optimization algorithms. The algorithmic scheme of the present implementation is summarized in Table 2.3[20]:

[18] In the pioneering work of Povirk [202], the Conjugate Gradient method was used for this type of optimization problems. It was demonstrated in author's thesis [297] that this approach is rather unsuitable as the global optimum is almost never reached.

[19] See, e.g., optimization tree of NEOS server [1] for a classification of different types of optimization algorithms.

[20] In the following text, the terminology commonly used in evolutionary computation is employed (see,

Steps 1–2 Randomly generate an initial population and assign a fitness to each individual. Initial temperature is set to $T_0 = T_{max} = \texttt{T\_frac}F_{avg}$ and minimal temperature is determined as $T_{min} = \texttt{T\_frac\_min}F_{avg}$, where F_{avg} is the average fitness value of the initial population.

Step 7 Select an appropriate operator. Each operator is assigned a certain probability of selection.

Step 8 Select an appropriate number of individuals (according to the operator) and generate possible replacements. To select individuals, we apply *normalized geometric ranking* scheme [102]: The probability of selection of the i-th individual is given by

$$p_i = q'(1-\texttt{q})^{r-1}, \qquad q' = \frac{\texttt{q}}{1-(1-\texttt{q})^{\texttt{pop\_size}}}, \tag{2.41}$$

where q is the probability of selecting the best individual in the population, r is the rank of the i-th individual with respect to its fitness, and pop_size is the population size.

Step 10 Look for an individual identical to possible replacement(s) in the population. If such individual(s) exists, no replacement is performed.

Steps 11–12 Replace old individual if

$$u(0,1) \leq \exp\left(F(I_{\text{old}}) - F(I_{\text{new}})\right)/T_t, \tag{2.42}$$

where $F(\cdot)$ is the fitness of a given individual, T_t is the actual temperature and $u(\cdot,\cdot)$ is a random number with the uniform distribution on a given interval.

Step 16 Decrease temperature

$$T_{t+1} = \texttt{T\_mult}T_t. \tag{2.43}$$

If actual temperature T_{t+1} is smaller than T_{min}, perform *reannealing* – i.e. perform steps #1–2 for, say, one half of the population.

2.5.2 List of operators

The following set of real-valued operators, proposed in [160], was implemented. Recall that denote L and U as vectors of lower/upper bounds on unknown variables, $u(a,b)$ and $u[a,b]$ as a real or integer random variable with the uniform distribution on a closed interval $\langle a,b\rangle$. Further, we denote the i-th chromozome of generation t as $CH_i(t)$, its genes are referred to as $ch_{ij}(t)$ and N stands for the number of unknown variables.

---

e.g., [81, 138, 159, 164]). Therefore, the objective function to be minimized is referred to as *fitness*, the set of possible solutions is denoted as *population*, the individual vectors are named as *individuals* and their respective components as *chromozomes*. Finally, the quantities written in typewriter font are parameters of the method, which must be defined by a user.

Uniform mutation: Let $k = u[1, N]$

$$ch_{ij}(t+1) = \begin{cases} u(L_j, U_j), & \text{if } j = k \\ ch_{ij}(t), & \text{otherwise,} \end{cases} \tag{2.44}$$

Boundary mutation: Let $k = u[1, N]$, $p = u(0, 1)$ and set:

$$ch_{ij}(t+1) = \begin{cases} L_j, & \text{if } j = k, p < .5 \\ U_j, & \text{if } j = k, p \geq .5 \\ ch_{ij}(t), & \text{otherwise} \end{cases} \tag{2.45}$$

Non-uniform mutation: Let $k = u[1, N]$, $p = u(0, 1)$ and set:

$$ch_{ij}(t+1) = \begin{cases} ch_{ij}(t) + (L_j - ch_{ij}(t))f, & \text{if } j = k, p < .5 \\ ch_{ij}(t) + (U_j - ch_{ij}(t))f, & \text{if } j = k, p \geq .5 \\ ch_{ij}(t), & \text{otherwise} \end{cases} \tag{2.46}$$

where $f = u(0, 1)(T_t/T_0)^{\mathtt{b}}$ and `b` is the shape parameter.

Multi-non-uniform mutation: Apply non-uniform mutation to all variables of CH_i.

Simple crossover: Let $k = u[1, N]$ and set:

$$ch_{il}(t+1) = \begin{cases} ch_{il}(t), & \text{if } l < k \\ ch_{jl}(t), & \text{otherwise} \end{cases} \qquad ch_{jl}(t+1) = \begin{cases} ch_{jl}(t), & \text{if } l < k \\ ch_{il}(t), & \text{otherwise} \end{cases}$$

Simple arithmetic crossover: Let $k = u[1, N]$, $p = u(0, 1)$ and set:

$$ch_{il}(t+1) = \begin{cases} pch_{il}(t) + (1-p)ch_{jl}(t), & \text{if } l = k \\ ch_{il}(t), & \text{otherwise} \end{cases} \tag{2.47}$$

$$ch_{jl}(t+1) = \begin{cases} pch_{jl}(t) + (1-p)ch_{il}(t), & \text{if } l = k \\ ch_{jl}(t), & \text{otherwise} \end{cases} \tag{2.48}$$

Whole arithmetic crossover: Simple arithmetic crossover applied to all variables of CH_i and CH_j.

Differential crossover: Let $p = u(0, 1)$, $j = [1, N]$ and $k = [1, N]$ such that $j \neq k$ and set:

$$CH_i(t+1) = CH_i(t) + p(CH_j(t) - CH_k(t)). \tag{2.49}$$

If $CH_i(t+1)$ is not feasible then a new random number p is generated until the feasibility condition is met or the maximum number of differential crossover applications `num_dif_max` is exceeded.

The interested reader may consult the works [104, 157] for more detailed information about the **RASA** method and discussion of its advantages and disadvantages with respect to alternative stochastic optimizers.

Chapter 3

MICROSCALE MODELING VIA PERIODIC FIELDS

The purpose of this chapter is to introduce a simple micromechanics-based approach to the analysis of random composites. Due to the complexity of the microstructure, recall Fig. 2.1a, the analysis is usually left to rely on incomplete geometrical information about the composite microstructure. The problem is not successfully resolved even when considering a large sample of composite as such displayed in Fig. 2.1b. Instead, it appears preferable to exploit information contained in various statistical descriptors discussed in detail in Chapter 2.

An essential ingredient of the present model applicable to both elastic and inelastic regimes is a carefully selected material *representative volume element* (RVE) replacing the real microstructure. Such a RVE is represented here by a *periodic unit cell* (PUC) consisting of a small number of particles, which statistically resembles the actual composite. For an early study on this subject we refer the reader to [202][1].

A number of ways can be used to accomplish this task. Here, following [202, 298], we offer a simple approach based on the microstructural statistics. In particular, the PUC is found from a certain optimization procedure. A random character of the microstructure is accounted for through the two-point probability function S_{mm} and/or the lineal path functions L_m introduced into an objective function. The procedure is outlined in Section 3.1 together with extensive numerical tests to examine the efficiency of stochastic optimization algorithm introduced in Section 2.5. Results are presented for the graphite-fiber tow impregnated by the polymer matrix.

A number of theoretical problems, generally beneficial to the designer, are selected to test the applicability of the present approach. Section 3.2 is concerned with numerical evaluation of effective mechanical properties of composites with periodic microstructures. Contribution due to local eigenstrains to the overall response is studied in Section 3.3; the specific example of thermal stresses is studied in more details. The eigenstress framework is extended in Section 3.4 to the modeling of linear viscoelastic materials and nonlinear viscoelasticity considered in Section 3.5[2].

3.1 Construction of the periodic unit cell

In this section we are concerned with one of the major goals of this work: determination of the periodic unit cell, which is statistically equivalent to the original microstructure. In achieving this, the knowledge about material's statistics acquired in Chapter 2 is used. In particular, the PUC is constructed by matching a selected microstructure describing

[1] Note that a definite choice of the number of particles within a unit cell generally depends on a problem one wishes to analyze. See, e.g., recent work [**?**] for more details.

[2] Extension to other deformation modes is rather straightforward; an interested reader may consult the works [33, 54, 70] and an excellent overview [161] for more information on this subject.

function of the real microstructure and the unit cell. To that end, an optimization procedure based on the least square method is implemented. The optimization problem then reduces to the minimization of an objective function involving the selected statistical descriptor. Although the required statistical information can be provided by any function presented in previous sections, the proper choice of statistical description may result in significant improvement of the optimization process [41, 216, 226, 247, 291].

The process of finding the minimum value of the objective function is divided into two steps: finding the *optimal positions* of fibers for fixed dimension of the unit cell and then generating the *optimal dimensions* of the unit cell. While the second step of this procedure represents an elementary one-dimensional minimization problem, the solution of the first problem requires the bound-constrained minimization of multi-dimensional, multi-modal and piecewise constant functions.

3.1.1 Objective function and problem definition

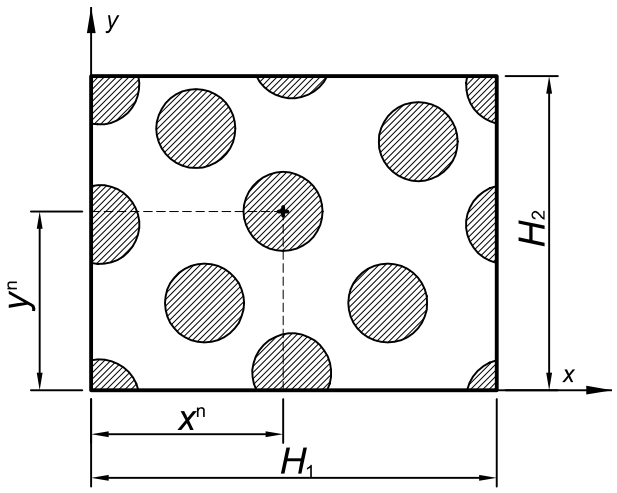

Figure 3.1: Geometry of the periodic unit cell

Consider a periodic unit cell consisting of N particles displayed in Fig. 3.1. The geometry of such a unit cell is determined by dimensions H_1 and H_2 and the x and y coordinates of all particle centers. The objective is to keep material's statistics of both the PUC and the actual composite as much similar as possible. At present, the particle locations together with an optimal ratio of cell dimensions H_1/H_2 are found by minimizing an objective function involving the two-point matrix probability function S_{mm}, matrix lineal path function L_m or combination of both, respectively,

$$F_S(\mathbf{x}^N, H_1, H_2) = \sum_{i=-i_{\max}}^{i_{\max}} \sum_{j=-j_{\max}}^{j_{\max}} \left(\overline{S}_{mm}(i,j) - S_{mm}(i,j)\right)^2, \tag{3.1}$$

$$F_L(\mathbf{x}^N, H_1, H_2) = \sum_{i=0}^{N_d-1} \sum_{j=0}^{N_\ell(i)-1} \left(\overline{L}_m(i,j) - L_m(i,j)\right)^2, \tag{3.2}$$

$$F_{S+L}(\mathbf{x}^N, H_1, H_2) = F_S(\mathbf{x}^N, H_1, H_2) + F_L(\mathbf{x}^N, H_1, H_2), \tag{3.3}$$

where $\mathbf{x}^N = \{x^1, y^1, \ldots, x^N, y^N\}^\mathsf{T}$ stores the positions of particle centers of the periodic unit cell, x^i and y^i correspond to the x and y coordinates of the i-th particle, H_1 and H_2 are the dimensions of the unit cell, $\overline{S}_{mm}$ and $\overline{L}_m$ stand for the value of L_m and S_{mm} functions corresponding to the target medium. Parameters $i_{\max}$ and $j_{\max}$ define the range of points, in which S_{mm} functions are matched[3], N_d denotes the number of rays of a sampling template and $N_\ell(i)$ is the number of pixels of the i-th sampling ray, see Fig. 2.3.

The minimization of objective functions (3.1)–(3.3) can be split into two steps, where each step corresponds to a single optimization problem. It proved advantageous to start with an optimal spatial distribution of particle centers for given of cell dimensions H_1 and H_2. The optimal ratio of cell dimensions then follows from a separate problem. Hence, the following optimization problem is solved first.

Optimal fiber configuration. For a given number of fibers N, dimensions of a unit cell H_1 and H_2 and statistical descriptor $D \in \{S, L, S+L\}$ find the configuration of particle centers $\mathbf{x}^N(H_1, H_2)$ such that

$$\mathbf{x}^N(H_1, H_2) \in \operatorname*{Argmin}_{\mathbf{x}^N \in \mathcal{B}} F_D(\mathbf{x}^N, H_1, H_2), \tag{P1}$$

where $\mathcal{B}$ denotes a set of admissible vectors $\mathbf{x}^N$,

$$\mathcal{B} = \left\{\mathbf{x}^N \in \mathbb{R}^{2N} : 0 \le x^i \le H_1, 0 \le y^i \le H_2,\ i = 1, \ldots, N\right\}, \tag{3.4}$$

and $\operatorname{Argmin} F$ denotes the set of (possibly non-unique) minimizers of an objective function F_D.

After solving the above problem, we are left with only two unknown parameters, H_1 and H_2, to be determined. Maintaining the same fiber volume fraction c_f for both the periodic unit cell and original microstructure imposes an additional constraint on a set of unit cell dimensions[4]. The second optimization problem thus reduces to the minimization of the objective function F_D with respect to the ratio $\eta = H_1/H_2$.

Optimal ratio H_1/H_2 . For known values of $\mathbf{x}^N(\eta)$ and for the fixed volume fraction of phases, find the ratio η^N such that:

$$\eta^N \in \operatorname*{Argmin}_{\eta \in \langle \eta_a; \eta_b \rangle} F_D(\mathbf{x}^N(\eta)), \tag{P2}$$

where values η_a and η_b should be chosen to cover all physically reasonable dimensions of the unit cell.

3.1.2 Golden Section Search method

The solution of problem (P2) can be obtained through the *Golden Section search* method [203, Chapter 10.1]. In principle, starting with an initial triplet of points a, b, c this

[3] Note that the periodicity of the S_{mm} function is exploited to determine values for indexes out of the range $0, 1, \ldots, (W-1) \times 0, 1, \ldots, (H-1)$, where W and H denote the width and height of the bitmap, respectively.

[4] See, e.g., [85] the discussion of the importance of this constraint in the context of modeling and simulation of random media.

method is based on generating a new point in locations, which divide intervals $\langle a; b\rangle$ or $\langle b; c\rangle$ in some prescribed ratio – the Golden section. The new point then replaces one of the points a, b, c according to its value and position. The essentials of this method are summarized in Table 3.1[5].

	GoldenSectionSearch$(f, a, b, c, e, \epsilon)$
1	Supply values $a < b < c$ such that $(f(a) > f(b)) \wedge (f(c) > f(b))$
2	**While** $((c - a) < \epsilon)$
3	Determine the new point d
4	**If** $(f(d) < f(b))$
5	$b = d$, update a, c with respect to step 1
6	**ElseIf** $(d < b)$
7	$a = d$
8	**Else**
9	$c = d$

Table 3.1: Golden Section search algorithm

Step 1 The initial points a and b correspond, in the present context, to values η_a and η_b in (P2) and the function value $f(\cdot)$ represents here the minimum value of function F_D found for the optimization problem (P1) for a given side ratio.

Step 3 The new point is located in the larger of two intervals $\langle a; b\rangle$ and $\langle b; c\rangle$, its distance from the point b is $(3 - \sqrt{5})/2$ times the length of a larger interval.

While solving the above problem is relatively simple, the solution to the first problem (P1) requires to locate the global minimum of multi-dimensional function, which is possesses a large number of plateaus and local minima (see Figs. 3.2a–3.4a for explicit examples). As suggested in [157, 291, 298], optimization problems of this kind can be tackled very efficiently with the help of problem solving systems based on principles of evolution such as the **RASA** algorithm introduced in Section 2.5.

3.1.3 Test examples

The goal here is to examine the efficiency and robustness of the **RASA** method for the problems addressed in the previous section. In particular, we will examine the ability of the algorithm to match the position of particles within artificial 5-fiber unit cell for different objective functions. Then, the effect of selected objective function on the found microstructure is investigated. Based on results of these experiments, a suitable strategy for the determination of equivalent periodic unit cells is chosen.

[5] For all computations performed herein, the parameters η_a and η_b were set to 1.0 and 2.0, respectively. To check the admissibility of these bounds, Step 1 of the Algorithm 3.1, recall that due to assumed periodicity of the microstructure statistical descriptors are a priori affected by periodicity, too. Moreover, for the side ratio η equal to 1 or 2, the period lengths are same for both coordinates. This regularity, however, does not appear in target functions (see Figs. 2.8, 2.9, 2.10 and 2.11) so that the value of function $F_D(\eta)$ for $\eta \in (1; 2)$ should be always smaller than for the interval endpoints.

Identification problem. To test performance of the **RASA** method for the solution of problem (P1), a square periodic unit cell consisting of 5 fibers with the same volume fraction as the idealized binary image with resolution 488×358 pixels was formed to simulate the target microstructure. In particular, the dimensions of the periodic unit cell were 50×50 pixels and the fiber diameter was considered 8 pixels. The sampling template with parameters $T_W = T_H = 49$ pixels and steps $\Delta_W = \Delta_H = 6$ pixels was used to determine the lineal path function L_m.

The goal of the optimization was to reconstruct this unit cell on the basis of L_m, S_{mm} and $L_m + S_{mm}$ functions, respectively. The dimension of the optimization problem was equal to eight[6], the real-valued entries of optimized vector were truncated to integer values to obtain individual coordinate centers. The individual parameters of the **RASA** method were set according to Table 3.2; the initial population was generated purely randomly. Iteration process was terminated, if a solution with a value of objective function smaller than 10^{-6} was found or a number of function evaluations exceeded 250,000. For each objective function, the algorithm was executed twenty times to minimize the influence of various random circumstances. For each run the number of function evaluations was recorded together with the overall computational time. The results for different statistical descriptors appear in Table 3.2[7].

Parameter	***Value***
`pop_size`	64
`q`	0.04
`p_uni_mut`	0.05
`p_bnd_mut`	0.05
`p_nun_mut`	0.05
`p_mnu_mut`	0.05
`p_smp_crs`	0.10
`p_sar_crs`	0.10
`p_war_crs`	0.10
`p_dif_crs`	0.50
`b`	2.0
`T_frac`	10^{-6}
`T_frac_min`	10^{-7}
`T_mult`	0.9
`num_success_max`	10×`pop_size`
`num_counter_max`	50×`pop_size`
`num_dif_max`	20

Table 3.2: Parameter settings for the RASA method

Evidently, the algorithm was successful for all optimization runs with the same pa-

[6] Indeed, thanks to the assumed periodicity of the microstructure, we may a priori set the center of one particle to $(0, 0)$, which reduces the number of unknowns to 8 instead of 10.

[7] The tests were run on a computer with Intel Celeron 700 MHz processor and 256MB RAM under the Linux operating system. The C++ code was compiled by **gcc 2.96** GNU complier with `-O3` optimization switch.

Descriptor	***Success rate***	***Number of evaluations***			***Total time***
		Min	Avg	Max	[s]
S_{mm}	20 / 20	7,641	31,318	59,502	593
L_m	20 / 20	22,022	43,001	108,347	43,655
$S_{mm} + L_m$	20 / 20	11,018	41,820	88,027	43,278

Table 3.3: Identification problem: Number of function evaluations

rameter settings, which demonstrates the algorithm robustness. Moreover, it is evident that the L_m-based optimization is substantially more complex, both in terms of number of function evaluation and especially with respect the computational time, which is roughly by two orders of magnitude larger.

To further manifest the complexity of the optimization problem (P1), two-dimensional sections of an objective function were constructed. To the end, the center of one fiber was successively placed in all pixels of the unit cell and the value of the objective function was calculated. The resulting landscapes of all objective functions, appearing in Figs. 3.2a–3.4a, clearly demonstrate that objective functions are non-convex and multi-modal[8], which further supports the choice of the global optimization algorithm **RASA**.

Figs. 3.2b–3.4b show examples of progress during different optimization runs together with the evolution of optimal unit cells. Evidently, even for relatively high values of objective function, the arrangement of the fibers within the unit cell is seemingly identical to the target configuration (up to the translation of the periodic unit cell, of course). This fact should be taken into account when judging the quality of the periodic unit cells obtained from approximation of real microstructures.

Effect of descriptor selection. As the next step, the effect of the selected statistical descriptor on the optimized periodic unit cell was addressed[9]. The 10-fiber square periodic unit cell with the same fiber volume fraction as bitmap 2.7a was considered[10]. A sampling template with parameters $T_W = T_H = 97$ pixels and $\Delta_W = \Delta_H = 12$ pixels was used to determine the matrix lineal path function L_m, the matching range of the S_{mm} function, Eq. (3.1), was set to $i_{\max} = j_{\max} = 48$ pixels. The stopping criterion as well as parameters setting of the **RASA** method are the same as in the previous example. The isotropized values of microstructural function obtained for S_{mm}, L_{mm} and combined objective functions are shown in Figs. 3.5, 3.6 and 3.7, respectively[11].

It is evident that the L_m-function based approximation procedure is able to fit the target lineal path function very well; the two-point probability function S_{mm}, however, is completely different from the target one. The situation is relatively better for the S_{mm} based reconstruction, where the target S_{mm} function is resolved very well (note relatively

[8] Another complication comes from the fact that positions of individual fibers are discrete variables; the objective function is then piecewise constant. Figs. 3.2a–3.4a are, however, constructed from data interpolated on a regular grid and hence does not show this feature.

[9] See the works [41, 226, 247, 291] for similar discussion in the context of reconstruction of random media.

[10] The dimensions of the unit cell were 71×71 pixels, the radius of the fiber was set to $R = 8$ pixels.

[11] Note that error bars drawn by thin lines appearing in Figs. 3.5–3.7 correspond to the scatter of the target data, while the thick error bars indicate the scatter of the function resulting from optimization.

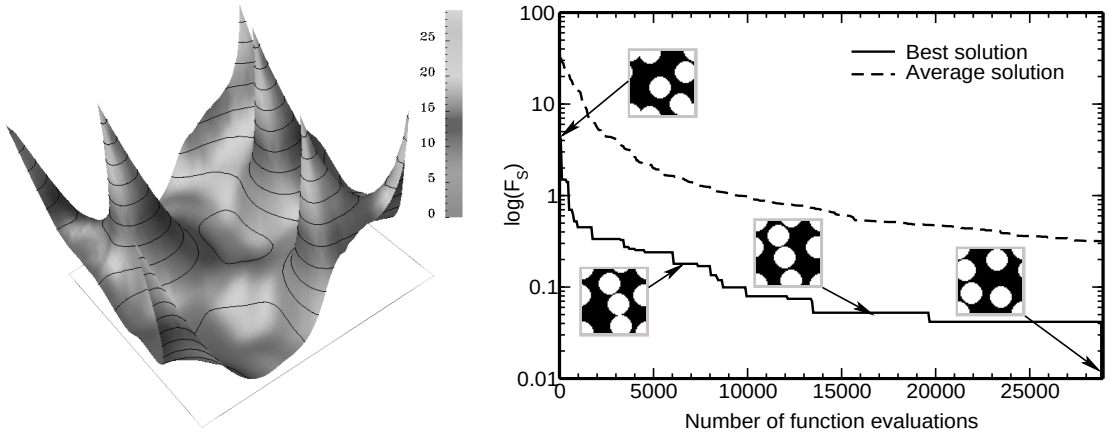

(a) (b)

Figure 3.2: S_{mm}-based optimization: (a) Objective function, (b) An example of optimization run

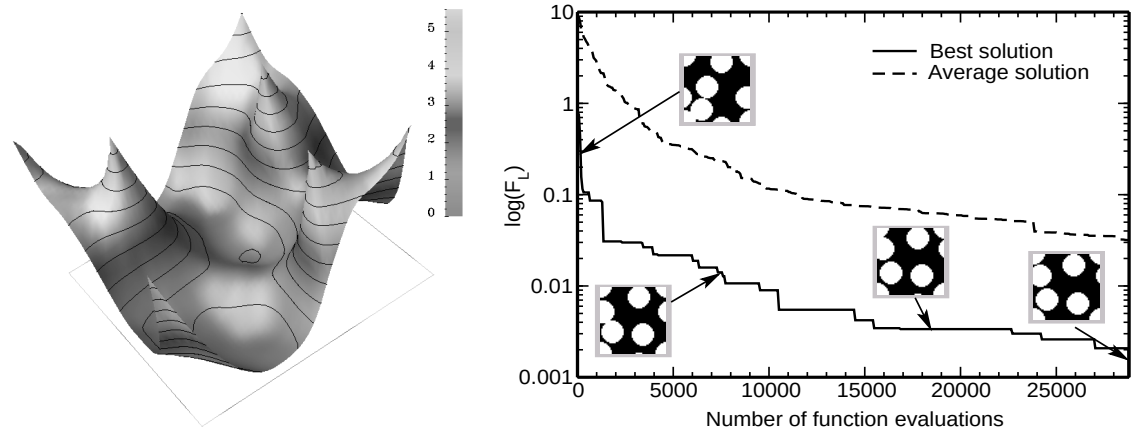

(a) (b)

Figure 3.3: L_m-based optimization: (a) Objective function, (b) An example of optimization run

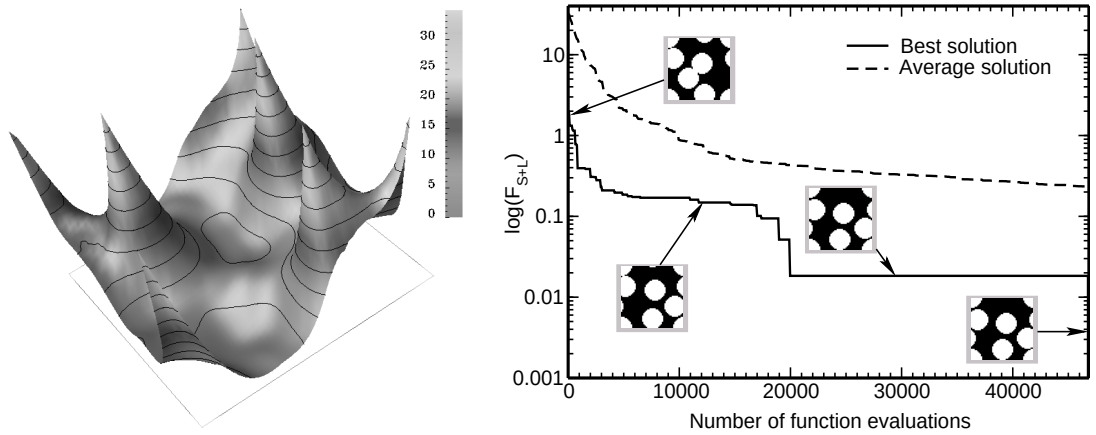

(a) (b)

Figure 3.4: $(S_{mm} + L_m)$-based optimization: (a) Objective function, (b) An example of optimization run

high isotropy of the reconstructed function evident from Fig. 3.5b) and the lineal path function L_{mm} follows the trend set by the original function, although the anisotropy of the reconstructed L_m function is somewhat higher than that of target function. As it can be expected, the best results were obtained by the combined approximation process, Fig. 3.7. Note that the isotropized value of the reconstructed function fits the target one almost perfectly, although there is a slight anisotropy introduced in the optimized function, especially for larger distances. On the other hand, the conformity of the L_m function is clearly much better then for the S_{mm}-based reconstruction. Therefore, the *combined optimization* appears to be the most appropriate and reliable choice for the definition of periodic unit cells, regardless of its computational complexity.

3.1.4 Determination of periodic unit cell

The principal objective of the present work is to construct a certain periodic unit cell, which may substitute the real microstructure when estimating the macroscopic response of a random composite subjected to uniform stresses or strains. In particular, we wish to assess a sensitivity of the proposed solution procedure to the size of the unit cell (number of particles within the PUC).

Here, this task is explored from the objective function point of view. The essential parts of the optimization procedure are reviewed in conjunction with the **RASA** method.

Finding the optimal fiber configuration. The **RASA** method, Table 2.3, was used to find the optimal fiber configuration with the set of real-coded genetic operators introduced in Section 2.5.2. The combined objective function (3.3) was considered in the optimization process. In all optimization runs, the initial population was generated purely randomly, the settings of individual parameters of the **RASA** were consistent with those presented in Table 3.2. Optimization process was terminated if one of the following conditions was met:

- Algorithm returned value $F_{S+L}(\mathbf{x}^N, H_1, H_2) \leq 10^{-6}$,
- Number of function evaluations exceeded 100,000.

The parameters $i_{\max}$ and $j_{\max}$, introduced in Eq. (3.1), were set to 48 pixels, the matrix lineal path function L_m was measured by a sampling template with dimensions $T_W = T_H = 97$ pixels and steps $\Delta_W = \Delta_H = 12$ pixels.

Finding the optimal side ratio. The Golden Section search method, Algorithm 3.1, with values $\eta_a = 1.0$, $\eta_b = 2.0$ was used. The whole optimization problem was terminated once the dimensions H_1 and H_2 of the unit cells corresponding to bounds η_a and η_b agreed up to a difference of one pixel.

The results appearing in Fig. 3.8 show a variation of the final minimum of the objective function F_{S+L} with respect to the number of particles (fibers) within the unit cell. Evidenly, the target value of the objective function 10^{-6} was too severe for the present approximation problem. However, a significant drop of the objective function can be observed already for 10 particles within the unit cell.

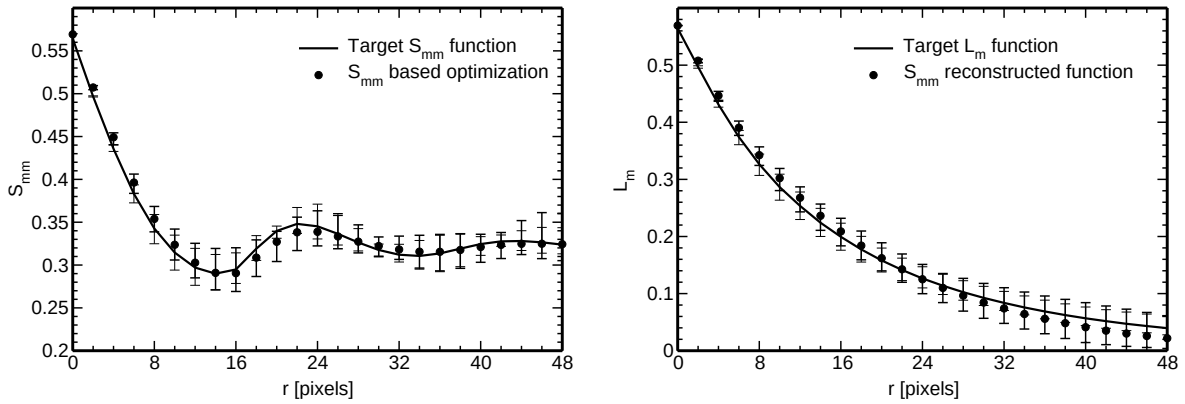

(a) (b)

Figure 3.5: S_{mm} based optimization results: (a) S_{mm} function, (b) L_m function

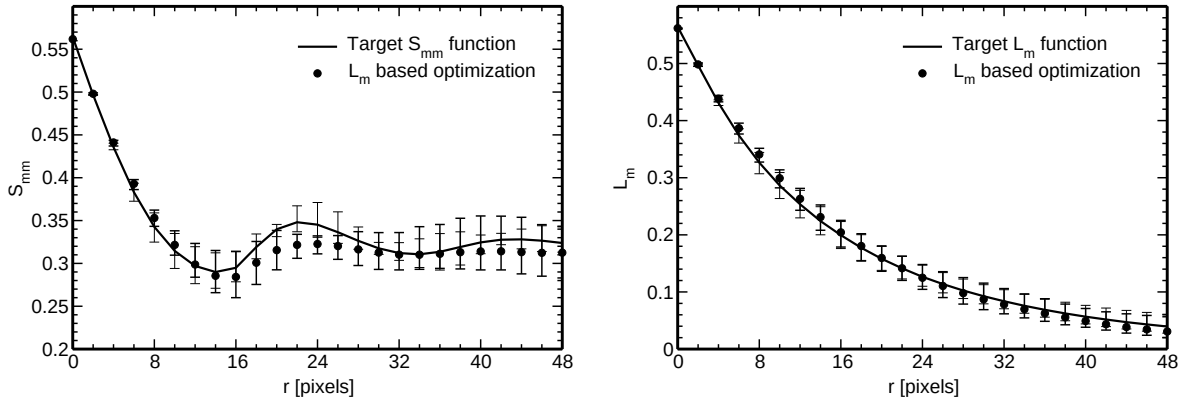

(a) (b)

Figure 3.6: L_m based optimization results: (a) S_{mm} function, (b) L_m function

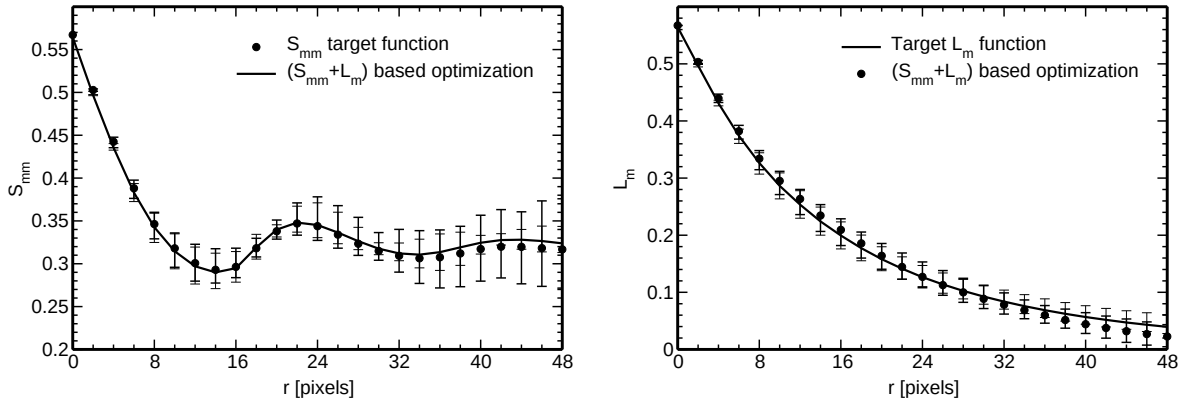

(a) (b)

Figure 3.7: $(S_{mm} + L_m)$ based optimization results: (a) S_{mm} function, (b) L_m function

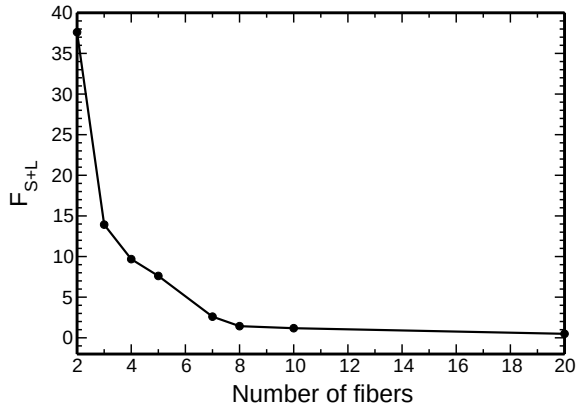

Figure 3.8: Variation of the objective function with respect to the number of particles in the PUC

Finally, some examples of the resulting unit cells are illustrated in Fig. 3.9 together with the hexagonal lattice shown for comparison. It is evident that periodic unit cells resulting from optimization are able to capture the clustering of particles in the original micrograph to some extent.

3.2 Elastic response of composites with periodic microstructure

This section illustrates the capability of the present approach by comparing the effective response of both the real composite and a selected set of associated *periodic unit cells*. With reference to the introductory part, the micromechanical analysis is restricted to elastic, linear and nonlinear viscoelastic response of a composite aggregate to a prescribed path of uniform macroscopic strains or stresses and uniform temperature change. The principle objective of this section is to offer the smallest periodic unit cell, which gives the same macroscopic *elastic response* as the real composite.

3.2.1 Problem setting

To narrow a vast body of material on this subject we limit our attention to studies dealing with the finite element analysis of the periodic unit cell [11, 22, 54, 57, 84, 98, 100, 149, 161, 241, 250, to cite a few]. This approach becomes particularly attractive when applied to "simple" microstructures such as those displayed in Fig. 3.9 and will be used throughout this section to estimate overall elastic moduli of a graphite fiber tow impregnated by polymer matrix, Fig. 2.1.

Consider a heterogeneous body V containing a very large number of identical periodic unit cells Y. The overall elastic behavior of such a composite is then governed by its microstructure, represented by a single unit cell Y, and by the behavior of individual

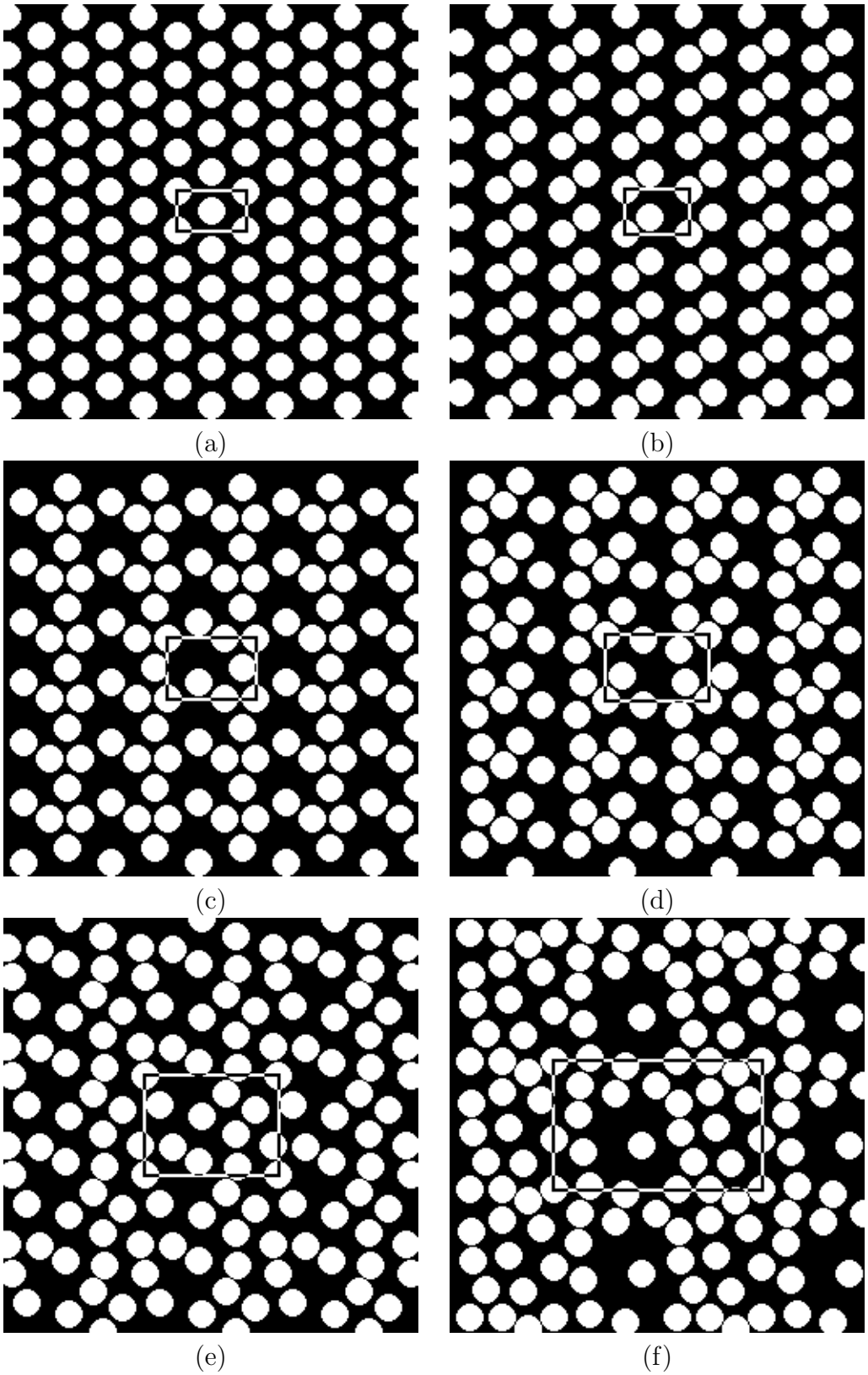

Figure 3.9: Periodic unit cells: (a) Hexagonal lattice, (b) 2-fiber PUC, (c) 4-fiber PUC, (d) 5-fiber PUC, (e) 10-fiber PUC, (f) 20-fiber PUC

phases described by displacement, strain and stress fields in the form[12]

$$\operatorname{div}\boldsymbol{\sigma}(\mathbf{x}) + \mathbf{b}(\mathbf{x}) = \mathbf{0} \qquad \text{in } V, \tag{3.5}$$
$$\boldsymbol{\varepsilon}(\mathbf{x}) = \nabla^S \mathbf{u}(\mathbf{x}) \qquad \text{in } V, \tag{3.6}$$
$$\boldsymbol{\sigma}(\mathbf{x}) = \mathsf{L}(\mathbf{x}) : \boldsymbol{\varepsilon}(\mathbf{x}) \qquad \text{in } V, \tag{3.7}$$
$$\boldsymbol{\varepsilon}(\mathbf{x}) = \mathsf{M}(\mathbf{x}) : \boldsymbol{\sigma}(\mathbf{x}) \qquad \text{in } V, \tag{3.8}$$

where $\mathbf{u}$ is the displacement field, $\boldsymbol{\varepsilon}$ and $\boldsymbol{\sigma}$ are the strain and stress fields, respectively, L is the stiffness tensor and M is the compliance tensor and $\nabla^S\mathbf{u}$ stands for the symmetric part of the gradient of the displacement field $\mathbf{u}$, $\nabla^S\mathbf{u}(\mathbf{x}) = \left(\nabla\mathbf{u}(\mathbf{x}) + \nabla^{\mathsf{T}}\mathbf{u}(\mathbf{x})\right)/2$ and $\mathbf{b}$ is the vector of body forces. Assuming n-phase composite with constant phase moduli and with reference to Eqs. (3.8), the elastic constitutive equations of the phases are given by

$$\boldsymbol{\sigma}_r(\mathbf{x}) = \mathsf{L}_r\boldsymbol{\varepsilon}_r(\mathbf{x}), \quad \boldsymbol{\varepsilon}_r(\mathbf{x}) = \mathsf{M}_r\boldsymbol{\sigma}_r(\mathbf{x}), \quad \text{in } V_r,\ r = 1, \ldots, n \tag{3.9}$$

where V_r denotes the domain occupied by the r-th phase. Define the following mechanical loading problems

$$\mathbf{u}_0(\mathbf{x}) = \boldsymbol{E}\cdot\mathbf{x} \qquad \text{on } \partial V, \tag{3.10}$$
$$\boldsymbol{p}_0(\mathbf{x}) = \boldsymbol{\Sigma}\cdot\mathbf{n}(\mathbf{x}) \qquad \text{on } \partial V, \tag{3.11}$$

where $\mathbf{u}_0$ and $\boldsymbol{p}_0$ are the displacement and traction vectors at the external boundary ∂V of the domain V of the composite; $\mathbf{n}$ is the outer unit normal to ∂V and $\boldsymbol{E}$ and $\boldsymbol{\Sigma}$ are the applied macroscopic uniform strain and stress fields, respectively. The macroscopic constitutive relations, corresponding to the *homogenized medium* are then provided by

$$\langle\boldsymbol{\sigma}(\mathbf{x})\rangle = \langle\mathsf{L}(\mathbf{x}) : \boldsymbol{\varepsilon}(\mathbf{x})\rangle = \sum_{r=1}^{n} c_r\mathsf{L}_r : \langle\boldsymbol{\varepsilon}_r(\mathbf{x})\rangle = \mathsf{L}^{\mathsf{hom}} : \boldsymbol{E}, \tag{3.12}$$
$$\langle\boldsymbol{\varepsilon}(\mathbf{x})\rangle = \langle\mathsf{M}(\mathbf{x}) : \boldsymbol{\sigma}(\mathbf{x})\rangle = \sum_{r=1}^{n} c_r\mathsf{M}_r : \langle\boldsymbol{\sigma}_r(\mathbf{x})\rangle = \mathsf{M}^{\mathsf{hom}} : \boldsymbol{\Sigma}, \tag{3.13}$$

where $\langle\cdot\rangle$ stands for the spatial average of a given field with respect to the domain V, c_r is the volume fraction of the r-th phase, and $\mathsf{L}^{\mathsf{hom}}$ and $\mathsf{M}^{\mathsf{hom}}$ are the effective stiffness and compliance tensors of the heterogenous material, respectively. Eqs. (3.12) and (3.13) follow directly from Hill's lemma [94]. He proved that for compatible strain and equilibrated stress fields satisfying either the affine displacements (3.12) or uniform tractions (3.13) boundary conditions the following relation holds

$$\langle\boldsymbol{\varepsilon}(\mathbf{x}) : \boldsymbol{\sigma}(\mathbf{x})\rangle = \boldsymbol{E} : \boldsymbol{\Sigma}, \tag{3.14}$$

and consequently

$$\boldsymbol{E} : \mathsf{L}^{\mathsf{hom}} : \boldsymbol{E} = \langle\boldsymbol{\varepsilon}(\mathbf{x}) : \mathsf{L}(\mathbf{x}) : \boldsymbol{\varepsilon}(\mathbf{x})\rangle\,, \tag{3.15}$$
$$\boldsymbol{\Sigma} : \mathsf{M}^{\mathsf{hom}} : \boldsymbol{\Sigma} = \langle\boldsymbol{\sigma}(\mathbf{x}) : \mathsf{M}(\mathbf{x}) : \boldsymbol{\sigma}(\mathbf{x})\rangle\,. \tag{3.16}$$

[12] See Appendix C for more detailed discussion on this topic.

Eq. (3.14) states in fact that the average of "microscopic" internal work is equal to the macroscopic work done by internal forces. The above relations provide the stepping stone for the derivation of effective properties of composite materials.

The following paragraphs outline evaluation of effective properties of a composite aggregate represented here by the periodic material models of Fig. 3.9. Two specific approaches corresponding to loading conditions (3.10) and (3.11) are discussed in the sequel.

3.2.2 Formulation based on strain approach

Consider a periodic unit cell Y (PUC) subjected to a uniform strain $\boldsymbol{E}$, see Eq. (3.10). In view of the periodicity of the unit cell, the strain and displacement fields in the PUC admit the following decomposition

$$\mathbf{u}(\mathbf{x}) = \boldsymbol{E} \cdot \mathbf{x} + \mathbf{u}^*(\mathbf{x}) \qquad \text{in } Y \tag{3.17}$$

$$\boldsymbol{\varepsilon}(\mathbf{x}) = \boldsymbol{E} + \boldsymbol{\varepsilon}^*(\mathbf{x}) \qquad \text{in } Y. \tag{3.18}$$

The first term in Eq. (3.17) corresponds to a displacement field in an effective homogeneous medium which has the same overall properties at the composite aggregate. The fluctuation part $\mathbf{u}^*$ enters Eq. (3.17) as a consequence of the presence of heterogeneities and, due to the periodicity of the microstructure, is Y-periodic as well; see, e.g., [18, 161, 222, 223, 241] and Appendix C for further discussion. The periodicity of $\mathbf{u}^*$ further implies that the average of $\boldsymbol{\varepsilon}^*$ in the unit cell vanishes as well, see, e.g, [161, 241] and references therein. Hence

$$\boldsymbol{\varepsilon}(\mathbf{x}) = \boldsymbol{E} + \boldsymbol{\varepsilon}^*(\mathbf{x}), \qquad \langle \boldsymbol{\varepsilon}^*(\mathbf{x}) \rangle = \frac{1}{Y} \int_Y \boldsymbol{\varepsilon}^*(\mathbf{x}) \, \mathrm{d}\mathbf{x} = \mathbf{0}. \tag{3.19}$$

Next, assume a virtual displacement in the form $\delta\mathbf{u}(\mathbf{x}) = \delta\mathbf{u}^*(\mathbf{x})$, with $\delta\mathbf{u}^*(\mathbf{x})$ being periodic. Then the principle of virtual work reads

$$\langle \delta\boldsymbol{\varepsilon}^*(\mathbf{x}) : \boldsymbol{\sigma}(\mathbf{x}) \rangle = \langle \delta\boldsymbol{\varepsilon}^*(\mathbf{x}) \rangle \, : \, \langle \boldsymbol{\sigma}(\mathbf{x}) \rangle = 0, \tag{3.20}$$

as $\langle \delta\boldsymbol{\varepsilon}^* \rangle = \mathbf{0}$ by Eq. (3.19). Note that Eq. (3.20) is essentially the Hill lemma introduced by Eq. (3.14).

Discretization.

Solving the above relation calls for a suitable numerical technique such as the Finite Element Method (FEM), see, e.g., [12, 21, 23, 242, 301]. To that end, we decompose the periodic unit cell Y into N_e disjoint elements Y_e, such that every element is contained only in one phase (i.e., the discretization "respects" the phase interfaces). In this framework the approximation of the fluctuating part of the displacement field $\mathbf{u}^*$ in Eq. (3.17), written in the engineering notation introduced in Appendix A, assumes the form

$$\{\mathsf{u}^*(\mathbf{x})\} = [\mathsf{N}(\mathbf{x})] \, \{\mathsf{r}\}, \tag{3.21}$$

where $[\mathsf{N}]$ represents shape functions for a given partition of the unit cell (the piecewise linear approximations of the displacement fields is used in the present study) and $\{\mathsf{r}\}$ is

the vector of unknown degrees of freedom. The corresponding strain field is then provided by

$$\{\varepsilon(\mathbf{x})\} = \{\mathsf{E}\} + [\mathsf{B}(\mathbf{x})]\,\{\mathsf{r}\}. \tag{3.22}$$

Introducing Eq. (3.22) into Eq. (3.20) gives for any kinematically admissible strains $\{\delta\varepsilon^*\} = [\mathsf{B}]\,\{\delta\mathsf{r}\}$ the associated system oflinear equations in the form

$$[\mathsf{K}]\,\{\mathsf{r}\} = \{\mathsf{f}\}, \tag{3.23}$$

where the stiffness matrix $[\mathsf{K}]$ of the system and the vector of generalized nodal forces $\{\mathsf{f}\}$ is obtained by the standard assembly A of contributions from individual elements [12, 21, 23, 242, 301]

$$[\mathsf{K}] = \mathop{\mathsf{A}}_{e=1}^{N_e} [\mathsf{K_e}]\,, \quad \text{where} \quad [\mathsf{K_e}] = \frac{1}{|Y|}\int_{Y_e} [\mathsf{B_e}]^{\mathsf{T}}\,[\mathsf{L_e}]\,[\mathsf{B_e}]\;\mathrm{d}Y_e, \tag{3.24}$$

$$\{\mathsf{f}\} = \mathop{\mathsf{A}}_{e=1}^{N_e} \{\mathsf{f_e}\}, \quad \text{where} \quad \{\mathsf{f_e}\} = -\frac{1}{|Y|}\int_{Y_e} [\mathsf{B_e}]^{\mathsf{T}}\,[\mathsf{L_e}]\,\{\mathsf{E}\}\,\mathrm{d}Y_e, \tag{3.25}$$

where $[\mathsf{B_e}]$ is the strain-displacement matrix and $[\mathsf{L_e}]$ is the material stiffness matrix of the e-th element, respectively. Note that constant strain triangles (CST) [12, 21, 301] are used in this work.

System (3.23) can be used to provide the finite element approximation of the coefficients of the effective stiffness matrix $\left[\mathsf{L}^{\mathsf{fem}}\right]$ as volume averages of the local fields derived from the solution of successive elasticity problems. To that end, the periodic unit cell is loaded, in turn, by each components of $\{\mathsf{E}\}$, while the other components vanish. The volume stress averages normalized with respect to $\{\mathsf{E}\}$ then furnish individual columns of $\left[\mathsf{L}^{\mathsf{fem}}\right]$.

3.2.3 Formulation based on stress approach

Sometimes it is desirable to apply the overall stress $\boldsymbol{\Sigma}$, Eq. (3.11), instead of the overall strain $\boldsymbol{E}$. Eq. (3.20) then modifies to

$$\langle \delta\boldsymbol{\varepsilon}(\mathbf{x}) : \boldsymbol{\sigma}(\mathbf{x})\rangle = \delta\boldsymbol{E} : \boldsymbol{\Sigma}. \tag{3.26}$$

Clearly, such a loading condition leaves us with unknown overall strain $\boldsymbol{E}$ and periodic displacement field $\mathbf{u}^*$ to be determined. Substituting Eq. (3.18) into Eq. (3.26) yields

$$\delta\boldsymbol{E} :\, \langle \mathbf{L}(\mathbf{x}) :\, (\boldsymbol{E} + \boldsymbol{\varepsilon}^*(\mathbf{x}))\rangle + \langle \delta\boldsymbol{\varepsilon}^*(\mathbf{x}) : \mathbf{L}(\mathbf{x}) : \boldsymbol{E}\rangle + \langle \delta\boldsymbol{\varepsilon}^*(\mathbf{x}) : \mathbf{L}(\mathbf{x}) : \boldsymbol{\varepsilon}^*(\mathbf{x})\rangle = \delta\boldsymbol{E} : \boldsymbol{\Sigma}. \tag{3.27}$$

Since the variations $\delta\boldsymbol{E}$ and $\delta\boldsymbol{\varepsilon}^*(\mathbf{x})$ are independent, the preceding equation can be split into two equalities

$$\begin{aligned} \delta\boldsymbol{E} : \boldsymbol{\Sigma} &= \delta\boldsymbol{E} :\, (\langle \mathbf{L}(\mathbf{x})\rangle \,:\, \boldsymbol{E} + \langle \mathbf{L}(\mathbf{x}) : \boldsymbol{\varepsilon}^*(\mathbf{x})\rangle) \\ 0 &= \langle \delta\boldsymbol{\varepsilon}^*(\mathbf{x}) : \mathbf{L}(\mathbf{x})\rangle \,:\, \boldsymbol{E} + \langle \delta\boldsymbol{\varepsilon}^*(\mathbf{x}) : \mathbf{L}(\mathbf{x}) : \boldsymbol{\varepsilon}^*(\mathbf{x})\rangle\,. \end{aligned} \tag{3.28}$$

Discretization.

Finally, following the same lines as in the previous paragraph, the FE discretization of Eqs. (3.21) and (3.22) provides the coupled linear system in the form [161]

$$\begin{bmatrix} \mathsf{K}_{11} & \mathsf{K}_{12} \\ \mathsf{K}_{21} & \mathsf{K}_{22} \end{bmatrix} \begin{Bmatrix} \mathsf{E} \\ \mathsf{r} \end{Bmatrix} = \begin{Bmatrix} \Sigma \\ 0 \end{Bmatrix}. \tag{3.29}$$

where, similarly to Eqs. (3.24)–(3.25),

$$[\mathsf{K}_{11}] = \mathop{\mathsf{A}}_{e=1}^{N_e} [\mathsf{K}_{11,\mathsf{e}}], \quad \text{where} \quad [\mathsf{K}_{11,\mathsf{e}}] = \frac{1}{|Y|} \int_{Y_e} [\mathsf{L}_\mathsf{e}] \, \mathrm{d}Y_e, \tag{3.30}$$

$$[\mathsf{K}_{21}]^{\mathsf{T}} = [\mathsf{K}_{12}] = \mathop{\mathsf{A}}_{e=1}^{N_e} [\mathsf{K}_{12,\mathsf{e}}], \quad \text{where} \quad [\mathsf{K}_{12,\mathsf{e}}] = \frac{1}{|Y|} \int_{Y_e} [\mathsf{L}_\mathsf{e}] [\mathsf{B}_\mathsf{e}] \, \mathrm{d}Y_e, \tag{3.31}$$

$$[\mathsf{K}_{22}] = \mathop{\mathsf{A}}_{e=1}^{N_e} [\mathsf{K}_{22,\mathsf{e}}], \quad \text{where} \quad [\mathsf{K}_{22,\mathsf{e}}] = \frac{1}{|Y|} \int_{Y_e} [\mathsf{B}_\mathsf{e}]^{\mathsf{T}} [\mathsf{L}_\mathsf{e}] [\mathsf{B}_\mathsf{e}] \, \mathrm{d}Y_e. \tag{3.32}$$

The above system of equations can be used to derive the finite element method approximation of the effective compliance matrix $\left[\mathsf{M}^{\mathsf{fem}}\right]$. In analogy with the strain approach, the periodic unit cell is loaded, in turn, by each of the components of $\{\Sigma\}$, while the other components vanish. The volume strain averages normalized with respect to $\{\Sigma\}$ then supply individual entries of $\left[\mathsf{M}^{\mathsf{fem}}\right]$.

In addition to this direct approach, the system (3.29) can be used to obtain an alternative characterization of the finite element approximation to the effective stiffness matrix $\left[\mathsf{L}^{\mathsf{fem}}\right]$. Indeed, when eliminating the vector of the fluctuating nodal displacements $\{\mathsf{r}\}$ we directly arrive at the form of the macroscopic constitutive law, compare with Eq. (3.12),

$$\{\Sigma\} = \left[\mathsf{L}^{\mathsf{fem}}\right] \{\mathsf{E}\}, \quad \text{where} \quad \left[\mathsf{L}^{\mathsf{fem}}\right] = [\mathsf{K}_{11}] - [\mathsf{K}_{12}] [\mathsf{K}_{22}]^{-1} [\mathsf{K}_{12}]^{\mathsf{T}}. \tag{3.33}$$

First, note that the term $[\mathsf{K}_{12}] [\mathsf{K}_{22}]^{-1} [\mathsf{K}_{12}]^{\mathsf{T}}$, appearing in the previous equation, can be interpreted as the difference between the classical Voight bound $[\mathsf{K}_{11}]$ [94, 267] (i.e., the volume average of the material stiffness matrix) and the finite element approximation of the homogenized stiffness matrix[13]. In addition, Eq. (3.33) allows the interpretation of the effective stiffness matrix as the static condensation (the Schur complement) of the $[\mathsf{K}]$ matrix with respect to the "internal" fluctuating degrees of freedom $\{\mathsf{r}\}$ while the "macroscopic" degrees of freedom $\{\mathsf{E}\}$ remain uncondensed. This shows the connection of the presented approach with the "algebraic homogenization" methods, see, e.g., [31, 47, 87, 121, 179].

3.2.4 Implementation issues

The last unresolved feature of the solution of systems (3.23) or (3.29) is the enforcement of the periodicity of the fluctuating displacement $\mathbf{u}^*$ (same displacements on opposite sides of the unit cell). Several methods can used to account for this condition [161, 277]: using the

[13] In fact, the introduced finite element approximation represents an upper bound to the homogenized stiffness matrix $\left[\mathsf{L}^{\mathsf{hom}}\right]$ in the sense that the inequality $\{\varepsilon\}^{\mathsf{T}}(\left[\mathsf{L}^{\mathsf{fem}}\right] - \left[\mathsf{L}^{\mathsf{hom}}\right])\{\varepsilon\} \geq 0$ holds for all $\{\varepsilon\}$ corresponding to the engineering representation of the strain tensor, Eq. (A.2). The proof of this statement can be found in [57].

possible symmetry of the periodic unit cell and loading, method of Lagrange multipliers, penalty techniques (see also Section 5.3) and, finally, elimination method, employed in this work unless stated otherwise. From the algorithmic point of view, the elimination method can be simply described as prescribing the same code numbers to the nodes on the opposite faces of the unit cell. The advantage of this method is a direct incorporation of the periodicity of the fluctuating without additional degrees of freedom (Lagrangian technique) or artificial constraints (penalty method). The disadvantage of this method is the inevitable increase of the bandwidth of the stiffness matrix (especially for 3D problems) and the need of specialized mesh generation procedures, which ensures that the opposite sides of a PUC are identically discretized [119, 277].

For two-dimensional microstructures considered in this chapter, the two-dimensional mesh generator **Triangle 1.3** [229] was used to generate finite element meshes complying with the periodic boundary conditions. To this end, the iterative procedure is used: in the first step, the triangular mesh is generated for a given configuration of fibers. Each fiber is approximated by an inscribed polygon with specified number of sides. Then, the position of the boundary nodes for the opposite sides of the unit cell is extracted from the mesh data and the nodes are matched together. In the next step, the nodes which are closer than a selected distance tolerance are removed and the mesh generator is executed again with the switch ensuring that there are no new points introduced on the boundary of the unit cell. Finally, the radius of the fiber is iteratively adjusted until the difference of volume fraction of the mesh matrix phase and the prescribed matrix volume fraction is smaller than a user-defined tolerance. Examples of the unit cell meshes generated by this procedure are shown in Fig. 3.10.

Finally, note that Eqs. (3.17) and (3.18) determine the fluctuating displacement up to the rigid body motion; to prevent singularity of the stiffness matrix, the displacement of the unit cell corners are constrained to zero value[14].

3.2.5 Numerical results

In keeping up with our promise we now present several numerical results derived for a given material system in order to provide estimates of the minimum size of the periodic unit cell with regard to the material effective properties. The generalized plane-strain state, introduced in Appendix A.2.1, is assumed throughout the analysis.

As an example we consider a composite system composed of graphite fibers embedded in the epoxy matrix[15]. Material properties are listed in Table 3.4.

Phase	E_A [GPa]	E_T [GPa]	G_T [GPa]	ν_A
Fiber	386	7.6	2.6	0.41
Matrix	5.5	5.5	1.96	0.40

Table 3.4: Elastic material properties of T-50/Epoxy system

[14] See, e.g., [124] for alternative methods for prescribing the periodic boundary conditions by boundary displacements $\mathbf{u}$.

[15] Note that fibers are assumed to be transversally isotropic, see Section A.2.1 for relation between engineering constants E_A, E_T, G_T and ν_A and material stifness tensor.

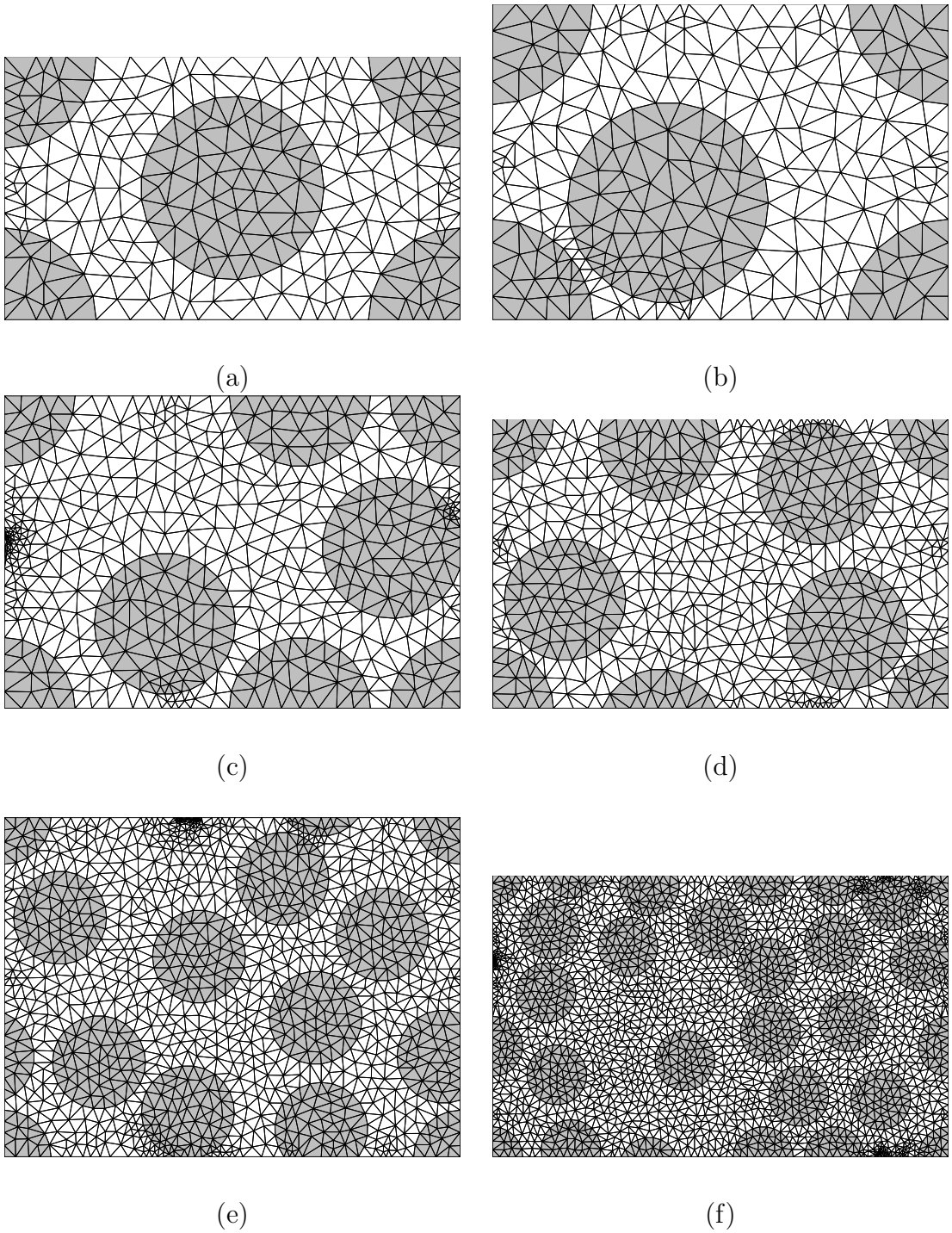

Figure 3.10: Periodic unit cells meshes: (a) Hexagonal lattice, (b) 2-fiber PUC, (c) 4-fiber PUC, (d) 5-fiber PUC, (e) 10-fiber PUC, (f) 20-fiber PUC.

Unit cell	$\mathsf{L}^{\mathsf{fem}}{}_{11}$ [GPa]	$\mathsf{L}^{\mathsf{fem}}{}_{22}$ [GPa]	$\mathsf{L}^{\mathsf{fem}}{}_{33}$ [GPa]	$\mathsf{L}^{\mathsf{fem}}{}_{44}$ [GPa]	c_f	***Total DOFs***	K ***size*** [kB]
Original	10.74	10.72	2.216	176.83	0.4357	34,312	140,937
2 fibers PUC	10.71	10.71	2.218	176.83	0.4357	502	236
5 fibers PUC	10.74	10.72	2.216	176.83	0.4357	1,120	746
10 fibers PUC	10.74	10.72	2.216	176.83	0.4357	2,942	2,380
Hexagonal array	10.74	10.74	2.217	176.83	0.4357	480	557

Table 3.5: Components of the effective stiffness matrix

First, to prove applicability of the proposed method, we compare the elastic moduli derived for the original microstructure, Fig 2.1, with those found for the periodic unit cells displayed in Fig. 3.9. Note that the solution of the original problem requires to process of the order of magnitude more equations than the solution based on the PUC approach.

Selected components of the effective stiffness matrix $\left[\mathsf{L}^{\mathsf{fem}}\right]$ together with the number of total degrees of freedom and memory requirements are stored in Table 3.5[16]. Results obtained for the hexagonal arrangements of fibers are provided for additional comparison. Evidently, the periodic unit cell is, unlike the hexagonal lattice corresponding to the transversally isotropic medium, capable of capturing a slight anisotropy associated with the real microstructure. In addition, the results in Table 3.5 also promote the PUC consisting of 5 fibers only as the smallest one we should consider for the evaluation of effective properties.

To further support the present approach we determined the mean value and standard deviation of effective stiffnesses derived from five independent runs for unit cells defined through a random cut of the original micrograph, Fig. 2.1(b). Dimensions of such a unit cell were selected to comply with dimensions found for the PUC consisting of 10 particles. Results, given in Table 3.7, are rather discouraging and should caution the reader against pursuing this approach.

Modulus	***Mean value*** [GPa]	***Standard deviation*** [GPa]	***Variation coefficient*** [%]
L_{11}	10.74	0.013	0.12
L_{22}	10.72	0.013	0.12
L_{33}	2.215	0.003	0.13

Table 3.6: Variation of effective stiffnesses for five ten-particle optimal PUC

Finally, to confirm our theoretical expectations, we investigated an influence of the proposed optimization technique on the effective moduli computed for the 10-fibers PUC derived from five independent optimization runs. Results stored in Table 3.6 show that the final moduli are not sensible to the particular fiber configuration (each optimization run provides a slight different fiber arrangements having, however, the same material's statistics up to the two-point probability and lineal path function).

[16] Note that the skyline scheme [12, 21] was used for the storage of the stiffness matrix $[\mathsf{K}]$; the bandwidth of the matrix was optimized by the Cuthill-McKee algorithm [42].

Modulus	*Mean value* [GPa]	*Standard deviation* [GPa]	*Variation coefficient* [%]
L_{11}	10.72	0.32	2.97
L_{22}	10.69	0.38	3.54
L_{33}	2.210	0.07	3.48

Table 3.7: Variation of effective stiffnesses for five randomly picked ten-particle PUC

3.3 Residual and thermal fields

Apart from mechanical loading, Eqs. (3.10) and (3.11), composite materials often experience loading by distribution of local eigenstrains or eigenstresses. Regardless of their origin they may be interpreted as internal loads in an otherwise elastic medium [51, 52, 174]. Thermal and viscoelastic strains, admitted in the present analysis, together with transformation strains discussed in Chapter 4 are specific examples of such fields. Extension to the modeling of inelastic deformation and various damage events such as fiber debonding and/or sliding by means of equivalent eigenstrains has also been successfully examined; see, e.g., [33, 52, 54, 55, 268, 235].

3.3.1 Macroscopic constitutive law

Consider the RVEs of Fig. 3.9. Further suppose that in addition to mechanical loading the periodic unit cell subjected to an eigenstress $\boldsymbol{\lambda}$ or eigenstrain $\boldsymbol{\mu}$ fields. The local constitutive equations (3.8) are then augmented to read, see Eqs. (A.14) and (A.16),

$$\boldsymbol{\sigma}(\mathbf{x}) = \mathbf{L}(\mathbf{x}) : \boldsymbol{\varepsilon}(\mathbf{x}) + \boldsymbol{\lambda}(\mathbf{x}), \qquad \boldsymbol{\varepsilon}(\mathbf{x}) = \mathbf{M}(\mathbf{x}) : \boldsymbol{\sigma}(\mathbf{x}) + \boldsymbol{\mu}(\mathbf{x}), \tag{3.34}$$

and similarly the phase constitutive equations, Eq. (3.9), become

$$\boldsymbol{\sigma}_r(\mathbf{x}) = \mathbf{L}_r : \boldsymbol{\varepsilon}_r(\mathbf{x}) + \boldsymbol{\lambda}_r, \qquad \boldsymbol{\varepsilon}_r(\mathbf{x}) = \mathbf{M}_r : \boldsymbol{\sigma}_r(\mathbf{x}) + \boldsymbol{\mu}_r, \tag{3.35}$$

for $r = 1, \ldots, n$, where the local phase eigenstrain $\boldsymbol{\mu}_r$ and eigenstress $\boldsymbol{\lambda}_r$ are related by

$$\boldsymbol{\mu}_r = -\mathbf{M}_r : \boldsymbol{\lambda}_r, \qquad \boldsymbol{\lambda}_r = -\mathbf{L}_r : \boldsymbol{\mu}_r. \tag{3.36}$$

To proceed we recall the stress control approach and rewrite Eq. (3.26) in the form

$$\langle \delta\boldsymbol{\varepsilon}(\mathbf{x}) : \boldsymbol{\sigma}(\mathbf{x}) \rangle = \langle \delta\boldsymbol{\varepsilon}(\mathbf{x}) : \mathbf{L}(\mathbf{x}) : \ (\boldsymbol{\varepsilon}(\mathbf{x}) + \boldsymbol{\lambda}(\mathbf{x})) \rangle = \delta\boldsymbol{E} : \boldsymbol{\Sigma}. \tag{3.37}$$

Discretization

With reference to Eq. (3.29) the resulting system of algebraic equations arising in the finite element formulation assumes the form

$$\begin{bmatrix} \mathsf{K}_{11} & \mathsf{K}_{12} \\ \mathsf{K}_{21} & \mathsf{K}_{22} \end{bmatrix} \begin{Bmatrix} \mathsf{E} \\ \mathsf{r} \end{Bmatrix} = \begin{Bmatrix} \boldsymbol{\Sigma} + \mathsf{f}_1 \\ \mathsf{f}_2 \end{Bmatrix}, \tag{3.38}$$

where the load vectors f_1 and f_2 resulting from the eigenstress fields are provided by

$$\{\mathsf{f}_1\} = \mathop{\mathsf{A}}_{e=1}^{N_e}\{\mathsf{f}_{1,\mathsf{e}}\}, \quad \text{where} \quad \{\mathsf{f}_{1,\mathsf{e}}\} = -\frac{1}{|Y|}\int_{Y_e}\{\lambda_\mathsf{e}\}\,\mathrm{d}Y_e, \tag{3.39}$$

$$\{\mathsf{f}_2\} = \mathop{\mathsf{A}}_{e=1}^{N_e}\{\mathsf{f}_{2,\mathsf{e}}\}, \quad \text{where} \quad \{\mathsf{f}_{2,\mathsf{e}}\} = -\frac{1}{|Y|}\int_{Y_e}[\mathsf{B}_\mathsf{e}]^{\mathsf{T}}\{\lambda_\mathsf{e}\}\,\mathrm{d}Y_e. \tag{3.40}$$

When excluding the eigenfields effects, the above relation (3.38) reduces to Eq. (3.29).

3.3.2 Thermal loads

Consider now a heterogeneous body subjected to an uniform temperature change $\Delta\theta$. The local phase eigenstrains $\{\mu_\mathsf{r}\}$ are then provided by, see Eq. (A.19), $\{\mu_\mathsf{r}\} = \{\mathsf{m}_\mathsf{r}\}\Delta\theta$, where the thermal strain vector $\{\mathsf{m}_\mathsf{r}\}$ lists the coefficients of thermal expansion of the phase r.

To obtain the approximation of the effective coefficient of the thermal expansion $\{\mathsf{m}^{\mathsf{fem}}\}$, the unit cell Y is subjected to the uniform temperature change $\Delta\theta$ equal to unity while the overall stress $\{\Sigma\}$ is set to zero. The components of the overall average strain $\{\mathsf{E}\}$ comply with the effective coefficients of thermal expansion $\{\mathsf{m}^{\mathsf{fem}}\}$.

An alternative approach relies on standard volume averaging. In particular, recall the strain volume average in the form

$$\boldsymbol{E} = \frac{1}{|Y|}\int_Y (\mathbf{M}(\mathbf{x}) : \boldsymbol{\sigma}(\mathbf{x}) + \boldsymbol{m}(\mathbf{x})\Delta\theta)\,\mathrm{d}Y, \tag{3.41}$$

which directly provides the macroscopic constitutive law

$$\frac{1}{|Y|}\int_Y (\mathbf{M}(\mathbf{x}) : \boldsymbol{\sigma}(\mathbf{x}) + \boldsymbol{m}(\mathbf{x})\Delta\theta)\,\mathrm{d}Y = \mathbf{M}^{\mathsf{hom}}\boldsymbol{\Sigma} + \boldsymbol{m}^{hom}\Delta\theta. \tag{3.42}$$

After introducing the mechanical and thermal stress concentration factors $\mathbf{B}(\mathbf{x})$ and $\boldsymbol{b}(\mathbf{x})$ such that [50]

$$\boldsymbol{\sigma}(\mathbf{x}) = \mathbf{B}(\mathbf{x}) : \boldsymbol{\Sigma} + \boldsymbol{b}(\mathbf{x})\Delta\theta, \tag{3.43}$$

we find

$$\boldsymbol{\Sigma} = \left(\int_Y \mathbf{M}(\mathbf{x}) : \mathbf{B}(\mathbf{x})\,\mathrm{d}Y\right) : \boldsymbol{\Sigma} + \left(\int_Y \mathbf{M}(\mathbf{x}) :\ (\boldsymbol{b}(\mathbf{x}) + \boldsymbol{m}(\mathbf{x}))\,\mathrm{d}Y\right)\Delta\theta. \tag{3.44}$$

When admitting only thermal effects, $\boldsymbol{\Sigma} = \mathbf{0}$, we get from (3.43)

$$\boldsymbol{\Sigma} = \sum_{r=1}^{n} c_r \int_{Y_r} \boldsymbol{b}(\mathbf{x})\,\mathrm{d}Y_r = \sum_{r=1}^{n} c_r \boldsymbol{b}_r = \mathbf{0}. \tag{3.45}$$

After combining Eqs. (3.42) and (3.45) we arrive at the overall thermal strain vector now given by

$$\boldsymbol{m}^{hom} = \frac{1}{|Y|}\int_Y \mathbf{M}(\mathbf{x}) : \boldsymbol{b}(\mathbf{x})\,\mathrm{d}Y + \langle \boldsymbol{m}(\mathbf{x})\rangle\,. \tag{3.46}$$

Assuming again piecewise uniform variation of phase thermal and elastic properties we finally get, using the engineering notation introduced in Appendix A,

$$\left[\mathsf{M}^{\mathsf{hom}}\right] = \sum_{r=1}^{n} c_r \left[\mathsf{M}_\mathsf{r}\right] \left[\mathsf{B}_\mathsf{r}\right], \qquad \{\mathsf{m}^{\mathsf{hom}}\} = \sum_{r=1}^{n} c_r \left(\left[\mathsf{M}_\mathsf{r}\right] \{\mathsf{b}_\mathsf{r}\} + \{\mathsf{m}_\mathsf{r}\}\right). \tag{3.47}$$

At this point it is perhaps useful to recall the Levin formula [143] that reads

$$\{\mathsf{m}\} = \sum_{r=1}^{n} c_r \left[\mathsf{B}_\mathsf{r}\right]^{\mathsf{T}} \{\mathsf{m}_\mathsf{r}\}. \tag{3.48}$$

Note that individual columns of the finite element based approximation to the matrix $\left[\mathsf{B}_\mathsf{r}^{\mathsf{fem}}\right]$ are found as volume averages of the local stresses derived from four independent elasticity problems when loading the unit cell, in turn, by each component of $\{\Sigma\}$ equal to unity, while the other components are set to zero. Finally, the 4×1 vector $\{\mathsf{b}_\mathsf{r}^{\mathsf{fem}}\}$ is identified with the phase volume average of the local stresses when subjecting the unit cell to the uniform temperature change $\Delta\theta = 1$ K.

3.3.3 Numerical results

Here we present some numerical results obtained for the graphite-epoxy composite system. The material properties are listed in Table 3.8. The analysis was carried out under generalized plane strain conditions.

Phase	E_A [GPa]	E_T [GPa]	G_T [GPa]	ν_A	α_A [K^{-1}]	α_T [K^{-1}]
Fiber	386	7.6	2.6	0.41	-1.2×10^{-6}	7×10^{-6}
Matrix	5.5	5.5	1.96	0.40	2.4×10^{-5}	2.4×10^{-5}

Table 3.8: Thermoelastic material properties of T-50/Epoxy system

The resulting effective thermal expansion coefficients for the selected periodic unit cells together with the results obtained with the Mori-Tanaka method [17, 172] and hexagonal arrangement of fibers are stored in Table 3.9. It turns out that the periodic unit cell derived from the optimization procedure is again able to reflect the slight geometrical anisotropy possessed by the current material.

Unit cell	$\mathsf{m}^{\mathsf{fem}}{}_1$	$\mathsf{m}^{\mathsf{fem}}{}_2$	$\mathsf{m}^{\mathsf{fem}}{}_4$	c_f
Original	2.269×10^{-5}	2.248×10^{-5}	-7.463×10^{-7}	0.436
2 fibers PUC	2.273×10^{-5}	2.244×10^{-5}	-7.463×10^{-7}	0.436
5 fibers PUC	2.269×10^{-5}	2.248×10^{-5}	-7.462×10^{-7}	0.436
10 fibers PUC	2.269×10^{-5}	2.249×10^{-5}	-7.462×10^{-7}	0.436
Hexagonal array	2.259×10^{-5}	2.259×10^{-5}	-7.462×10^{-7}	0.436
Mori-Tanaka	2.250×10^{-5}	2.250×10^{-5}	-7.464×10^{-7}	0.436

Table 3.9: Components of the effective thermal expansion coefficients [K^{-1}]

Relation	$\mathsf{m}^{\mathsf{fem}}{}_1$	$\mathsf{m}^{\mathsf{fem}}{}_2$	$\mathsf{m}^{\mathsf{fem}}{}_4$
Equation (3.38)	2.269×10^{-5}	2.249×10^{-5}	-7.462×10^{-7}
Equation (3.47)	2.269×10^{-5}	2.249×10^{-5}	-7.462×10^{-7}
Equation (3.48)	2.269×10^{-5}	2.249×10^{-5}	-7.462×10^{-7}

Table 3.10: Comparison of relations (3.38), (3.48) and (3.47) for 5-fiber PUC [K^{-1}]

Next, Table 3.10 shows that the values of effective coefficients of thermal expansion obtained using relations (3.38), (3.47_2) and (3.48) are identical.

Finally, the distribution of the local stresses resulting from loading the hexagonal periodic unit cell by the overall strain E_{12} and uniform temperature change $\Delta\theta = 1$ K is presented in Figure 3.11.

3.4 Linear viscoelastic response

Majority of material systems currently at the forefront of engineering interest experience the time dependent behavior at sustained loading. Examples include polymer matrix composite systems also examined in the present work. Constitutive relations that describe the time dependent deformation of such systems usually assume linearly elastic response of fibers while a linear viscoelastic model is appropriate for polymer matrices in most practical applications. Inventory of contributions to viscoelastic analysis of composites includes [32, 79, 88, 141, 144, 181, 224, 241, 249, 272, 293, to cite a few]. This section revisits the subject in conjunction with the present modeling framework. Again, the generalized plane strain, see Section A.2.1, is assumed in this section.

3.4.1 Macroscopic constitutive law

Following the procedure discussed in Section A.3, the constitutive equations for a viscoelastic matrix phase can be cast in the incremental form analogous to the Section 3.3,

$$\{\Delta\sigma_{\mathsf{m}}(t_i)\} = \left[\mathsf{L}_{\mathsf{m}}(\widehat{E}(t_i),\nu)\right]\{\Delta\varepsilon_{\mathsf{m}}(t_i)\} + \{\Delta\lambda_{\mathsf{m}}(t_i)\}, \tag{3.49}$$

where the instantaneous material stiffness matrix $[\mathsf{L}(t_i)]$ is defined in terms of time-dependent Young's modulus $\widehat{E}(t_i)$, see Eq. (A.38) and time-independent Poisson's ratio ν; the matrix eigenstress increment $\{\Delta\lambda_{\mathsf{m}}(t_i)\}$ is provided by Eqs. (A.42)–(A.43). As the fiber is assumed to remain linearly elastic during the loading history,

$$\{\Delta\sigma_{\mathsf{f}}\} = [\mathsf{L}_{\mathsf{f}}(k,l,m,n)]\{\Delta\varepsilon_{\mathsf{f}}\}, \tag{3.50}$$

where the time-independent material stiffness matrix of the transversally isotropic fiber is provided by Eq. (A.29).

The above description of the material properties on the microscale is sufficient to determine the local stress and strain fields by increments of the overall strain, $\{\mathsf{E}\}$, or stress $\{\Sigma\}$. Indeed, consider an incremental form of Eq. (3.37)

$$\left\langle\{\delta\varepsilon\}^{\mathsf{T}}\{\Delta\sigma\}\right\rangle = \{\delta\mathsf{E}\}^{\mathsf{T}}\{\Delta\Sigma\}. \tag{3.51}$$

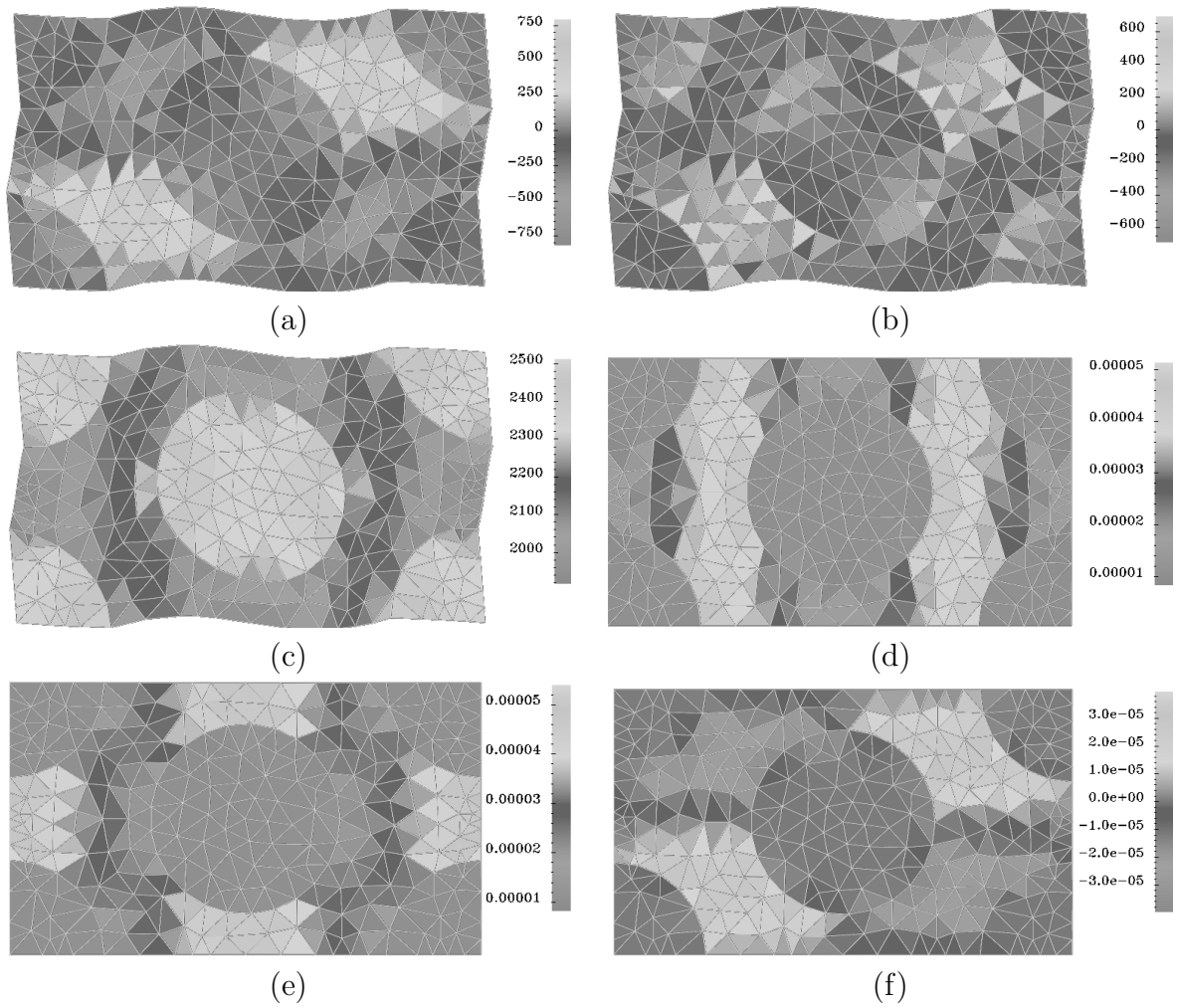

Figure 3.11: Distribution of local stresses $\boldsymbol{\sigma}$ within the periodic unit cell Y, (a) stress σ_{11} due to E_{12}, (b) stress σ_{12} due to E_{12}, (c) stress σ_{22} due to E_{12}, (d) strain ε_{11} due to $\Delta\theta = 1$, (e) strain ε_{22} due to $\Delta\theta = 1$, (f) strain ε_{12} due to $\Delta\theta = 1$

Substituting the local strain increment $\{\Delta\varepsilon\} = \{\Delta\mathsf{E}\} + \{\Delta\varepsilon^*\}$ together with local phase constitutive equations (3.49) and (3.50) into Eq. (3.51) provides the desired incremental form of Eq. (3.38) as

$$\begin{bmatrix} \mathsf{K}_{11}(t_i) & \mathsf{K}_{12}(t_i) \\ \mathsf{K}_{21}(t_i) & \mathsf{K}_{22}(t_i) \end{bmatrix} \begin{Bmatrix} \Delta\mathsf{E}(t_i) \\ \Delta\mathsf{r}(t_i) \end{Bmatrix} = \begin{Bmatrix} \Delta\Sigma(t_i) + \Delta\mathsf{f}_1(t_i) \\ \Delta\mathsf{f}_2(t_i) \end{Bmatrix}. \tag{3.52}$$

Finally, after eliminating the fluctuating displacements vector $\{\Delta\mathsf{r}(t_i)\}$, we arrive at the incremental form of the macroscopic constitutive law, compare with Eq. (3.33),

$$\{\Delta\Sigma(t_i)\} = \left[\mathsf{L}^{\mathsf{fem}}(t_i)\right] \{\Delta\mathsf{E}(t_i)\} + \{\Delta\Lambda^{\mathsf{fem}}(t_i)\}, \tag{3.53}$$

where

$$\left[\mathsf{L}^{\mathsf{fem}}(t_i)\right] = [\mathsf{K}_{11}(t_i)] - [\mathsf{K}_{12}(t_i)]\,[\mathsf{K}_{22}(t_i)]^{-1}\,[\mathsf{K}_{12}(t_i)]^{\mathsf{T}} \tag{3.54}$$

$$\{\Delta\Lambda^{\mathsf{fem}}(t_i)\} = -\{\Delta\mathsf{f}_1(t_i)\} + [\mathsf{K}_{12}(t_i)]\,[\mathsf{K}_{22}(t_i)]^{-1}\,\{\Delta\mathsf{f}_2(t_i)\}, \tag{3.55}$$

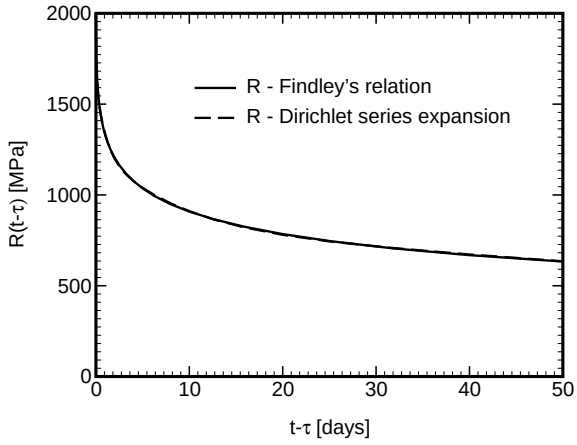

Figure 3.12: Relaxation function

Also note that, when prescribing the overall strain only, the system of equations (3.52) reduces to

$$[\mathsf{K}_{22}(t_i)]\,\{\Delta\mathsf{r}(t_i)\} = -\,[\mathsf{K}_{21}(t_i)]\,\{\Delta\mathsf{E}(t_i)\} + \{\Delta\mathsf{f}_2(t_i)\}. \tag{3.56}$$

3.4.2 Numerical results

As an example, consider an artificial composite system listed in Table 3.11 with the matrix properties taken from [62].

Phase	E_A [GPa]	E_T [GPa]	G_T [GPa]	ν_A	a $[\text{GPa}]^{-1}$	b $[\text{GPa}]^{-1}$	n
Fiber	386	7.6	2.6	0.41	×	×	×
Matrix	×	×	×	0.40	0.474	0.0214	0.3526

Table 3.11: Linear viscoelastic material properties of T-50/Epoxy system

The time dependent material properties of the epoxy matrix were derived experimentally from a set of well cured specimens, so that the material aging was neglected [62]. The resulting experimental data were approximated by Findley's law

$$J(t,\tau) = a + b(t-\tau)^n, \qquad R(t,\tau) = \frac{1}{a + b(t-\tau)^n}, \tag{3.57}$$

with constants of the model a, b and n given in Table 3.11 for the time given in minutes. The corresponding relaxation function $R(t-\tau)$ appears in Fig. 3.12. Seven elements of the Dirichlet series expansion Eq. (A.33) uniformly distributed in $\log(t-\tau)$ over the period of approximately 100 days were assumed. The fit of the relaxation function Eq. (3.57_2) by Eq. ($A.34_2$) is plotted in Fig. 3.12.

As before, the Cartesian coordinate system with the x_3-axis directed along the fiber direction in the generalized plane strain state is assumed. In the present study, the numerical results are presented for loading applied within the transverse plane section of

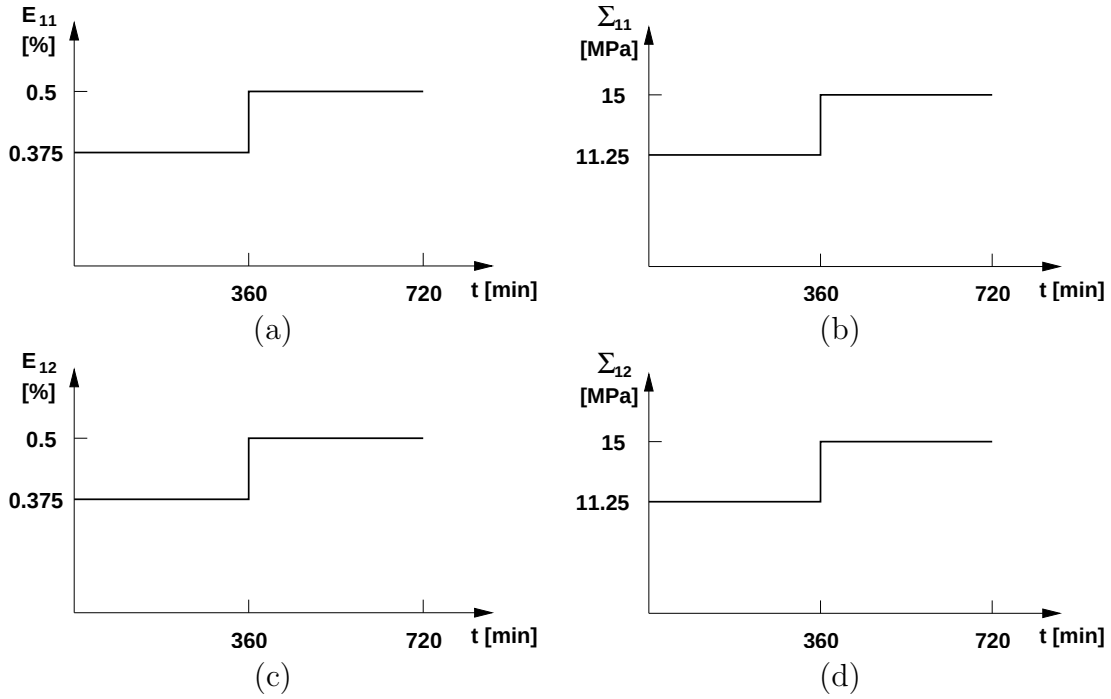

Figure 3.13: Imposed loading: (a), (b) creep test, (c), (d) relaxation test

the composite aggregate only. Both the strain and stress control loading conditions are considered in simulations. Fig. 3.13 illustrates the time variation of the applied load.

The first set of figures (Figs. 3.14-3.17) represents the composite response derived from the unit cell model. The macroscopic creep behavior is considered first. Fig. 3.14 shows the time variation of the overall strain developed under pure tensile and shear stress loading conditions, respectively (Fig. 3.13a,b). Similar response resulting from the strain loading conditions is plotted in Fig. 3.15. Individual results suggest that at least 5-fibers PUC should be used in numerical simulations to provide sufficiently accurate response of the actual composite, Fig. 2.1. Note that the same characteristic of the present material system was discovered when studying a pure elastic behavior of such composites, see Section 3.2.5. However, unlike the results derived assuming pure elasticity, the viscoelastic response of the hexagonal array model slightly deviates from that found using the statistically equivalent unit cells. Nevertheless, a very low contrast in material parameters in the transverse direction promotes the hexagonal array model as a reasonable substitute for more complicated unit cells when the fiber volume fraction is sufficiently large.

Quite different conclusion, however, can be drawn from Fig. 3.16. The macroscopic response plotted in Fig. 3.16 provides evidence that increasing the material contrast leads to a noticeable difference in the material response derived from the hexagonal array model and statistically optimal unit cells. To arrive at such a result we simply replaced the actual transversally isotropic fiber with the isotropic one ($E = E_A$ and $\nu = \nu_A$) to attain a higher contrast between the material properties of the fiber and matrix phases. Also note a possible change in the smallest RVE to be considered for numerical simulations (10-fibers UC). Additional support for using the optimal unit cells instead of the hexagonal

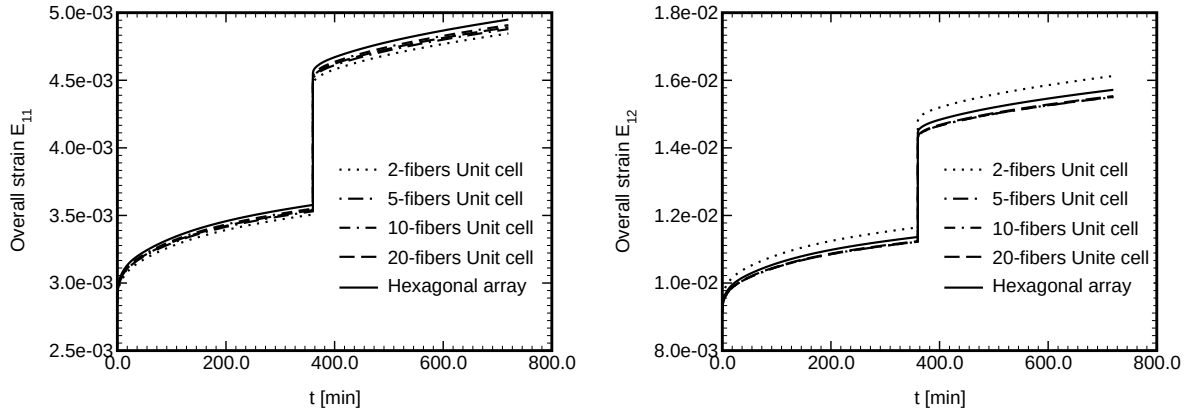

(a) (b)

Figure 3.14: Overall response – Unit cell models: creep test

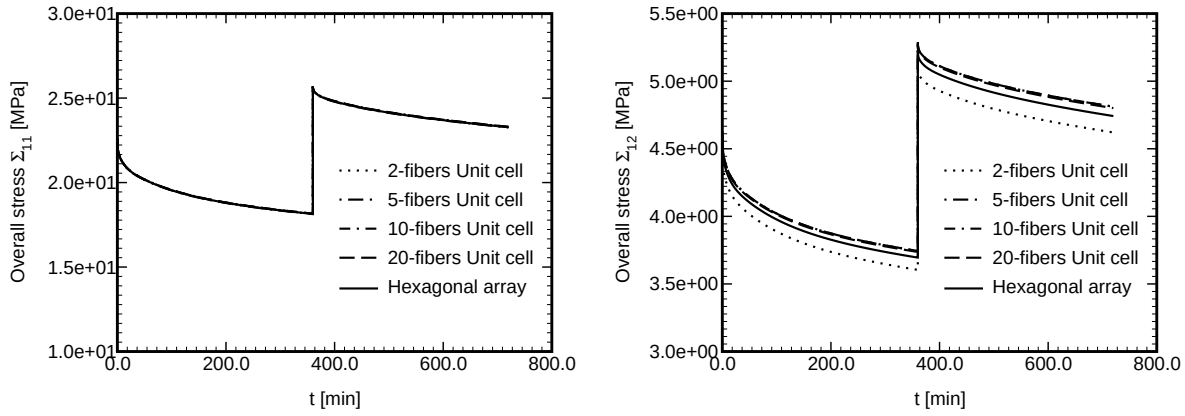

(a) (b)

Figure 3.15: Overall response – Unit cell models: relaxation test

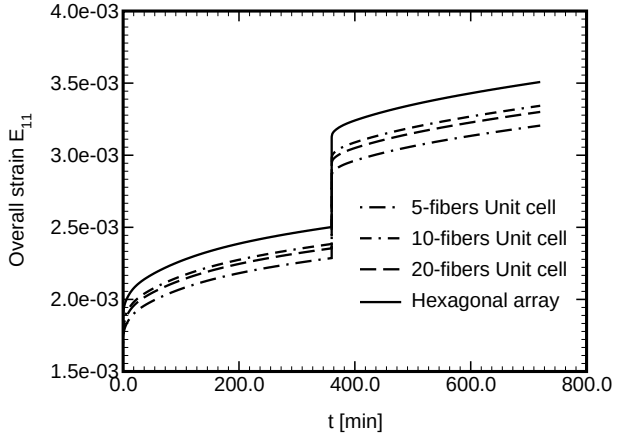

Figure 3.16: Overall response – Unit cell models: creep test assuming isotropic fiber

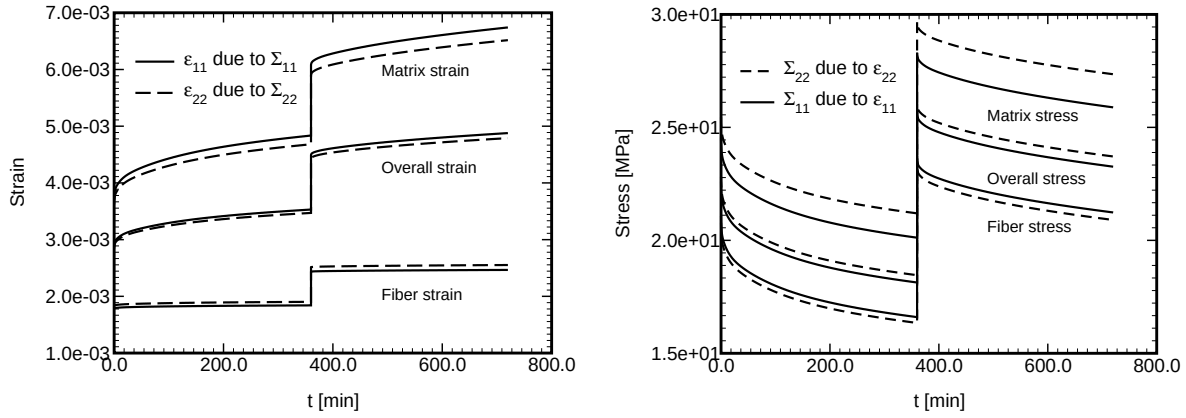

(a) (b)

Figure 3.17: Overall and local response – Unit cell models: (a) creep test, (b) relaxation test

array model is provided by Fig. 3.17 suggesting an anisotropic character of the present medium. Such a result cannot be attained by simple periodic unit cells. The present approach, which draws on the existence of a unit cell statistically equivalent to the actual composite system, is therefore preferable.

3.5 Nonlinear viscoelastic response

The aim of this section is to extend the modeling framework introduced for linearly viscoelastic materials to non-linearly viscoelastic response of the matrix phase. The generalized compressible multi-mode Leonov model, discussed in detail in Section A.4, is considered as a representative of constitutive laws suitable for the description of the time-dependent behavior exhibited by such materials systems. The incremental formulation of the present material model, Eq. (A.53), allows us to apply the theory developed in the previous section to the selected constitutive law in a rather straightforward way[17]. Recall that the generalized plane strain, Section A.2.1, is again assumed in this section.

3.5.1 Macroscopic constitutive law

To include the effects of the matrix phase nonlinearity into the problem formulation, the incremental form of the stress-strain relation is, in analogy with Section 3.4, formulated in terms of the time dependent material stiffness matrix $[\mathsf{L}_\mathsf{m}(t_i)]$ and the matrix phase eigenstress increment $\{\Delta\lambda_\mathsf{m}(t_i)\}$,

$$\{\Delta\sigma_\mathsf{m}(t_i)\} = \left[\mathsf{L}_\mathsf{m}(\widehat{G}(t_i), K)\right] \{\Delta\varepsilon_\mathsf{m}(t_i)\} + \{\Delta\lambda_\mathsf{m}(t_i)\}, \tag{3.58}$$

where the matrix $[\mathsf{L}(t_i)]$ is defined in terms of the time-independent bulk modulus K and the time-dependent shear modulus $\widehat{G}(t_i)$, Eq. (A.54); the matrix eigenstress increment $\{\Delta\lambda_\mathsf{m}(t_i)\}$ follows from Eqs. (A.55)–(A.58). Assumptions of the linearly elastic

[17] An interested reader may inspect [270, 254, 259, and references therein] for more detailed discussion of the presented material model and [15, 54, 231] for further alternative approaches and related topics to the subject of this section.

behavior and transverse isotropy of the fiber phase makes possible to write the fiber incremental stress-strain relationship in the familiar form

$$\{\Delta\sigma_{\mathsf{f}}\} = [\mathsf{L}_{\mathsf{f}}(k,l,m,n)]\,\{\Delta\varepsilon_{\mathsf{f}}\}, \tag{3.59}$$

where the fiber stiffness matrix $[\mathsf{L}_{\mathsf{f}}]$ is again defined in terms of the time-independent Hill's moduli k, l, m and n. Finally, the incremental form of the Hill lemma,

$$\big\langle \{\delta\varepsilon\}^{\mathsf{T}}\{\Delta\sigma(t_i)\}\big\rangle = \{\delta\mathsf{E}\}^{\mathsf{T}}\{\Delta\Sigma(t_i)\}, \tag{3.60}$$

yields the homogenized constitutive equations

$$\{\Delta\Sigma(t_i)\} = \big[\mathsf{L}^{\mathsf{fem}}(t_i)\big]\,\{\Delta\mathsf{E}(t_i)\} + \{\Delta\Lambda^{\mathsf{fem}}(t_i)\}, \tag{3.61}$$

with the instantaneous effective stiffness matrix $\big[\mathsf{L}^{\mathsf{fem}}(t_i)\big]$ defined by Eq. (3.54) and the increment of the overall eigenstress $\{\Lambda^{\mathsf{fem}}\}$ provided by Eq. (3.55).

3.5.2 Numerical results

The material system consisting of graphite fibers embedded in the PR100/2+EM100E epoxy resin was selected for the purpose of the present numerical study. The parameters of the Leonov model were determined by a set of creep experiments reported in [259] and by a subsequent transformation of creep kernel [261]. The generalized Maxwell model consisting of ten elements was used to approximate the time-dependent behavior of the matrix phase, see Section A.4. Resulting material data appear in Table 3.12. The elastic properties of the fiber phase were again selected the same as those listed in Table 3.4.

Parameter		***Value***
	A [s]	4.854×10^{14}
	τ_0 [MPa]	1.57
	K [MPa]	5030
μ	η_μ [MPa·s]	G_μ [MPa]
1	1.4664×10^{1}	1.1479×10^{0}
2	1.0194×10^{3}	1.0293×10^{1}
3	2.4024×10^{4}	2.4589×10^{1}
4	2.7624×10^{5}	2.8396×10^{1}
5	2.9746×10^{6}	3.0671×10^{1}
6	4.6200×10^{7}	4.2446×10^{1}
7	4.7063×10^{8}	4.9675×10^{1}
8	5.7611×10^{9}	6.1870×10^{1}
9	8.9183×10^{10}	1.0178×10^{2}
10	7.2765×10^{13}	7.2765×10^{2}

Table 3.12: Nonlinear viscoelastic material properties of PR100/2+EM100E epoxy resin

Only the strain control is imposed in the present study as the results of Section 3.4.2 demonstrate that the selection of the minimal PUC does not depend on a particular form

of invoked loading conditions. Each unit cell is subjected to overall strain with a constant rate through the whole loading process; in particular, strain rates 10^{-3} s^{-1}, 10^{-4} s^{-1} and 10^{-5} s^{-1} are considered.

First, the sensitivity of the overall response with respect to a selected time step Δt is addressed. To that end, the hexagonal unit cell was subjected to the overall shear strain loading $\dot{E}_{12} = 10^{-4}$ s^{-1} and the overall stress response was computed for time steps $10, 1$ and 0.1 s, respectively. Results, appearing in Fig. 3.18, indicate that the overall response is not very sensitive with respect to the selected time step (setting $\Delta t = 1$ s gives sufficiently precise results) and that no spurious oscillations [15, 260] appear for the selected time steps and integration scheme.

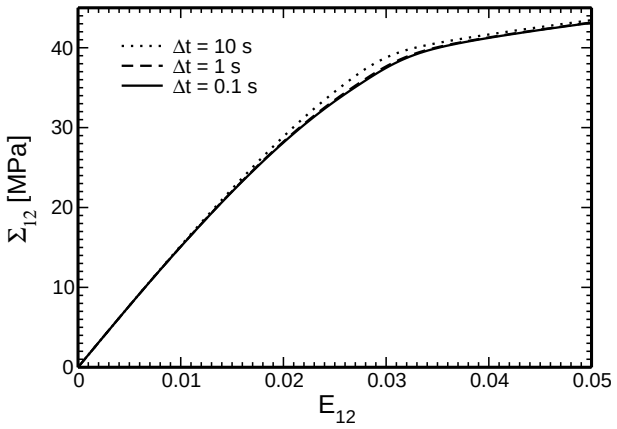

Figure 3.18: Hexagonal array: Sensitivity with respect to time step

The following set of figures, Figs. 3.19a–d, shows the response of individual periodic unit cells for loaded by constant strain rates $\dot{E}_{11}$ and $\dot{E}_{12}$. In all cases, the integration step Δt was considered 1 s. Note that only the $\dot{E}_{11} = 10^{-4}$ s^{-1} loading case was considered since the overall stress response Σ_{11} is practically independent of a chosen loading rate[18]. The displayed results show that the overall shear response is considerably more sensitive to the microstructure configuration than in the case of the linear viscoelasticity. Evidently, all PUCs, thanks to almost identical elastic properties, behave very similarly during the initial stage of the loading. In a later stage of the loading process, however, the details of local fields distribution come into effect and cause a noticeable shift of individual responses. Nevertheless, the obtained results allow us to conclude that the 10 fiber PUC is sufficient for the simulation of the overall composite response.

[18] This fact actually follows from the separation of the volumetric and deviatoric response in the Leonov model, see Eq. (A.52). Indeed, due to small values of shear stresses resulting from the volumetric loading, demonstrated in Fig. 3.11f, the instantaneous shear modulus $\widehat{G}(t_i)$ remains practically constant during the deformation process and thus the composite effectively behaves as a linear elastic solid. See also Fig. 4.9 for demonstration of this fact for the HS-based modeling.

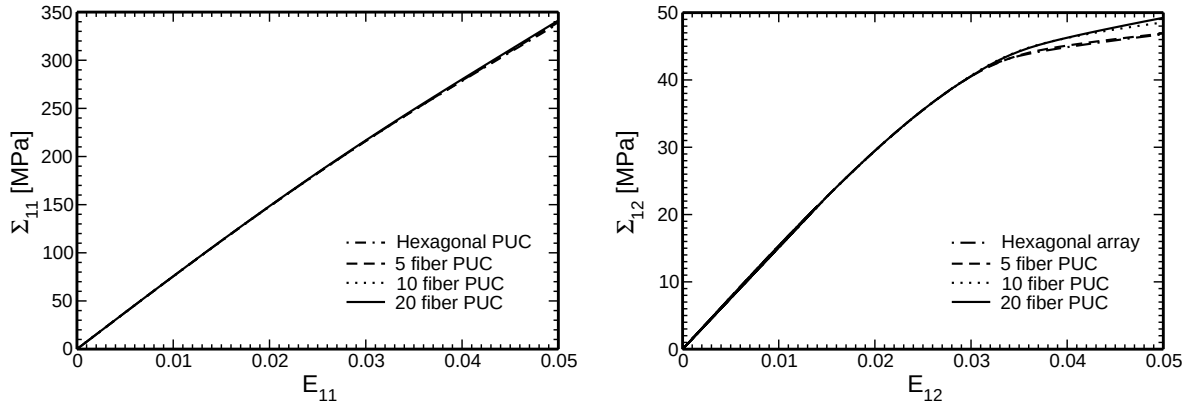

(a) (b)

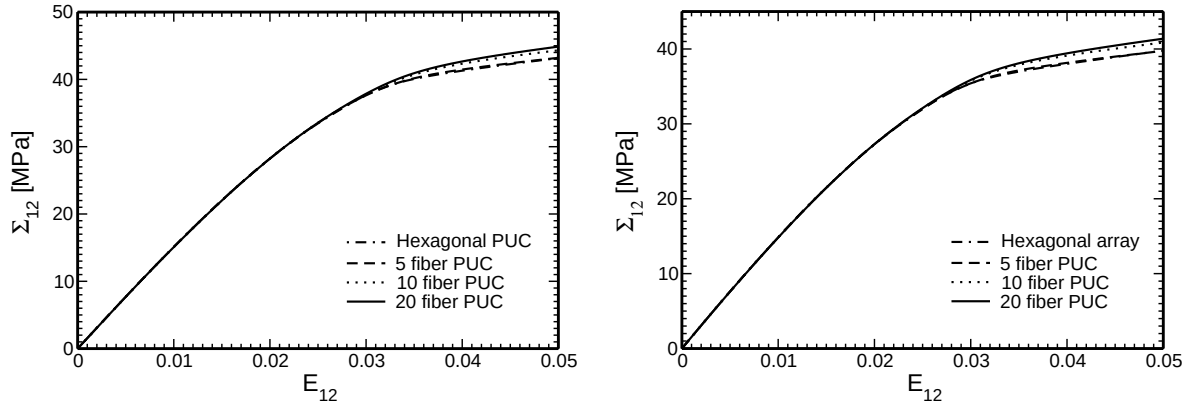

(c) (d)

Figure 3.19: Overall response – Unit cell models: (a) $\dot{E}_{11} = 10^{-4}$ s^{-1}, (b) $\dot{E}_{12} = 10^{-3}$ s^{-1}, (c) $\dot{E}_{12} = 10^{-4}$ s^{-1}, (d) $\dot{E}_{12} = 10^{-5}$ s^{-1}

Chapter 4

MICROSCALE MODELING VIA EXTENDED HASHIN-SHTRIKMAN VARIATIONAL PRINCIPLES

Basic energy principles were reviewed in the preceding chapter to derive effective thermoelastic material properties of a random composite assuming periodic distribution of the microstructure. Another approach is available when analyzing material elements having a length scale sufficiently large compared to the microstructural length scale so it can be treated as statistically representative of the composite. Such a traditional definition of a representative volume element (RVE) is adopted in the present chapter when deriving the generalized macroscopic constitutive equations of composite systems with statistically homogeneous distribution of phases.

To be consistent with the problems discussed in the previous section we select again the graphite fiber tow embedded in the polymer matrix as a representative of the two-phase disordered composite media. Random character of fibers arrangement, typical for such material systems, is conveniently described by the two-point probability function. When used with the Hashin-Shtrikman variational principles this function provides sufficient information for obtaining bounds on the thermo-elastic material properties of real composites with statistically homogeneous microstructure.

In particular, Hashin and Shtrikman [89] presented two alternative representations of energy functions by incorporating polarization fields relative to a homogeneous reference (comparison) medium. In this chapter, we focus on theoretical aspects associated with the variational formulation for anisotropic and non-homogeneous bodies with either prescribed displacements $\mathbf{u} = \overline{\mathbf{u}}$ or tractions $\mathbf{p} = \overline{\mathbf{p}}$ along the entire boundary ∂V of the composite. In addition, eigenstrains (stress free strains) or eigenstresses are admitted in the present formulation.

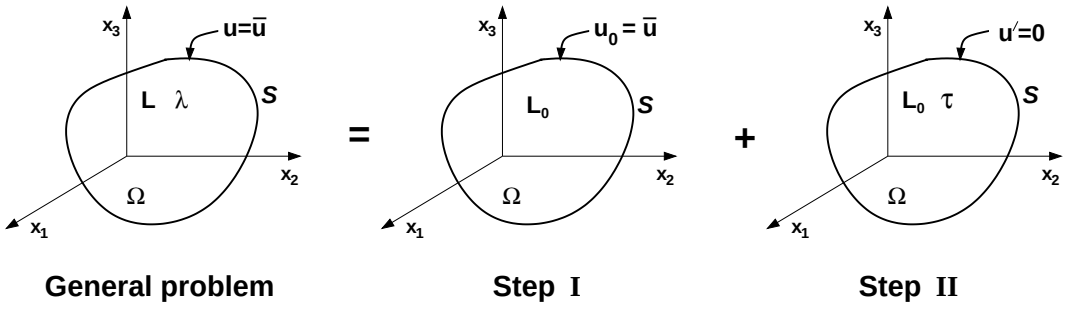

Figure 4.1: Body with prescribed surface displacements including eigenstresses

4.1 Body with prescribed surface displacements and eigenstresses

With reference to the general problem displayed in Fig. 4.1 we consider an anisotropic and heterogeneous body loaded by an affine displacement field $\mathbf{u}_0(\mathbf{x}) = \boldsymbol{E} \cdot \mathbf{x}$. The local constitutive law including eigenstresses $\boldsymbol{\lambda}$ then reads

$$\boldsymbol{\sigma}(\mathbf{x}) = \mathbf{L}(\mathbf{x}) : \boldsymbol{\varepsilon}(\mathbf{x}) + \boldsymbol{\lambda}(\mathbf{x}) \qquad \text{in } V, \tag{4.1}$$

$$\mathbf{u} = \overline{\mathbf{u}} \qquad \text{on } \partial V. \tag{4.2}$$

As suggested by Hashin-Shtrikman [89], the local stress and strain fields in Eq. (4.1) can be found from two auxiliary boundary value problems, Fig. 4.1. The procedure starts from assuming a geometrically identical body with a certain reference homogeneous, but generally anisotropic, medium with stiffness tensor $\mathbf{L}_0$ and the same prescribed displacements. The corresponding uniform strain $\boldsymbol{E}$ and stress $\boldsymbol{\Sigma}$ fields are related through constitutive law in the form

$$\boldsymbol{\Sigma} = \mathbf{L}_0 : \boldsymbol{E} \qquad \text{in } V, \tag{4.3}$$

$$\mathbf{u}_0 = \overline{\mathbf{u}} \qquad \text{on } \partial V. \tag{4.4}$$

Following the idea of Hashin and Shtrikman [89], we introduce the symmetric stress polarization tensor $\boldsymbol{\tau}$ such that

$$\boldsymbol{\sigma}(\mathbf{x}) = \mathbf{L}_0 : \boldsymbol{\varepsilon}(\mathbf{x}) + \boldsymbol{\tau}(\mathbf{x}). \tag{4.5}$$

In addition, denote

$$\mathbf{u}'(\mathbf{x}) = \mathbf{u}(\mathbf{x}) - \mathbf{u}_0 \qquad \text{in } V, \tag{4.6}$$

$$\mathbf{u}'(\mathbf{x}) = \mathbf{0} \qquad \text{on } \partial V, \tag{4.7}$$

and

$$\boldsymbol{\varepsilon}'(\mathbf{x}) = \boldsymbol{\varepsilon}(\mathbf{x}) - \boldsymbol{E} \qquad \text{in } V, \tag{4.8}$$

$$\boldsymbol{\sigma}'(\mathbf{x}) = \boldsymbol{\sigma}(\mathbf{x}) - \boldsymbol{\Sigma} \qquad \text{in } V. \tag{4.9}$$

The objective is to formulate a variational principle describing the behavior of the non-homogeneous and anisotropic material subjected to known eigenstresses and prescribed boundary displacements. Schematic representation of this problem is displayed in Fig. 4.1. Provided that both $\boldsymbol{\sigma}$ and $\boldsymbol{\Sigma}$ fields are statically admissible, the following equations have to be satisfied (see, e.g., [21, 97, 75, 131])

$$\operatorname{div}(\mathbf{L}_0 : \boldsymbol{\varepsilon}(\mathbf{x}) + \boldsymbol{\tau}(\mathbf{x})) = \mathbf{0} \qquad \text{in } V, \tag{4.10}$$

$$\boldsymbol{\tau}(\mathbf{x}) - (\mathbf{L}(\mathbf{x}) - \mathbf{L}_0) : \boldsymbol{\varepsilon}(\mathbf{x}) - \boldsymbol{\lambda}(\mathbf{x}) = \mathbf{0} \qquad \text{in } V, \tag{4.11}$$

$$\mathbf{u}' = \mathbf{0} \qquad \text{on } \partial V. \tag{4.12}$$

4.1.1 Variational principle

A formulation equivalent to Eqs. (4.10) and (4.11) may be obtained by performing a variation of the extended two-field functional

$$\begin{aligned} U(\boldsymbol{\tau}, \boldsymbol{\varepsilon}') \;=\; & \frac{1}{2} \int_V \big(\boldsymbol{E} : \boldsymbol{\Sigma} - (\boldsymbol{\tau}(\mathbf{x}) - \boldsymbol{\lambda}(\mathbf{x})) : (\mathbf{L}(\mathbf{x}) - \mathbf{L}_0)^{-1} : (\boldsymbol{\tau}(\mathbf{x}) - \boldsymbol{\lambda}(\mathbf{x})) \\ & + \; 2\boldsymbol{\tau}(\mathbf{x}) : \boldsymbol{E} + \boldsymbol{\varepsilon}'(\mathbf{x}) : \boldsymbol{\tau}(\mathbf{x}) + \boldsymbol{\lambda}(\mathbf{x}) : \mathbf{L}^{-1}(\mathbf{x}) : \boldsymbol{\lambda}(\mathbf{x}) \big) \, \mathrm{d}\mathbf{x}. \end{aligned} \tag{4.13}$$

Setting the first variation of the functional equal to zero, i.e.,

$$\begin{aligned}\delta U(\boldsymbol{\tau},\boldsymbol{\varepsilon}') &= -\frac{1}{2}\int_V \{2\delta\boldsymbol{\tau}(\mathbf{x}) : [(\mathbf{L}(\mathbf{x})-\mathbf{L}_0)^{-1} : (\boldsymbol{\tau}(\mathbf{x})-\boldsymbol{\lambda}(\mathbf{x})) - \boldsymbol{\varepsilon}(\mathbf{x})] \\ &+ \delta\boldsymbol{\tau}(\mathbf{x}) : \boldsymbol{\varepsilon}'(\mathbf{x}) - \delta\boldsymbol{\varepsilon}'(\mathbf{x}) : \boldsymbol{\tau}(\mathbf{x})\}\,\mathrm{d}\mathbf{x} = 0\end{aligned} \tag{4.14}$$

we find that Eq. (4.11) is one of the stationarity conditions for $U(\boldsymbol{\tau},\boldsymbol{\varepsilon}')$, while the second condition, Eq. (4.10), follows after recasting the remaining terms in the brackets. Finally, it can be proven that the stationary value $U(\boldsymbol{\tau}^*,\boldsymbol{\varepsilon}'^*)$ of the functional equals to the actual potential energy stored in the anisotropic heterogeneous body

$$U(\boldsymbol{\tau}^*,\boldsymbol{\varepsilon}'^*) = \frac{1}{2}\int_V (\boldsymbol{\varepsilon}(\mathbf{x})-\boldsymbol{\mu}(\mathbf{x})) : \mathbf{L}(\mathbf{x}) : (\boldsymbol{\varepsilon}(\mathbf{x})-\boldsymbol{\mu}(\mathbf{x}))\,\mathrm{d}\mathbf{x}, \tag{4.15}$$

where $\boldsymbol{\mu} = -\mathbf{L}^{-1} : \boldsymbol{\lambda}$ is the vector of eigenstrains (stress-free strains). The function $U(\boldsymbol{\tau},\boldsymbol{\varepsilon}')$ attains its maximum if $(\mathbf{L}-\mathbf{L}_0)$ is positive definite and its minimum if $(\mathbf{L}-\mathbf{L}_0)$ is negative definite[1].

To make use of H-S functional, Eq. (4.13), or its variation, Eq. (4.14), one has to express $\boldsymbol{\varepsilon}'$ via the polarization tensor $\boldsymbol{\tau}$ and non-local fourth-order operator $\boldsymbol{\epsilon}_0^*(\cdot)$[2]

$$\boldsymbol{\varepsilon}'(\mathbf{x}) = \boldsymbol{\varepsilon}(\mathbf{x}) - \boldsymbol{E} = \int_V \boldsymbol{\epsilon}_0^*(\mathbf{x}-\mathbf{x}') :\ (\boldsymbol{\tau}(\mathbf{x}') - \langle\boldsymbol{\tau}\rangle)\ \mathrm{d}\mathbf{x}', \tag{4.16}$$

Introducing Eq. (4.16) into Eq. (4.13) gives

$$\begin{aligned}U(\boldsymbol{\tau}) &= \frac{1}{2}\int_V \big(\boldsymbol{E} : \boldsymbol{\Sigma} - (\boldsymbol{\tau}(\mathbf{x})-\boldsymbol{\lambda}(\mathbf{x})) : (\mathbf{L}(\mathbf{x})-\mathbf{L}_0)^{-1} : (\boldsymbol{\tau}(\mathbf{x})-\boldsymbol{\lambda}(\mathbf{x})) + 2\boldsymbol{\tau}(\mathbf{x}) : \boldsymbol{E} \\ &+ \boldsymbol{\tau}(\mathbf{x}) :\ \int_V \boldsymbol{\epsilon}_0^*(\mathbf{x}-\mathbf{x}') :\ (\boldsymbol{\tau}(\mathbf{x}') - \langle\boldsymbol{\tau}\rangle)\ \mathrm{d}\mathbf{x}' + \boldsymbol{\lambda}(\mathbf{x}) : \mathbf{L}^{-1}(\mathbf{x}) : \boldsymbol{\lambda}(\mathbf{x})\Big)\ \mathrm{d}\mathbf{x}.\end{aligned} \tag{4.17}$$

4.1.2 Extension to random composites

If each phase of a randomly arranged composite is homogeneous with moduli $\mathbf{L}_r, r = 1,\ldots,n$, the material stiffness matrix in the sample α can be expressed as [18, 49, 133, 285],

$$\mathbf{L}(\mathbf{x},\alpha) = \sum_{r=1}^{n} \chi_r(\mathbf{x},\alpha)\mathbf{L}_r. \tag{4.18}$$

With the help of Eq. (2.11), the ensemble average of $\mathbf{L}$ is

$$\overline{\mathbf{L}(\mathbf{x})} = \sum_{r=1}^{n} S_r(\mathbf{x})\mathbf{L}_r. \tag{4.19}$$

[1] Recall that we say that a fourth order tensor $\mathbf{L}$ is positive definite if $\boldsymbol{\varepsilon} : \mathbf{L} : \boldsymbol{\varepsilon} > 0$ for all symmetric second-order tensors $\boldsymbol{\varepsilon}$. The proof of extremality can be found in Hashin and Shtrikman's original work [89] for $\boldsymbol{\lambda} = \mathbf{0}$ and in [204] for general case.

[2] See Appendix A and reference herein for additional information regarding this matter. The subscript "0" is used to identify this operator with the homogeneous reference medium. Note that the operator $-\boldsymbol{\epsilon}_0^*$ is often denoted as $\boldsymbol{\Gamma}$ in the literature (see, e.g., [49, 133, 134, 285, 286]).

Similarly, the trial fields for $\boldsymbol{\tau}$ and eigenstress $\boldsymbol{\lambda}$ at any point $\mathbf{x}$ located in the sample α together with their respective ensemble averages are written as

$$\boldsymbol{\tau}(\mathbf{x},\alpha)=\sum_{r=1}^{n}\chi_r(\mathbf{x},\alpha)\boldsymbol{\tau}_r(\mathbf{x}),\qquad \overline{\boldsymbol{\tau}(\mathbf{x})}=\sum_{r=1}^{n}S_r(\mathbf{x})\boldsymbol{\tau}_r(\mathbf{x}), \tag{4.20}$$

$$\boldsymbol{\lambda}(\mathbf{x},\alpha)=\sum_{r=1}^{n}\chi_r(\mathbf{x},\alpha)\boldsymbol{\lambda}_r(\mathbf{x}),\qquad \overline{\boldsymbol{\lambda}(\mathbf{x})}=\sum_{r=1}^{n}S_r(\mathbf{x})\boldsymbol{\lambda}_r(\mathbf{x}). \tag{4.21}$$

The ensemble average of quadratic term $\boldsymbol{\tau}:\boldsymbol{\epsilon}_{\mathbf{0}}^{*}:\boldsymbol{\tau}$ depends on two-point probability functions, i.e.,

$$\overline{\boldsymbol{\tau}(\mathbf{x},\alpha):\boldsymbol{\epsilon}_{\mathbf{0}}^{*}(\mathbf{x}-\mathbf{x}'):\boldsymbol{\tau}(\mathbf{x}',\alpha)}=\sum_{r=1}^{n}\sum_{s=1}^{n}S_{rs}(\mathbf{x},\mathbf{x}')\boldsymbol{\tau}_r(\mathbf{x}):\boldsymbol{\epsilon}_{\mathbf{0}}^{*}(\mathbf{x}-\mathbf{x}'):\boldsymbol{\tau}_s(\mathbf{x}'). \tag{4.22}$$

To facilitate the solution of the present problem the material is assumed to be ergodic and statistically homogeneous. Therefore,

$$\overline{\mathbf{L}}=\sum_{r=1}^{n}c_r\mathbf{L}_r,\quad \overline{\boldsymbol{\tau}(\mathbf{x})}=\sum_{r=1}^{n}c_r\boldsymbol{\tau}_r(\mathbf{x}),\quad \overline{\boldsymbol{\lambda}(\mathbf{x})}=\sum_{r=1}^{n}c_r\boldsymbol{\lambda}_r(\mathbf{x}). \tag{4.23}$$

Substituting Eqs. (4.23) into Eq. (4.17) yields the extended averaged form of the Hashin-Shtrikman principle

$$\begin{aligned}\overline{U(\boldsymbol{\tau},\alpha)} &= \frac{1}{2}\int_V \boldsymbol{E}:\boldsymbol{\Sigma}\,\mathrm{d}\mathbf{x} \\ &- \frac{1}{2}\sum_r\int_V\left(c_r(\boldsymbol{\tau}_r(\mathbf{x})-\boldsymbol{\lambda}_r(\mathbf{x})):(\mathbf{L}_r-\mathbf{L}_0)^{-1}:(\boldsymbol{\tau}_r(\mathbf{x})-\boldsymbol{\lambda}_r(\mathbf{x}))-2c_r\boldsymbol{\tau}_r(\mathbf{x}):\boldsymbol{E}\right)\mathrm{d}\mathbf{x} \\ &- \frac{1}{2}\sum_r\sum_s\int_V\boldsymbol{\tau}_r(\mathbf{x}):\int_V\boldsymbol{\epsilon}_{\mathbf{0}}^{*}(\mathbf{x}-\mathbf{x}'):\left[S_{rs}(\mathbf{x}-\mathbf{x}')\boldsymbol{\tau}_s(\mathbf{x}')-2c_s\langle\boldsymbol{\tau}\rangle\right]\mathrm{d}\mathbf{x}'\,\mathrm{d}\mathbf{x}.\end{aligned} \tag{4.24}$$

4.1.3 Approximate solution

Following Hashin and Shtrikman [90] and assuming a piecewise uniform variation of the eigenstress vector $\boldsymbol{\lambda}$ and the polarization stress $\boldsymbol{\tau}$, i.e, $(\boldsymbol{\lambda}_r(\mathbf{x})=\boldsymbol{\lambda}_r,\boldsymbol{\tau}_r(\mathbf{x})=\boldsymbol{\tau}_r)$, setting $\langle\boldsymbol{\tau}\rangle=\sum_r c_r\boldsymbol{\tau}_r$ and then performing variation with respect to $\boldsymbol{\tau}_r$ yield the extended form of the stationarity condition. Employing engineering notation introduced in Appendix A, the stationarity conditions yield the following system of linear equations,

$$\sum_{s=1}^{n}\left(\delta_{rs}c_r([\mathsf{L_r}]-[\mathsf{L_0}])^{-1}-[\mathsf{A_{rs}}]\right)\{\tau_\mathsf{s}\}=c_r\{\mathsf{E}\}+c_r([\mathsf{L_r}]-[\mathsf{L_0}])^{-1}\{\lambda_\mathsf{r}\},r=1,\ldots,n, \tag{4.25}$$

where the microstructure-dependent matrices $[\mathsf{A_{rs}}]$ are independent of $\mathbf{x}$ and are given by

$$[\mathsf{A_{rs}}]=\int_V[\epsilon_0^{*}](\mathbf{x}-\mathbf{x}')\left(S_{rs}(\mathbf{x}-\mathbf{x}')-c_rc_s\right)\mathrm{d}\mathbf{x}'. \tag{4.26}$$

A symbolic inversion of the system (4.25) provides the solution for unknown components of the polarization stress $\{\tau_r\}$ in the form[3]

$$\{\tau_r\} = \sum_{s=1}^{n} c_s \left[\mathsf{T}_{rs}\right] \left(\{\mathsf{E}\} + (\left[\mathsf{L}_s\right] - \left[\mathsf{L}_0\right])^{-1}\{\lambda_s\}\right), \tag{4.27}$$

from which

$$\{\overline{\tau}\} = \sum_{r=1}^{n}\sum_{s=1}^{n} c_r c_s \left[\mathsf{T}_{rs}\right] \left(\{\mathsf{E}\} + (\left[\mathsf{L}_s\right] - \left[\mathsf{L}_0\right])^{-1}\{\lambda_s\}\right). \tag{4.28}$$

Hence, according to (4.1) and (4.5), the overall constitutive law can be written as

$$\{\Sigma\} = \left[\mathsf{L}^{\mathsf{HS}}\right]\{\mathsf{E}\} + \{\Lambda^{\mathsf{HS}}\}, \tag{4.29}$$

where

$$\left[\mathsf{L}^{\mathsf{HS}}\right] = \left[\mathsf{L}_0\right] + \sum_{r=1}^{n}\sum_{s=1}^{n} c_r c_s \left[\mathsf{T}_{rs}\right], \tag{4.30}$$

$$\{\Lambda^{\mathsf{HS}}\} = \sum_{r=1}^{n}\sum_{s=1}^{n} c_r c_s \left[\mathsf{T}_{rs}\right] (\left[\mathsf{L}_s\right] - \left[\mathsf{L}_0\right])^{-1}\{\lambda_s\}. \tag{4.31}$$

In general, solving Eq. (4.25) calls for an efficient method to tackle Eq. (4.26). A suitable method of attack for obtaining the matrices $[\mathsf{A}_{rs}]$ numerically for a binary representation of real microstructures is presented in the Appendix B. In addition, explicit forms of matrices $[\mathsf{T}_{rs}]$ for a two-phase medium are provided.

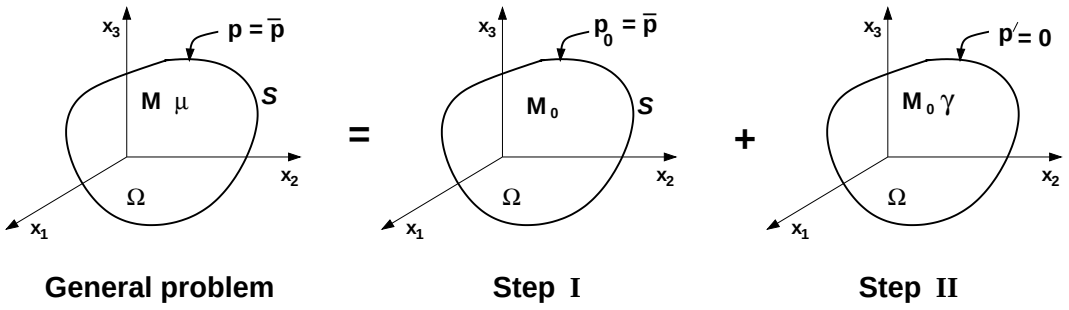

Figure 4.2: Body with prescribed surface tractions including eigenstrains

4.2 Body with prescribed surface tractions and eigenstrains

Recall that the primary variational principle of Hashin and Shtrikman, Eq. (4.13), modified to account for the presence of initial stresses, can be used to derive the effective stiffness matrix $\left[\mathsf{L}^{\mathsf{HS}}\right]$ and overall eigenstress $\{\Lambda^{\mathsf{HS}}\}$ of the composite medium. Similarly, employing its dual counterpart, one may arrive at the effective compliance matrix $\left[\mathsf{M}^{\mathsf{HS}}\right]$

[3] Note that matrices $[\mathsf{T}_{rs}]$ correspond to individual blocks of the inverse of the left-hand side matrix of the system (4.25).

and overall eigenstrain $\{\Upsilon^{\mathsf{HS}}\}$. In such a case the boundary value problem discussed in Section 4.1 is modified according to Fig. 4.2.

In particular, suppose that surface tractions $\overline{\mathbf{p}} = \boldsymbol{\Sigma} \cdot \mathbf{n}$ compatible with uniform stress $\boldsymbol{\Sigma}$ are applied along the boundary ∂V of a homogeneous comparison medium (Step I) characterized by the compliance tensor $\mathbf{M}_0$. The corresponding uniform strain $\boldsymbol{E}$ then follows from the constitutive law

$$\boldsymbol{E} = \mathbf{M}_0 : \boldsymbol{\Sigma} \qquad \text{in } V, \tag{4.32}$$

$$\mathbf{p}_0 = \overline{\mathbf{p}} \qquad \text{on } \partial V. \tag{4.33}$$

The local stress $\boldsymbol{\sigma}(\mathbf{x})$ at point $\mathbf{x}$ in V is found by superimposing the solution of the local problem displayed in Fig. 4.2 Step II. The respective governing equations are then given by

$$\boldsymbol{\varepsilon}(\mathbf{x}) = \mathbf{M}(\mathbf{x}) : \boldsymbol{\sigma}(\mathbf{x}) + \boldsymbol{\mu}(\mathbf{x}) \qquad \text{on } V, \tag{4.34}$$

$$\mathbf{p} = \overline{\mathbf{p}} \qquad \text{on } \partial V. \tag{4.35}$$

$$\boldsymbol{\varepsilon}(\mathbf{x}) = \mathbf{M}_0 : \boldsymbol{\sigma}(\mathbf{x}) + \boldsymbol{\gamma}(\mathbf{x}) \qquad \text{in } V, \tag{4.36}$$

$$0 = \varepsilon'_{ij,kl}(\mathbf{x}) + \varepsilon'_{kl,ij}(\mathbf{x}) - \varepsilon'_{ik,jl}(\mathbf{x}) - \varepsilon'_{jl,ik}(\mathbf{x}) \qquad \text{in } V, \tag{4.37}$$

$$\mathbf{0} = \boldsymbol{\gamma}(\mathbf{x}) - (\mathbf{M}(\mathbf{x}) - \mathbf{M}_0) : \boldsymbol{\sigma}(\mathbf{x}) - \boldsymbol{\mu}(\mathbf{x}) \qquad \text{in } V, \tag{4.38}$$

$$\mathbf{p}'(\mathbf{x}) = \mathbf{p}(\mathbf{x}) - \mathbf{p}_0 \qquad \text{in } V, \tag{4.39}$$

$$\mathbf{p}' = \mathbf{0} \qquad \text{on } \partial V, \tag{4.40}$$

where $\boldsymbol{\mu}(\mathbf{x})$ is the local eigenstrain and $\boldsymbol{\gamma}(\mathbf{x})$ is called the polarization strain.

4.2.1 Variational principle

The compatibility equation (4.37) together with Eq. (4.38) follows from the extended energy functional given by

$$\begin{aligned} V(\boldsymbol{\gamma}, \boldsymbol{\sigma}') &= \frac{1}{2} \int_V \big(\boldsymbol{\Sigma} : \boldsymbol{E} - (\boldsymbol{\gamma}(\mathbf{x}) - \boldsymbol{\mu}(\mathbf{x})) : (\mathbf{M}(\mathbf{x}) - \mathbf{M}_0)^{-1} : (\boldsymbol{\gamma}(\mathbf{x}) - \boldsymbol{\mu}(\mathbf{x})) \\ &+ 2\boldsymbol{\gamma}(\mathbf{x}) : \boldsymbol{\Sigma} + \boldsymbol{\sigma}'(\mathbf{x}) : \boldsymbol{\gamma}(\mathbf{x}) \big) \, \mathrm{d}\mathbf{x}. \end{aligned} \tag{4.41}$$

Again, performing a variation with respect to unknown quantities $\boldsymbol{\gamma}$ and $\boldsymbol{\sigma}'$ gives

$$\begin{aligned} \delta V(\boldsymbol{\gamma}, \boldsymbol{\sigma}') &= -\frac{1}{2} \int_V \{ 2\delta\boldsymbol{\gamma}(\mathbf{x}) : [(\mathbf{M}(\mathbf{x}) - \mathbf{M}_0)^{-1} : (\boldsymbol{\gamma}(\mathbf{x}) - \boldsymbol{\mu}(\mathbf{x})) - \boldsymbol{\sigma}(\mathbf{x})] \\ &+ \delta\boldsymbol{\gamma}(\mathbf{x}) : \boldsymbol{\sigma}'(\mathbf{x}) - \delta\boldsymbol{\sigma}'(\mathbf{x}) : \boldsymbol{\gamma}(\mathbf{x}) \} \, \mathrm{d}\mathbf{x}. \end{aligned} \tag{4.42}$$

Setting $\delta V(\boldsymbol{\gamma}, \boldsymbol{\sigma}') = 0$ we immediately recover Eq. (4.38), while the compatibility conditions, Eq. (4.37), follow after recasting the remaining terms in the brackets. As for the primary variational principle, it can be shown that the stationary value $V(\boldsymbol{\gamma}^*, \boldsymbol{\sigma}^{*\prime})$ of the functional $V(\boldsymbol{\gamma}, \boldsymbol{\sigma}')$ equals the actual potential energy stored in the anisotropic and heterogeneous body

$$V(\boldsymbol{\gamma}^*, \boldsymbol{\sigma}^{*\prime}) = \frac{1}{2} \int_V (\boldsymbol{\sigma}(\mathbf{x}) : \mathbf{M}(\mathbf{x}) : \boldsymbol{\sigma}(\mathbf{x}) + 2\boldsymbol{\sigma}(\mathbf{x}) : \boldsymbol{\mu}(\mathbf{x})) \, \mathrm{d}\mathbf{x}. \tag{4.43}$$

The functional V attains its maximum ($\delta^2 V < 0$) if $(\mathbf{M} - \mathbf{M}_0)$ is positive definite and its minimum if $(\mathbf{M} - \mathbf{M}_0)$ is negative definite[4].

To reduce the number of unknown quantities we first write $\boldsymbol{\sigma}'$ in terms of the polarization strain $\boldsymbol{\gamma}$ and a non-local operator $\boldsymbol{\sigma}_{\mathbf{0}}^*(\cdot)$[5]

$$\boldsymbol{\sigma}'(\mathbf{x}) = \boldsymbol{\sigma}(\mathbf{x}) - \boldsymbol{\Sigma} = \int_V \boldsymbol{\sigma}_{\mathbf{0}}^*(\mathbf{x} - \mathbf{x}') : (\boldsymbol{\gamma}(\mathbf{x}') - \langle \boldsymbol{\gamma} \rangle)\, \mathrm{d}\mathbf{x}' - \mathbf{M}_0^{-1} : (\boldsymbol{\gamma}(\mathbf{x}) - \langle \boldsymbol{\gamma} \rangle). \quad (4.44)$$

Next, in analogy with the primary principle, we introduce Eq. (4.44) into the dual variational principle Eq. (4.41) to get

$$\begin{aligned} V(\boldsymbol{\gamma}) &= \frac{1}{2} \int_V \Big(\boldsymbol{\Sigma} : \boldsymbol{E} - (\boldsymbol{\gamma}(\mathbf{x}) - \boldsymbol{\mu}(\mathbf{x})) : (\mathbf{M}(\mathbf{x}) - \mathbf{M}_0)^{-1} : (\boldsymbol{\gamma}(\mathbf{x}) - \boldsymbol{\mu}(\mathbf{x})) + 2\boldsymbol{\gamma}(\mathbf{x}) : \boldsymbol{\Sigma} \\ &+ \boldsymbol{\gamma}(\mathbf{x}) : \int_V \boldsymbol{\sigma}_{\mathbf{0}}^*(\mathbf{x} - \mathbf{x}') : (\boldsymbol{\gamma}(\mathbf{x}') - \langle \boldsymbol{\gamma} \rangle)\, \mathrm{d}\mathbf{x}' - \boldsymbol{\gamma}(\mathbf{x}) : \mathbf{M}_0^{-1} : (\boldsymbol{\gamma}(\mathbf{x}) - \langle \boldsymbol{\gamma} \rangle) \Big)\, \mathrm{d}\mathbf{x}. \end{aligned} \quad (4.45)$$

4.2.2 Extension to random composites

Assuming that each phase r of a randomly arranged composite is homogeneous with the compliance tensor $\mathbf{M}_r, r = 1, \ldots, n$, we write in analogy with Section 4.1 the material compliance tensor, the polarization strain $\boldsymbol{\gamma}$ and eigenstrain $\boldsymbol{\mu}$ in the sample α as

$$\mathbf{M}(\mathbf{x}, \alpha) = \sum_{r=1}^{n} \chi_r(\mathbf{x}, \alpha) \mathbf{M}_r, \quad \boldsymbol{\gamma}(\mathbf{x}, \alpha) = \sum_{r=1}^{n} \chi_r(\mathbf{x}, \alpha) \boldsymbol{\gamma}_r(\mathbf{x}), \quad \boldsymbol{\mu}(\mathbf{x}, \alpha) = \sum_{r=1}^{n} \chi_r(\mathbf{x}, \alpha) \boldsymbol{\mu}_r(\mathbf{x}),$$

with the respective ensemble averages for a given ergodic and statistically homogeneous material (compare with Eqs. (4.20)–(4.24))

$$\overline{\mathbf{M}} = \sum_{r=1}^{n} c_r \mathbf{M}_r, \quad \overline{\boldsymbol{\gamma}(\mathbf{x})} = \sum_{r=1}^{n} c_r \boldsymbol{\gamma}_r(\mathbf{x}), \quad \overline{\boldsymbol{\mu}(\mathbf{x})} = \sum_{r=1}^{n} c_r \boldsymbol{\mu}_r(\mathbf{x}). \quad (4.46)$$

The ensemble average of the quadratic term $\boldsymbol{\gamma} : \boldsymbol{\sigma}_{\mathbf{0}}^* : \boldsymbol{\gamma}$ yields, in analogy with Eq. (4.22),

$$\overline{\boldsymbol{\gamma}(\mathbf{x}, \alpha) : \boldsymbol{\sigma}_{\mathbf{0}}^*(\mathbf{x} - \mathbf{x}') : \boldsymbol{\gamma}(\mathbf{x}', \alpha)} = \sum_{r=1}^{n} \sum_{s=1}^{n} S_{rs}(\mathbf{x} - \mathbf{x}') \boldsymbol{\gamma}_r(\mathbf{x}) : \boldsymbol{\sigma}_{\mathbf{0}}^*(\mathbf{x} - \mathbf{x}') : \boldsymbol{\gamma}_s(\mathbf{x}'). \quad (4.47)$$

[4] See again [89] for the proof for the case $\boldsymbol{\gamma} = \mathbf{0}$ and [204] for general situation.

[5] The operator $\boldsymbol{\sigma}_{\mathbf{0}}^*(\cdot)$ can be identified with the operator $\boldsymbol{\epsilon}_{\mathbf{0}}^*(\cdot)$ when replacing $\boldsymbol{\gamma}$ for $\boldsymbol{\tau}$ and $\boldsymbol{\sigma}_{\mathbf{0}}^*$ for $\boldsymbol{\epsilon}_{\mathbf{0}}^*$ in Eq. (B.13) and suitably modifying the boundary term to reflect the traction boundary conditions. As for properties of tensor $\boldsymbol{\sigma}_{\mathbf{0}}^*$ the reader is referred to Appendix B, Eqs. (B.23) and (B.29). Recall that subscript "0" stands for the homogeneous reference medium. Note that operator $-\boldsymbol{\sigma}_{\mathbf{0}}^*(\cdot) - \mathbf{M}_0^{-1}\delta(\cdot)$ is sometimes denoted as $\boldsymbol{\Delta}$, (see, e.g., [133, 134, 286]).

Substituting Eqs. (4.46) and (4.47) into Eq. (4.45) readily provides the extended averaged form of the dual Hashin-Shtrikman principle

$$\begin{aligned}\overline{V(\boldsymbol{\gamma},\alpha)} &= \frac{1}{2}\int_V \boldsymbol{\Sigma} : \boldsymbol{E}\,\mathrm{d}\mathbf{x} \qquad (4.48)\\ &- \frac{1}{2}\sum_r \int_V \left(c_r(\boldsymbol{\gamma}_r(\mathbf{x})-\boldsymbol{\mu}_r(\mathbf{x})) : (\mathbf{M}_r-\mathbf{M}_0)^{-1}(\boldsymbol{\gamma}_r(\mathbf{x})-\boldsymbol{\mu}_r(\mathbf{x})) - 2c_r\boldsymbol{\gamma}_r(\mathbf{x}) : \boldsymbol{\Sigma}\right)\mathrm{d}\mathbf{x}\\ &+ \frac{1}{2}\sum_r\sum_s \int_V \boldsymbol{\gamma}_r(\mathbf{x}) : \int_V \boldsymbol{\sigma}_{\mathbf{0}}^{*}(\mathbf{x}-\mathbf{x}') : \left[S_{rs}(\mathbf{x}-\mathbf{x}')\boldsymbol{\gamma}_s(\mathbf{x}') - c_r\langle\boldsymbol{\gamma}\rangle\right]\mathrm{d}\mathbf{x}'\,\mathrm{d}\mathbf{x}\\ &- \frac{1}{2}\sum_r \int_V c_r\boldsymbol{\gamma}_r(\mathbf{x}) : \mathbf{M}_0^{-1} : (\boldsymbol{\gamma}_r(\mathbf{x})-\langle\boldsymbol{\gamma}\rangle)\,\mathrm{d}\mathbf{x}.\end{aligned}$$

4.2.3 Approximate solution

In analogy with Eq. (4.25) and [90] we further admit only piecewise uniform variation of eigenstrain tensor $\boldsymbol{\mu}$ and polarization strain tensor $\boldsymbol{\gamma}$ ($\boldsymbol{\mu}_r(\mathbf{x})=\boldsymbol{\mu}_r, \boldsymbol{\gamma}_r(\mathbf{x})=\boldsymbol{\gamma}_r$). Next, after setting $\langle\boldsymbol{\gamma}\rangle=\sum_r \boldsymbol{\gamma}_r c_r$ and performing variation with respect to $\boldsymbol{\gamma}_r$ we arrive at the extended form of the stationarity conditions

$$\begin{aligned}& c_r\left[(\mathbf{M}_r-\mathbf{M}_0)^{-1}+\mathbf{M}_0^{-1}\right] : \boldsymbol{\gamma}_r(\mathbf{x})\\ &- \sum_{s=1}^{n}\int_V \left\{\boldsymbol{\sigma}_{\mathbf{0}}^{*}(\mathbf{x}-\mathbf{x}')\left[S_{rs}(\mathbf{x}-\mathbf{x}')-c_rc_s\right]+\mathbf{M}_0^{-1}c_rc_s\right\} : \boldsymbol{\gamma}_s(\mathbf{x}')\,\mathrm{d}\mathbf{x}' =\\ &= c_r\boldsymbol{\Sigma}+(\mathbf{M}_r-\mathbf{M}_0)^{-1} : \boldsymbol{\mu}_r(\mathbf{x})c_r,\ r=1,2,\ldots,n, \qquad (4.49)\end{aligned}$$

or, following Eq. (4.25), again in the engineering notation,

$$\begin{aligned}&\sum_{s=1}^{n}\left(\delta_{rs}c_r\left(([\mathsf{M_r}]-[\mathsf{M_0}])^{-1}+[\mathsf{M_0}]^{-1}\right)-c_rc_s\,[\mathsf{M_0}]^{-1}-[\mathsf{B_{rs}}]\right)\{\gamma_\mathsf{s}\}\\ &= c_r\{\Sigma\}+c_r([\mathsf{M_r}]-[\mathsf{M_0}])^{-1}\{\mu_\mathsf{r}\}, r=1,2,\ldots,n, \qquad (4.50)\end{aligned}$$

where evaluation of the microstructure-dependent matrices $[\mathsf{B_{rs}}]$

$$[\mathsf{B_{rs}}]=\int_V [\sigma_0^{*}]\,(\mathbf{x}-\mathbf{x}')\,(S_{rs}(\mathbf{x}-\mathbf{x}')-c_rc_s)\,\mathrm{d}\mathbf{x}', \qquad (4.51)$$

is again outlined in the Appendix B. Similarly to Eqs. (4.27) and (4.28) we write after symbolic inversion of Eq. (4.50) the desired components of the polarization tensor $\{\gamma_\mathsf{r}\}$ in the form

$$\{\gamma_\mathsf{r}\}=\sum_{s=1}^{n} c_s\,[\mathsf{R_{rs}}]\left(\{\Sigma\}+([\mathsf{M_s}]-[\mathsf{M_0}])^{-1}\{\mu_\mathsf{s}\}\right), \qquad (4.52)$$

and finally

$$\{\overline{\gamma}\}=\sum_{r=1}^{n}\sum_{s=1}^{n} c_rc_s\,[\mathsf{R_{rs}}]\left(\{\Sigma\}+([\mathsf{M_s}]-[\mathsf{M_0}])^{-1}\{\mu_\mathsf{s}\}\right). \qquad (4.53)$$

The macroscopic constitutive law is now given by

$$\{\mathsf{E}\}=\left[\mathsf{M}^{\mathsf{HS}}\right]\{\Sigma\}+\{\Upsilon^{\mathsf{HS}}\}, \qquad (4.54)$$

with

$$\left[\mathsf{M}^{\mathsf{HS}}\right] = [\mathsf{M}_0] + \sum_{r=1}^{n}\sum_{s=1}^{n} c_r c_s \left[\mathsf{R}_{\mathsf{rs}}\right], \tag{4.55}$$

$$\{\Upsilon^{\mathsf{HS}}\} = \sum_{r=1}^{n}\sum_{s=1}^{n} c_r c_s \left[\mathsf{R}_{\mathsf{rs}}\right] \left([\mathsf{M}_{\mathsf{s}}] - [\mathsf{M}_0]\right)^{-1} \{\mu_{\mathsf{s}}\}. \tag{4.56}$$

4.3 Linear elasticity and thermal strains

To make comparisons with the finite element approach we consider again the graphite fiber tow of Fig. 2.2. The primary goal is to recover the effective thermo-elastic properties already derived in Chapter 3 by the finite element approach.

Starting with the primary H-S variational principle, Section 4.1, the thermo-elastic macroscopic constitutive law receives the form[6]

$$\{\Sigma\} = \left[\mathsf{L}^{\mathsf{HS}}\right]\{\mathsf{E}\} + \{\Lambda^{\mathsf{HS}}\} = \left[\mathsf{L}^{\mathsf{HS}}\right]\left(\{\mathsf{E}\} - \{\mathsf{m}^{\mathsf{HS}}\}\Delta\theta\right), \tag{4.57}$$

where $\{\mathsf{m}^{\mathsf{HS}}\}$ is the overall thermal strain vector of the expansion coefficients. To fill individual entries in $\left[\mathsf{L}^{\mathsf{HS}}\right]$ and $\{\mathsf{m}^{\mathsf{HS}}\}$ requires first to solve Eq. (4.31) for unknown components of vectors $\{\tau_{\mathsf{r}}\}$. Eqs. (4.1) and (4.5) then readily provide the average stress $\{\Sigma\}$ as

$$\{\Sigma\} = \sum_{r=1}^{n} c_r \left\{[\mathsf{L}_{\mathsf{r}}]\left([\mathsf{L}_{\mathsf{r}}] - [\mathsf{L}_0]\right)^{-1}\{\tau_{\mathsf{r}}\} + [\mathsf{L}_{\mathsf{r}}]\left(\left([\mathsf{L}_{\mathsf{r}}] - [\mathsf{L}_0]\right)^{-1} - [\mathsf{I}]\right)\{\mathsf{m}_{\mathsf{r}}\}\Delta\theta\right\}. \tag{4.58}$$

Referring to Section 3.2.5 the coefficients of the stiffness matrix $\left[\mathsf{L}^{\mathsf{HS}}\right]$ are found from solutions of four successive elasticity problems. In each solution the medium, free of thermal strains, is subjected to overall strain $\{\mathsf{E}\}$ with only one nonzero component of unit magnitude. The overall stress, resulting from Eq. (4.58), then furnishes the column of the (4×4) matrix $\left[\mathsf{L}^{\mathsf{HS}}\right]$ corresponding to the selected nonzero component of $\{\mathsf{E}\}$ as a function of $[\mathsf{L}_0]$. Therefore, having properly chosen components of the stiffness matrix of the comparison medium $[\mathsf{L}_0]$ we may arrive either at the lower or upper bound on elastic stiffnesses of heterogeneous media. In particular, we select $[\mathsf{L}_0]$ as an artificial material with coefficients $[\mathsf{L}_0]_{ij} \overset{<}{>} [\mathsf{L}_{\mathsf{r}}]_{ij}$ smallest (largest) of all $[\mathsf{L}_{\mathsf{r}}]_{ij}$ in V[7].

Results appear in Table 4.1[8]. The FFT combined with the generalized trapezoid rule is used to evaluate the microstructure dependent matrices $[\mathsf{A}_{\mathsf{rs}}]$ (recall Section 2.3.1 and Appendix B).

The thermal strain coefficients are obtained in the similar way by setting $\{\mathsf{E}\} = \{0\}$ and applying the temperature change $\Delta\theta$ equal to unity. The stress from Eq. (4.58) is the

[6] In accordance with Chapter 3, the generalized plane strain state is assumed. See Section A.2.1 for more details and notation used hereafter.

[7] Precisely speaking, to avoid singularities of matrices $[\mathsf{L}_{\mathsf{r}}] - [\mathsf{L}_0]$, we used values $(1+\epsilon)\,[\mathsf{L}_{\mathsf{r}}]$ when selecting the matrix with smallest entries and values $(1-\epsilon)\,[\mathsf{L}_{\mathsf{r}}]$ when selecting matrix with largest entries with the value ϵ set to $\approx 10^{-4}$.

[8] Material properties of individual phases are taken from Table 3.8. The UB and LB columns in Tables 4.1–4.4 correspond to the lower bound (the matrix $[\mathsf{L}_0]$ with the smallest entries) and to the upper bound (the matrix selected $[\mathsf{L}_0]$ the largest entries), respectively.

Bitmap	$\mathsf{L}^{\mathsf{HS}}{}_{11}$			$\mathsf{L}^{\mathsf{HS}}{}_{22}$			$\mathsf{L}^{\mathsf{HS}}{}_{33}$		
resolution	LB	FEM	UB	LB	FEM	UB	LB	FEM	UB
122 × 84	10.733	10.740	10.770	10.713	10.724	10.746	2.211	2.215	2.218
244 × 179	10.740	10.740	10.777	10.720	10.724	10.752	2.209	2.216	2.216
488 × 358	10.730	10.740	10.763	10.721	10.724	10.754	2.209	2.216	2.216
976 × 716	10.730	10.740	10.763	10.721	10.724	10.764	2.209	2.216	2.216

Table 4.1: Effective elastic stiffnesses [GPa]

overall eigenstress $\{\Lambda^{\mathsf{HS}}\}$. The overall thermal strain $\{\mathsf{m}^{\mathsf{HS}}\}$ then follows from (4.58) as

$$\{\mathsf{m}^{\mathsf{HS}}\} = -\left[\mathsf{L}^{\mathsf{HS}}\right]^{-1}\{\Lambda^{\mathsf{HS}}\}. \tag{4.59}$$

Results are summarized in Table 4.2.

Bitmap	$\mathsf{m}^{\mathsf{HS}}{}_1 \times 10^5$			$\mathsf{m}^{\mathsf{HS}}{}_2 \times 10^5$			$\mathsf{m}^{\mathsf{HS}}{}_4 \times 10^7$			c_f
resolution	LB	FEM	UB	LB	FEM	UB	LB	FEM	UB	
122 × 84	2.248	2.269	2.278	2.230	2.248	2.253	-7.488	-7.463	-7.504	0.438
244 × 179	2.256	2.269	2.285	2.236	2.248	2.259	-7.455	-7.463	-7.471	0.436
488 × 358	2.256	2.269	2.287	2.237	2.248	2.260	-7.455	-7.463	-7.471	0.436
976 × 716	2.256	2.269	2.287	2.237	2.248	2.260	-7.455	-7.463	-7.471	0.436

Table 4.2: Effective coefficients of thermal expansion [K^{-1}]

If the stress control is applied, the dual variational principle Eq. (4.41) can be invoked to derive the coefficients of the compliance matrix $\left[\mathsf{M}^{\mathsf{HS}}\right]$. As for $\left[\mathsf{L}^{\mathsf{HS}}\right]$ they follow again from solutions of four successive elasticity problems. In each solution the medium, free of thermal strains, is subjected to overall stress $\{\Sigma\}$ with only one nonzero component of unit magnitude. The overall strain, given by

$$\{\mathsf{E}\} = \left[\mathsf{M}^{\mathsf{HS}}\right]\{\Sigma\} + \{\Upsilon^{\mathsf{HS}}\} = \left[\mathsf{M}^{\mathsf{HS}}\right]\{\Sigma\} + \{\mathsf{m}^{\mathsf{HS}}\}\Delta\theta, \tag{4.60}$$

then furnishes a column of the (4×4) matrix $\left[\mathsf{M}^{\mathsf{HS}}\right]$ corresponding to the selected nonzero component of $\{\Sigma\}$. Depending on individual entries of the compliance matrix $[\mathsf{M}_0]$ we may obtain either the lower or upper bound on the effective elastic compliance matrix of a heterogeneous medium. In particular, we select $[\mathsf{M}_0]$ as an artificial material with coefficients $[\mathsf{M}_0]_{ij} \lessgtr [\mathsf{M}_\mathsf{r}]_{ij}$ smallest (largest) of all $[\mathsf{M}_\mathsf{r}]_{ij}$ in V. Results are stored in Table 4.3.

Bitmap	$\mathsf{M}^{\mathsf{HS}}{}_{11}$			$\mathsf{M}^{\mathsf{HS}}{}_{22}$			$\mathsf{M}^{\mathsf{HS}}{}_{33}$		
resolution	LB	FEM	UB	LB	FEM	UB	LB	FEM	UB
244 × 179	1.4293	1.4307	1.4312	1.4312	1.4325	1.4330	4.517	4.521	4.524
488 × 358	1.4298	1.4307	1.4317	1.4316	1.4325	1.4334	4.518	4.521	4.525
976 × 716	1.4298	1.4307	1.4318	1.4317	1.4325	1.4334	4.519	4.521	4.525

Table 4.3: Effective elastic compliances [GPa^{-1}] $\times 10^4$

Eq. (4.60) can be further used to provide the overall coefficients of thermal expansion when setting $\Delta\theta = 1$ and $\{\mathsf{\Sigma}\} = \{\mathsf{0}\}$. As expected, they were found identical with those derived from the primary variational principle. Similar agreement between elastic stiffnesses and compliances is evident from Table 4.4[9].

Bitmap resolution	IP-LB $\mathsf{L}^{\mathsf{HS}}{}_{11}$	P-LB $\mathsf{L}^{\mathsf{HS}}{}_{11}$	D-LB $\mathsf{M}^{\mathsf{HS}-1}{}_{11}$	P-UB $\mathsf{L}^{\mathsf{HS}}{}_{11}$	D-UP $\mathsf{M}^{\mathsf{HS}-1}{}_{11}$	IP-UB $\mathsf{L}^{\mathsf{HS}}{}_{11}$
244 × 179	10.744	10.759	10.759	10.772	10.772	10.754
488 × 358	10.744	10.755	10.755	10.766	10.766	10.754
976 × 716	10.744	10.754	10.754	10.765	10.765	10.754

Bitmap resolution	IP-LB $\mathsf{L}^{\mathsf{HS}}{}_{33}$	P-LB $\mathsf{L}^{\mathsf{HS}}{}_{33}$	D-LB $\mathsf{M}^{\mathsf{HS}-1}{}_{33}$	P-UB $\mathsf{L}^{\mathsf{HS}}{}_{33}$	D-UP $\mathsf{M}^{\mathsf{HS}-1}{}_{33}$	IP-UB $\mathsf{L}^{\mathsf{HS}}{}_{33}$
244 × 179	2.211	2.211	2.213	2.216	2.216	2.214
488 × 358	2.211	2.210	2.210	2.215	2.215	2.214
976 × 716	2.211	2.210	2.210	2.215	2.215	2.214

Table 4.4: Effective elastic compliances [GPa^{-1}]

Clearly, the finite element solutions from Chapter 3 fall within individual bounds provided by Hashin-Shtrikman variational principles. Tables 4.1 and 4.2 further demonstrate insensivity of the solution to the selected bitmap resolution, as long as the volume fraction of the inclusion is the same (see Section 2.4.3). In addition, attributed to the assumed statistical homogeneity, the results confirm a slight anisotropy of the present medium suggested by the results from the previous chapter. In terms of computer time, the efficiency of the present approach when compared to the FEM analysis is doubtless. Nevertheless, to fully accept this method a number of other numerical assement, particularly for more complex material behavior, are needed.

4.4 Linear viscoelasticity

This section outlines implementation of the H-S principles to solve the viscoelastic problem as an alternative to the FEM analysis discussed in Chapter 3. This approach may become advantageous over the sometimes time consuming implementation of finite elements, particularly when no information about the nature of local fields is needed, but instead a notion about the phase volume averages of field variables is sufficient in simulations of the material behavior.

4.4.1 Macroscopic constitutive law

To introduce the viscoelastic effects we first recall Eq. (A.37). Then, in analogy with Eqs. (3.53) and (3.56), the incremental form of Eq. (4.29) becomes

$$\{\Delta\mathsf{\Sigma}(t_i)\} = \left[\mathsf{L}^{\mathsf{HS}}(t_i)\right]\{\Delta\mathsf{E}(t_i)\} + \{\Delta\mathsf{\Lambda}^{\mathsf{HS}}(t_i)\}. \tag{4.61}$$

[9] Letters P and D in Table 4.4 stand for the primary and dual variational principles, respectively, and IP denotes results obtained from the primary variational principle when assuming the statistically isotropic material.

Note that the fiber phase is assumed elastic and linear viscoelastic behavior of the matrix phase is governed by incremental relations (A.41)–(A.43), i.e.,

$$[\mathsf{L}_\mathsf{f}] = [\mathsf{L}(k,l,m,n)]\,, \qquad \{\lambda_\mathsf{f}\} = \{\mathsf{0}\}, \tag{4.62}$$

$$[\mathsf{L}_\mathsf{m}(t_i)] = \left[\mathsf{L}(\widehat{E}(t_i),\nu)\right], \qquad \{\Delta\lambda_\mathsf{m}(t_i)\} = \sum_{\mu=1}^{M}\{\Delta\lambda_{\mathsf{m},\mu}(t_i)\}. \tag{4.63}$$

Eq. (4.61) then drives the solution of a viscoelastic problem under strain control loading conditions suitable for modeling the stress relaxation.

To find the solution to a stress control viscoelastic problem such as creep experiment, we replace Eq. (4.54) by its incremental counterpart such that

$$\{\Delta\mathsf{E}(t_i)\} = \left[\mathsf{M}^{\mathsf{HS}}(t_i)\right]\{\Delta\Sigma(t_i)\} + \{\Delta\Upsilon^{\mathsf{HS}}(t_i)\}. \tag{4.64}$$

4.4.2 Numerical results

To compare the present approach with the finite element estimates of Section 3.4 we consider again the material system of Fig. 2.1b with the respective binary images displayed in Figs. 2.2 and 2.7 and the elastic properties stored in Table 3.11. Both the strain and stress control loading conditions are considered in simulations. The same loading conditions as in Section 3.4, Fig. 3.13, are considered. Furthermore, recall that the primary H-S principle may be invoked to simulate the relaxation response while the dual H-S principle should be called to study the creep behavior. In both instances, however, the resulting representation of the viscoelastic response is governed by the selection of a homogeneous comparison medium ($[\mathsf{L}_0]\,, [\mathsf{M}_0]$). To this end, we draw the reader's attention to Fig. 4.3. First, recall Table 3.11 and notice that the matrix moduli are indeed weaker than those of fiber. Therefore, according to [89], we select the matrix phase to fill individual entries of $[\mathsf{L}_0]$ and $[\mathsf{M}_0]$ providing we search for a lower bound on the relaxation response (Fig. 4.3a) and an upper bound on the creep response (Fig. 4.3b), respectively. The fiber phase is then selected to yield estimates on opposite bounds. A number of other results, contained within the H-S bounds, can be derived when mixing individual phases to set $[\mathsf{L}_0]$ and $[\mathsf{M}_0]$ (e.g., $[\mathsf{L}_0] = \frac{1}{2}([\mathsf{L}_\mathsf{f}] + [\mathsf{L}_\mathsf{m}])$)[10].

Fig. 4.3 gives some idea of this approach assuming hexagonal packing of fibers. One noteworthy feature of the hexagonal array model is the correspondence of the periodic hexagonal unit cell with the Mori-Tanaka averaging technique. It is well known that the Mori-Tanaka estimates of the overall response of composites with weak matrices correspond to the lower and upper bounds derived from the primary and dual H-S variational principles [276], respectively. From this point of view one may also judge the results derived from the periodic hexagonal unit cell (solid lines in Fig. 4.3a,b). Therefore, in order to make the results found from the H-S variational principles comparable with those derived previously using the optimal unit cells, we selected the matrix phase to create the 4×4 homogeneous stiffness $[\mathsf{L}_0]$ and compliance $[\mathsf{M}_0]$ matrices. Also note that these matrices are kept constant throughout the integration process. This assumption is acceptable since the instantaneous moduli of the matrix phase do not vary considerably for the selected time-stepping procedure[11].

[10] See article [53] for systematic study of this idea.

[11] See Section 4.5.2 for the demonstration of this fact in the context of nonlinear viscoelasticity.

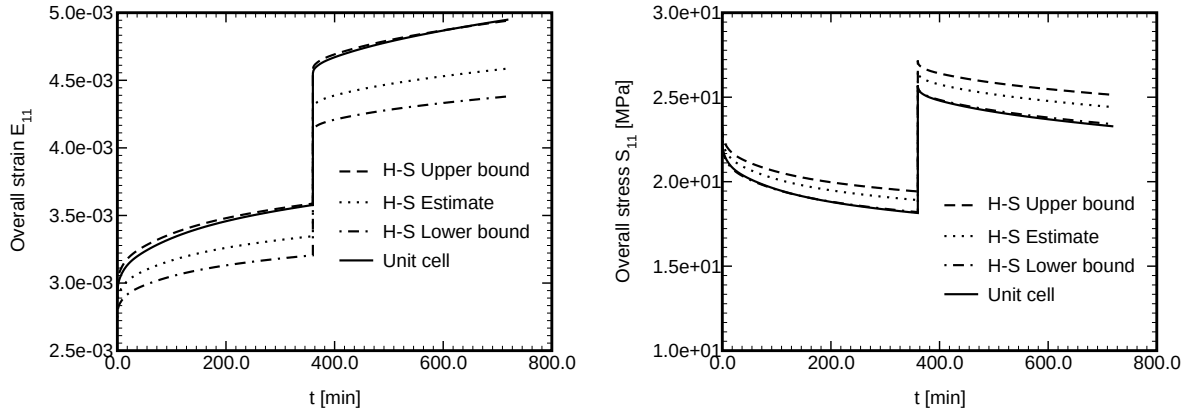

(a) (b)

Figure 4.3: Overall response – hexagonal packing: (a) creep test, (b) relaxation test

As outlined in Section 4.1, evaluation of the overall response of random composites requires first selection of a RVE. Binary images of the RVE of the present material system, Fig. 2.1b, which complies with requirements discussed in Section 2.1, are displayed in Fig. 2.7. The RVEs of Fig. 2.7 were employed to evaluate the microstructure dependent matrices in Eqs. (4.26) and (4.51). The effect of bitmap resolution on the overall response was examined first. Results appear in Figs. 4.4 and 4.5. Evidently, even low resolution of 244×179 pixels provides sufficiently accurate results. This should also hold for combined loading. Such a result is quite encouraging, particularly if one would like to increase the size of the RVE.

Fig. 4.6 further confirms ability of this approach to model an anisotropic character of the present material system already suggested by the FEM analysis of optimal periodic unit cells. Finally, we bring some comparison between the UC analysis and the H-S variational principles plotted in Fig. 4.7. As expected, recall our previous discussion on H-S bounds, the relaxation data obtained from 5-fibers periodic UC correlates fairly well with the H-S lower bound and similarly the creep response of UC is found close to the H-S upper bound. Thus the applicability of both approaches to simulate the viscoelastic behavior of statistically homogeneous material systems such as the one under present study is confirmed.

4.5 Nonlinear viscoelasticity

Following the route set by the finite element method approach, the results of the linear viscoelasticity are extended to non-linear viscoelastic materials in this section. Similarly to the finite element procedure, it appears advantageous to consider the incremental form of the Leonov model introduced in Section A.4 to estimate the overall response of the selected material system. Then, the transformation field framework used in the linear viscoelasticity case can be easily extended to nonlinearly viscoelastic response.

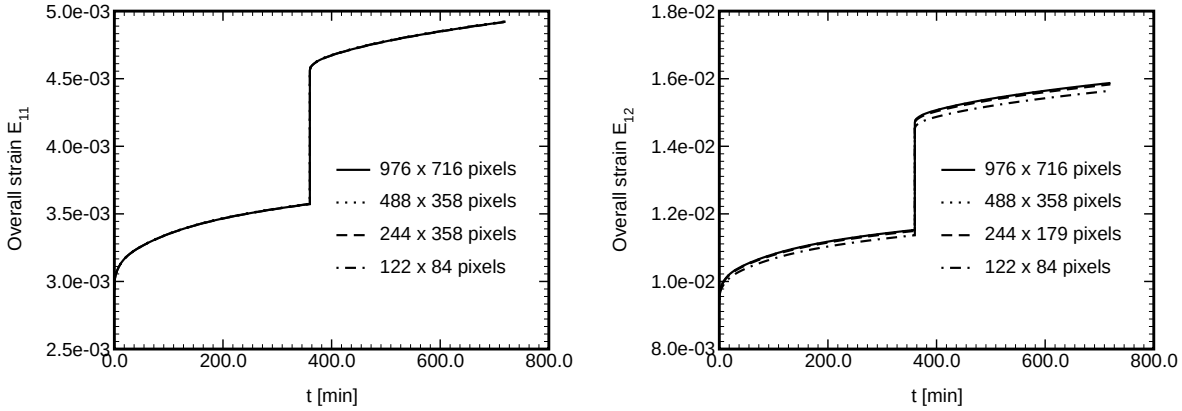

Figure 4.4: Overall response – Hashin-Shtrikman principle: creep test

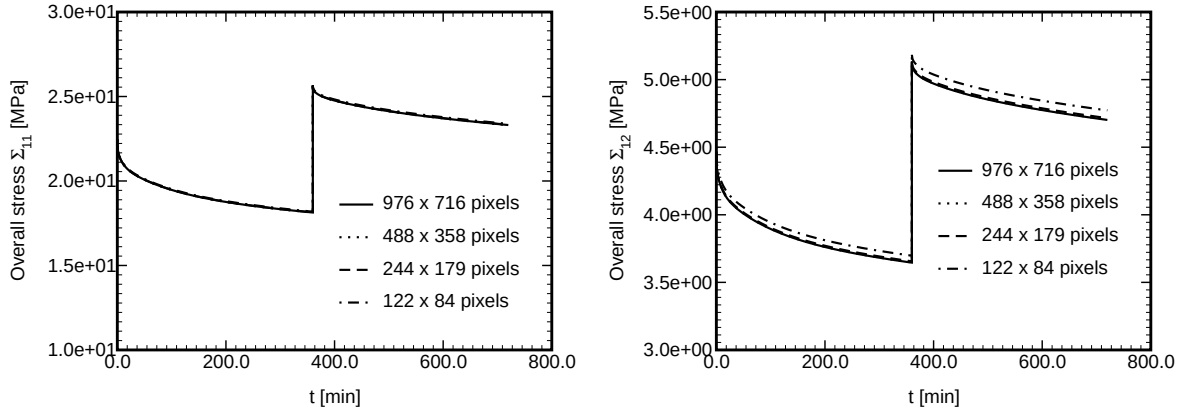

Figure 4.5: Overall response – Hashin-Shtrikman principle: relaxation test

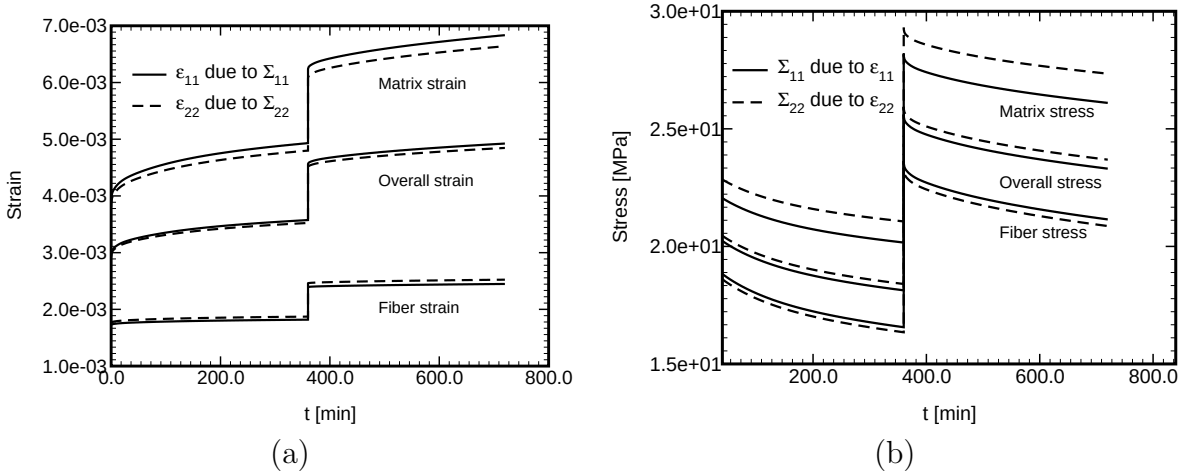

Figure 4.6: Overall and local response – Hashin-Shtrikman principle: (a) creep test, (b) relaxation test

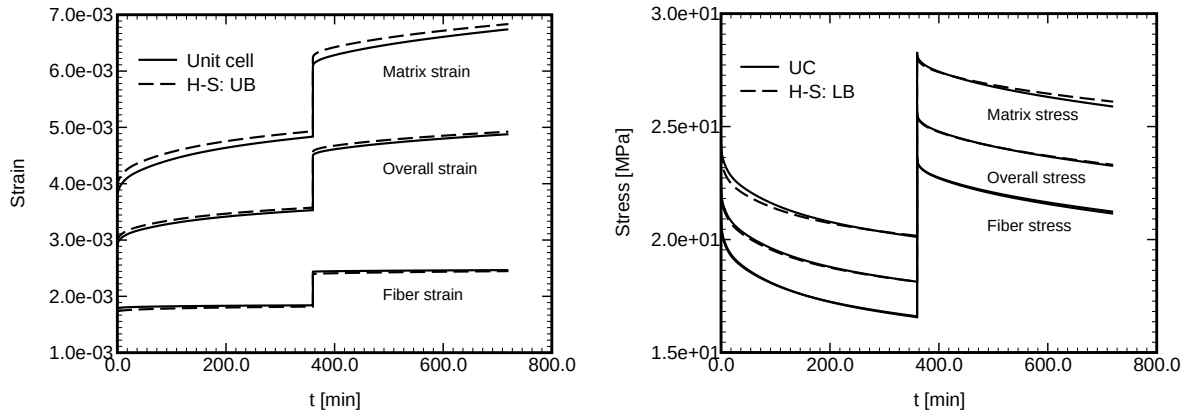

(a) (b)

Figure 4.7: Overall and local response – UC vs. H-S: (a) creep test, (b) relaxation test

4.5.1 Macroscopic constitutive law

The incremental form of stress-strain relationship for a linearly elastic and transversally isotropic fiber phase assumes the familiar form

$$\{\Delta\sigma_{\mathsf{f}}\} = [\mathsf{L}_{\mathsf{f}}(k,l,m,n)]\,\{\Delta\varepsilon_{\mathsf{f}}\}, \tag{4.65}$$

where, similarly to Eq. (4.62), the fiber stiffness matrix $[\mathsf{L}_{\mathsf{f}}]$ is defined in terms of time-independent Hill's moduli k, l, m and n. Following the procedure discussed in Section A.4, the incremental constitutive equations for the matrix phase is given by

$$\{\Delta\sigma_{\mathsf{m}}(t_i)\} = \left[\mathsf{L}_{\mathsf{m}}(\widehat{G}(t_i), K)\right]\{\Delta\varepsilon_{\mathsf{m}}(t_i)\} + \{\Delta\lambda_{\mathsf{m}}(t_i)\}, \tag{4.66}$$

where the instantaneous material stiffness matrix $[\mathsf{L}(t_i)]$ is defined in terms of the time-independent bulk modulus K and the time-dependent shear modulus $\widehat{G}(t_i)$, see Eq. (A.54). The matrix eigenstress increment $\{\Delta\lambda_{\mathsf{m}}(t_i)\}$ then follows from Eqs. (A.55)–(A.58).

The overall response to a strain loading increment $\{\Delta\mathsf{E}(t_i)\}$ is then, in analogy to Eq. (4.61), provided by

$$\{\Delta\Sigma(t_i)\} = \left[\mathsf{L}^{\mathsf{HS}}(t_i)\right]\{\Delta\mathsf{E}(t_i)\} + \{\Delta\Lambda^{\mathsf{HS}}(t_i)\}, \tag{4.67}$$

and the relation

$$\{\Delta\mathsf{E}(t_i)\} = \left[\mathsf{M}^{\mathsf{HS}}(t_i)\right]\{\Delta\Sigma(t_i)\} + \{\Delta\Upsilon^{\mathsf{HS}}(t_i)\} \tag{4.68}$$

can be used to determine the overall response to an overall stress increment $\{\Delta\Sigma(t_i)\}$.

4.5.2 Numerical results

The composite system with material parameters identical to the data presented in Section 3.5.2 is used for numerical experiments performed in this section. Similarly to the finite element approach, only the loading by constant overall strain rate is investigated. Further, based on results of the previous section, the reference stiffness matrix $[\mathsf{L}_0]$ was

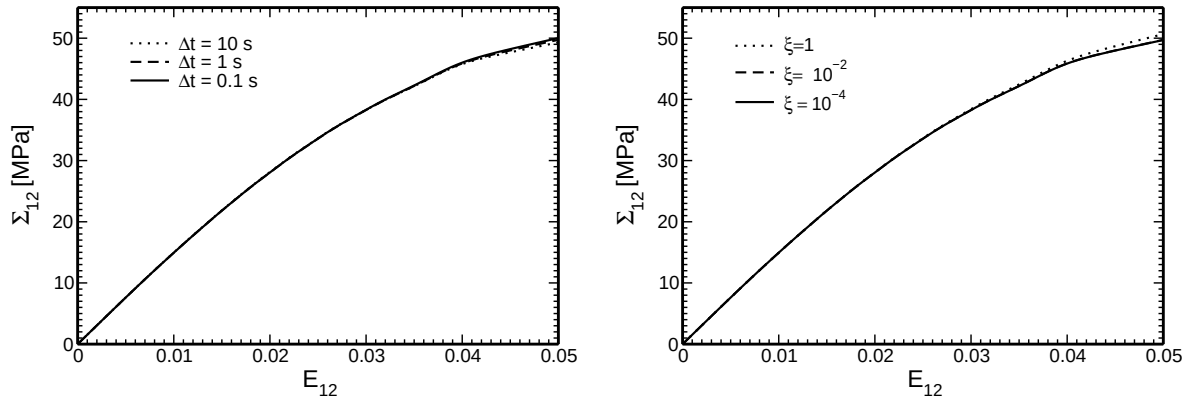

(a) (b)

Figure 4.8: Overall response – hexagonal packing for $\dot{E}_{12} = 10^{-4}$ s^{-1}: (a) Sensitivity with respect to time step, (b) Sensitivity with respect to reference medium update

selected as the smallest of all $[\mathsf{L}_\mathrm{r}]_{ij}$ appearing in the RVE. Recall that the generalized plane strain is again assumed in the analysis.

First, the sensitivity of the overall response with respect to time step Δt and the choice of the reference stiffness matrix $[\mathsf{L}_0]$ is analyzed. To study the influence of the reference stiffness matrix $[\mathsf{L}_0]$, the ratio $|1 - \widehat{G}(t_i)/\widehat{G}_{\mathrm{ref}}|$ was used to control updating of the reference medium. If this ratio exceeded a given tolerance ξ, the reference value $\widehat{G}_{\mathrm{ref}}$ was set to $\widehat{G}(t_i)$ and the reference stiffness matrix $[\mathsf{L}_0]$ was set to the corresponding value. In addition, the computation was run with time steps 10 s, 1 s and 0.1 s, respectively, to asses the influence of the chosen time step. The results of these experiments for an isotropic microstructure with the same volume fraction as the original material appear in Fig. 4.8. Apparently, the H-S based procedure is rather insensitive to the selected time step as well as to updating of the reference medium; to get practically indistinguishable overall response it suffices to set the value of $\Delta t = 1$ s and $\xi = 0.01$.

As the second step, an effect of a bitmap resolution on the overall response of the composite material is addressed. Similarly to linear elasticity and viscoelasticity, the results displayed in Fig. 4.9 again demonstrate the insensivity of the overall response on a bitmap resolution; in particular, the bitmap with dimensions 488×358 pixels gives results identical to the highest resolution 976×716 pixels for both E_{11} and E_{12} loading.

The following set of figures, Figs. 4.11a–d, shows the overall response for various rates of overall strain loading together with the finite element method results presented for the comparison.

Evidently, the agreement between the H-S based approach and the finite element modeling is satisfactory for E_{11} loading. This can be, similarly to the finite element approach, attributed to the negligible shear stresses developed during the loading process and to the assumption of linear volumetric response of the Leonov model (see footnote on page 62). The results found for the shear loading E_{12}, however, demonstrate that the H-S based approach substantially overestimates the overall shear stress, especially in later stage of the loading process. To shed a light on this phenomenon, the distribution of the instantaneous shear modulus $\widehat{G}$ for the hexagonal periodic unit cell is plotted in Fig. 4.10.

Evidently, the shear modulus $\widehat{G}$ is no longer phasewise constant at the end of the

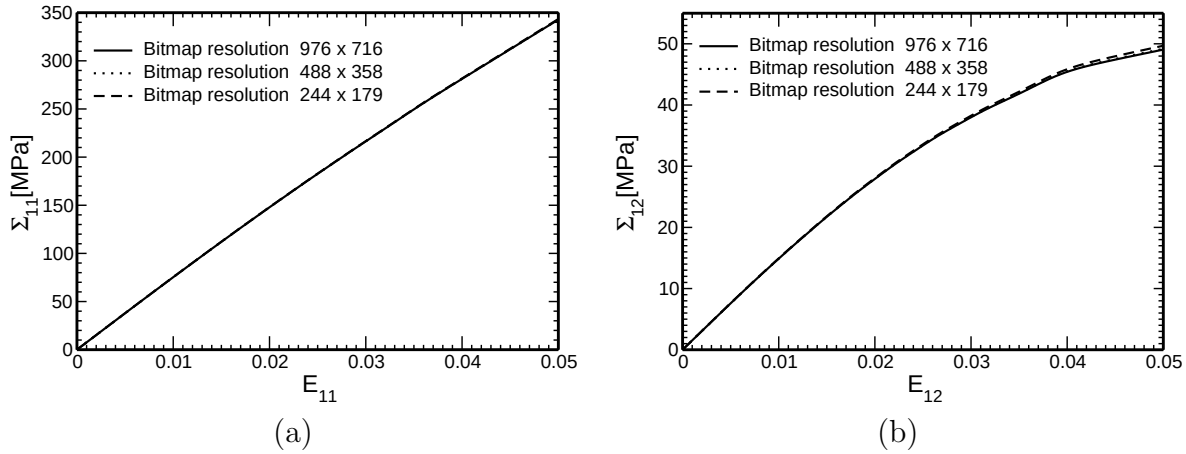

(a) (b)

Figure 4.9: Overall response – Hashin-Shtrikman principle: Effect of a bitmap resolution (a) $\dot{E}_{11} = 10^{-4}$ s^{-1}, (b) $\dot{E}_{12} = 10^{-4}$ s^{-1}

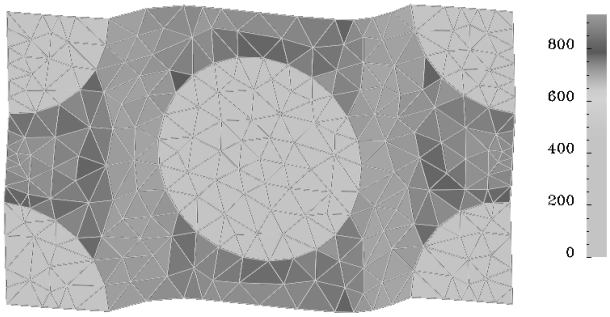

Figure 4.10: Hexagonal array: distribution of instantaneous matrix shear modulus at the end of loading for $\dot{E}_{12} = 10^{-5}$ s^{-1}.

loading interval. Thus, the assumption of the homogeneity of phase moduli, Eq. (4.3), is no longer valid, which results in a substantial deterioration of the performance of the Hashin-Shtrikman based approach. Nevertheless, the maximum difference between the H-S and the FEM modeling is approximately 10%; if such a modeling error is acceptable or taken into account (using, for example, the goal-adapted modeling framework [185]), the proposed procedure can be employed as an efficient substitute to the finite element method.

Finally, for the sake of completeness, the anisotropic character of the examined material system predicted by the Hashin-Shtrikman based approach is demonstrated by plotting phase stresses due to E_{11} and E_{22} loading, see Figs. 4.12a and 4.12b.

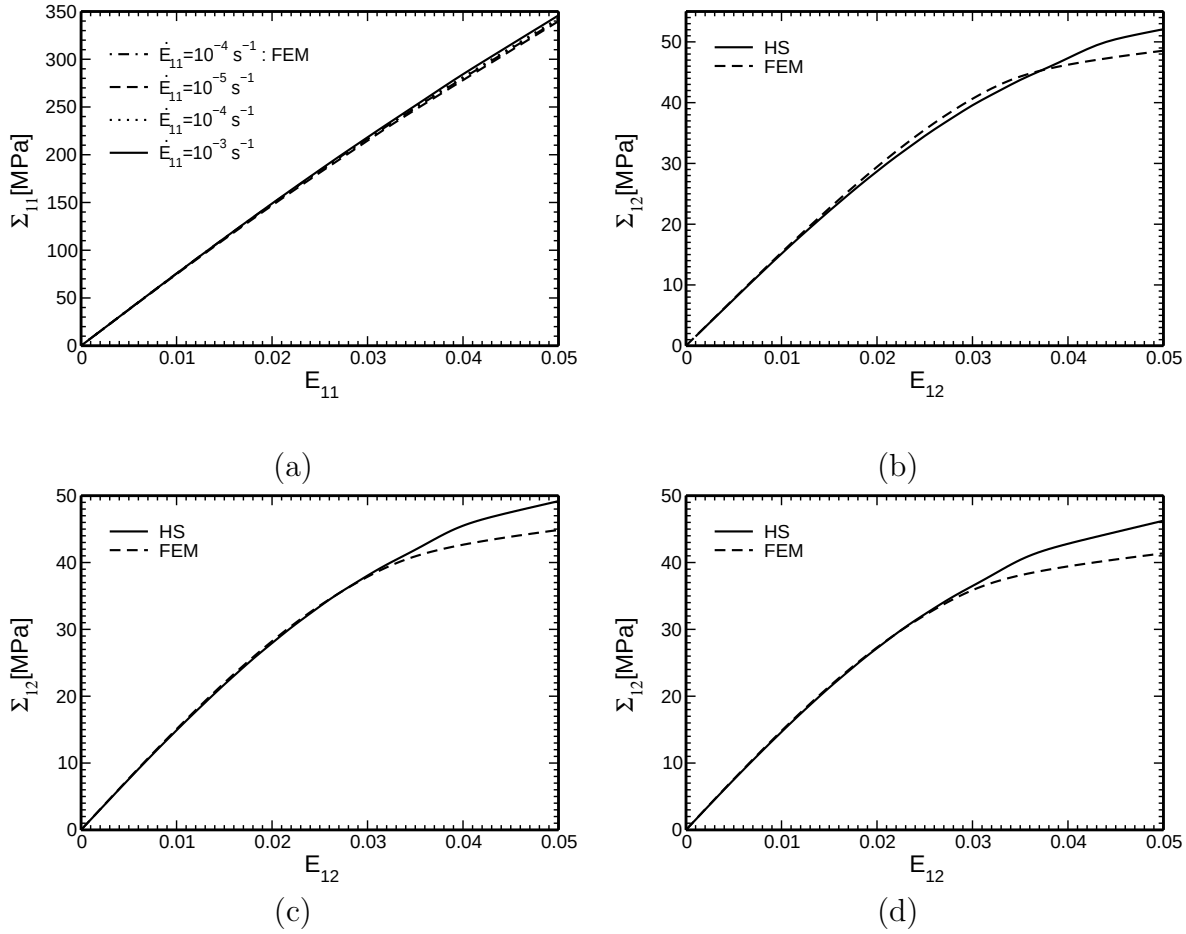

Figure 4.11: Overall response: Hashin-Shtrikman variational principles, (a) $\dot{E}_{11} = 10^{-4}$ s^{-1}, (b) $\dot{E}_{12} = 10^{-3}$ s^{-1}, (c) $\dot{E}_{12} = 10^{-4}$ s^{-1}, (d) $\dot{E}_{12} = 10^{-5}$ s^{-1}.

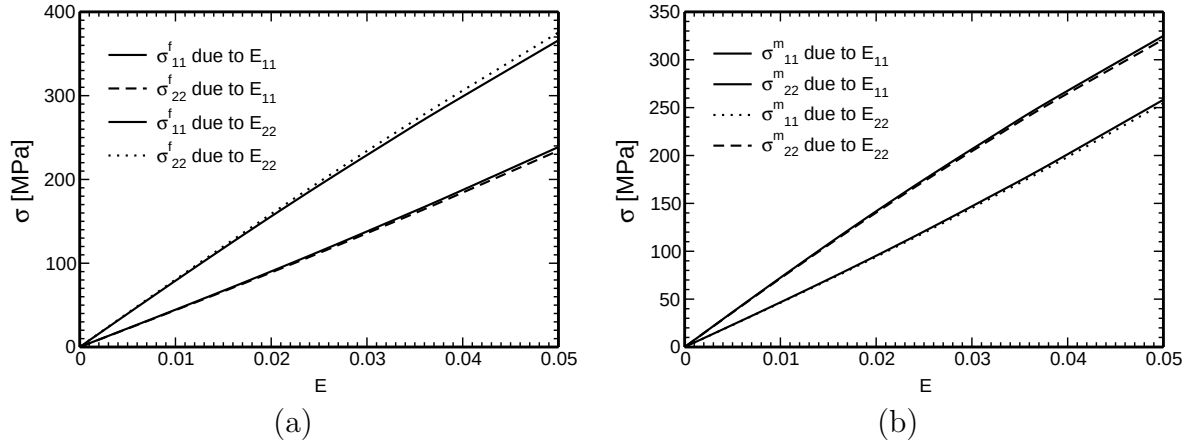

Figure 4.12: Local response – Hashin-Shtrikman principle (a) Fiber phase, (b) Matrix phase

Chapter 5

MESOSCALE MODELING VIA PERIODIC FIELDS

Employing the ideas introduced in Chapter 3 for the modeling of composites with irregular distribution of reinforcements, the present chapter deals with the possibility of application of these principles to the plain weave composite modeling[1]. It is an experimentally confirmed fact that the overall behavior of such composites is strongly influenced by its geometrical details. In this context, the waviness, misalignment and nonuniform cross-sectional aspect ratio of tows in the longitudinal direction [128, 190, 214, 294], resulting from manufacturing process, play the main role in assessing the effective behavior of such composites.

In this regard, the formulation of a reliable and accurate geometrical and numerical model is of paramount importance. Note that idealized models of geometry, which do not account for reinforcement imperfections, are not valid for carefully prepared laboratory samples. It thus appears inevitable to replace such models with a geometrical model, which is still simple and computationally attractive, but yet reflects, at least to some extent, the real geometry of a composite. In achieving this goal, we follow the path set in Chapter 3 and formulate a certain optimal periodic unit cell, which is derived by matching material statistics of a target microstructure, obtained for a two-dimensional section(s) of a three-dimensional microstructure, and the searched PUC[2]. In the present work, the configuration of the optimal PUC cell provided by the three-dimensional geometrical model of Kuhn and Charalambides [135] is implemented. Once the parameters of geometrical model are known, the finite element method approach is employed to acquire the overall mesoscopic response of the selected material system.

The chapter is organized as follows. Section 5.1 introduces the present geometrical model of plain weave composite and determines a set of parameters needed for the description of the Periodic Unit Cell. Then, detailed formulation of the optimization problem used to derive an optimal PUC is presented and the performance of the **RASA** algorithm for solving the present problem is examined. The numerical evaluation of the overall response of woven composites by the finite element method including the effect of local eigenstresses fields is studied in Section 5.2. Finally, the application of the H-S microscale modeling is demonstrated for the construction of failure surfaces of a 6×6 braided composite with prestressed fibers in Section 5.3.

---

[1] Recall that plain weave textile composites consist of mutually orthogonal *warp* and *fill* tows which are interlaced. See, e.g., [40] for more details and systematic classification of other types of textile composites.

[2] approach closely resembles the problem of reconstructing three-dimensional microstructure from two-dimensional data (the key problem in *mathematical morphology*, see [238]). Although techniques for constructing three dimensional microstructural images have been recently introduced [146, 176, 253, and references therein], they are rather complicated and extremely computationally demanding even for elastic materials. Moreover, it was demonstrated in [152, 292] that, at least for some classes of materials, the data obtained from two-dimensional sections determine the three-dimensional microstructural configuration with satisfactory details.

5.1 Construction of the periodic unit cell

As suggested in the introductory part, a realistic model of composite geometry is needed in order to obtain reliable estimates of both the local and overall response of real composites under certain loading conditions. However, such a model, to be statistically representative of the composite, might be quite complex leading to an enormous computational effort. The computational feasibility on the other hand calls for rather simple models usually specified in terms of small periodic unit cells. The present section attempts to reconcile these competing requirements by formulating a small periodic unit cell, which yet incorporates the knowledge of real composite geometry with various types of reinforcement imperfections.

5.1.1 Geometry of the periodic unit cell

In this contribution, only the irregularities represented by disordered path of the fiber tow are considered. In general, such imperfections can be quantified by taking images of tow cross-section along its longitudinal axis [128, 190, 294]. Literature offers a manifold of geometric models for the description of plain weave geometry with varying level of sophistication; namely, the piecewise constant or linear geometry [30, 191, 300], sinusoidal models with either elliptical [228, 281] or lenticular [34, 43, 177, 264] cross-section and CAD/CAM-based modeling [240, 275, 277] have been applied to the description of plain weave composite geometry. In this work, the model of fabric weave composite proposed by Kuhn and Charalambides [135] is used as it is reasonably simple to implement and takes typical features of real composites, reported in [294], into account. The present model is fully determined by parameters a, b, g and h, see Fig. 5.1.

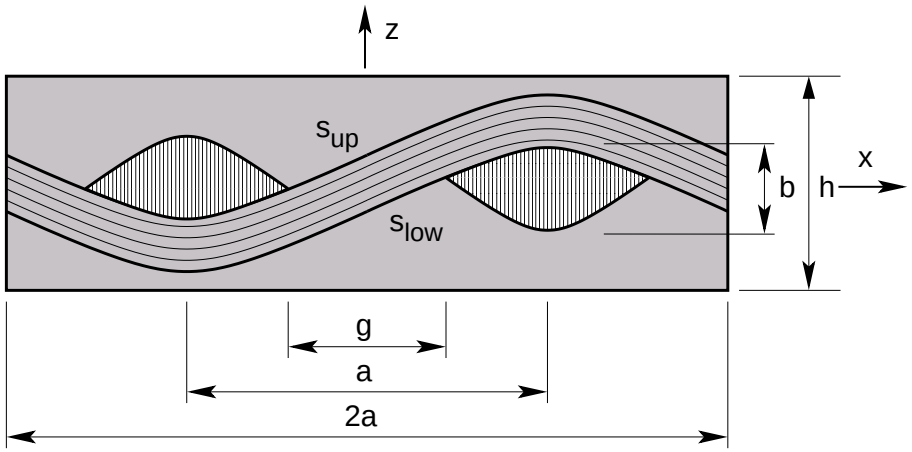

Figure 5.1: Geometrical parameters of a plain weave PUC

The profile of the warp tow centroid p_c is described by the relation

$$p_c(x) = -\sin\left(\frac{\pi x}{a}\right), \tag{5.1}$$

while the profile of the fill tow centroid follows from the previous relation by an appropriate change of x and y coordinates and the sign (see Eq. (5.8)). To maintain compatibility

between warp and fill tows, the internal profiles of tows p_i are provided by

$$p_i(x) = \sin\left(\frac{\pi|x|}{a}\right). \tag{5.2}$$

The external profile p_e is derived from analogous relation with amplitude modified to take into account the non-symmetry of tows and the presence of the gap between tows g,

$$p_e(x) = (1+\beta)\sin\left(\frac{\pi(|x|-g/2)}{a-g}\right) - \beta, \tag{5.3}$$

with the coefficient β defined as

$$\beta = \sin\left(\frac{\pi g}{2a}\right). \tag{5.4}$$

The auxiliary functions R, F_H and F_R are used to linearly interpolate these one dimensional functions in order to obtain representation of lower and upper surfaces of individual tows,

$$F_H(x) = H\left(|x| - \frac{g}{2}\right) - H\left(|x| + \frac{g}{2} - a\right), \tag{5.5}$$

$$R(x) = \begin{cases} x/g + 1/2, & |x| \le g/2, \\ H(x), & g/2 < |x| \le a - g/2, \\ (\operatorname{sgn}(x)a - x)/g + 1/2, & a - g/2 < |x| \le a, \end{cases} \tag{5.6}$$

$$F_R(\eta, x, y) = R(\eta \operatorname{sgn}(y)x), \tag{5.7}$$

where H stands for the Heaviside function, sgn denotes the signum function and parameter $\eta = 1$ is used for the upper surface of a tow while $\eta = -1$ corresponds to the lower surface of a tow. Finally, the warp and fill tow surfaces are determined by

$$s_{\text{warp}}(\eta, x, y) = s_{\text{tow}}(\eta, x, y), \qquad s_{\text{fill}}(\eta, x, y) = -s_{\text{tow}}(-\eta, y, x), \tag{5.8}$$

where the general tow surface function $s_{\text{tow}}(\eta, x, y)$ for positions $|x| \le a$ and $|y| \le a$ is defined as

$$s_{\text{tow}}(\eta, x, y) = \frac{b}{2}F_H(y)\left(\operatorname{sgn}(y)p_c(x) + \eta F_R(\eta, x, y)p_i(y) + \eta F_R(-\eta, x, y)p_e(y)\right). \tag{5.9}$$

Finally, the orientation of fibers within the tows is assumed to be parallel to the centroid axes of the tows; the corresponding angles of rotation are given by

$$\theta_y^{\text{warp}}(x, y) = \arctan\left(-\frac{\pi b}{2a}\operatorname{sgn}(y)\cos(\frac{\pi x}{a})\right), \tag{5.10}$$

$$\theta_x^{\text{fill}}(x, y) = \arctan\left(-\frac{\pi b}{2a}\operatorname{sgn}(x)\cos(\frac{\pi y}{a})\right). \tag{5.11}$$

For the transverse cross-sectional plane located in the middle of the weave, the fill and

warp bundle surface functions s_{fill} and s_{warp}, reduce to, see Fig. 5.1,

$$s_{\text{low}}(x) = \begin{cases} \frac{b}{2}\left(\sin\left(\frac{\pi x}{a}\right) - \frac{x(1-\delta)}{g} - \frac{1}{2}(1+\delta)\right) & 0 \le x < \frac{g}{2} \\ -\frac{b}{2}\left(1 + (1+\beta)\sin\left(\frac{\pi(2x-g)}{2(a-g)} - \beta\right)\right) & \frac{g}{2} \le x \le \frac{a}{2} \end{cases}, \tag{5.12}$$

$$s_{\text{up}}(x) = \begin{cases} \frac{b}{2}\left(\sin\left(\frac{\pi x}{a}\right) - \frac{x(1-\delta)}{g} + \frac{1}{2}(1+\delta)\right) & 0 \le x < \frac{g}{2} \\ \frac{b}{2}\left(\sin\left(\frac{\pi x}{a}\right) + \delta\right) & \frac{g}{2} \le x \le \frac{a}{2} \end{cases}, \tag{5.13}$$

$\delta = (1+\beta)cos(\beta)$. Values of function s_{low} and s_{up} for $x > a/2$ and $x < 0$ follow from obvious symmetry of the PUC.

5.1.2 Objective function and problem definition

Having chosen the model for the description of the geometry of a PUC, one needs to define a certain objective function, which quantifies the difference between the original microstructure and the idealized periodic unit cell. Following the general procedure discussed in Chapter 2, the fundamental *bundle characteristic function* $\chi_f(x,z)$[3] is introduced first. Using Eqs. (5.12)–(5.13), the function $\chi_f(x,z)$ is simply provided by the relation

$$\chi_f(x,z) = \begin{cases} 1, & \text{if } s_{\text{low}}(x) \le z \le s_{\text{up}}(x) \\ 0, & \text{otherwise} \end{cases}, \tag{5.14}$$

i.e., $\chi_f(x,z)$ is equal to one if a point (x,z) is located in the domain occupied by the bundle phase Y_f and zero otherwise.

Similarly to the microscale analysis, the characteristic function χ_f can be employed to discretize the PUC cross section into the form of a $W \times H$ bitmap. Then, assuming the periodicity of the microstructure, the two point probability function S_{rs} can be efficiently computed by the discrete Fourier transform, recall Eq. (2.33),

$$S_{rs}(m,n) = \frac{1}{WH}\text{IDFT}\{\text{DFT}\{\chi_r(m,n)\}\overline{\text{DFT}\{\chi_s(m,n)\}}\}, \tag{5.15}$$

where the phases r and s are considered as either bundle phase f or the matrix phase m, respectively. The matrix lineal path function L_m for a given digitized periodic unit cell can be determined by the sampling template method introduced in Section 2.3.2.

To determine optimal parameters of the periodic unit cell, the parameters a, b, g and h are found by minimizing certain objective functions. Similarly to Chapter 3, objective functions incorporating the the two-point matrix probability function S_{mm}, matrix lineal

[3] The index f in the bundle characteristic function is used to maintain the consistency with notation used in Chapter 2 and to distinguish the index from the bundle height b, see Fig. 5.1.

path function L_m or their combination are considered,

$$F_S(\mathbf{x}) = \sum_{i=-i_{\max}}^{i_{\max}} \sum_{j=-j_{\max}}^{j_{\max}} \left(\overline{S}_{mm}(i,j) - S_{mm}(i,j)\right)^2, \tag{5.16}$$

$$F_L(\mathbf{x}) = \sum_{i=0}^{N_d-1} \sum_{j=0}^{N_\ell(i)-1} \left(\overline{L}_m(i,j) - L_m(i,j)\right)^2, \tag{5.17}$$

$$F_{S+L}(\mathbf{x}) = F_S(a,b,h,g) + F_L(a,b,h,g) \tag{5.18}$$

where, similarly to Section 3.1.1, $\mathbf{x} = \{a,b,h,g\}^\mathsf{T}$ is the vector of unknown dimensions of the PUC, $\overline{S}_{mm}$ and $\overline{L}_m$ are the values of L_m and S_{mm} functions corresponding to the target microstructure, parameters $i_{\max}$ and $j_{\max}$ define the range of points, in which S_{mm} functions are matched, N_d denotes the number of rays of a sampling template and $N_\ell(i)$ is the number of pixels of the i-th sampling ray, respectively. Then, the following optimization problem is solved to determine the optimal parameters of a periodic unit cell.

Optimal plain weave periodic unit cell. For a selected statistical descriptor $D \in \{S, L, S+L\}$ find the parameters of the PUC $\mathbf{x}$ such that

$$\mathbf{x} \in \operatorname*{Argmin}_{\mathbf{x}\in\mathcal{B}} F_D(\mathbf{x}), \tag{P3}$$

where $\mathcal{B}$ denotes a set of admissible unit cell parameters,

$$\mathcal{B} = \left\{\mathbf{x} \in \mathbb{R}^4 : L_i \le x_i \le U_i, i = 1,\ldots,N\right\}, \tag{5.19}$$

where L_i and U_i denote the lower and upper bounds on unit cell parameters, selected, e.g., on the basis of image analysis.

The numerical experiments reported in [299] allow us to anticipate that the **RASA** algorithm, described in Section 2.5, is fully capable of solving the optimization problem (P3). The next section investigates this fact for selected objective functions.

5.1.3 Test examples

In this section, the performance and robustness of the selected global optimization method is tested for a set of carefully chosen optimization problems. First, the ability of the algorithm to determine the parameters of a periodic unit cell with known parameters is investigated. Then, optimal unit cells are generated for artificial microstructures exhibiting typical imperfections observed in micrographs of real composites.

Identification problem

To test the sensitivity of the optimization process, three different bitmaps with resolution 128×16, 256×32 and 512×64 pixels were constructed for a unit cell determined by parameters $a = 10, h = 3, g = b = 1$. For each bitmap the optimization algorithm was run 20 times to minimize the influence of various random circumstances. The computation

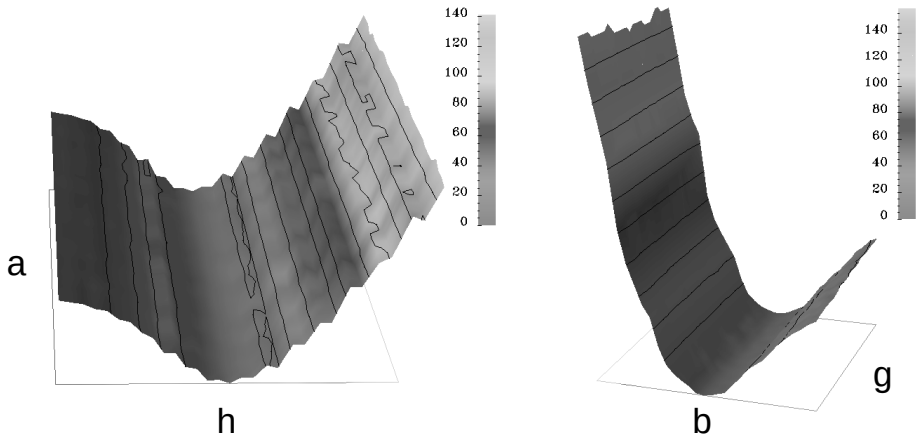

(a) (b)

Figure 5.2: S_{mm}-based objective function for bitmap resolution 128×16 pixels, (a) $a \times h$, (b) $b \times g$

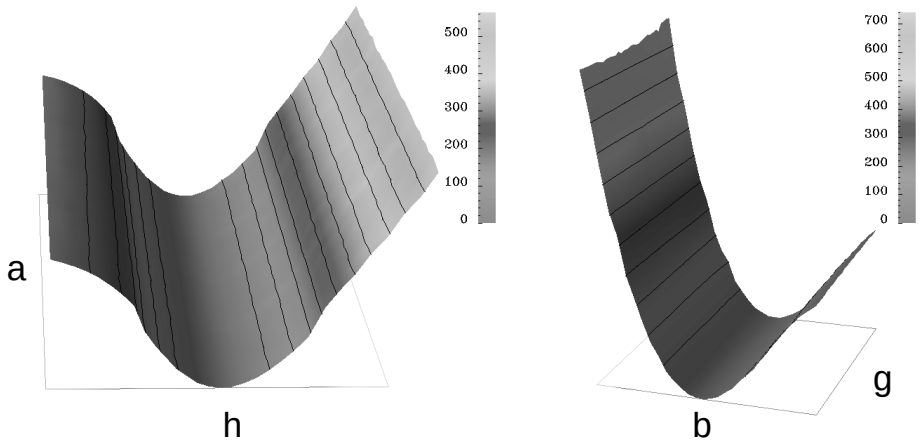

(a) (b)

Figure 5.3: S_{mm}-based objective function for bitmap resolution 256×32 pixels, (a) $a \times h$, (b) $b \times g$

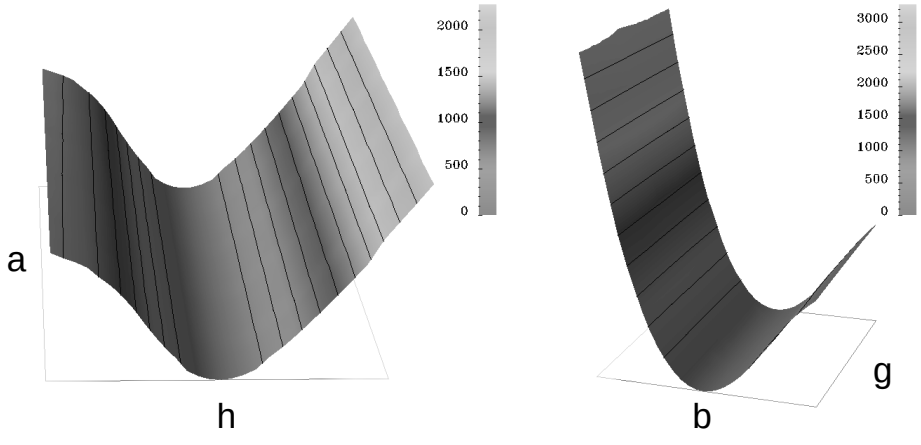

(a) (b)

Figure 5.4: S_{mm}-based objective function for bitmap resolution 512×64 pixels, (a) $a \times h$, (b) $b \times g$

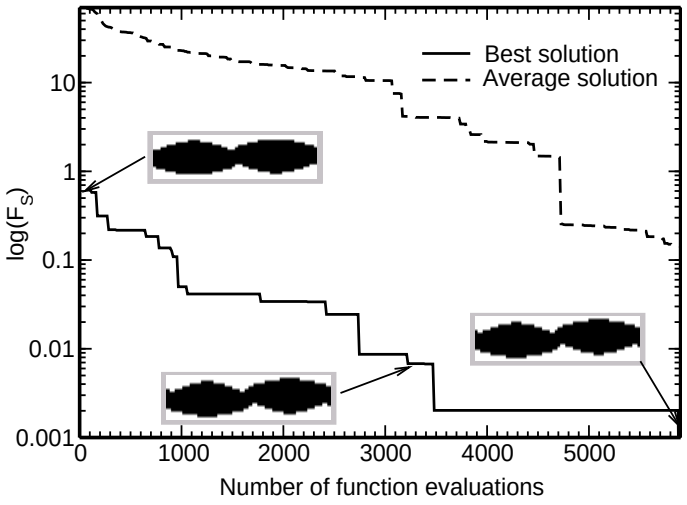

(a)

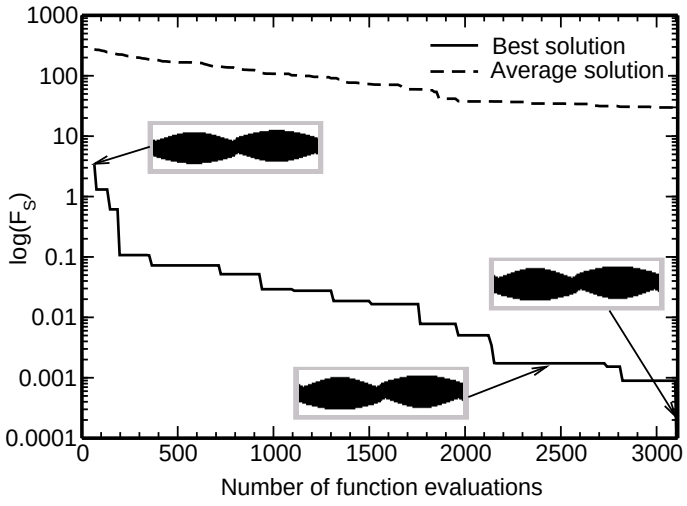

(b)

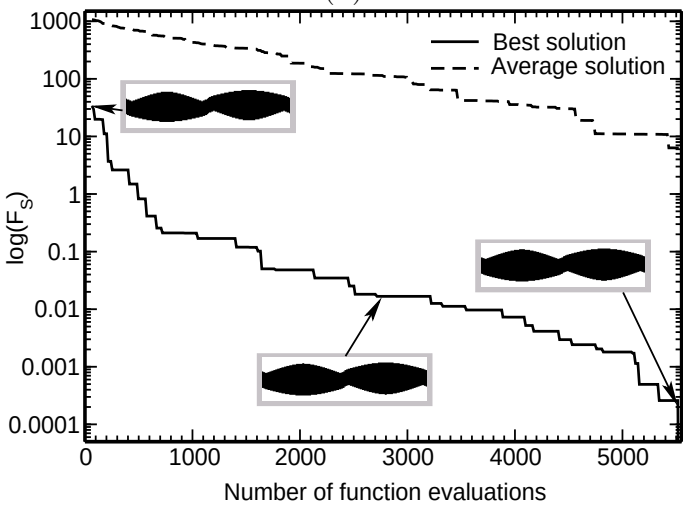

(c)

Figure 5.5: Examples of optimization progress for S_{mm}-based objective function, (a) bitmap resolution 128×16 pixels, (b) bitmap resolution 256×32 pixels, (c) bitmap resolution 512×64 pixels

was terminated if the algorithm returned a value smaller than 10^{-6} or if the number of objective function evaluations exceeded 50,000. The parameters of the **RASA** method were selected according to the Table 3.2 with bounds set to 50% and 200% of the target values. The S_{mm}-based objective function was considered first. The matching range $i_{\min}$–$i_{\max}$ and $j_{\min}$–$j_{\max}$, introduced in Eq. (5.16), was set to comply with the dimension of a unit cell. For each run, minimum and maximum values of searched geometric parameters were recorded. The results of this experiment are listed in Tables 5.1 and 5.2. In addition, Table 5.1 provides information on the average number of function calls and the average time needed to complete the optimization run for individual bitmaps[4]. As expected, the optimization process converged for every run, which again confirms the robustness of the **RASA** algorithm. A typical convergence progress of the optimization method, showing an average and the best individual in the population, is displayed, together with the PUC evolution, in Figs. 5.5a–c.

Bitmap resolution	***Success rate***	***Number of evaluations*** Min	Avg	Max	***Total time*** [s]
128×16	20 / 20	1,106	2,826	6,321	169
256×32	20 / 20	2,336	3,542	5,320	1,016
512×64	20 / 20	2,716	4,581	12,457	6,648

Table 5.1: S_{mm}-based identification: Number of function evaluations

Resolution	$a_{\min}$	$a_{\max}$	$h_{\min}$	$h_{\max}$
128×16	9.8442	10.1010	2.9961	3.0119
256×32	9.9253	10.0217	2.9959	3.0020
512×64	9.9726	10.0259	2.9986	3.0009
Resolution	$b_{\min}$	$b_{\max}$	$g_{\min}$	$g_{\max}$
128×16	0.9924	1.0065	0.9688	1.1010
256×32	0.9968	1.0002	0.9831	1.0141
512×64	0.9988	1.0009	0.9917	1.0157

Table 5.2: Geometrical parameters of the PUC : S_{mm}-based optimization

In general, recall Table 5.1, the number of required iterations as well as the time needed for convergence depends on the bitmap resolution. As expected, with higher resolution the computation process becomes more expensive as the range of an objective function increases by an order of magnitude. Nevertheless, all considered bitmap resolutions, at least for the present problem, provide comparable results in terms of accuracy of the searched geometric characteristics.

Finally, to further demonstrate the problem complexity, the objective functions for different bitmap resolutions are shown in Figs. 5.2–5.4. It is clearly visible that the

[4] All tests were performed on a computer with Intel Celeron 700 MHz processor with 256MB RAM under the Linux operating system. The C++ code was compiled by **gcc 2.96** GNU complier with `-O3` optimization switch. The library **FFTW 2.1.3** [60] was called to compute the discrete Fourier Transform.

objective function for the lowest bitmap resolution is rather noisy; this effect is, however, easily resolved by increasing the bitmap resolution to 256×32 pixels. Another difficulty comes from the fact that, similarly to Chapter 3, the objective function is piecewise constant due to a finite resolution of a bitmap. Although this fact is not apparent from Figs 5.2–5.4, plotted form a data interpolated on a regular grid, it can be easily deduced from results shown in Table 5.2. Finally, landscapes of objective functions reveal that the objective functions are substantially more sensitive to parameters h and b than to a and g. This corresponds well with higher accuracy of identified parameters h and b, observed in Table 5.2.

The similar numerical experiments were repeated for the F_L and F_{S+L} objective functions for the bitmap resolution 256×32 pixels. Note that sampling templates with parameters $T_W = T_H = H/2$ and $\Delta_W = \Delta_H = H/8$ were used for the determination of the lineal path function L_{mm}. The statistics of the obtained numerical parameters together with the number of function calls and overall computational time are stored in Tables 5.3 and 5.4. Note that both optimization problems, being based on the L_m function, are about ten times more time consuming. This again highlights the remarkable efficiency of the FFTW library; note, however, that the situation is much better than for the microstructural analysis, where this ratio was even higher, see Table 3.3. Moreover, both objective functions result in geometrical parameters determined with a precision comparable to the S_{mm}-based optimization. This suggests that the scatter of the geometrical parameters is caused solely by the discretization of the microstructure not by the objective function or the selected optimization method.

Descriptor	***Success rate***	***Number of evaluations***			***Total time***
		Min	Avg	Max	[s]
L_m	20 / 20	3,059	5,842	9,295	12,592
$L_m + S_{mm}$	20 / 20	1,196	4,909	30,699	11,804

Table 5.3: L_m and $L_m + S_{mm}$-based identification: Number of function evaluations

Descriptor	$a_{\min}$	$a_{\max}$	$h_{\min}$	$h_{\max}$
L_m	9.9227	10.0407	2.9967	3.0020
$L_m + S_{mm}$	9.9243	10.0196	2.9977	3.0023
Descriptor	$b_{\min}$	$b_{\max}$	$g_{\min}$	$g_{\max}$
L_m	0.9973	1.0005	0.9855	1.0143
$L_m + S_{mm}$	0.9969	1.0009	0.9864	1.0139

Table 5.4: Geometrical parameters of the PUC : L_m-based optimization, combined optimization

Finally, for the sake of completeness, examples of typical objective runs together with the plot of objective functions are shown in Figs. 5.6–5.7.

To summarize this study, the presented results support the choice of the selected optimization method; furthermore, the resolution of the bitmap 256×32 is sufficient to obtain the search geometrical parameters with a reasonable precision.

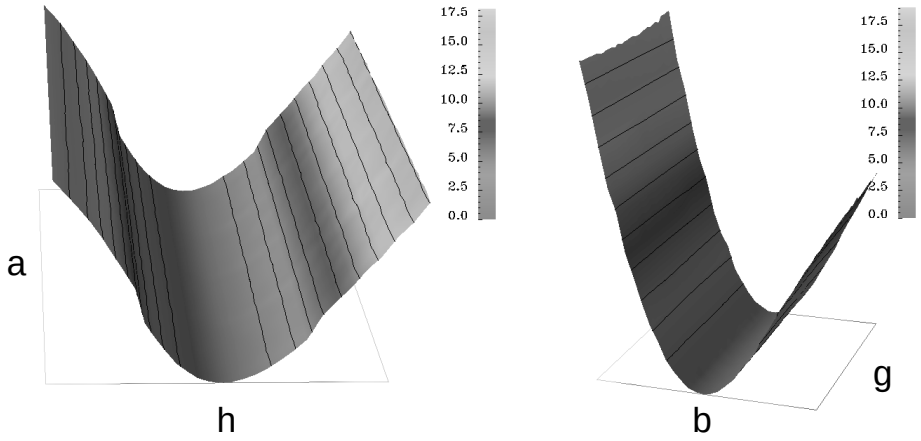

(a) (b)

Figure 5.6: L_m-based objective function for bitmap resolution 256×32 pixels, (a) $a \times h$, (b) $b \times g$

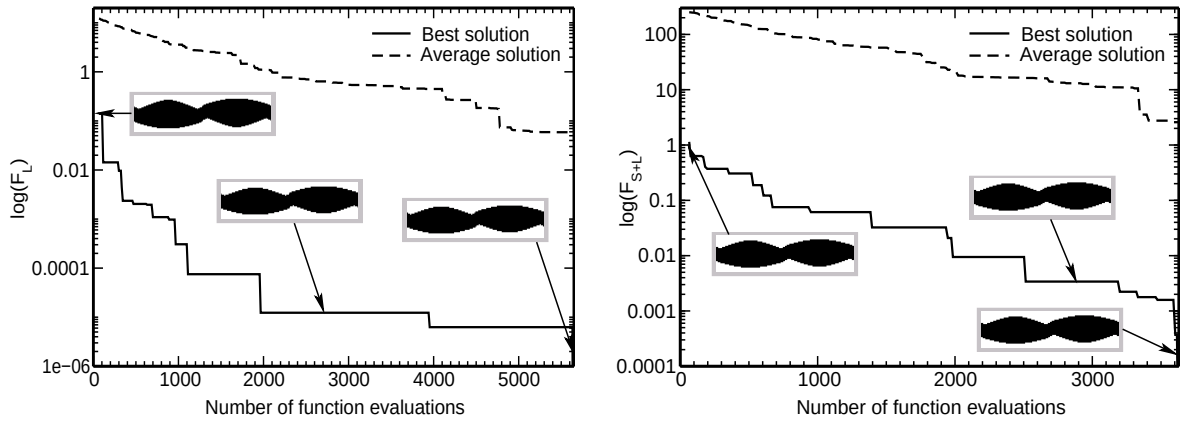

(a) (b)

Figure 5.7: Examples of optimization progress for bitmap resolution 256×32 pixels, (a) L_m-based objective function, (b) $(S_{mm} + L_m)$-based objective function

5.1.4 Mesostructures with typical tow misalignments

As a representative of digitized images of real-world multilayered plain weave composites a set of three artificial bitmaps exhibiting various in-situ observed imperfections, reported in [25, 128, 214, 294], was generated. In particular, the "samples" formed by two unit cells with different layer and bundle heights (see Fig. 5.8b), two identical unit cells shifted by a (see Fig. 5.8c) and by $a/2$ (see Fig. 5.8d) are considered in this work[5]. Note that in the following text, the microstructure displayed in Fig. 5.8b is referred to as PUC #1, while the unit cells displayed in Figs. 5.8c–d are denoted as PUC #2 and PUC #3, respectively. Based on the results of the sensitivity analysis in the previous section, the PUC #1 was

[5] The parameters of the bitmap 5.8b are $a = 10, h = 3, b = g = 1$ for the lower layer and $a = 10, h = 4.5, b = 1.5, g = 1$ for the upper one; the remaining bitmaps correspond to a unit cell with $a = 10, h = 3, b = g = 1$.

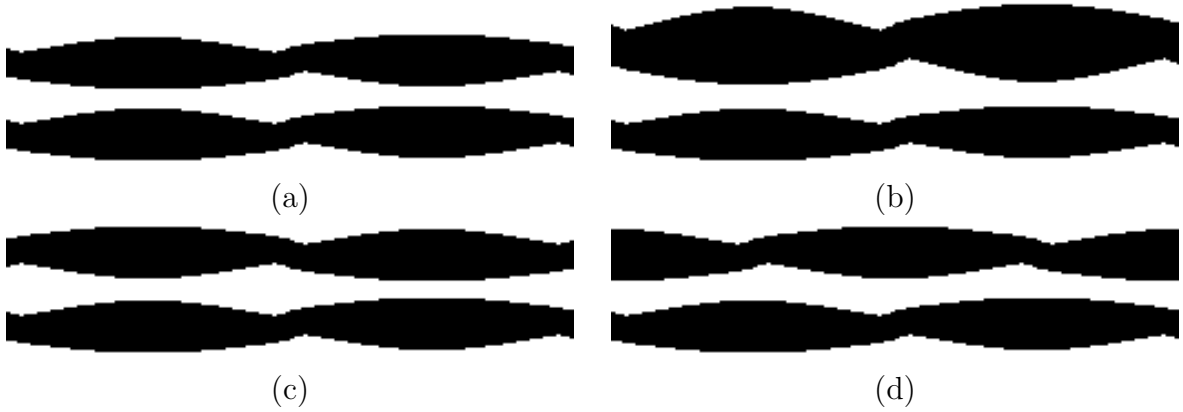

Figure 5.8: Artificial bitmaps of mesoscale geometry with typical tow misalignments, (a) ideal stacking, (b) different layer heights, (c) layers shifted by a, (d) layers shifted by $a/2$

discretized as a bitmap with the dimensions 256×92 pixels and the PUC #2–3 were represented by bitmaps with resolution 256×64 pixels.

For each artificial mesostructure bitmap, the statistically optimal periodic unit cell based on S_{mm}, L_m and $S_{mm} + L_m$ descriptors was found[6]. The target value for each optimization problem was set to 10^{-6} and the maximum number of function evaluations was restricted to 25,000. Each optimization problem was executed ten times to verify that the global optimum was reached and to determine the scatter of geometrical parameters. The resulting optimal values obtained for individual bitmaps are stored in Table 5.5. Note that the identified parameters, similarly to the results of Section 3.1.3, differ quite substantially for individual statistical descriptors; the precision of the identified parameters, however, appears to be slightly higher for combined reconstruction problem.

5.2 Numerical evaluation of the overall response

Geometrical parameters derived in the previous section can be introduced into the unit cell model described in Section 5.1.1 to generate an equivalent periodic unit cell that represents a real composite. Such a unit cell can be then used within the framework of the finite element method-based homogenization to arrive at the desired approximation of the effective material behavior. Although a variety of works devoted to this topic can be found in the literature [30, 34, 43, 84, 194, 195, 230, 277, 278, 288, 290, to name a few], the analysis of the mesoscopic periodic unit cell subjected to a distribution of eigenstresses together with the stress-controlled homogenization has not been, to author's best knowledge, addressed yet.

5.2.1 Problem setting

To introduce the subject, consider a mesoscale PUC with the local coordinate systems defined such that the local x_1 axis x_1^ℓ is aligned with the fiber direction. Hereafter,

[6] The sampling templates with parameters identical to those considered in the previous section were used for the computation of the lineal path function L_m.

Periodic Unit Cell #1				
Descriptor	a	h	b	g
S_{mm}	10.235 ± 0.023	3.792 ± 0.002	1.250 ± 0.001	1.726 ± 0.012
L_m	10.316 ± 0.018	3.785 ± 0.003	1.252 ± 0.001	1.766 ± 0.016
$S_{mm} + L_m$	10.098 ± 0.015	3.754 ± 0.000	1.249 ± 0.000	1.014 ± 0.005
Periodic Unit Cell #2				
Descriptor	a	h	b	g
S_{mm}	9.931 ± 0.017	2.964 ± 0.001	0.995 ± 0.001	0.990 ± 0.005
L_m	10.863 ± 0.023	2.956 ± 0.002	0.996 ± 0.001	1.013 ± 0.008
$S_{mm} + L_m$	9.975 ± 0.004	2.964 ± 0.001	0.994 ± 0.001	0.988 ± 0.005
Periodic Unit Cell #3				
Descriptor	a	h	b	g
S_{mm}	11.171 ± 0.032	3.046 ± 0.001	0.996 ± 0.001	0.670 ± 0.012
L_m	8.351 ± 0.033	2.887 ± 0.003	0.964 ± 0.001	0.247 ± 0.012
$S_{mm} + L_m$	10.841 ± 0.016	3.045 ± 0.001	0.998 ± 0.001	0.715 ± 0.007

Table 5.5: Geometrical parameters of mesoscale PUCs

following the introductory Chapter 1, this level of sophistication will be referred to as *mesoscale* to make distinction from the evaluation of effective properties of individual tows found from the analysis on *microscale*, considered in Chapter 3. Further suppose that the PUC is subjected to a prescribed overall stress $\boldsymbol{\Sigma}_{\text{meso}}$. Following the discussion in Section 3.2, the local displacement field $\mathbf{u}_{\text{meso}}(\mathbf{x})$ on mesoscale admits the following decomposition

$$\mathbf{u}_{\text{meso}}(\mathbf{x}) = \boldsymbol{E}_{\text{meso}} \cdot \mathbf{x} + \mathbf{u}^*_{\text{meso}}(\mathbf{x}), \tag{5.20}$$

where $\mathbf{u}^*_{\text{meso}}(\mathbf{x})$ represents a periodic fluctuation of the local displacement field due to the presence of heterogeneities and $\boldsymbol{E}_{\text{meso}}$ is the overall strain tensor. The local strain tensor then assumes the form

$$\boldsymbol{\varepsilon}_{\text{meso}}(\mathbf{x}) \;\; = \;\; \boldsymbol{E}_{\text{meso}} + \boldsymbol{\varepsilon}^*_{\text{meso}}(\mathbf{x}), \tag{5.21}$$

where the fluctuating part $\boldsymbol{\varepsilon}^*_{\text{meso}}(\mathbf{x})$ vanishes under volume averaging. The goal now becomes the evaluation of local fields within the mesoscopic unit cell and then their averaging to arrive at the searched macroscopic response. To proceed, we first write the principle of virtual work (Hill's lemma) in the form

$$\begin{aligned} \delta\boldsymbol{E}_{\text{meso}} : \boldsymbol{\Sigma}_{\text{meso}} &= \langle \delta\boldsymbol{\varepsilon}_{\text{meso}}(\mathbf{x}) : \boldsymbol{\sigma}_{\text{meso}}(\mathbf{x}) \rangle = \left\langle \delta\boldsymbol{\varepsilon}^{\ell}_{\text{meso}}(\mathbf{x}) : \boldsymbol{\sigma}^{\ell}_{\text{meso}}(\mathbf{x}) \right\rangle \\ &= \left\langle \left(\delta\boldsymbol{E}^{\ell}_{\text{meso}} + \delta\boldsymbol{\varepsilon}^{\ell}_{\text{meso}}(\mathbf{x}) \right) \, : \boldsymbol{\sigma}^{\ell}_{\text{meso}}(\mathbf{x}) \right\rangle, \end{aligned} \tag{5.22}$$

where $\langle \cdot \rangle$ now denotes averaging with respect to the mesoscopic PUC Y_{meso}. The stress field written in the local coordinate system then reads

$$\boldsymbol{\sigma}^{\ell}_{\text{meso}}(\mathbf{x}) = \mathbf{L}^{\ell}_{\text{meso}}(\mathbf{x}) : \, \left(\boldsymbol{E}^{\ell}_{\text{meso}} + \boldsymbol{\varepsilon}^{*\ell}_{\text{meso}}(\mathbf{x}) \right) + \boldsymbol{\lambda}^{\ell}_{\text{meso}}(\mathbf{x}). \tag{5.23}$$

Relating the strain tensors in local and global coordinate systems by well-known relations $\boldsymbol{E}^{\ell}_{\text{meso}} = \mathbf{T}_{\varepsilon} : \boldsymbol{E}_{\text{meso}}$, $\boldsymbol{\varepsilon}^{*\ell}_{\text{meso}} = \mathbf{T}_{\varepsilon} : \boldsymbol{\varepsilon}^*_{\text{meso}}$, see Section A.1.1, and inserting Eq. (5.23) into

Eq. (5.22) yields the stationarity conditions of the given problem, i.e., the following system

$$\begin{aligned} \delta\boldsymbol{E}_{\text{meso}} : \boldsymbol{\Sigma}_{\text{meso}} &= \delta\boldsymbol{E}_{\text{meso}} : \big\langle \mathbf{T}_{\varepsilon}(\mathbf{x}) : \big[\mathbf{L}^{\ell}_{\text{meso}}(\mathbf{x}) : \mathbf{T}_{\varepsilon}(\mathbf{x}) : (\boldsymbol{E}_{\text{meso}} + \boldsymbol{\varepsilon}^{*}_{\text{meso}}(\mathbf{x})) \\ &+ \boldsymbol{\lambda}^{\ell}_{\text{meso}}(\mathbf{x})\big]\big\rangle , \qquad (5.24) \\ 0 &= \big\langle \delta\boldsymbol{\varepsilon}^{*}_{\text{meso}}(\mathbf{x}) : \mathbf{T}_{\varepsilon}(\mathbf{x}) : \big[\mathbf{L}^{\ell}_{\text{meso}}(\mathbf{x}) : \mathbf{T}_{\varepsilon}(\mathbf{x}) : (\boldsymbol{E}_{\text{meso}} + \boldsymbol{\varepsilon}^{*}_{\text{meso}}(\mathbf{x})) \\ &+ \boldsymbol{\lambda}^{\ell}_{\text{meso}}(\mathbf{x})\big]\big\rangle , \qquad (5.25) \end{aligned}$$

has to be satisfied for all kinematically admissible variations $\delta\boldsymbol{E}_{\text{meso}}$ and $\delta\boldsymbol{\varepsilon}^{*}_{\text{meso}}$.

5.2.2 Discretization

To obtain an approximate solution of the above system of equations, the finite element method discretization is again employed. We start from decomposing the mesoscale periodic unit cell Y_{meso} into N_e disjoint elements Y_e with the discretization respecting the interfaces between individual tows and the matrix phase. Employing the engineering notation introduced in Appendix A, the approximation of the fluctuating part of the displacement field $\mathbf{u}^{*}_{\text{meso}}$, written in the *global* coordinate system, yields

$$\{\mathsf{u}^{*}_{\text{meso}}(\mathbf{x})\} = [\mathsf{N}(\mathbf{x})]\,\{\mathsf{r}_{\text{meso}}\}, \qquad (5.26)$$

where $[\mathsf{N}]$ represents, as usual, the matrix of shape functions for a given partition of the unit cell[7] and $\{\mathsf{r}_{\text{meso}}\}$ is the vector of unknown degrees of freedom. The corresponding approximation of the strain field is then provided by

$$\{\varepsilon_{\text{meso}}(\mathbf{x})\} = \{\mathsf{E}_{\text{meso}}\} + [\mathsf{B}(\mathbf{x})]\,\{\mathsf{r}_{\text{meso}}\}, \qquad (5.27)$$

where $[\mathsf{B}]$ is the strain-displacement matrix. Introducing Eq. (5.27) into Eq. (5.22) gives, for any kinematically admissible strains $\{\delta\varepsilon^{*}_{\text{meso}}\} = [\mathsf{B}]\,\{\delta\mathsf{r}_{\text{meso}}\}$ and $\{\delta\mathsf{E}_{\text{meso}}\}$, the associated system of linear equations in the form

$$\begin{bmatrix} \mathsf{K}_{11} & \mathsf{K}_{12} \\ \mathsf{K}_{21} & \mathsf{K}_{22} \end{bmatrix} \begin{Bmatrix} \mathsf{E}_{\text{meso}} \\ \mathsf{r}_{\text{meso}} \end{Bmatrix} = \begin{Bmatrix} \Sigma_{\text{meso}} + \mathsf{f}_1 \\ \mathsf{f}_2 \end{Bmatrix}. \qquad (5.28)$$

The individual stiffness matrices and vectors of generalized nodal forces are obtained by the assembly of contributions for individual elements,

$$\begin{aligned} [\mathsf{K}_{11}] &= \mathop{\mathsf{A}}_{e=1}^{N_e} [\mathsf{K}_{11,\mathsf{e}}], \quad \text{where} \quad [\mathsf{K}_{11,\mathsf{e}}] = \frac{1}{|Y_{\text{meso}}|}\int_{Y_e} [\mathsf{T}_{\varepsilon,\mathsf{e}}]^{\mathsf{T}} \left[\mathsf{L}^{\ell}_{\text{meso},\mathsf{e}}\right] \mathrm{d}Y_e, \qquad (5.29) \\ [\mathsf{K}_{21}]^{\mathsf{T}} = [\mathsf{K}_{12}] &= \mathop{\mathsf{A}}_{e=1}^{N_e} [\mathsf{K}_{12,\mathsf{e}}], \quad \text{where} \quad [\mathsf{K}_{12,\mathsf{e}}] = \frac{1}{|Y_{\text{meso}}|}\int_{Y_e} [\mathsf{T}_{\varepsilon,\mathsf{e}}]^{\mathsf{T}} \left[\mathsf{L}^{\ell}_{\text{meso},\mathsf{e}}\right] \left[\widehat{\mathsf{B}}_{\mathsf{e}}\right] \mathrm{d}Y_e, \\ [\mathsf{K}_{22}] &= \mathop{\mathsf{A}}_{e=1}^{N_e} [\mathsf{K}_{22,\mathsf{e}}], \quad \text{where} \quad [\mathsf{K}_{22,\mathsf{e}}] = \frac{1}{|Y_{\text{meso}}|}\int_{Y_e} \left[\widehat{\mathsf{B}}_{\mathsf{e}}\right]^{\mathsf{T}} \left[\mathsf{L}^{\ell}_{\text{meso},\mathsf{e}}\right] \left[\widehat{\mathsf{B}}_{\mathsf{e}}\right] \mathrm{d}Y_e, \\ \{\mathsf{f}_1\} &= \mathop{\mathsf{A}}_{e=1}^{N_e} \{\mathsf{f}_{1,\mathsf{e}}\}, \quad \text{where} \quad \{\mathsf{f}_{1,\mathsf{e}}\} = \frac{-1}{|Y_{\text{meso}}|}\int_{Y_e} [\mathsf{T}_{\varepsilon,\mathsf{e}}]^{\mathsf{T}} \{\lambda^{\ell}_{\text{meso},\mathsf{e}}\}\, \mathrm{d}Y_e, \\ \{\mathsf{f}_2\} &= \mathop{\mathsf{A}}_{e=1}^{N_e} \{\mathsf{f}_{2,\mathsf{e}}\}, \quad \text{where} \quad \{\mathsf{f}_{2,\mathsf{e}}\} = \frac{-1}{|Y_{\text{meso}}|}\int_{Y_e} \left[\widehat{\mathsf{B}}_{\mathsf{e}}\right]^{\mathsf{T}} \{\lambda^{\ell}_{\text{meso},\mathsf{e}}\}\, \mathrm{d}Y_e, \end{aligned}$$

[7] Linear tetrahedral elements are used in this study; this choice of elements is consistent with the piecewise linear approximations of the displacement field.

where the "rotated" displacement-strain matrix $\left[\widehat{\mathsf{B}}_{\mathsf{e}}\right]$ is defined by the relation $\left[\widehat{\mathsf{B}}_{\mathsf{e}}\right] = [\mathsf{T}_{\varepsilon,\mathsf{e}}]\,[\mathsf{B}_{\mathsf{e}}]$. The local-global transformation is parametrized by three Euler angles ψ, ϑ and φ, see Section A.1.1, based on relations (5.10)[8]. Finally, observe that for the case of strain controlled homogenization, the system of equations (5.29)–(5.30) reduces to

$$[\mathsf{K}_{22}]\,\{\mathsf{r}_{\mathrm{meso}}\} = -\,[\mathsf{K}_{21}]\,\{\mathsf{E}_{\mathrm{meso}}\} + \{\mathsf{f}_2\}. \tag{5.30}$$

5.2.3 Mesh generation

An important step of the mesoscale modeling is preparation of a 3D mesh of warp and fill bundles and matrix phase complying with the requirements of mesh periodicity. This task is far from being trivial; see, e.g., recent works [118, 119, 277] addressing this issue[9]. In this work, the ideas of *matched mesh generation*, proposed in [277], are implemented to the automated mesh generator program **T3D** [219][10].

In the past, a wide class of algorithms for generation of triangular and tetrahedral meshes has been established, among which three basic strategies–the tree based approach, the Advancing Front Technique and the Delaunay triangulation–have proven particularly successful (see, e.g., [220] for an exhaustive review of various methods).

The present code employs the Advancing Front technique to generate high quality unstructured 3D meshes. First, the geometry of the PUC is introduced: the model is described by a boundary representation consisting of *vertices*, *curves*, *surfaces*, *patches* and *regions*. Topologically, each region is formed by a set of non self-intersecting boundary surfaces and patches, each of which is bounded by a set of curves. Each curve is determined by two end vertices and the control polygon, if appropriate. Note that each surface is assumed to be surrounded by exactly four boundary curves. The rational Bezier entities are used to describe curves and surfaces, while a patch is planar entity bounded by a set of planar curves. Then, to enforce the periodicity of the microstructure, the curve, surface and patch entities corresponding to an opposite face of the PUC are tagged as *control* or *subordinate* and pointers to control entity are assigned for the subordinate ones. Next, in order to control the element size gradation and to implement the spatial localization, an octree is built around the unit cell to be discretized.

The mesh generation then proceeds in a hierarchical manner. First, the model vertices are discretized. Then curves are segmented using the mass curve of the required element density as described in [220]. If a curve to be discretized is tagged as subordinate, segments from the control curve are simply copied to the current entity. The two-dimensional Advancing Front technique is then used to triangulate surfaces and patches. Again, if an entity to be discretized is tagged as subordinate, the surface or patch mesh from the control entity is directly copied to the processed entity. Finally, the individual regions are meshed using the three-dimensional Advancing Front algorithm. At this stage of mesh generation, the boundary entities of each region are already discretized consistently with

[8] In the present implementation, the center of gravity of each element was used to determine the values of Euler angles, which are supposed to be constant on a given element.

[9] Note that there exist alternative approaches for enforcing the periodicity of the fluctuating displacement field; see Section 3.2.4 for more detailed discussion and Section 5.3.2 for a particular example.

[10] This code was developed by Dr. D. Rypl from the department of Structural Mechanics, Faculty of Civil Engineering. I would like to express my thanks and gratitude to Dr. Rypl for his numerous suggestions and inspiring discussion on the topic of this section.

respect to the unit cell periodicity. Further discussion together with detailed description of individual steps of the **T3D** program can be found in monograph [220]. Examples of tetrahedral meshes of a plain-weave unit cell generated by the described algorithm are displayed in Figs. 5.9 and 5.11.

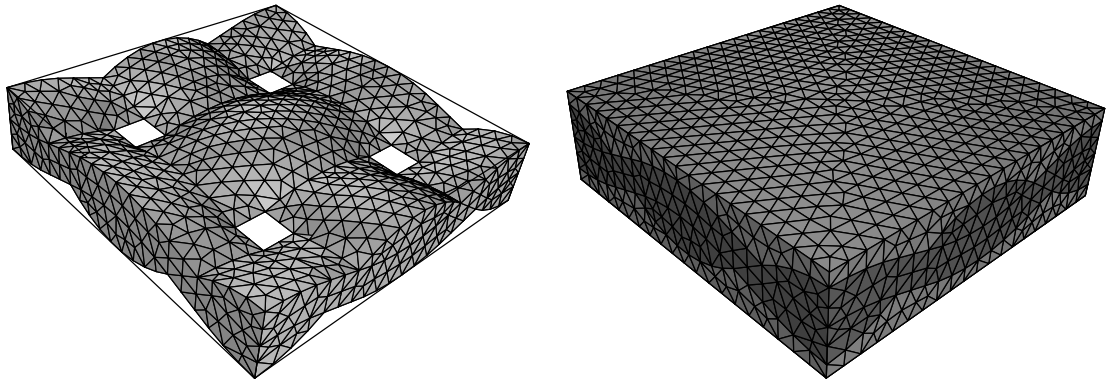

(a) (b)

Figure 5.9: Mesoscale finite element meshes

5.2.4 Numerical examples

We start from the sensitivity study of the overall elastic properties with respect to the mesh size. To this end, the sequence of finite element meshes corresponding to decreasing mesh size was generated by the algorithm described in the previous section. The elastic properties of the matrix and the bundle phases were taken from Section 3.2.5. The resulting coefficients of the homogenized stiffness matrix for the unit cell with parameters $a = 10$, $h = 3$ and $g = b = 1$ together with the memory requirements appear in Table 5.6. The presented results indicate that the discretization with the default mesh size equal to 1.0 is sufficient to deliver the effective elastic properties with a reasonable precision; therefore, this mesh size is used in all the following analyses. Finally, the distribution of fluctuating displacement $\mathbf{u}^*_{\text{meso}}$ within the periodic unit cell for various loading cases is plotted in Fig. 5.10.

Mesh size	$\mathsf{L}^{\text{fem}}{}_{11}$ [GPa]	$\mathsf{L}^{\text{fem}}{}_{12}$ [GPa]	$\mathsf{L}^{\text{fem}}{}_{33}$ [GPa]	$\mathsf{L}^{\text{fem}}{}_{44}$ [GPa]	$\mathsf{L}^{\text{fem}}{}_{66}$ [GPa]	c_f	***Total DOFs***	***Memory*** [kB]
2.5	26.537	7.503	11.385	2.259	2.942	0.3549	1,008	1,742
2.0	26.501	7.494	11.379	2.262	2.954	0.3601	1,512	3,073
1.5	26.243	7.519	11.374	2.264	2.962	0.3648	2,595	6,977
1.0	25.250	7.494	11.370	2.265	2.966	0.3678	5,712	22,412
0.75	25.234	7.494	11.369	2.264	2.967	0.3690	14,304	111,829

Table 5.6: Comparison of the effective mesoscale stiffness matrix components for different mesh sizes

As the next step, the effect of scatter of individual identified parameters is addressed. The minimum and maximum dimensions were taken from the S_{mm}-based identification

(a) $E_{11} = 1$

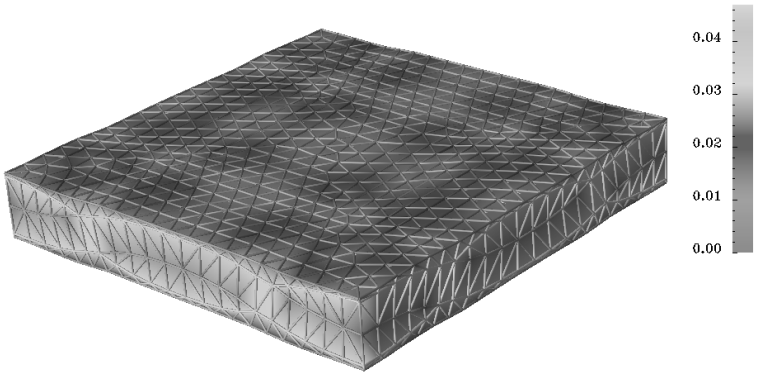

(b) $E_{33} = 1$

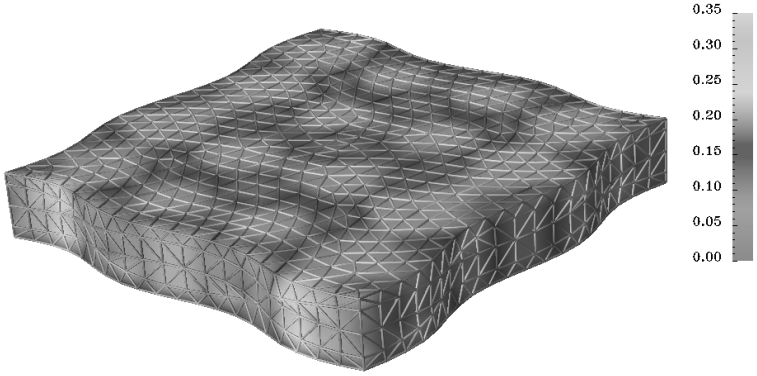

(c) $E_{12} = 1$

(d) $E_{23} = 1$

Figure 5.10: Mesoscale fluctuating displacement $\mathbf{u}^*_{\text{meso}}$

problem for the bitmap dimensions 256×32, see Table 5.2. The results stored in the Table 5.7 show that the difference in effective elastic moduli due to uncertainty in mesoscale PUC parameters is approximately comparable to the discretization error observed in Table 5.6. Moreover, the deviation of the $\mathsf{L}^{\mathsf{fem}}{}_{11}$ entry can be attributed to a relatively large difference in the bundle volume fraction for the analyzed unit cells.

Dimensions	$\mathsf{L}^{\mathsf{fem}}{}_{11}$ [GPa]	$\mathsf{L}^{\mathsf{fem}}{}_{12}$ [GPa]	$\mathsf{L}^{\mathsf{fem}}{}_{33}$ [GPa]	$\mathsf{L}^{\mathsf{fem}}{}_{44}$ [GPa]	$\mathsf{L}^{\mathsf{fem}}{}_{66}$ [GPa]	c_f
Minimal	25.247	7.496	11.371	2.264	2.965	0.3674
Maximal	25.217	7.508	11.384	2.247	2.922	0.3554

Table 5.7: Effects of uncertainties in mesoscale PUC dimensions

Finally, we present the comparison of effective elastic properties for artificial bitmaps and corresponding statistically optimized unit cells obtained in Section 5.1.4. The finite element meshes corresponding to the artificial mesostructure appear in Fig. 5.11[11]. , while the effective elastic properties of the target microstructure and the statistically optimized unit cells are stored in Table 5.8.

Periodic Unit Cell #1						
Descriptor	$\mathsf{L}^{\mathsf{fem}}{}_{11}$ [GPa]	$\mathsf{L}^{\mathsf{fem}}{}_{12}$ [GPa]	$\mathsf{L}^{\mathsf{fem}}{}_{33}$ [GPa]	$\mathsf{L}^{\mathsf{fem}}{}_{44}$ [GPa]	$\mathsf{L}^{\mathsf{fem}}{}_{66}$ [GPa]	c_f
S_{mm}	21.100	7.499	11.401	2.265	2.868	0.3386
L_m	22.698	7.503	11.410	2.235	2.842	0.3312
$S_{mm} + L_m$	23.334	7.490	11.383	2.255	2.925	0.3567
Target	23.324	7.453	11.384	2.269	2.963	0.3678
Periodic Unit Cell #2						
Descriptor	$\mathsf{L}^{\mathsf{fem}}{}_{11}$ [GPa]	$\mathsf{L}^{\mathsf{fem}}{}_{12}$ [GPa]	$\mathsf{L}^{\mathsf{fem}}{}_{33}$ [GPa]	$\mathsf{L}^{\mathsf{fem}}{}_{44}$ [GPa]	$\mathsf{L}^{\mathsf{fem}}{}_{66}$ [GPa]	c_f
S_{mm}	25.341	7.500	11.375	2.257	2.947	0.3635
L_m	26.309	7.494	11.372	2.259	2.959	0.3671
$S_{mm} + L_m$	25.121	7.495	11.376	2.256	2.956	0.3629
Target	24.786	7.467	11.370	2.266	2.965	0.3678
Periodic Unit Cell #3						
Descriptor	$\mathsf{L}^{\mathsf{fem}}{}_{11}$ [GPa]	$\mathsf{L}^{\mathsf{fem}}{}_{12}$ [GPa]	$\mathsf{L}^{\mathsf{fem}}{}_{33}$ [GPa]	$\mathsf{L}^{\mathsf{fem}}{}_{44}$ [GPa]	$\mathsf{L}^{\mathsf{fem}}{}_{66}$ [GPa]	c_f
S_{mm}	27.629	7.471	11.362	2.268	2.997	0.3752
L_m	27.464	7.393	11.349	2.279	3.027	0.3872
$S_{mm} + L_m$	27.095	7.473	11.371	2.258	2.966	0.3678
Target	24.694	7.416	11.374	2.273	2.972	0.3670

Table 5.8: Effective properties of statistically optimized mesoscale PUCs

Evidently, the best correspondence between the artificial micrographs and the periodic

[11] Note that for mesh generation, the unit cells were shifted by $a/2$ compared to bitmaps displayed in Fig. 5.8.

unit cell was reached for the PUC #1 microstructure where the optimization procedure predicts the in-plane properties with approximately the same error as the one resulting from the discretization. Note that analogously to Section 3.1.3, the combined reconstruction procedure yields the best results. The periodic unit cell based on parameters identified for PUC #2 correctly predicts the bundle volume fraction; it does not, however, take into account the different inclination of tows in individual layers which results in a slight overestimation of $\mathsf{L}^{\mathsf{fem}}{}_{11}$ modulus. Note that its value for combined reconstruction is, however, closer to the "correct" one that for the standard unit cell. The most severe differences can be observed for the PUC #3 microstructure. As follows from Table 5.5, all the optimized unit cell exhibit substantially smaller value of gap between individual tows g to accommodate the layer shift present in the target micrograph, which leads to overestimating of the bundle volume fraction c_f resulting in a higher value in-plane component $\mathsf{L}^{\mathsf{fem}}{}_{11}$.

The obtained results allow us to conclude that the proposed procedure can be efficiently used for multilayered composites with possibly varying layers heights provided that the relative shift of individual layers is not very large or approximately equal to the unit cell half-width. In the opposite case, it appears to be necessary to formulate the optimized unit cell in terms of at least two-layered composite, too. Note, however, that the difference of cross-sections corresponding to planes $x = \pm a$ and $y = \pm a$, see Fig. 5.11c, calls for microstructural information supplied in the form of bitmaps taken from several location of a composite in two orthogonal directions rather than for only one bitmap considered in this work. A more complex three-dimensional periodic unit cell also inevitably leads to a substantial increase of computational demands, which somehow limits its applicability to real-world problems.

5.3 Prestress analysis on mesoscale

The purpose of this section is to address, in the present modeling framework, the effect of initial fiber prestress on the macroscopic response of 6×6 braided weave composite, the basic building block of the woven composite tubes [283, 284]. Here, we limit our attention to a two-scale problem with the loading conditions applied on mesoscale. The attention is given to the quantification of the influence of specific arrangement of reinforcements on the overall response derived on mesoscale.

5.3.1 Geometrical model

For modeling purposes we limit our attention to a two-ply composite tube. Depending on winding speed and orientation the number of tows within periodically repeating regions may vary. In our particular case, the mesoscale unit cell consists of two plies where each ply contains six tows. Overall properties of this mixture are found from the homogenization procedure carried out on the microscale, see Chapters 2 and 3. All six tows are aligned along the same direction, but they interlace through individual plies thus creating a typical woven structure of the composite. This is shown schematically in Fig. 5.12a.

The shape of the tow cross-section is derived from images of the real composite structure. With the help of the **LUCIE** image analyzer such a micrograph can be transformed into a binary image and further analyzed to provide all geometrical parameters to build

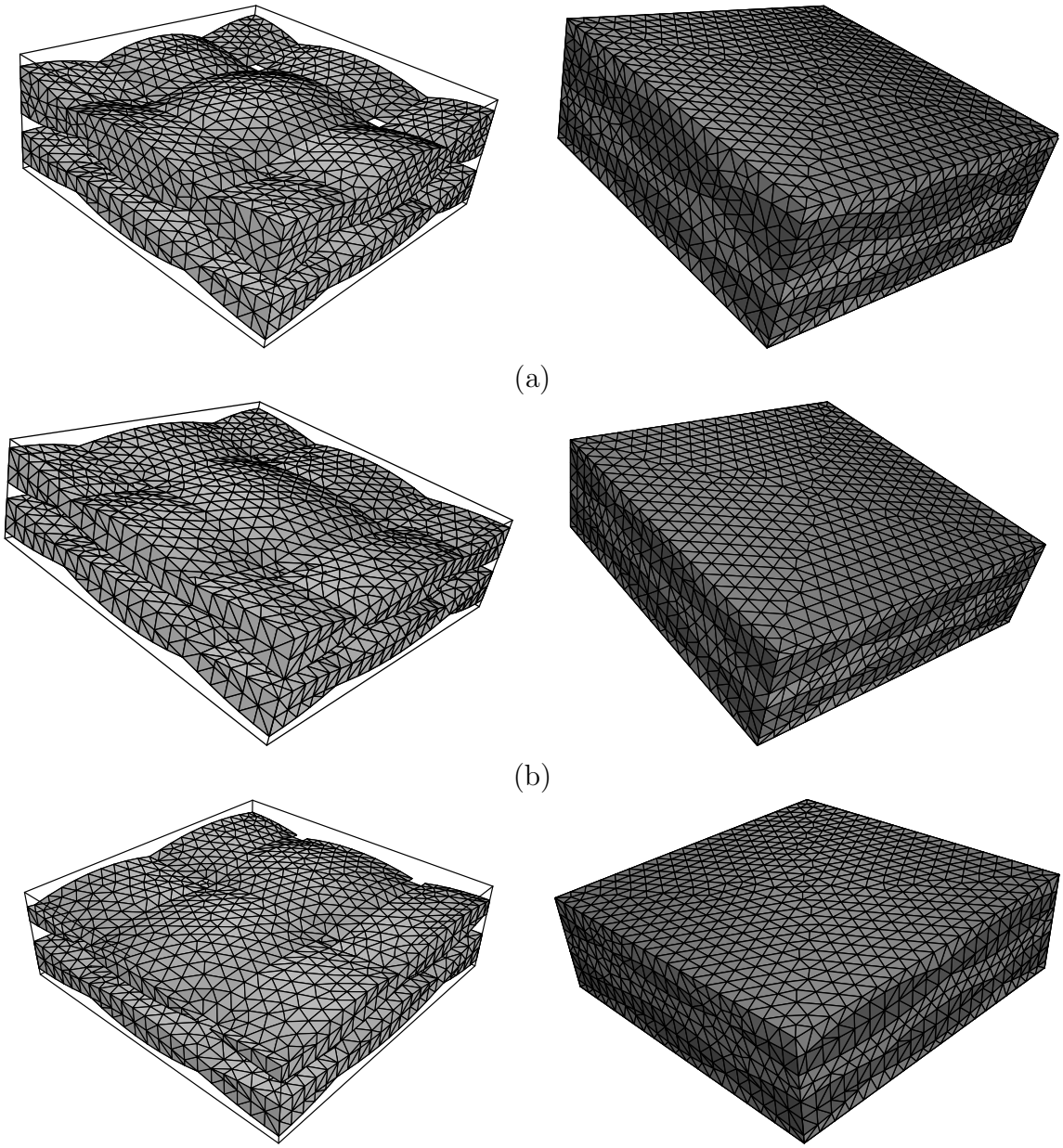

(a)

(b)

(c)

Figure 5.11: Mesoscale meshes, (a) PUC #1, (b) PUC #2, (c) PUC #3

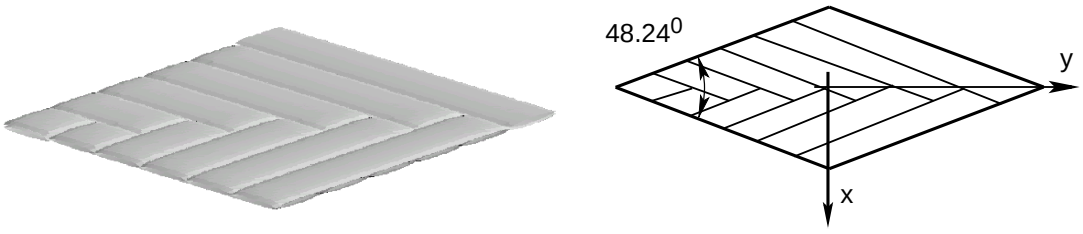

(a) (b)

Figure 5.12: Braided weave composite: (a) Weave layup, (b) Global coordinate system

an idealized geometrical model. The microscopic images of a real tube suggest that every tow is impregnated by the polymer matrix. The interface layer between the two adjacent tows is approximately 0.02 mm thick. The same thickness is considered between the two tows, which are parallel to each other and lay in the same ply. Due to interweaving the tow cross-section varies along the tow middle-curve. Linear interpolation is used in the transition zone to reflect this phenomenon.

The geometrical model derived from this data, however, is not very suitable for computational modeling using the finite element method. The main drawback is a very thin interface layer. Its discretization inevitably results in very small elements spread over a large region of the unit cell thus leading to enormous computational effort, but not substantially increasing the accuracy of the numerical model. Therefore, in order to arrive at a feasible numerical model, some action must be taken. A suitable method of attack appears in replacing the interface layer by contact elements with zero thickness and appropriate interfacial material properties.

5.3.2 Periodic boundary conditions

Another complication is caused by the fact that, due to a complexity of the periodic unit cell, it appears to be prohibitively difficult to generate the finite element mesh respecting the periodic boundary conditions. Therefore, a simple penalty-based method is used to prescribe the periodic boundary conditions. To that end, the displacements of a given node, referred to *subordinate*, on one face of the unit cell are defined as a linear function of the displacement of specific control nodes on the opposite face of the unit cell[12]. This relation can be written as

$$\{\mathsf{r}_{\mathrm{meso,s}}\} = [\mathsf{P}]\,\{\mathsf{r}_{\mathrm{meso,c}}\}, \tag{5.31}$$

where the $\mathsf{r}_{\mathrm{meso,s}}$ and $\mathsf{r}_{\mathrm{meso,c}}$ denote nodal unknowns corresponding to nodes located on opposite faces of the PUC and $[\mathsf{P}]$ is the matrix containing the weights corresponding to given nodes (values of shape functions of the element face, which contains the projection of a node on the opposite unit cell face).

To incorporate the periodicity condition into the problem formulation, we order the degrees of freedom in such a way that the vector of unknown nodal fluctuating displacements can be written as

$$\{\mathsf{r}_{\mathrm{meso}}\} = \left\{ \begin{array}{c} \mathsf{r}_{\mathrm{meso,i}} \\ \mathsf{r}_{\mathrm{meso,s}} \\ \mathsf{r}_{\mathrm{meso,c}} \end{array} \right\}, \tag{5.32}$$

where $\mathsf{r}_{\mathrm{meso,i}}$ denote the internal degrees of freedom. The discrete form of periodicity condition than can be simply written as

$$\{0\} = [0, \mathsf{I}, -\mathsf{P}]\,\{\mathsf{r}_{\mathrm{meso}}\} = [\mathsf{G}]\,\{\mathsf{r}_{\mathrm{meso}}\}. \tag{5.33}$$

To arrive at the system of equations corresponding to Eq. (5.28), consider the mini-

[12] Here, the linearity of the nodal basis function is employed.

mization of the following quadratic function

$$\begin{aligned}\Pi_\rho(\{\mathsf{E}_{\rm meso}\},\{\mathsf{r}_{\rm meso}\}) &= \frac{1}{2}\left(\{\mathsf{E}_{\rm meso}\}^{\mathsf{T}}[\mathsf{K}_{11}]\{\mathsf{E}\}+\{\mathsf{r}_{\rm meso}\}^{\mathsf{T}}[\mathsf{K}_{22}]\{\mathsf{r}_{\rm meso}\}\right)\\ &+ \{\mathsf{E}_{\rm meso}\}^{\mathsf{T}}[\mathsf{K}_{12}]\{\mathsf{r}_{\rm meso}\}+\{\mathsf{E}_{\rm meso}\}^{\mathsf{T}}(\{\Sigma\}_{\rm meso}+\{\mathsf{f}_1\})+\{\mathsf{r}_{\rm meso}\}^{\mathsf{T}}\{\mathsf{f}_2\}\\ &+ \frac{\rho}{2}\{\mathsf{r}_{\rm meso}\}^{\mathsf{T}}[\mathsf{G}]^{\mathsf{T}}[\mathsf{G}]\{\mathsf{r}_{\rm meso}\},\end{aligned} \tag{5.34}$$

where the last term was introduced to account for the periodicity of the fluctuating fields $\mathsf{r}_{\rm meso}$, see Eq. (5.33). The results of standard penalty theory (see, e.g., [213, and references herein]) ensure that the periodicity constraint is satisfied asymptotically as $\rho \to \infty$. In practical computations, the value of ρ is selected as large as possible while keeping the parameter low enough to minimize the effect of round-off errors[13].

Finally, it can be easily seen that the system of linear equations corresponding to the stationarity conditions of the penalized formulation yields the following system of equations

$$\begin{bmatrix} \mathsf{K}_{11} & \mathsf{K}_{12} \\ \mathsf{K}_{21} & \mathsf{K}_{22}+\rho[\mathsf{G}]^{\mathsf{T}}[\mathsf{G}] \end{bmatrix} \begin{Bmatrix} \mathsf{E}_{\rm meso} \\ \mathsf{r}_{\rm meso} \end{Bmatrix} = \begin{Bmatrix} \Sigma_{\rm meso}+\mathsf{f}_1 \\ \mathsf{f}_2 \end{Bmatrix}. \tag{5.35}$$

5.3.3 Numerical results

This section demonstrates two possible outputs of the aforementioned homogenization procedure. The first example provides effective elastic properties of the woven composite material. The second example deals with the analysis of failure behavior of a given composite system and its dependence on a fiber prestress.

Homogenized properties

To determine coefficients of the effective stiffness matrix, the periodic unit cell is loaded, in turn, by each of six components of $\{\mathsf{E}_{\rm meso}\}$, while the other components vanish. The volume averages of the stress tensor, transformed into the global coordinate system, then furnish the individual columns of $\left[\mathsf{L}^{\mathsf{fem}}\right]$.

Material parameters of individual bundles were taken from Table 3.5 with out-of-plane components of the effective stiffness tensor, which are not provided by the previous 2D analysis, estimated by the Mori-Tanaka method [17]. Resulting values of individual components of the material stiffness matrix are stored in Table 5.9. The selected coordinate system is evident from Fig. 5.12b. The effective material is fully anisotropic resulting from complicated geometrical arrangement of fiber tows. Moreover, the results indicate strong coupling between in-plane shear and normal components (entries L_{16} and L_{26}), which must be taken into account in the design and analysis of such composite systems.

Failure behavior analysis

To obtain a qualitative description of failure behavior of the present composite system, we constructed failure surfaces for a bi-axial loading specified in terms of overall in-plane stresses. To this end, the material system is loaded by a certain combination of two overall stresses. Then, this loading is proportionally increased until the Hill failure criterion, see

[13] The value $\rho = 10^{10}$ was found to comply with these conditions for the present study.

Stiffness matrix entry	***Bundle***	***Effective***
L_{11}	176.8	69.75
L_{22}	10.74	81.83
L_{33}	10.72	9.085
L_{12}	6.897	23.64
L_{13}	6.897	5.630
L_{23}	6.319	5.684
L_{44}	2.216	2.903
L_{55}	4.861	3.009
L_{66}	4.861	22.18
L_{16}	–	28.03
L_{26}	–	27.16

Table 5.9: Material properties of mesoscale unit cell [GPa]

Eq. (A.59), is reached at least at one material (integration) point. The resulting stress values then define one vertex of a failure surface. Successive application of this procedure for appropriate load combinations then yields the approximation of a failure surface. The material parameters, taken from [279], considered in the present failure criterion are shown in Table 5.10.

Y_{11}	Y_{22}	Y_{33}	Y_{12}	Y_{13}	Y_{23}
56.6	56.6	2342	48.7	48.7	48.7

Table 5.10: Bundle strength properties [MPa]

It was demonstrated in [56, 269] that fiber prestress can substantially influence inelastic and failure behavior of unidirectional fibrous laminates. To extend this study to the current material system, consider a uniform fiber prestress $\lambda^{\ell}_{33,f}$ introduced in the fiber in the direction of its axis[14]. The magnitude of prestress on the level of fiber tow, $\boldsymbol{\lambda}_{\text{meso}}$, follows from Hashin-Shtrikman variational principles, Eq. (4.31).

When introduced within the context of failure analysis, the presence of fiber prestress just alters the original shape of the resulting failure surface. Results of this computation are shown in Figs. 5.13 and 5.14. Note that each failure surface in Fig. 5.13 was approximated by a polygon with 64 vertices while the surface presented in Fig. 5.14 was constructed from 4096 values.

The results show that the overall response of the braided composite is strongly anisotropic. Obviously, the resistance of the composite attains its maximum for the combination of tensile and compressive loads, when favorable stress distribution causes large stresses in the axial directions of two bundle systems, where the bundle strength is very high (see Table 5.9). The effect of fiber prestress seems to be rather negligible for the selected failure criterion and material system. The same, however, might not be true for

[14] Recall that the local coordinate system is selected such that the local x^{ℓ}_3 axis is aligned with the fiber direction.

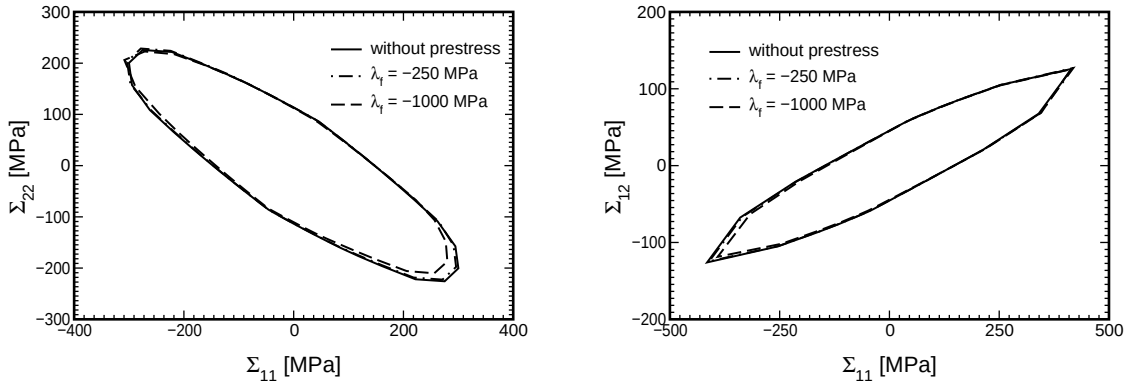

(a) (b)

Figure 5.13: Failure envelope in (a) $\Sigma_{\text{meso},11} \times \Sigma_{\text{meso},22}$ stress space, (b) $\Sigma_{\text{meso},22} \times \Sigma_{\text{meso},12}$ stress space

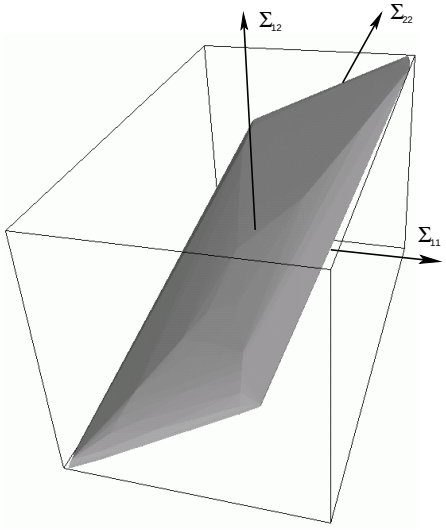

Figure 5.14: Failure envelope in $\Sigma_{\text{meso},11} \times \Sigma_{\text{meso},22} \times \Sigma_{\text{meso},12}$ stress space

more detailed failure laws, which might include nonlinearity at the contact surfaces of individual tows or within the fiber tow itself.

Chapter 6

CONCLUSIONS AND FUTURE WORK

The aim of this chapter is to briefly summarize the major results obtained in the present thesis and to comment and compare the related work found in literature not explicitly mentioned in the previous text. Moreover, the possible extensions and directions of further research are indicated.

A number of topics related to determination of the effective behavior of composite materials with disordered microstructure is addressed in this thesis. Two reliable and efficient approaches are introduced in the present work. Although different at their theoretical formulation, both approaches are closely tied to the same statistical descriptors generally used to quantify the morphology of random microstructures. The first approach follows well-established procedures which incorporate various periodic unit cell models combined with the finite element method. On the microscale level, the complexity of real microstructures is reflected in more complicated unit cells having larger number of particles. The required number of reinforcements and their arrangement is determined such that the macroscopic response of a unit cell is identical to the behavior of a real composite. A simple and intuitive approach based on microstructural statistics is proposed to derive such periodic unit cells. The conceptually similar methodology is used on the mesoscale level for definition of the statistically optimal periodic unit cell for plain weave composites. The second approach is based on extended Hashin-Shtrikman variational principles, which directly incorporate two-point probability functions into the problem formulation.

The literature overview in Chapter 1 summarizes previous research and trends in the fields of the Representative Volume Element definition, modeling and quantification of microstructural morphology, global stochastic optimization methods and numerical as well as analytical modeling on micro and mesoscale levels.

The stepping stone in the present approach is the knowledge of either two-point probability or lineal path functions for digitized media. Details regarding these descriptors are given in Chapter 2 together with methods for their numerical evaluation with emphasis put on possible anisotropy of the microstructural descriptors. In addition, this chapter describes series of tests addressing the validity of statistical isotropy and ergodicity assumptions suggested for the unidirectional graphite fiber-reinforced composite impregnated by the polymer matrix. Finally, the stochastic optimization algorithm **RASA**, based on combination of the Parallel Simulated Annealing, the Differential Evolution method and real-encoded Genetic Algorithms, is introduced. The obvious disadvantage of this algorithm is a large number of parameters of this method, which can eventually lead to a tedious and time-consuming tuning procedure. This restriction, however, does not seem to be important in the current work as all optimization problems encountered in this thesis were successfully solved using identical parameters setting displayed in Table 3.2. Although most of the material presented in Chapter 2 is not very new, see, e.g., [19, 255, 257], such a detailed and self-contained treatment including the description of algorithms for numerical evaluation of the statistical descriptors cannot be easily found

in the literature. Moreover, the performance of the **RASA** algorithm was also independently demonstrated by a successful application of this algorithm to several problems of Civil and Geotechnical Engineering, see [114, 132].

Chapter 3 outlines generation of optimal unit cells for fiber reinforced composite materials by matching the material statistics of both the unit cell and real material in terms of two-point probability function, lineal path function or a combination of both. Note that other systems such as ceramic or metal matrix systems may also benefit from the present work. The resulting optimization problem is divided into two separate sub-problems and each of them solved by an appropriate optimization procedure. The finite element discretization of the unit cell problem together with the mesh generation procedure are implemented. Finally, the applicability of the present approach is confirmed by evaluating effective thermoelastic system from both the small period unit cells (five to ten fibers unit cells) and considerably larger unit cells having of two orders of magnitude more particles (three to five hundred fibers). An excellent match is found. These results are further extended to linear and non-linear viscoelastic response of random composites for both the overall stress and overall strain loading cases. Note that the dimensions of minimal periodic unit cells (approximately 4 fiber diameters) correspond well with the analytical results of Drugan and Willis [49] and Drugan [48].

The Hashin-Shtrikman variational principles are the main topic of Chapter 4. Both the displacement and traction based formulations are revisited in conjunction with random composites and extended to account for the presence of initial stresses or strains. An efficient numerical procedure based on the FFT which directly exploits digitized images of real microstructures is implemented. Fourier transform applied when solving the resulting integral equations is rather advantageous as it allows an arbitrary choice of the reference medium so that often encountered anisotropy of individual phases creates no obstacles in the solution procedure. When compared to the unit cell technique, this method is more efficient and thus preferable when evaluating the macroscopic elastic and linearly viscoelastic response of real composites. For the nonlinearly viscoelastic materials, however, the difference between the finite element modeling and Hashin-Shtrikman variational principles becomes more pronounced. This agrees well with similar results obtained for, e.g., the Mori-Tanaka method by Lagoudas et al. [139] and for the transformation field analysis by Dvorak et al. [54]. The present formulation of the Hashin-Shtrikman variational principles employs the ideas of Willis [286] and Drugan and Willis [49]; the only work somehow related to numerical application of Hashin-Shtrikman variational principles to the analysis of real-world materials I am aware of is Accrosi and Nemat-Nasser [4]; it is, however, restricted only to very special artificial microstructures and isotropic constituents. Moreover, such a systematic comparison of Hashin-Shtrikman and finite element based modeling for non-isotropic composites has not been, to author's best knowledge, presented yet.

Statistically optimal unit cells for plain-weave fabric composites derived on basis of the principles set for unidirectional fibrous composites are introduced in Chapter 5. The model of Kuhn and Charalambides [135] is implemented to describe the geometry of a given composite system. A number of numerical tests is executed to quantify the sensitivity and precision of the optimal unit cell parameters with respect to a bitmap resolution and the selected statistical descriptor. Subsequently, this methodology is applied to the determination of the periodic unit cells corresponding to artificial micrographs based

on various imperfections consistent with in-situ observations of real composite media. Geometrical parameters derived from the proposed optimization procedure are then used to generate the finite element meshes by the Advancing Front method-based code **T3D**. The numerical homogenization based on the stress-controlled approach incorporating a general eigenstress distribution is formulated and implemented. The quality of the unit cells resulting from the optimization procedure is then addressed from the point of view of effective elastic properties. The obtained results show the applicability and the limitation of the proposed procedure: in particular, it turns out that this methodology is applicable for multilayered composite systems with non-uniform layer heights but not very different shift of individual layers or with layers shifted by unit cell half-width. In other cases, however, it appears to be necessary to formulate the optimized unit cell in terms of at least two-layered composite.

Finally, the application of the uncoupled modeling approach based on combination of the Hashin-Shtrikman variational principles and the finite element analysis is demonstrated for the study of the failure envelopes of woven composite tubes. The results demonstrate the strong anisotropy of the overall response and the insensivity of the overall failure behavior with respect to the fiber prestress for the analyzed composite system. The results and ideas presented in this chapter seem to be new; the significance of more complex unit cell for simulation of overall response of woven composites has been recently advocated by Jekabsons and Byström [115].

Although a variety of problems were addressed and solved in the present work, there still remains several possible extensions. The first possible improvement is increasing efficiency of the optimization procedure based on the lineal path function. This can be accomplished either by more sophisticated implementation of the lineal path function evaluation and, in addition, as indicated by results presented in [298], the number of function evaluations can be substantially reduced by implementing problem-dependent operators in the **RASA** algorithm. The second refinement can be based on application non-linear version of Hashin-Shtrikman variational principles [200] for estimation of the overall response of composites with a nonlinearly viscoelastic matrix phase. Another interesting topic is definition of a more complex mesoscale periodic unit cells which incorporates shift of individual layers in x and y directions combined with fast solution strategies for efficient analysis of multi-layered periodic unit cells. Finally, very interesting and challenging topic is the derivation of Hashin-Shtrikman variational bounds and estimates, similar to those introduced in Chapter 3, for plain-weave composite systems.

BIBLIOGRAPHY

[1] *Homepage of* `neos` *server*, `http://www-fp.mcs.anl.gov/otc/Guide`.

[2] *Homepage of* `openddx` *program*, `http://www.opendx.org`.

[3] J. Aboudi, *Mechanics of composite materials : A unified micromechanical approach*, Studies in Applied Mechanics, vol. 29, Elsevier, 1991.

[4] M.L. Accorsi and S. Nemat-Nasser, *Bounds on the overall elastic and instantaneous elastoplastic moduli of periodic composites*, Mechanics of Materials **5** (1986), no. 3, 209–220.

[5] G. Allaire, *Homogenization and 2-scale convergence*, SIAM Journal on Mathematical Analysis **23** (1992), no. 6, 1482–1518.

[6] G. Allaire and M. Briane, *Multiscale convergence and reiterated homogenization*, Proceedings of the Royal Society of Edinburgh Section A - Mathematics **126** (1996), no. 2, 297–342.

[7] M. Axelsen, *Quantitative description of the morphology and microdamage of composite materials*, Ph.D. thesis, Aalborg University, 1995.

[8] I. Babuška, *Homogenization and its applications. Mathematical and computational problems*, Numerical solution of partial differential equations III, SYNSPADE 1975, Academic Press, 1976, pp. 89–116.

[9] ———, *The computational aspects of the homogenization problem*, Computing Methods in Applied Science and Engineering, 1979, I (Proceedings, IRIA, Paris) (R. Glowinski and J.-L. Lions, eds.), Lecture Notes in Mathematics, no. 704, Springer-Verlag, 1979, pp. 309–316.

[10] I. Babuška, B. Andersson, P. J. Smith, and K. Levin, *Damage analysis of fiber composites Part I: Statistical analysis on fiber scale*, Computer Methods in Applied Mechanics and Engineering **172** (1999), no. 1–4, 27–77.

[11] N. S. Bakhvalov and A. V. Knyazev, *Efficient computation of averaged characteristics of composites of a periodic structure of essentially different materials*, Soviet Math. Doklady **42** (1991), no. 1, 57–62.

[12] K. J. Bathe, *Finite element procedures*, second ed., Prentice Hall, 1995.

[13] P.Z. Bazant and S.T. Wu, *Dirichlet series creep function for aging concrete*, Journal of Engineering Mechanics ASCE **99** (1973), no. EM2, 367–387.

[14] D. Beasley, D.R. Bull, and R.R. Martin, *An overview of Genetic Algorithms: Part 1, Foundations*, University Computing **15** (1993), no. 2, 58–69.

[15] J. G. J. Beijer and J. L. Spoormaker, *Solution strategies for FEM analysis with nonlinear viscoelastic polymers*, Computers & Structures **80** (2002), no. 14–15, 1213–1229.

[16] A. Bensoussan, J.L. Lions, and Papanicolau, *Asymptotic analysis for periodic structures*, Studies in mathematics and its applications, vol. 5, North Holland Publishing Company, 1978.

[17] Y. Benveniste, *A new approach to the application of Mori-Tanaka theory in composite materials*, Mechanics of Materials **6** (1987), 147–157.

[18] M. J. Beran, *Statistical continuum theories*, Monographs in Statistical Physics, Interscience Publishers, 1968.

[19] J. G. Berryman, *Measurement of spatial correlation functions using image processing techniques*, Journal of Applied Physics **57** (1984), no. 7, 2374–2384.

[20] J. G. Berryman and S. C. Blair, *Use of digital image analysis to estimate fluid permeability of porous materials : Application of two-point correlation function*, Journal of Applied Physics **60** (1986), no. 6, 1930–1938.

[21] Z. Bittnar and J. Šejnoha, *Numerical methods in structural engineering*, ASCE Press, 1996.

[22] J. F. Bourgat, *Numerical experiments with the homogenization method for operators with periodic coefficients*, Computing Methods in Applied Science and Engineering, 1997, I (Proceedings, IRIA, Paris) (R. Glowinski and J.-L. Lions, eds.), Lecture Notes in Mathematics, no. 704, Springer-Verlag, 1979, pp. 330–356.

[23] D. Braess, *Finite elements. Theory, fast solvers and applications in solid mechanics*, Cambridge University Press, 1997.

[24] M. Brdička, L. Samek, and B. Sopko, *Mechanika kontinua [Continuum mechanics]*, Academia, 2000.

[25] K.B. Breiling and D.O. Adams, *Effects of layer nesting on compression-loaded 2-D woven textile composites*, Journal of Composite Materials **30** (1996), no. 15, 1710–1728.

[26] M. E. Brewster and G. Beylkin, *A multiresolution strategy for numerical homogenization*, Applied and Computational Harmonic Analysis **2** (1995), no. 4, 327–349.

[27] B. Budiansky, *On the elastic moduli of some heterogeneous materials*, Journal of the Mechanics and Physics of Solids **13** (1965), 223–227.

[28] C.S. Burrus and T. W. Parks, *DFT/FFT and convolution algorithms: Theory and implementation*, Topics in Digital Signal Processing, A Wiley-Interscience Publication, 1985.

[29] V. A. Buryachenko, J. Pagano, R. Y. Kim, and J. E. Spowart, *Quantitative description and numerical simulation of random microstructures of composites and their effective elastic moduli*, International Journal of Solids and Structures **40** (2003), no. 1, 47–72.

[30] J. Byström, N. Jekabsons, and J. Varna, *An evaluation of different models for prediction of elastic properties of woven composites*, Composites Part B: Engineering **31** (2000), no. 1, 7–20.

[31] M. M. Cecchi and F. Marcuzzi, *A fast numerical homogenization algorithm for finite element analysis*, International Journal for Numerical Methods in Engineering **46** (1999), no. 10, 1639–1649.

[32] J.L. Chaboche, *Thermodynamic formulation of constitutive equations and application to the viscoplasticity and viscoelasticity of metals and polymers*, International Journal of Solids and Structures **34** (1997), 2239–2254.

[33] J.L. Chaboche, S. Kruch, J.F. Maire, and T. Pottier, *Towards a micromechanics based inelastic and damage modeling of composites*, International Journal of Plasticity **17** (2001), no. 4, 411–439.

[34] C. Chapman and J. Whitcomb, *Effect of assumed tow architecture on predicted moduli and stresses in plain weave composites*, Journal of Composite Materials **29** (1995), no. 16, 2134–2159.

[35] R.M. Christensen, *Theory of viscoelasticity: An introduction*, Academic Press, New York, 1971.

[36] P. W. Chung and K. K. Tamma, *Woven fabric composites - developments in engineering bounds, homogenization and applications*, International Journal for Numerical Methods in Engineering **45** (1999), no. 12, 1757–1790.

[37] C. Conca and S. Natesan, *Numerical methods for elliptic partial differential equations with rapidly oscillating coefficients*, Computer Methods in Applied Mechanics and Engineering **192** (2003), no. 1–2, 47–76.

[38] C. Conca and M. Vanninathan, *Homogenization of periodic structures via Bloch decomposition*, SIAM Journal on Applied Mathematics **57** (1997), no. 6, 1639–1659.

[39] P. B. Corson, *Correlation functions for predicting properties of heterogenous materials. I. Eperimental measurement of spatial correlation functions in multiphase solids*, Journal of Applied Physics **45** (1974), no. 7, 3159–3164.

[40] B.N. Cox and G. Flanagan, *Handbook of analytical methods for textile composites*, NASA Contractor Report 4750, Langley Research Center, 1997, `http://techreports.larc.nasa.gov/ltrs`.

[41] D. Cule and S. Torquato, *Generating random media from limited microstructural information via stochastic optimization*, Journal of Applied Physics **86** (1999), no. 6, 3428–3437.

[42] E. Cuthill and J. McKee, *Reducing the bandwidth of sparse symmetric matrices*, Proceedings of ACM National Conference, Association of Computing Machinery, 1969.

[43] A. Dasgupta, R. K. Agarwal, and S. M. Bhandarkar, *Three-dimensional modeling of woven-fabric composites for effective thermo-mechanical and thermal properties*, Composites Science and Technology **56** (1996), no. 3, 209–223.

[44] A. Dasgupta and S.M. Bhandarkar, *Effective thermomechanical behavior of plain-weave fabric-reinforced composites using homogenization theory*, Journal of Engineering Materials and Technology-Transactions of the ASME **116** (1994), no. 1, 99–105.

[45] R. Derr, *Statistical modeling of microstructure with applications to effective property computation in materials science*, Ph.D. thesis, University of North Carolina, 1999, Also available as `http://citeseer.nj.nec.com/derr99statistical.html`.

[46] R. Derr and C. Ji, *Fitting microstructural models in material science*, Preprint, 2000, Also available as `http://citeseer.nj.nec.com/derr00fitting.html`.

[47] M. Dorobantu and B. Engquist, *Wavelet-based numerical homogenization*, SIAM Journal on Numerical Analysis **35** (1998), no. 2, 540–559.

[48] W.J. Drugan, *Micromechanics-based variational estimates for a higher-order nonlocal constitutive equation and optimal choice of effective moduli for elastic composites*, Journal of the Mechanics and Physics of Solids **48** (2000), no. 6–7, 1359 – 1387.

[49] W.J. Drugan and J.R. Willis, *A micromechanics-based nonlocal constitutive equation and estimates of representative volume element size for elastic composites*, Journal of the Mechanics and Physics of Solids **44** (1996), no. 4, 497–524.

[50] G. J. Dvorak, *On uniform fields in heterogeneous media*, Proceedings of the Royal Society of London Series A - Mathematical, Physical and Engineering Sciences **431** (1990), no. 1881, 89–110.

[51] ———, *Transformation field analysis of inelastic composite materials*, Proceedings of the Royal Society of London Series A - Mathematical, Physical and Engineering Sciences **437** (1992), no. 1900, 311–327.

[52] G. J. Dvorak and Y. Benveniste, *On transformation strains and uniform fields in multiphase elastic media*, Proceedings of the Royal Society of London Series A - Mathematical, Physical and Engineering Sciences **437** (1992), no. 1900, 291–310.

[53] G. J. Dvorak and M. V. Srinivas, *New estimates of overall properties of heterogeneous solids*, Journal of the Mechanics and Physics of Solids **47** (1999), no. 4, 899–920.

[54] G. J. Dvorak, Bahei-El-Din Y.A., and A.M. Wafa, *Implementation of the transformation field analysis for inelastic composite-materials*, Computational Mechanics **14** (1994), no. 3, 201–228.

[55] G. J. Dvorak and J. Zhang, *Transformation field analysis of damage evolution in composite materials*, Journal of the Mechanics and Physics of Solids **49** (2001), no. 11, 2517–2541.

[56] G.J. Dvorak and M. Šejnoha, *Initial failure maps for fibrous CMC laminates*, Journal of the American Ceramic Society **78** (1995), no. 1, 205–210.

[57] J. Dvořák, *A reliable numerical method for computing homogenized coefficients*, Tech. Report MAT-31, Mathematical Institute, Danish Technical University, Lyngby, Denmark, 1994.

[58] A. Einstein, *Eine neue bestimmung der moleküldimensionen*, Annalen der Physic **19,34** (1906,1911), 289–305,591–592.

[59] J.W. Eischen and S. Torquato, *Determining elastic behavior of composites by the boundary-element method*, Journal of Applied Physics **74** (1993), no. 1, 159–170.

[60] M. Erigo and S.G. Johnson, *FFTW: An adaptive software architecture for the FFT*, Proceedings of the 1998 IEEE International Conference on Acoustics, Speech and Signal Processing, ICASSP98, vol. 3, IEEE, New York, 1998, (See also `http://www.fftw.org`), pp. 1381–1384.

[61] J. D. Eshelby, *The determination of the elastic field of an ellipsoidal inclusion and related problems*, Proceeding of Royal Society, Series A **241** (1957), 376–396.

[62] F. Fára, *Komplexní hodnocení objemových změn kompozitních soustav, [Complex evaluation of volume changes in composite systems]*, Ph.D. thesis, Czech Technical University in Prague, Faculty of Civil Engineering, Prague, Czech Republic, 1990.

[63] J. Fish and V. Belsky, *Multigrid method for periodic heterogeneous media. 1. Convergence studies for one-dimensional case*, Computer Methods in Applied Mechanics and Engineering **126** (1995), no. 1–2, 1–16.

[64] _____, *Multigrid method for periodic heterogeneous media. 2. multiscale modeling and quality-control in multidimensional case*, Computer Methods in Applied Mechanics and Engineering **126** (1995), no. 1–2, 17–38.

[65] _____, *Generalized aggregation multilevel solver*, International Journal for Numerical Methods in Engineering **40** (1997), no. 23, 4341–4361.

[66] J. Fish, W. Chen, and G. Nagai, *Non-local dispersive model for wave propagation in heterogeneous media: one-dimensional case; multi-dimensional case*, International Journal for Numerical Methods in Engineering **54** (2002), no. 3, 331–346; 347–363.

[67] J. Fish and K. Shek, *Computational plasticity and viscoplasticity for composite materials and structures*, Composites Part B: Engineering **29** (1998), no. 5, 613–619.

[68] _____, *Finite deformation plasticity for composite structures: Computational models and adaptive strategies*, Computer Methods in Applied Mechanics and Engineering **172** (1999), no. 1–4, 145–174.

[69] _____, *Multiscale analysis of large-scale nonlinear structures and materials*, International Journal for Computational Civil and Structural Engineering **1** (2000), no. 1, 79–90.

[70] J. Fish, K. Shek, M. Pandheeradi, and M. S. Shephard, *Computational plasticity for composite structures based on mathematical homogenization: Theory and practice*, Computer Methods in Applied Mechanics and Engineering **148** (1997), no. 1–2, 53–73.

[71] J. Fish, A. Suvorov, and V. Belsky, *Automated adaptive multilevel solver*, Computer Methods in Applied Mechanics and Engineering **149** (1997), no. 1–4, 267–287.

[72] J. Fish and Q. Yu, *Multiscale damage modelling for composite materials: Theory and computational framework*, International Journal for Numerical Methods in Engineering **52** (2001), no. 1–2, 161–191.

[73] _____, *Computational mechanics of fatigue and life predictions for composite materials and structures*, Computer Methods in Applied Mechanics and Engineering **191** (2003), no. 43, 4827–4849.

[74] J. Fish, Q. Yu, and K. Shek, *Computational damage mechanics for composite materials based on mathematical homogenization*, International Journal for Numerical Methods in Engineering **45** (1999), no. 11, 1657–1679.

[75] B.M. Fraeijs de Vebeuke, *A course in elasticity*, Springer Verlag, New York, 1979.

[76] J. Gajdošík, M. Šejnoha, and J. Zeman, *Příprava geometrického modelu pro mikromechanickou analýzu [Preparation of geometrical model for micromechanical analysis]*, Stavební obzor **12** (2003), no. 3, 80–82.

[77] S. Ghosh, K. Lee, and P. Raghavan, *A multi-level computational model for multi-scale damage analysis in composite and porous materials*, International Journal of Solids and Structures **38** (2001), no. 14, 2335–2385.

[78] S. Ghosh, Z. Nowak, and K. Lee, *Tessellation-based computational methods for the characterization and analysis of heterogeneous microstructures*, Composites Science and Technology **57** (1997), no. 9–10, 1187–1210.

[79] L. V. Gibiansky and S. Torquato, *New method to generate three-point bounds on effective properties of composites: Application to viscoelasticity*, Journal of the Mechanics and Physics of Solids **46** (1998), no. 4, 749–783.

[80] R. F. Gibson, *Principles of composite material mechanics*, McGraw-Hill, 1994.

[81] D. Goldberg, *Genetic Algorithms in Search, Optimization and Machine Learning*, Addison-Wesley, 1989.

[82] B. Gommers, I. Verpoest, and P. Van Houtte, *The Mori-Tanaka method applied to textile composite materials*, Acta Materialia **46** (1998), no. 6, 2223–2235.

[83] L. Greengard and J. Helsing, *On the numerical evaluation of elastostatic fields in locally isotropic two-dimensional composites*, Journal of the Mechanics and Physics of Solids **46** (1998), no. 8, 1441–1462.

[84] J.M. Guedes and N. Kikuchi, *Preprocessing and postprocessing for materials based on the homogenization method with adaptive finite elements method*, Computer Methods in Applied Mechanics and Engineering **83** (1991), no. 2, 143–198.

[85] A.A. Gusev, *Representative volume element size for elastic composites: A numerical study*, Journal of the Mechanics and Physics of Solids **45** (1996), no. 9, 1449–1459.

[86] S. I. Haan, P. G. Charalambides, and M. Suri, *A specialized finite element for the study of woven composites*, Computational Mechanics **27** (2001), no. 6, 445–462.

[87] W. Hackbusch and S.A. Sauter, *Composite finite elements for the approximation of PDEs on domains with complicated micro-structures*, Numerische Mathematik **75** (1997), no. 4, 447–472.

[88] Z. Hashin, *Analysis of composite materials - A survey*, Journal of Applied Mechanics - Transactions of the ASME **50** (1983), no. 3, 481–505.

[89] Z. Hashin and S. Shtrikman, *On some variational principles in anisotropic and non-homogeneous elasticity*, Journal of the Mechanics and Physics of Solids **10** (1962), 335–342.

[90] _____, *A variational approach to the theory of elastic behavior of multiphase materials*, Journal of the Mechanics and Physics of Solids **11** (1963), 127–140.

[91] S. Hazanov and C. Huet, *Order relationships for boundary-conditions effect in heterogeneous bodies smaller than the representative volume*, Journal of the Mechanics and Physics of Solids **42** (1994), no. 12, 1995–2011.

[92] R. Hill, *A theory of the yielding and plastic flow of anisotropic materials*, Proceeding of Royal Society, Series A **193** (1948), 281–290.

[93] ———, *The elastic behavior of a crystalline aggregate*, Proceedings of the Physical Society, London, A **65** (1952), 349–354.

[94] ———, *Elastic properties of reinforced solids - Some theoretical principles*, Journal of the Mechanics and Physics of Solids **11** (1963), 357–372.

[95] ———, *Theory of mechanical properties of fibre-strengthened materials: I. Elastic behaviour*, Journal of the Mechanics and Physics of Solids **12** (1964), 199–212.

[96] ———, *A self-consistent mechanics of composite materials*, Journal of the Mechanics and Physics of Solids **13** (1965), 213–222.

[97] I. Hlaváček and J. Nečas, *Mathematical theory of elastic and elastoplastic bodies : An introduction*, Elsevier, Amsterdam, 1981.

[98] S.J. Holister and N. Kikuchi, *A comparison of homogenisation and standard analyses for periodic porous composites*, Computational Mechanics **10** (1992), 73–95.

[99] J. H. Holland, *Adaptation in Natural and Artificial Systems*, University of Michigan Press, 1975.

[100] A. Holmbom, L.E. Persson, and N. Svanstedt, *A homogenization procedure for computing effective moduli and microstresses in elastic composite-materials*, Composites Engineering **2** (1992), no. 4, 249–259.

[101] T.Y. Hou and X.H. Wu, *A multiscale finite element method for elliptic problems in composite materials and porous media*, Journal of Computational Physics **134** (1997), no. 1, 169–189.

[102] C. R. Houck, J. A. Joines, and M. G Kay, *A Genetic Algorithm for function OpTimization: A Matlab implementation*, Tech. Report NCSU-IE TR 95-09, North Carolina State University, 1995,
`http://www.fmmcenter.ncsu.edu/fac_staff/joines/papers/gaot.ps`.

[103] O. Hrstka and A. Kučerová, *Improvements of the different types of binary and real coded genetic algorithms preventing the premature convergence*, submitted for publication, 2001.

[104] O. Hrstka, A. Kučerová, M. Lepš, and J. Zeman, *A competitive comparison of different types of evolutionary algorithms*, The Sixth International Conference on the Applications of Artificial Intelligence to Civil and Structural Engineering (B.V.H. Topping and B. Kumar, eds.), Civil-Comp Press, 2001, pp. 87–88.

[105] B. Hudec, *Základy počítačové grafiky [Elements of computer graphics]*, CTU, 1993.

[106] C. Huet, *Application of variational concepts to size effects in elastic heterogeneous bodies*, Journal of the Mechanics and Physics of Solids **38** (1990), no. 6, 813–841.

[107] ———, *Coupled size and boundary-condition effects in viscoelastic heterogeneous and composite bodies*, Mechanics of Materials **12** (1999), no. 1, 787–829.

[108] L. Ingber, *Simulated annealing: Practice versus theory*, Mathematical and Computer Modelling **18** (1993), no. 11, 29–57.

[109] ———, *Adaptive simulated annealing (ASA): Lessons learned*, Control and Cybernetics **25** (1995), no. 1, 33–54.

[110] T. Ishikawa and T.W. Chou, *Elastic behavior of woven hybrid composites*, Journal of Composite Materials **16** (1982), 2–19.

[111] ———, *Stiffness and strength behavior of woven fabric composites*, Journal of Materials Science **17** (1982), no. 11, 3211–3220.

[112] ———, *One-dimensional micromechanical analysis of woven fabric composites*, AIAA Journal **21** (1983), no. 12, 1714–1721.

[113] T. Ishikawa, M. Matsushima, Y. Hayashi, and T.W. Chou, *Experimental confirmation of the theory of elastic-moduli of fabric composites*, Journal of Composite Materials **19** (1985), no. 5, 443–458.

[114] T. Janda, M. Šejnoha, and P. Kuklík, *Mixed experimental and numerical approach to evaluation of material parameters of clayey soils*, International Journal of Geotechnical Engineering (2002), accepted for publication.

[115] N. Jekabsons and J. Byström, *On the effect of stacked fabric layers on the stiffness of a woven composite*, Composites Part B: Engineering **33** (2002), no. 8, 619–629.

[116] M. Jiang, M. Ostoja-Starzewski, and I. Jasiuk, *Scale-dependent bounds on effective elastoplastic response of random composites*, Journal of the Mechanics and Physics of Solids **49** (2001), no. 3, 655–673.

[117] V.V. Jikov, S.M. Kozlov, and O.A. Oleinik, *Homogenization of differential operators and integral functionals*, Springer-Verlag, 1994.

[118] H. J. Kim and C.C. Swan, *Algorithms for automated meshing and unit cell analysis of periodic composites with hierarchical tri-quadratic tetrahedral elements*, International Journal for Numerical Methods in Engineering **58** (2003), no. 11, 1683–1711.

[119] ———, *Voxel-based meshing and unit-cell analysis of textile composites*, International Journal for Numerical Methods in Engineering **56** (2003), no. 7, 977–1006.

[120] S. Kirkpatrick, C.D. Gelatt, Jr., and M. P. Vecchi, *Optimization by Simulated Annealing*, Science **220** (1983), 671–680.

[121] S. Knapek, *Matrix-dependent multigrid homogenization for diffusion problems*, SIAM Journal on Scientific Computing **20** (1998), no. 2, 515–533.

[122] W. Kohler and G. C. Papanicolau, *Bound for the overall conductivity of random media*, Macroscopic properties of disordered media (R. Burridge, S. Childress, and G. Papanicolau, eds.), Lecture Notes in Physics, vol. 24, Courant Institute, Springer-Verlag, Berlin, 1982, pp. 111–130.

[123] A.N. Kolmogorov and S.V. Fomin, *Základy teorie funkcí a funkcionální analýzy [Introductory real analysis]*, SNTL, [Dover: New York], 1975,[1970].

[124] V. Kouznetsova, W. A. M. Brekelmans, and P. T. Baaijens, *An approach to micro-macro modeling of heterogeneous materials*, Computational Mechanics **27** (2001), no. 1, 37–48.

[125] V. Kouznetsova, M. G. D. Geers, and W. A. M. Brekelmans, *Multi-scale constitutive modelling of heterogeneous materials with a gradient-enhanced computational homogenization scheme*, International Journal for Numerical Methods in Engineering **54** (2002), no. 8, 1235–1260.

[126] V. Kovařík, *Teorie vazkopružnosti [Theory of viscoelasticity]*, Lecture notes 3, Centre for Composite Materials and Structures, Klokner Institute, Czech Technical University in Prague, 1992.

[127] ———, *Distributional concept of the elastic viscoelastic correspondence principle*, Journal of Applied Mechanics, Transactions of the ASME **62** (1995), no. 4, 847–852.

[128] M. Košek and B. Košková, *Analysis of yarn wavy path periodicity of textile composites using Discrete Fourier Transform*, ICCE/6, 1999.

[129] A. Krauz and H. Eyring, *Deformation kinetics*, Willey-Interscience, 1975.

[130] A.F. Kregers and Y.G. Malbardis, *Determination of the deformability of three-dimensionally reinforced composites by stiffness averaging method*, Polymer Mechanics **1** (1978), no. 1, 3–8.

[131] W. Kreher and W. Pompe, *Internal stresses in heterogeneous solids*, Physical Research, vol. 9, Akademie-Verlag, Berlin, 1989.

[132] T. Krejčí, M. Šejnoha, and J. Šejnoha, *Improved prognosis of prestress losses in the cylindrical part of containment of the nuclear power plant*, Proceedings of the 3rd congress of Croatian Society of Mechanics (P. Marović, ed.), Croatian Society of Mechanics, 2000, pp. 607–614.

[133] E. Kröner, *Bounds and effective elastic moduli of disordered materials*, Journal of the Mechanics and Physics of Solids **25** (1977), 137–155.

[134] ———, *Statistical modelling*, Modelling of small deformation of polycrystals (J. Gittus and J. Zarka, eds.), Elsevier Applied Science Publishers, 1986, pp. 229–291.

[135] J. L. Kuhn and P. G. Charalambides, *Modeling of plain weave fabric composite geometry*, Journal of Composite Materials **33** (1999), no. 3, 188–220.

[136] J.L. Kuhn, Haan S.I., and P.G. Charalambides, *A semi-analytical method for the calculation of the elastic micro-fields in plain weave fabric composites subjected to in-plane loading*, Journal of Composite Materials **33** (1999), no. 3, 221–266.

[137] J. Kvasnica, *Statistická fyzika [Statistical physics]*, second ed., Academia, 1998.

[138] V. Kvasnička, J. Pospíchal, and P. Tiňo, *Evolučné algoritmy [Evolutionary algorithms]*, STU Bratislava, 2000.

[139] D. C. Lagoudas, A. C. Gavazzi, and H. Nigam, *Elastoplastic behavior of metal matrix composites based on incremental plasticity and the Mori-Tanaka averaging scheme*, Computational Mechanics **8** (1991), 193–203.

[140] N. Laws, *The elastic response of composite materials*, p. 465, International Atomic Energy Agency, Vienna, 1980.

[141] N. Laws and R.E. McLaughin, *Self-consistent estimates for the viscoelastic creep compliance of composite materials*, Proceedings of the Royal Society of London A **359** (1978), 251–273.

[142] A.I. Leonov, *Nonequilibrium thermodynamics and rheology of viscoelastic polymer media*, Journal of Rheology **15** (1976), 85.

[143] I.M. Levin, *Determination of composite material elastic and thermoelastic constants*, Mechanika Tvjordovo Tela **11** (1976), no. 6, 1937–145.

[144] J. Li and G. J. Weng, *A unified approach from elasticity to viscoelasticity to viscoplasticity of particle-reinforced solids*, International Journal of Plasticity **14** (1998), no. 1–3, 193–208.

[145] M. Li, S. Ghosh, O. Richmond, H. Weiland, and T. N. Rouns, *Three dimensional characterization and modeling of particle reinforced metal matrix composites: I. Quantitative description of microstructural morphology, II. Damage characterization*, Materials Science and Engineering A **265, 266** (1999), no. 1–2, 1–2, 153–173, 221–240.

[146] M. Li, S. Ghosh, T. N. Rouns, H. Weiland, O. Richmond, and W. Hunt, *Serial sectioning method in the construction of 3-D microstructures for particle-reinforced MMCs*, Materials Characterization **41** (1998), no. 2–3, 81–95.

[147] B. Lu and S. Torquato, *Lineal-path function for random heterogeneous materials*, Physical Review E **45** (1992), no. 2, 922–929.

[148] D. Lukkassen, G. Nguetseng, and P. Wall, *Two scale convergence*, International Journal of Pure and Applied Mathematics **2** (2002), no. 1, 35–86.

[149] D. Lukkassen, L.-E. Persson, and P. Wall, *Some engineering and mathematical aspects on the homogenization method*, Composites Engineering **5** (1995), no. 5, 519–531.

[150] S.W. Mahfoud and D. E. Goldberg, *A genetic algorithm for parallel simulated annealing*, Parallel Problem Solving from Nature (R. Manner and B. Manderick, eds.), vol. 2, North-Holland, Amsterdam, 1992, pp. 301–310.

[151] S.W. Mahfoud and D.E. Goldberg, *Parallel recombinative simulated annealing: A genetic algorithm*, Parallel Computing **21** (1995), no. 1, 1–28.

[152] C. Mahwart, S. Torquato, and R. Hilfer, *Stochastic reconstruction of sandstones*, Physical Review E **62** (2000), no. 1, 893–899.

[153] K. Z. Markov, *On the cluster bounds for the effective properties of microcraked solids*, Journal of the Mechanics and Physics of Solids **46** (1998), no. 2, 357–388.

[154] B. Marvalová, *Určení efektivních mechanických vlastností kompozitů vyztužených tkaninou plátnové vazby [Determination of effective elastic properties of woven fabric reinforced composites]*, Habilitation thesis, Technical University of Liberec, 2000.

[155] A.M. Matache, I. Babuška, and C. Schwab, *Generalized p-FEM in homogenization*, Numerische Mathematik **86** (2000), no. 2, 319–375.

[156] A.M. Matache and C. Schwab, *Homogenization via p-FEM for problems with microstructure*, Applied Numerical Mathematics **33** (2000), no. 1–4, 43–59.

[157] K. Matouš, M. Lepš, J. Zeman, and M. Šejnoha, *Applying genetic algorithms to selected topics commonly encountered in engineering practice*, Computer Methods in Applied Mechanics and Engineering **190** (2000), no. 13–14, 1629–1650.

[158] S.A. Meguid and G.D. Hu, *A new finite element for treating plane thermomechanical heterogeneous solids*, International Journal for Numerical Methods in Engineering **44** (1999), no. 4, 567–585.

[159] Z. Michalewicz, *Genetic Algorithms + Data Structures = Evolution Programs*, third ed., Springer-Verlag, 1996.

[160] Z. Michalewicz, T. D. Logan, and S. Swaminathan, *Evolutionary operators for continuous convex parameter spaces*, Proceedings of the 3rd Annual Conference on Evolutionary Programming (River Edge, NJ) (A.V. Sebald and L.J. Fogel, eds.), World Scientific Publishing, 1994, pp. 84–97.

[161] J. C. Michel, H. Moulinec, and P. Suquet, *Effective properties of composite materials with periodic microstructure: A computational approach*, Computer Methods in Applied Mechanics and Engineering **172** (1999), 109–143.

[162] ———, *A computational scheme for linear and non-linear composites with arbitrary phase contrast*, International Journal for Numerical Methods in Engineering **52** (2001), no. 1–2, 139–160.

[163] C. Miehe, *Strain-driven homogenization of inelastic microstructures and composites based on an incremental variational formulation*, International Journal for Numerical Methods in Engineering **55** (2002), no. 11, 1285–1322.

[164] K. Miettinen, P. Neittaanmäki, M.M. Mäkelä, and J. Périaux (eds.), *Evolutionary algorithms in engineering and computer science: Recent advances in genetic algorithms, evolutionary strategies, evolutionary programming, genetic programming and industrial applications*, John Wiley & Sons, 1999.

[165] G. W. Milton, *Bounds on the elastic and transport properties of two-component composites*, Journal of the Mechanics and Physics of Solids **30** (1982), no. 3, 177–191.

[166] ———, *On characterizing the set of possible effective tensors composites: The variational method and the translation method*, Communications in Pure and Applied Mathematics **43** (1990), no. 1, 63–125.

[167] ———, *The theory of composites*, Cambridge Monographs on Applied and Computational Mathematics, vol. 6, Cambridge University Press, 2002.

[168] G. W. Milton and R.V. Kohn, *Variational bounds for the effective moduli of anisotropic composites*, Journal of the Mechanics and Physics of Solids **36** (1988), no. 6, 597–629.

[169] G. W. Milton and N. Phan-Thien, *New bounds on effective elastic moduli of 2-component materials*, Proceedings of the Royal Society of London A **380** (1982), no. 1779, 305–331.

[170] R. C. Morgan and I. Babuška, *An approach for constructing families of homogenized equations for periodic media. 1. An integral representation and its consequences*, SIAM Journal on Mathematical Analysis **22** (1991), no. 1, 19–33.

[171] ———, *An approach for constructing families of homogenized equations for periodic media. 2. Properties of the kernel*, SIAM Journal on Mathematical Analysis **22** (1991), no. 1, 1–15.

[172] T. Mori and K. Tanaka, *Average stress in matrix and average elastic energy of elastic materials with misfitting inclusions*, Acta Metallurgica **21** (1973), 571.

[173] H. Moulinec and P. Suquet, *A numerical method for computing the overall response of non-linear composites with complex microstructure*, Computer Methods in Applied Mechanics and Engineering **157** (1998), no. 1–2, 1998.

[174] T. Mura, *Micromechanics of defects in solids*, Monographs and textbooks on mechanics of solids and fluids, vol. 3, Martinus Nijhoof Publishers, 1982.

[175] F. Murat and L. Tartar, *H-convergence*, Topics in the Mathematical Theory of Composite Materials (R.V. Kohn and A. Cherkaev, eds.), Progress in Nonlinear Differential Equations and Their Applications, vol. 31, Birkhäuser, 1997, pp. 21–44.

[176] G. Nagai, T. Yamada, and A. Wada, *Accurate modeling and fast solver for the stress analysis of concrete materials based on digital image processing technique*, International Journal for Computational Civil and Structural Engineering **1** (2001).

[177] N.K. Naik and P.S. Shembekar, *Elastic behavior of woven fabric composites. 1. Lamina analysis*, Journal of Composite Materials **26** (1992), no. 15, 2196–2225.

[178] V. Nesi, D.R.S. Talbot, and J.R. Willis, *Translation and related bounds for the response of a nonlinear composite conductor*, Proceedings of the Royal Society of London A **455** (1999), no. 1990, 3687–3707.

[179] N. Neuss, W. Jager, and G. Wittum, *Homogenization and multigrid*, Computing **66** (2001), no. 1, 1–26.

[180] G. Nguetseng, *A general convergence result for a functional related to the theory of homogenization*, SIAM Journal of Mathematical Analysis **20** (1989), no. 3, 608–623.

[181] H.V. Ngyuen, J. Pastor, and D. Muller, *A method for predicting linear viscoelastic behavior of composites, a comparison of other methods an experimental validation*, European Journal of Mechanics A **14** (1995), no. 6, 939–960.

[182] A.N. Norris, *A differential scheme for the effective elastic moduli of composites*, Mechanics of Materials **4** (1985), no. 1, 1–16.

[183] J. T. Oden and K. S. Vemaganti, *Adaptive modelling of composite structures : Modelling error estimation*, International Journal for Computational Civil and Structural Engineering **1** (2000), no. 1, 1–16.

[184] ———, *Estimation of local modeling error and goal-oriented adaptive modeling of heterogeneous materials I. Error estimates and adaptive algorithms*, Journal of Computational Physics **164** (2000), no. 1, 22–47.

[185] J.T. Oden and S. Prudhomme, *Adaptive modeling in computational mechanics*, TICAM Report 02-05, Texas Institute of Computational and Applied Mathematics, The University of Texas, Austin, 2002, `http://www.ticam.utexas.edu/reports/2002.html`.

[186] H. Okada, Y. Fukui, and N. Kumazawa, *Homogenization method for heterogeneous materials based on boundary element method*, Computers & Structures **79** (2001), no. 20–21, 1839–1850.

[187] M. Ostoja-Starzewski, *Random field models in heterogeneous materials*, International Journal of Solids and Structures **35** (1998), no. 19, 2429–2455.

[188] ———, *The use, misuse, and abuse of stochastic random media*, Proceeding of European Conference on Computational Mechanics, 2001.

[189] H. Owhadi, *Approximation of the effective conductivity of ergodic media by periodization*, Tech. Report math.PR/0201062, `http://xxx.lanl.gov`, 2002.

[190] C.M. Pastore, *Quantification of processing artifacts in textile composites*, Composites Manufacturing **4** (1993), no. 4, 217–226.

[191] C.M. Pastore, A.E. Bogdanovich, and Y.A. Gowayed, *Applications of a mesovolume-based analysis for textile composite structures*, Composites Engineerings **3** (1993), no. 2, 181–194.

[192] C.M. Pastore and Y.A. Gowayed, *A self-consistent fabric geometry model - modification and application of a fabric geometry model to predict the elastic properties of textile composites*, Journal of Composites Technology & Research **16** (1994), no. 1, 32–36.

[193] B. Patzák, *Výpočetní modely pro beton [Computational models of concrete]*, Ph.D. thesis, CTU in Prague, Faculty of Civil Engineering, 1996.

[194] P. Paumelle, A. Hassim, and F. Léné, *Composites with woven reinforcements : Calculation and parameter analysis of the properties of the homogeneous equivalent*, Recherche Aerospatiale **1** (1990), 1–12.

[195] ———, *Microstress analysis in woven composite structure*, Recherche Aerospatiale **6** (1991), 47–62.

[196] S. Pecullan, L. V. Gibiansky, and S. Torquato, *Scale effects on the elastic behavior of periodic and hierarchical two-dimensional composites*, Journal of the Mechanics and Physics of Solids **47** (1999), no. 7, 1509–1542.

[197] P. Pedregal, *Variational methods in nonlinear elasticity*, Society for Industrial and Applied Mathematics, 2000.

[198] P. Ponte Castañeda, *The effective mechanical properties of non-linear isotropic composites*, Journal of the Mechanics and Physics of Solids **39** (1991), no. 1, 45–71.

[199] ———, *Second-order homogenization estimates for nonlinear composites incorporating field fluctuations: I–theory, II–applications*, Journal of the Mechanics and Physics of Solids **50** (2002), no. 4, 737–757, 759–782.

[200] P. Ponte Castañeda and P. Suquet, *Nonlinear composites*, Advances in Applied Mechanics, vol. 34, 1998, pp. 171–302.

[201] P. Ponte Casteñada and J.R. Willis, *The effect of spatial distribution on the effective behaviour of composite materials and cracked media*, Journal of the Mechanics and Physics of Solids **43** (1995), no. 12, 1919–1951.

[202] G. L. Povirk, *Incorporation of microstructural information into models of two-phase materials*, Acta metallurgica et materialia **43** (1995), no. 8, 3199–3206.

[203] W. H. Press, S. A. Teukolsky, W. T. Vetterling, and B. P. Flannergy, *Numerical recipes in C*, second ed., Cambridge University Press, 1992, Also available as `http://www.nr.com`.

[204] P. Procházka, *Základy mechaniky složených materialů [Elements of mechanics of composite materials]*, Academia Praha, 2001.

[205] R. Pyrz, *Correlation of microstructure variability and local stress field in two-phase materials*, Materials Science and Engineering **A177** (1994), 253–259.

[206] J. Quintanilla and S. Torquato, *Microstructure functions for a model of statistically inhomogeneous random media*, Physical Review E **55** (1997), no. 2, 1558–1565.

[207] I.S. Raju and J.T. Wang, *Classical laminate theory models for woven fabric composites*, Journal of Composites Technology & Research **16** (1994), no. 4, 289–303.

[208] K. Rektorys, *Variační metody v inženýrských problémech a v problémech matematické fyziky [Variational Methods in Mathematics, Science, and Engineering]*, second ed., Academia Praha,[Reidel Publishing Company], 2001,[1980].

[209] Z.-Y. Ren and Q.-S. Zheng, *A quantitative study of minimum sizes of representative volume elements of cubic polycrystals – numerical experiments*, Journal of the Mechanics and Physics of Solids **50** (2002), no. 4, 881–893.

[210] A. Reuss, *Berechnung der Fliessgrenze von Mischkristallen auf Grund der Plastizatätsbedingung für eirkristalle*, Zietschirft für Angewandte Matematik und Mechanik **9** (1929), 49.

[211] M.D. Rintoul and S. Torquato, *Reconstruction of the structure of dispersions*, Journal of Colloid and Interface Science **186** (1997), no. 2, 467–476.

[212] B.D. Ripley, *Modelling of spatial patterns*, Journal of the Royal Statistical Society - Series B (methodological) **39** (1977), no. 2, 172–192.

[213] T. Roubíček, *Relaxation in optimization theory and variational calculus*, Walter de Gruyter, 1997.

[214] A. K. Roy, *Comparison of in situ damage assessment in unbalanced fabric composite and model laminate of planar (one-directional) crimping*, Composites Science and Technology **58** (1998), no. 11, 1793–1801.

[215] A. K. Roy and S. Sihn, *Development of a three-dimensional mixed variational model for woven composites. I. Mathematical formulation; II. Numerical solution and validation*, International Journal of Solids and Structures **38** (2001), no. 34–35, 5935–5947; 5949–5962.

[216] M. G. Rozman and M. Utz, *Efficient reconstruction of multiphase morphologies from correlation functions*, Physical Review E **63** (2001), 066701–1–066701–8.

[217] ———, *Uniqueness of reconstruction of multiphase morphologies from two-point correlation function*, Physical Review Letters **89** (2002), no. 13, 135501–1–135501–4.

[218] W. Rudin, *Real and complex analysis*, McGraw-Hill, 1966.

[219] D. Rypl, *T3D program homepage*, `http://ksm.fsv.cvut.cz/ dr/t3d.html`.

[220] ———, *Sequential and parallel generation of unstructured 3D meshes*, vol. 2, CTU Reports, no. 3, Czech Technical University in Prague, 1998.

[221] K. Sab, *On the homogenization and the simulation of random materials*, European Journal of Mechanics A-Solids **11** (1992), no. 5, 585–607.

[222] E. Sanchez-Palencia, *Nonhomogeneous media and vibration theory*, Lecture Notes in Physics, vol. 127, Springer-Verlag, 1980.

[223] E. Sanchez-Palencia and A. Zaoui (eds.), *Homogenization techniques for composite media*, Lecture notes in Physics, vol. 272, Springer-Verlag, Berlin, 1987.

[224] R.A. Schapery, *On viscoelastic deformation and failure behavior of composite materials with distributed flaws*, Advances in Aerospace Structures and Materials (S.S. Wang and W.J. Renton, eds.), ASME, New York, 1981, pp. 5–20.

[225] Z. Shan and A.M. Gokhale, *Representative volume element for non-uniform microstructures*, Computational Materials Science **24** (2002), 361–379.

[226] N. Sheehan and S. Torquato, *Generating microstructures with specified correlation functions*, Journal of Applied Physics **89** (2001), no. 1, 53–60.

[227] P.S. Shembekar and N.K. Naik, *Elastic behavior of woven fabric composites. 2. Laminate analysis*, Journal of Composite Materials **26** (1992), no. 15, 2226–2246.

[228] S. Z. Sheng and S.V. Hoa, *Three dimensional micro-mechanical modeling of woven fabric composites*, Journal of Composite Materials **35** (2001), no. 19, 1701–1729.

[229] J. R. Shewchuk, *Triangle 1.3 program homepage,* `http://www.cs.cmu.edu/quake/triangle.html`.

[230] S. Shkoller and G. Hegemier, *Homogenization of plain weave composites using two-scale convergence*, International Journal of Solids and Structures **32** (1995), no. 6–7, 783–794.

[231] O. van der Sluis, P. H. J. Vosbeek, P. J. G. Schreurs, and H. E. H. Meijer, *Homogenization of heterogeneous polymers*, International Journal of Solids and Structures **36** (1999), no. 21, 3193–3214.

[232] P. Smith and S. Torquato, *Computer simulation results for the two-point probability function of composite media*, Journal of Computational Physics **76** (1988), 176–191.

[233] V. P. Smyshlyaev and J. R. Willis, *A 'non-local' variational approach to the elastic energy minimization of martensitic polycrystals*, Proceedings of Royal Society A: Mathematical, Physical and Engineering Sciences **454** (1998), no. 1974, 1573–1614.

[234] ———, *On the relaxation of a three-well energy*, Proceedings of Royal Society A: Mathematical, Physical and Engineering Sciences **455** (1999), no. 1983, 779–815.

[235] M.V. Srinivas, *Micromechanical modeling of composite plies and laminates*, Ph.D. thesis, Rensselaer Polytechnic Institute, Troy, New York, 1997.

[236] R. Storn, *On the usage of differential evolution for function optimization*, NAPHIS 1996, Berkeley, 1996, pp. 519–523.

[237] R. Storn and K. Price, *Differential Evolution : A simple and efficient adaptive scheme for global optimization over continuous spaces*, Tech. Report TR-95-012, University of Berkeley, 1995.

[238] D. Stoyan, W.S. Kendall, and W.S. Mecke, *Stochastic geometry and its applications*, Akademie-Verlag Berlin, 1987.

[239] M. Stroeven, H. Askes, and L.J. Sluys, *A numerical approach to determine Representative Volumes for granular materials*, Fifth World Congress on Computational Mechanics (WCCM V) (H.A. Mang, F.G. Rammerstorfer, and J. Eberhardsteiner, eds.), Vienna University of Technology, 2002, `http://wccm.tuwien.ac.at`, pp. 1–16.

[240] W. Sun, F. Lin, and X. Hu, *Computer-aided design and modeling of composite unit cells*, Composites Science and Technology **61** (2001), no. 2, 289–299.

[241] P. Suquet, *Elements of homogenization for inelastic solid mechanics*, Homogenization Techniques for Composite Media (E. Sanchez-Palencia and A. Zaoui, eds.), Lecture notes in Physics, vol. 272, Springer-Verlag, Berlin, 1987, pp. 194–278.

[242] B. Szabó and I. Babuška, *Finite element analysis*, John Wiley & Sons, 1991.

[243] A. Tabiei and W. Yi, *Comparative study of predictive methods for woven fabric composite elastic properties*, Composite Structures **58** (2002), no. 1, 149–164.

[244] N. Takano, Y. Uetsuji, Y. Kashiwagi, and M. Zako, *Hierarchical modelling of textile composite materials and structures by the homogenization method*, Modelling and Simulation in Materials Science and Engineering **7** (1999), no. 2, 207–231.

[245] N. Takano, M. Zako, T. Okazaki, and K. Terada, *Microstructure-based evaluation of the influence of woven architecture on permeability by asymptotic homogenization theory*, Composites Science and Technology **62** (2002), no. 10–11, 1347–1356.

[246] D. R. S. Talbot and J. R. Willis, *Variational principles for inhomogeneous nonlinear media*, IMA Journal of Applied Mathematics **35** (1985), no. 1, 39–54.

[247] M.S. Talukdar, O. Torsaeter, and M.A. Ionnidis, *Stochastic reconstruction of particulate media from two-dimensional images*, Journal of Colloid and Interphase Science **248** (2002), no. 2, 419–428.

[248] P. Tan, L. Tong, and G.P. Steven, *Modelling for predicting the mechanical properties of textile composites - A review*, Composites Part A-Applied Science and Manufacturing **28** (1997), no. 11, 903–922.

[249] L. Tartar, *Memory effects and homogenization*, Archive for Rational Mechanics and Analysis **111** (1990), no. 2, 121–133.

[250] J. L. Teplý and G. J. Dvorak, *Bound on overall instantaneous properties of elastic-plastic composites*, Journal of the Mechanics and Physics of Solids **36** (1988), no. 1, 29–58.

[251] K. Terada, M. Hori, T. Kyoya, and N. Kikuchi, *Simulation of the multi-scale convergence in computational homogenization approaches*, International Journal of Solids and Structures **37** (2000), no. 16, 2285 – 2311.

[252] K. Terada and N. Kikuchi, *A class of general algorithms for multi-scale analyses of heterogeneous media*, Computer Methods in Applied Mechanics and Engineering **190** (2001), no. 40–41, 5427–5464.

[253] K. Terada, T. Miura, and N. Kikuchi, *Digital image-based modeling applied to the homogenization analysis of composite materials*, Computational Mechanics **20** (1997), no. 4, 331–346.

[254] T.A. Tervoort, *Constitutive modelling of polymer glasses. Finite, nonlinear viscoelastic behaviour of polycarbonate*, Ph.D. thesis, Technische Universitet Eindhoven, 1996, `http://www.mate.tue.nl/mate/publications/index.php/4`.

[255] S. Torquato, *Random heterogenous media: Microstructure and improved bounds on effective properties*, Applied Mechanics Review **44** (1991), no. 2, 37–76.

[256] ———, *Effective stiffness tensor of composite media-I.Exact series expansion*, Journal of the Mechanics and Physics of Solids **45** (1997), no. 9, 1421–1448.

[257] ———, *Random heterogeneous materials: Microstructure and macroscopic properties*, Springer-Verlag, 2001.

[258] S. Torquato and G. Stell, *Microstructure of two-phase random media.I. The n-point probability functions*, Journal of Chemical Physics **77** (1982), no. 4, 2071–2077.

[259] R. Valenta, *Určení materiálovych parametrů pro popis nelineárně viskoelastického chování epoxidové pryskyřice PR100/2+EM100E [Determination of material parameters for the description of nonlinear viscoelastic behavior of the PR100/2+EM100E epoxy resin]*, Bažant Prize essay, Faculty of Civil Engineering, CTU in Prague, 2001.

[260] ———, *Numerická implementace Leonova modelu, [Numerical implementation of Leonov's model]*, Bažant Prize essay, Faculty of Civil Engineering, CTU in Prague, 2002.

[261] R. Valenta, J. Šejnoha, and M. Šejnoha, *Transformace funkce dotvarování na relaxační funkci [Transformation of creep function into relaxation function]*, Submitted for publication, 2002.

[262] O. van der Sluis, P.J.G. Schreurs, W.A.M. Brekelmans, and H.E.H. Meijer, *Overall behaviour of heterogeneous elastoviscoplastic materials: Effect of microstructural modelling*, Mechanics of Materials **32** (2000), no. 8, 449–462.

[263] P. Vandeurzen, J. Ivens, and I. Verpoest, *Micro-stress analysis of woven fabric composites by multilevel decomposition*, Journal of Composite Materials **32** (1998), no. 7, 623–651.

[264] Ph. Vandeurzen, I. Verpoest, and J. Ivens, *A three-dimensional micromechanical analysis of woven-fabric composites: I. Geometric analysis;II. Elastic analysis*, Composites Science and Technology **56** (1996), no. 11, 1303–1315;1317–1327.

[265] J. Černý, *Thermodynamical approach to the traveling salesman problem: An efficient simulation algorithm*, Journal of Optimization Theory and Applications **45** (1985), 41–51.

[266] K. S. Vemaganti and J. T. Oden, *Estimation of local modeling error and goal-oriented adaptive modeling of heterogeneous materials; Part II: A computational environment for adaptive modeling of heterogeneous elastic solids*, Computer Methods in Applied Mechanics and Engineering **190** (2001), no. 46–47.

[267] W. Voight, *Über die Beziehung zwischen den beiden Elastizitätskonstanten isotroper Köper*, Wiedemanns Annalen der Physics und Chemie **34** (1889), 537–587.

[268] M. Šejnoha, *Micromechanical analysis of unidirectional fibrous composite plies and laminates*, CTU Reports, vol. 3, Czech Technical University in Prague, 1999.

[269] M. Šejnoha and K. Matouš, *Nonlinear analysis of initially prestressed laminates*, Contributions to computational mechanics in Civil Engineering, CTU Reports, vol. 3, CTU in Prague, 1999, pp. 55–68.

[270] M. Šejnoha and J. Šejnoha, *Multi-scale modeling in engineering*, Journal of Theoretical and Applied Mechanics (2003), accepted for publication.

[271] M. Šejnoha and J. Zeman, *Micromechanical analysis of random composites*, vol. 6, CTU Reports, no. 1, Czech Technical University in Prague, 2002.

[272] A. M. Wafa, *Application of the transformation field analysis to inelastic composite materials and structures*, Ph.D. thesis, Rensselaer Polytechnic Institute, Troy, New York, 1994.

[273] J. L. Walpole, *On bounds for the overall moduli of heterogeneous systems I, II*, Journal of the Mechanics and Physics of Solids **14** (1966), 151, 289.

[274] ———, *Elastic behaviour of composite materials: Theoretical foundations*, Advances in Applied Mechanics **11** (1981), 169–242.

[275] G. Weissenbach, L. Limmer, and D. Brown, *Representation of local stiffness variation in textile composites*, Polymers & Polymer Composites **5** (1997), no. 2, 95–101.

[276] G. J. Weng, *The theoretical connection between Mori-Tanaka's theory and Hashin-Shtrikman-Walpole bounds*, International Journal of Engineering Science **28** (1990), 1111–1120.

[277] R. Wentorf, R. Collar, M. S. Shephard, and J. Fish, *Automated modeling for complex woven mesostructures*, Computer Methods in Applied Mechanics and Engineering **172** (1999), no. 1–4, 273–291.

[278] J. Whitcomb, J. Noh, and C. Chapman, *Evaluation of various approximate analyses for plain weave composites*, Journal of Composite Materials **33** (1999), no. 21, 1958–1980.

[279] J. Whitcomb and K. Sriregan, *Effect of various approximations on predicted progressive failure in plain weave composites*, Composite Structures **34** (1996), no. 1, 13–20.

[280] J. Whitcomb and X.D. Tang, *Effective moduli of woven composites*, Journal of Composite Materials **35** (2001), no. 23, 2127–2144.

[281] J. Whitcomb and K. S. Woo, *Enhanced direct stiffness method for finite-element analysis of textile composites*, Composite Structures **28** (1994), no. 4, 385–390.

[282] J. Whitcomb, K. S. Woo, and S. Gundapaneni, *Macro finite-element for analysis of textile composites*, Journal of Composite Materials **28** (1994), no. 7, 607–618.

[283] M. Wierer, *Multi-scale analysis of woven composites*, Master's thesis, Faculty of Civil Engineering, Czech Technical University in Prague, 2002.

[284] M. Wierer, J. Zeman, M. Šejnoha, and J. Šejnoha, *Effect of fiber prestress on the behavior of woven composite tubes*, Fifth World Congress on Computational Mechanics (WCCM V) (H.A. Mang, F.G. Rammerstorfer, and J. Eberhardsteiner, eds.), Vienna University of Technology, 2002, `http://wccm.tuwien.ac.at`, pp. 1–10.

[285] J. R. Willis, *Bounds and self-consistent estimates for the overall properties of anisotropic composites*, Journal of the Mechanics and Physics of Solids **25** (1977), 185–202.

[286] ———, *Variational and related methods for the overall properties of composites*, Advances in Applied Mechanics, vol. 21, 1981, pp. 2–74.

[287] J.R. Willis, *A polarization approach to scattering of elastic waves. I. scattering by a single inclusion; II. multiple scattering from inclusions*, Journal of the Mechanics and Physics of Solids **28** (1980), 287–305; 307–327.

[288] K. Woo and J. D. Whitcomb, *Three-dimensional failure analysis of plain weave textile composites using a global/local finite element method*, Journal of Composite Materials **30** (1996), no. 9, 984–1003.

[289] ———, *Effects of fiber tow misalignment on the engineering properties of plain weave textile composites*, Composite Structures **37** (1997), no. 3–4, 281–417.

[290] _____, *A post-processor approach for stress analysis of woven textile composites*, Composites Science and Technology **60** (2000), no. 5, 693–704.

[291] C. L. Y. Yeong and S. Torquato, *Reconstructing random media*, Physical Review E **57** (1998), no. 1, 495–506.

[292] _____, *Reconstructing random media. II. Three-dimensional media from two-dimensional cuts*, Physical Review E **58** (1998), no. 1, 224–233.

[293] Y.-M. Yi, S.-H. Park, and S.-K. Youn, *Asymptotic homogenization of viscoelastic composites with periodic microstructures*, International Journal of Solids and Structures **35** (1998), no. 17, 2039–2055.

[294] S.W. Yurgartis, K. Morey, and J. Jortner, *Measurement of yarn shape and nesting in plain-weave composites*, Composites Science and Technology **46** (1993), no. 1, 39–50.

[295] S. P. Yushanov and A. E. Bogdanovich, *Stochastic theory of composite materials with random waviness of the reinforcements*, International Journal of Solids and Structures **35** (1998), no. 22, 2901–2930.

[296] _____, *Fiber waviness in textile composites and its stochastic modeling*, Mechanics of Composite Materials **36** (2000), no. 4, 297–318.

[297] J. Zeman, *Analysis of mechanical properties of fiber-reinforced composites with random microstructure*, Master's thesis, Czech Technical University in Prague, 2000.

[298] J. Zeman and M. Šejnoha, *Numerical evaluation of effective properties of graphite fiber tow impregnated by polymer matrix*, Journal of the Mechanics and Physics of Solids **49** (2001), no. 1, 69–90.

[299] _____, *On determination of periodic unit cell for plain weave fabric composites*, Engineering Mechanics **1–2** (2002), no. 9, 65–74.

[300] Y.C. Zhang and J. Harding, *A numerical micromechanics analysis of the mechanical properties of a plain weave composite*, Computers & Structures **36** (1990), no. 5, 839–844.

[301] O.C. Zienkiewicz, *The finite element method*, third ed., McGraw-Hill Book Company, 1977.

Appendix A

CONSTITUTIVE MODELS

The purpose of this chapter is to gather information related to various constitutive models used throughout the text. In addition, explicit relations between tensorial and engineering representation of different quantities are presented to complement the notation introduced on page xiii. Although the majority of the presented material is well-known, we hope that such a relatively systematic treatment will improve clarity of the present work and highlight relation between individual models.

A.1 Vectorial representation of second-order tensors

Standard engineering representation of stress and strain tensors (see, e.g., [21, 24, 75]) is employed throughout the text. Assuming the Cartesian coordinate system with axes x_1, x_2 and x_3, the symmetric second-order Cauchy stress tensor $\boldsymbol{\sigma}$ is then represented as a 6×1 vector,

$$\{\sigma\} = \{\sigma_{11}, \sigma_{22}, \sigma_{33}, \sigma_{13}, \sigma_{23}, \sigma_{12}\}^{\mathsf{T}}, \tag{A.1}$$

and the symmetric second-order tensor of small strains $\boldsymbol{\varepsilon}$ is written as a 6×1 vector

$$\{\varepsilon\} = \{\varepsilon_{11}, \varepsilon_{22}, \varepsilon_{33}, 2\varepsilon_{13}, 2\varepsilon_{23}, 2\varepsilon_{12}\}^{\mathsf{T}}. \tag{A.2}$$

The similar approach is used for polarization stresses $\boldsymbol{\tau}$ and strains $\boldsymbol{\gamma}$

$$\{\tau\} = \{\tau_{11}, \tau_{22}, \tau_{33}, \tau_{13}, \tau_{23}, \tau_{12}\}^{\mathsf{T}}, \tag{A.3}$$

$$\{\gamma\} = \{\gamma_{11}, \gamma_{22}, \gamma_{33}, 2\gamma_{13}, 2\gamma_{23}, 2\gamma_{12}\}^{\mathsf{T}} \tag{A.4}$$

and for eigenstress $\boldsymbol{\lambda}$ and eigenstrain $\boldsymbol{\mu}$ tensors

$$\{\lambda\} = \{\lambda_{11}, \lambda_{22}, \lambda_{33}, \lambda_{13}, \lambda_{23}, \lambda_{12}\}^{\mathsf{T}}, \tag{A.5}$$

$$\{\mu\} = \{\mu_{11}, \mu_{22}, \mu_{33}, 2\mu_{13}, 2\mu_{23}, 2\mu_{12}\}^{\mathsf{T}}. \tag{A.6}$$

The inverse a_{ij}^{-1} of a second-order tensor a_{ij} is given by the relation $a_{ik}^{-1}a_{kj} = \delta_{ij}$, where $\boldsymbol{\delta}$ is Kronecker's second-order unit tensor with vectorial representation $\{\delta\}$

$$\{\delta\} = \{1, 1, 1, 0, 0, 0\}^{\mathsf{T}}. \tag{A.7}$$

The trace $\mathrm{Tr}\,\boldsymbol{a} = a_{kk}$ of a second-order tensor a_{ij} can be written in vectorial representation as

$$\mathrm{Tr}\,\{\mathsf{a}\} = \{\delta\}^{\mathsf{T}}\{\mathsf{a}\}, \tag{A.8}$$

and the deviatoric part of a second-order tensor $\boldsymbol{a}$, given by $a'_{ij} = a_{ij} - \frac{1}{3}\delta_{ij}a_{kk}$, can be obtained as

$$\{\mathsf{a}'\} = \{\mathsf{a}\} - \frac{1}{3}\{\delta\}^{\mathsf{T}}\{\mathsf{a}\}\{\delta\}. \tag{A.9}$$

Note for the sake of completeness that the deviatoric part of the stress tensor $\boldsymbol{\sigma}$ is denoted as $\boldsymbol{s} \equiv \boldsymbol{\sigma'}$ and the deviatoric part of the strain tensor $\boldsymbol{\varepsilon}$ is denoted as $\boldsymbol{e} \equiv \boldsymbol{\varepsilon'}$.

A.1.1 Global-local transformations

Vector transformations. Recall that the relation between vector $\{\mathsf{r}^{\ell}\}$ in the local coordinate system and the global coordinate system $\{\mathsf{r}^{\mathrm{g}}\}$ are provided in terms of transformation matrix $[\mathsf{T}]$, $\{\mathsf{r}^{\ell}\} = [\mathsf{T}]\,\{\mathsf{r}^{\mathrm{g}}\}$ [24, 97]. If the rotation is defined in terms of Euler's angles ψ, ϑ and φ, this matrix is provided by

$$[\mathsf{T}] = \begin{bmatrix} \cos\varphi\cos\psi - \sin\varphi\cos\vartheta\sin\psi & \cos\varphi\sin\psi + \sin\varphi\cos\vartheta\cos\psi & \sin\varphi\sin\vartheta \\ -\sin\varphi\cos\psi - \cos\varphi\cos\vartheta\sin\psi & -\sin\varphi\sin\psi + \cos\varphi\cos\vartheta\cos\psi & \cos\varphi\sin\vartheta \\ \sin\vartheta\sin\psi & -\sin\vartheta\cos\psi & \cos\vartheta \end{bmatrix}. \tag{A.10}$$

Note that this parameterization corresponds to successive rotation of global coordinate axes by angle ψ about the x_3 axis, then by angle ϑ about the rotated x_1' axis and finally to rotation about the transformed x_3'' axis by angle φ to obtain the local coordinate system x_1^{ℓ}, x_2^{ℓ} and x_3^{ℓ}.

Stress transformations. The transformation of stresses from the local to the global coordinate systems is provided by means of fourth-order tensor $\mathbf{T}_{\boldsymbol{\sigma}}$, $\boldsymbol{\sigma}^{\boldsymbol{\ell}} = \mathbf{T}_{\boldsymbol{\sigma}} : \boldsymbol{\sigma}^{\mathbf{g}}$, with $\mathbf{T}_{\boldsymbol{\sigma}}$ defined as $(T_\sigma)_{ijkl} = T_{ik}T_{jl}$ (see, e.g., [24, 97]). The matrix form of the tensor $\mathbf{T}_{\boldsymbol{\sigma}}$ is written as

$$[\mathsf{T}_\sigma] = \begin{bmatrix} \mathsf{T}_{11}^2 & \mathsf{T}_{12}^2 & \mathsf{T}_{13}^2 & 2\mathsf{T}_{12}\mathsf{T}_{13} & 2\mathsf{T}_{11}\mathsf{T}_{13} & 2\mathsf{T}_{11}\mathsf{T}_{12} \\ \mathsf{T}_{21}^2 & \mathsf{T}_{22}^2 & \mathsf{T}_{23}^2 & 2\mathsf{T}_{22}\mathsf{T}_{23} & 2\mathsf{T}_{21}\mathsf{T}_{23} & 2\mathsf{T}_{21}\mathsf{T}_{22} \\ \mathsf{T}_{31}^2 & \mathsf{T}_{32}^2 & \mathsf{T}_{33}^2 & 2\mathsf{T}_{32}\mathsf{T}_{33} & 2\mathsf{T}_{31}\mathsf{T}_{33} & 2\mathsf{T}_{31}\mathsf{T}_{32} \\ \mathsf{T}_{31}\mathsf{T}_{21} & \mathsf{T}_{32}\mathsf{T}_{22} & \mathsf{T}_{33}\mathsf{T}_{23} & \mathsf{T}_{32}\mathsf{T}_{23}+\mathsf{T}_{33}\mathsf{T}_{22} & \mathsf{T}_{33}\mathsf{T}_{21}+\mathsf{T}_{31}\mathsf{T}_{23} & \mathsf{T}_{31}\mathsf{T}_{22}+\mathsf{T}_{32}\mathsf{T}_{21} \\ \mathsf{T}_{31}\mathsf{T}_{11} & \mathsf{T}_{32}\mathsf{T}_{12} & \mathsf{T}_{33}\mathsf{T}_{13} & \mathsf{T}_{32}\mathsf{T}_{13}+\mathsf{T}_{33}\mathsf{T}_{12} & \mathsf{T}_{33}\mathsf{T}_{11}+\mathsf{T}_{31}\mathsf{T}_{13} & \mathsf{T}_{32}\mathsf{T}_{11}+\mathsf{T}_{31}\mathsf{T}_{12} \\ \mathsf{T}_{21}\mathsf{T}_{11} & \mathsf{T}_{32}\mathsf{T}_{12} & \mathsf{T}_{23}\mathsf{T}_{13} & \mathsf{T}_{23}\mathsf{T}_{12}+\mathsf{T}_{22}\mathsf{T}_{13} & \mathsf{T}_{23}\mathsf{T}_{11}+\mathsf{T}_{21}\mathsf{T}_{13} & \mathsf{T}_{11}\mathsf{T}_{22}+\mathsf{T}_{21}\mathsf{T}_{12} \end{bmatrix}. \tag{A.11}$$

Strain transformations. Similarly to the stress transformation, the strain in a local coordinate system is provided by $\boldsymbol{\varepsilon}^{\boldsymbol{\ell}} = \mathbf{T}_{\boldsymbol{\varepsilon}} : \boldsymbol{\varepsilon}^{\mathbf{g}}$, where, in the tensorial notation, $\mathbf{T}_{\boldsymbol{\varepsilon}} = \mathbf{T}_{\boldsymbol{\sigma}}$. The matrix form of $\mathbf{T}_{\varepsilon}$, however, is different from Eq. (A.11),

$$[\mathsf{T}_\varepsilon] = \begin{bmatrix} \mathsf{T}_{11}^2 & \mathsf{T}_{12}^2 & \mathsf{T}_{13}^2 & \mathsf{T}_{12}\mathsf{T}_{13} & \mathsf{T}_{11}\mathsf{T}_{13} & \mathsf{T}_{11}\mathsf{T}_{12} \\ \mathsf{T}_{21}^2 & \mathsf{T}_{22}^2 & \mathsf{T}_{23}^2 & \mathsf{T}_{22}\mathsf{T}_{23} & \mathsf{T}_{21}\mathsf{T}_{23} & \mathsf{T}_{21}\mathsf{T}_{22} \\ \mathsf{T}_{31}^2 & \mathsf{T}_{32}^2 & \mathsf{T}_{33}^2 & \mathsf{T}_{32}\mathsf{T}_{33} & \mathsf{T}_{31}\mathsf{T}_{33} & \mathsf{T}_{31}\mathsf{T}_{32} \\ 2\mathsf{T}_{31}\mathsf{T}_{21} & 2\mathsf{T}_{32}\mathsf{T}_{22} & 2\mathsf{T}_{33}\mathsf{T}_{23} & \mathsf{T}_{32}\mathsf{T}_{23}+\mathsf{T}_{33}\mathsf{T}_{22} & \mathsf{T}_{33}\mathsf{T}_{21}+\mathsf{T}_{31}\mathsf{T}_{23} & \mathsf{T}_{31}\mathsf{T}_{22}+\mathsf{T}_{32}\mathsf{T}_{21} \\ 2\mathsf{T}_{31}\mathsf{T}_{11} & 2\mathsf{T}_{32}\mathsf{T}_{12} & 2\mathsf{T}_{33}\mathsf{T}_{13} & \mathsf{T}_{32}\mathsf{T}_{13}+\mathsf{T}_{33}\mathsf{T}_{12} & \mathsf{T}_{33}\mathsf{T}_{11}+\mathsf{T}_{31}\mathsf{T}_{13} & \mathsf{T}_{32}\mathsf{T}_{11}+\mathsf{T}_{31}\mathsf{T}_{12} \\ 2\mathsf{T}_{21}\mathsf{T}_{11} & 2\mathsf{T}_{32}\mathsf{T}_{12} & 2\mathsf{T}_{23}\mathsf{T}_{13} & \mathsf{T}_{23}\mathsf{T}_{12}+\mathsf{T}_{22}\mathsf{T}_{13} & \mathsf{T}_{23}\mathsf{T}_{11}+\mathsf{T}_{21}\mathsf{T}_{13} & \mathsf{T}_{11}\mathsf{T}_{22}+\mathsf{T}_{21}\mathsf{T}_{12} \end{bmatrix}. \tag{A.12}$$

Finally, recall that the following useful relations hold for matrices $[\mathsf{T}_\varepsilon]$ and $[\mathsf{T}_\sigma]$

$$[\mathsf{T}_\varepsilon]^{-1} = [\mathsf{T}_\sigma]^{\mathsf{T}}, \qquad [\mathsf{T}_\sigma]^{-1} = [\mathsf{T}_\varepsilon]^{\mathsf{T}}. \tag{A.13}$$

A.2 Linear elasticity

We start with the simplest material model of linear elasticity with general eigenstrains and eigenstresses. In this context, the stress-strain relationship is given by [21, 50, 97, 174]

$$\boldsymbol{\sigma}(\mathbf{x}) = \mathbf{L}(\mathbf{x}) : \boldsymbol{\varepsilon}(\mathbf{x}) + \boldsymbol{\lambda}(\mathbf{x}), \tag{A.14}$$

where L_{ijkl} is the fourth-order tensor material stiffness tensor. Thanks to symmetries $L_{ijkl} = L_{klij} = L_{jikl}$, the matrix representation of the tensor L_{ijkl} is provided by

$$[\mathsf{L}] = \begin{bmatrix} L_{1111} & L_{1122} & L_{1133} & L_{1123} & L_{1113} & L_{1112} \\ L_{2211} & L_{2222} & L_{2233} & L_{2223} & L_{2213} & L_{2212} \\ L_{3311} & L_{3322} & L_{3333} & L_{3323} & L_{3313} & L_{3312} \\ L_{2311} & L_{2322} & L_{2333} & L_{2323} & L_{2313} & L_{2312} \\ L_{1311} & L_{1322} & L_{1333} & L_{1323} & L_{1313} & L_{1312} \\ L_{1211} & L_{1222} & L_{1233} & L_{1223} & L_{1213} & L_{1212} \end{bmatrix}. \tag{A.15}$$

The relation (A.14) then can be written in engineering notation as

$$\{\sigma(\mathbf{x})\} = [\mathsf{L}(\mathbf{x})]\,\{\varepsilon(\mathbf{x})\} + \{\lambda(\mathbf{x})\}. \tag{A.16}$$

The elastic compliance tensor M_{ijkl} is the inverse of the fourth-order tensor L_{ijkl} given by relation $M_{ijmn}L_{mnkl} = I_{ijkl}$, where $I_{ijkl} = \frac{1}{2}\left(\delta_{ik}\delta_{jl} + \delta_{il}\delta_{jk}\right)$ is the fourth-order unit tensor. The matrix representation of the tensor $\mathbf{M}$ is given by

$$[\mathsf{M}] \;=\; \begin{bmatrix} M_{1111} & M_{1122} & M_{1133} & 2M_{1123} & 2M_{1113} & 2M_{1112} \\ M_{2211} & M_{2222} & M_{2233} & 2M_{2223} & 2M_{2213} & 2M_{2212} \\ M_{3311} & M_{3322} & M_{3333} & 2M_{3323} & 2M_{3313} & 2M_{3312} \\ 2M_{2311} & 2M_{2322} & 2M_{2333} & 4M_{2323} & 4M_{2313} & 4M_{2312} \\ 2M_{1311} & 2M_{1322} & 2M_{1333} & 4M_{1323} & 4M_{1313} & 4M_{1312} \\ 2M_{1211} & 2M_{1222} & 2M_{1233} & 4M_{1223} & 4M_{1213} & 4M_{1212} \end{bmatrix} \tag{A.17}$$

and the matrix form of a strain-stress relationship $\boldsymbol{\varepsilon} = \mathbf{M} : \boldsymbol{\sigma} + \boldsymbol{\mu}$ is then provided by

$$\{\varepsilon(\mathbf{x})\} = [\mathsf{M}(\mathbf{x})]\,\{\sigma(\mathbf{x})\} + \{\mu(\mathbf{x})\}. \tag{A.18}$$

The matrices $[\mathsf{L}]$ and $[\mathsf{M}]$ are mutual inverses, $[\mathsf{L}]\,[\mathsf{M}] = [\mathsf{I}]$. Therefore, only the matrix representation of stiffness tensor $[\mathsf{L}]$ is explicitly presented in the following text; the form of the compliance matrix follows from $[\mathsf{M}] = [\mathsf{L}]^{-1}$. Note that the number of independent material parameters can be reduced either by accepting certain assumption about the stress state in a body (see Section A.2.1) or employing symmetries of a material.

Thermally induced eigenstrains. For eigenstrains induced by temperature change $\Delta\theta$, the eigenstress tensor $\boldsymbol{\mu}$ reads as

$$\boldsymbol{\mu}(\mathbf{x}) = \boldsymbol{m}(\mathbf{x})\Delta\theta(\mathbf{x}), \tag{A.19}$$

where $\boldsymbol{m}$ stores the coefficients of thermal expansion. In the engineering notation, the thermal expansion tensor can be written as 6×1 vector

$$\{\mathsf{m}\} = \{\alpha_1, \alpha_2, \alpha_3, 0, 0, 0\}^{\mathsf{T}}. \tag{A.20}$$

It follows from Eq. (A.18) that the eigenstress vector $\{\lambda\}$ assumes the form

$$\{\lambda(\mathbf{x})\} = -\,[\mathsf{L}(\mathbf{x})]\,\{\mu(\mathbf{x})\} = -\,[\mathsf{L}(\mathbf{x})]\,\{\mathsf{m}(\mathbf{x})\}\Delta\theta. \tag{A.21}$$

Isotropic material. For isotropic material, the stiffness matrix is determined by two independent constants. If the material constants are Young's modulus E and Poisson's ratio ν, the stiffness matrix $[\mathsf{L}]$ can be expressed as 6×6 matrix [21, 97, 161]

$$[\mathsf{L}] = \frac{E}{(1+\nu)(1-2\nu)} \begin{bmatrix} 1-\nu & \nu & \nu & 0 & 0 & 0 \\ \nu & 1-\nu & \nu & 0 & 0 & 0 \\ \nu & \nu & 1-\nu & 0 & 0 & 0 \\ 0 & 0 & 0 & \frac{1}{2}(1-2\nu) & 0 & 0 \\ 0 & 0 & 0 & 0 & \frac{1}{2}(1-2\nu) & 0 \\ 0 & 0 & 0 & 0 & 0 & \frac{1}{2}(1-2\nu) \end{bmatrix}. \tag{A.22}$$

In case that the material constants are the bulk modulus K and the shear modulus G, these relations change to [21, 97, 161]

$$[\mathsf{L}] = \begin{bmatrix} K+\frac{4}{3}G & K-\frac{2}{3}G & K-\frac{2}{3}G & 0 & 0 & 0 \\ K-\frac{2}{3}G & K+\frac{4}{3}G & K-\frac{2}{3}G & 0 & 0 & 0 \\ K-\frac{2}{3}G & K-\frac{2}{3}G & K+\frac{4}{3}G & 0 & 0 & 0 \\ 0 & 0 & 0 & G & 0 & 0 \\ 0 & 0 & 0 & 0 & G & 0 \\ 0 & 0 & 0 & 0 & 0 & G \end{bmatrix}. \tag{A.23}$$

Transversally isotropic material. In view of the assumptions of the generalized plane strain discussed in Section A.2.1, the transversally isotropic material with x_3 as the axis of rotational symmetry is considered. Employing Hill's notation [95], the stiffness tensor L can be represented by the 6×6 matrix in the form

$$[\mathsf{L}] = \begin{bmatrix} (k+m) & (k-m) & l & 0 & 0 & 0 \\ (k-m) & (k+m) & l & 0 & 0 & 0 \\ l & l & n & 0 & 0 & 0 \\ 0 & 0 & 0 & p & 0 & 0 \\ 0 & 0 & 0 & 0 & p & 0 \\ 0 & 0 & 0 & 0 & 0 & m \end{bmatrix}. \tag{A.24}$$

The parameters k, m, n, p and l are related to the material engineering constants $E_{\mathrm{A}}, E_{\mathrm{T}}$, ν_{A}, G_{A} and G_{T} using the following relations,

$$\begin{aligned} &k = -[1/G_{\mathrm{T}} - 4/E_{\mathrm{T}} + 4\nu_{\mathrm{A}}^2/E_{\mathrm{A}}]^{-1}, \quad l = 2k\nu_{\mathrm{A}}, \\ &n = E_{\mathrm{A}} + 4k\nu_{\mathrm{A}}^2 = E_{\mathrm{A}} + l^2/k, \qquad\quad m = G_{\mathrm{T}}, \quad p = G_{\mathrm{A}}. \end{aligned} \tag{A.25}$$

A.2.1 Generalized plane strain

The generalized plane strain corresponds to idealization of stress and strain distribution in unidirectional composites, which are characterized by the invariance under the translation along the axial direction x_3 (see, e.g., [97, 161]). It is further assumed that the material is orthotropic with the axial direction x_3 identical to the direction of orthotropy. Then, the out-of plane shear stresses vanish and the only non-zero components of the strain and stress tensors are $\varepsilon_{11}, \varepsilon_{12}, \varepsilon_{22}, \varepsilon_{33}$ and $\sigma_{11}, \sigma_{12}, \sigma_{22}, \sigma_{33}$, respectively. Note that due to assumed perfect bonding between individual phases the components ε_{33} and σ_{33} attain constant values. Thus, the stress tensor $\boldsymbol{\sigma}$ and strain tensor $\boldsymbol{\varepsilon}$ have a 4×1 vector representations,

$$\{\sigma\} = \{\sigma_{11}, \sigma_{22}, \sigma_{12}, \sigma_{33}\}^{\mathsf{T}}, \qquad \{\varepsilon\} = \{\varepsilon_{11}, \varepsilon_{22}, 2\varepsilon_{12}, \varepsilon_{33}\}^{\mathsf{T}}. \tag{A.26}$$

The representation of eigenstress, eigenstrain, polarization stress and strain tensors follow the principles set by Eqs. (A.3)–(A.6). Finally, for the sake of completeness, the explicit form of 4×4 stiffness matrices for material symmetries discussed in the three-dimensional case are presented.

Isotropic material – (E, ν)**.**

$$[\mathsf{L}] = \frac{E}{(1+\nu)(1-2\nu)} \begin{bmatrix} 1-\nu & \nu & 0 & \nu \\ \nu & 1-\nu & 0 & \nu \\ 0 & 0 & \frac{1}{2}(1-2\nu) & 0 \\ \nu & \nu & 0 & 1-\nu \end{bmatrix} \tag{A.27}$$

Isotropic material – (K, G)**.**

$$[\mathsf{L}] = \begin{bmatrix} K+\frac{4}{3}G & K-\frac{2}{3}G & 0 & K-\frac{2}{3}G \\ K-\frac{2}{3}G & K+\frac{4}{3}G & 0 & K-\frac{2}{3}G \\ 0 & 0 & G & 0 \\ K-\frac{2}{3}G & K-\frac{2}{3}G & 0 & K+\frac{4}{3}G \end{bmatrix} \tag{A.28}$$

Transversally isotropic material.

$$[\mathsf{L}] = \begin{bmatrix} (k+m) & (k-m) & 0 & l \\ (k-m) & (k+m) & 0 & l \\ 0 & 0 & m & 0 \\ l & l & 0 & n \end{bmatrix} \tag{A.29}$$

Coefficients of thermal expansion. The tensor of thermal expansion coefficients $\{\mathsf{m}\}$ for the generalized plane strain can be expressed in the form of 4×1 vector

$$\{\mathsf{m}\} = \{\alpha_1, \alpha_2, 0, \alpha_3\}^{\mathsf{T}}. \tag{A.30}$$

A.3 Linear viscoelasticity

The traditional approach in linear viscoelasticity relies on the so-called correspondence principle (see, e.g., [35, 126] and references therein), which can be also employed to relate the overall viscoelastic properties of heterogenous media to its effective elastic properties (see, e.g., [88, 127, 141, 144, 181, 241, 293, to cite a few]. However, this procedure generally needs a numerical inversion of the Laplace or Fourier transform of the viscoelasticity solution, which introduces serious difficulties.

The presented approach avoids this complication by formulating the constitutive equations in the explicit incremental scheme that is derived by converting the integral equations into a rate-type form and by subsequent integration under certain simplifying assumptions [13]. The resulting relations are simple to implement, naturally fit into the eigenstress/strain framework (Eqs. (A.16) and (A.18)) and can be easily extended to nonlinear viscoelastic model described in Section A.4.1.

For a smooth history of the applied stress $\sigma(\cdot)$, the one-dimensional stress response at a time t is given by [21, 35, 126]

$$\varepsilon(t) = J(t,t_0)\sigma(t_0) + \int_{t_0}^{t} J(t,\tau)\frac{\mathrm{d}\sigma(\tau)}{\mathrm{d}\tau}\,\mathrm{d}\tau, \tag{A.31}$$

where $J(\cdot,\cdot)$ is the creep compliance. Similarly, the strain response at a time t for a smooth history of applied strain $\varepsilon(\cdot)$ is provided by

$$\sigma(t) = R(t,t_0)\varepsilon(t_0) + \int_{t_0}^{t} R(t,\tau)\frac{\mathrm{d}\varepsilon(\tau)}{\mathrm{d}\tau}\,\mathrm{d}\tau, \tag{A.32}$$

where $R(\cdot,\cdot)$ is the creep relaxation function.

A.3.1 Dirichlet series expansion

To formulate the constitutive equations for viscoelastic constituents in the differential form, the degenerate Dirichlet kernels

$$J(t,\tau) = \sum_{\mu=1}^{M} \frac{1}{D_\mu(\tau)}\left(1 - \exp\left[y_\mu(\tau) - y_\mu(t)\right]\right), \tag{A.33}$$

$$R(t,\tau) = \sum_{\mu=1}^{M} E_\mu(\tau)\exp\left[y_\mu(\tau) - y_\mu(t)\right], \tag{A.34}$$

where $y_\mu(t) = (t/\Theta_\mu)^{q_\mu}$, are used to approximate the creep and relaxation functions $J(t,\tau)$ and $R(t,\tau)$, respectively. Retardation times Θ_μ must satisfy certain rules necessary for the success of calculation [13, 193] and the coefficient q_μ is introduced in order to reduce the number of terms of the Dirichlet expansions. Parameters D_μ and E_μ are usually obtained by fitting the creep or relaxation functions via Eqs. (A.33) using the method of least squares.

Recall that the compliance function of a linear viscoelastic material represents the strain at time t due to a unit stress applied at time τ and kept constant, while the relaxation function represents the stress at time t due to a unit strain applied at time τ and held constant (compare with Eqs. (A.33) and (A.34)). Therefore, when written in the form of Dirichlet series, these functions can be interpreted by representation provided by the Kelvin and Maxwell chains, respectively (see Fig. A.1). For example, the Maxwell chain model gives the local stress in the form

$$\sigma(\mathbf{x}) = \sum_{\mu=1}^{M} \sigma_\mu(\mathbf{x}), \tag{A.35}$$

where σ_μ, called hidden stress, represents the stress in the μ-th Maxwell unit, which satisfies the differential constitutive equation

$$\frac{\mathrm{d}\sigma_\mu(t)}{\mathrm{d}t} + \sigma_\mu(t)\frac{\mathrm{d}y_\mu(t)}{\mathrm{d}t} = E_\mu(t)\frac{\mathrm{d}\varepsilon(t)}{\mathrm{d}t}, \qquad \frac{\mathrm{d}y_\mu(t)}{\mathrm{d}t} = \frac{E_\mu(t)}{\eta_\mu(t)}, \tag{A.36}$$

where $E_\mu(\cdot)$ and $y_\mu(\cdot)$ are Young's modulus and viscous resistance coefficients of the μ-th unit, respectively. Similar equations can be formulated for the Kelvin model (see, e.g., [13, 21, 35, 193] for more details).

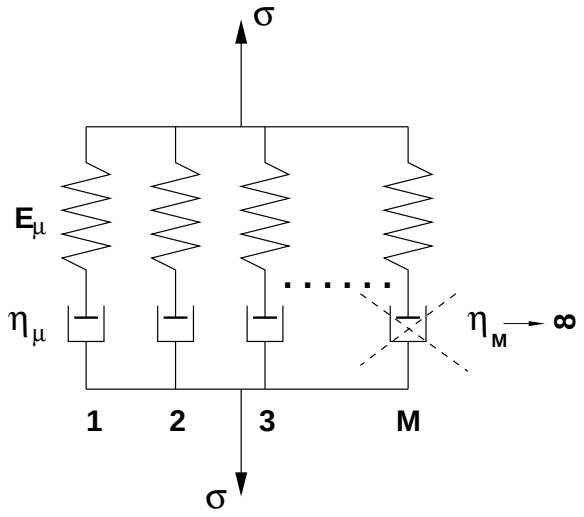

Figure A.1: Maxwell chain rheological model

A.3.2 Generalized Maxwell model

Numerical solution of the viscoelastic problem is based on dividing the time axis into equi-sized intervals of length Δt_i. Suppose that at the beginning of the i-th interval $\langle t_i, t_{i+1}\rangle$, the stresses $\sigma_\mu(t_i), \mu = 1, 2, \ldots, M$, are known. Assuming that $\mathrm{d}y_\mu/\,\mathrm{d}t$, $\mathrm{d}\varepsilon/\,\mathrm{d}t$ and E_μ are constant on a given interval with $E_\mu = E_\mu(t_i + \Delta t_i/2)$, the incremental form of Eq. (A.36) can be written as [13, 21, 193]

$$\Delta\sigma(t_i) = \widehat{E}(t_i)\Delta\varepsilon(t_i) + \Delta\lambda(t_i), \tag{A.37}$$

where the instantaneous Young's modulus $\widehat{E}(t_i)$ and eigenstress increment $\Delta\lambda(t_i)$ are provided by

$$\widehat{E}(t_i) = \sum_{\mu=1}^{M} \widehat{E}_\mu(t_i) = \sum_{\mu=1}^{M} E_\mu(t_i - \Delta t_i/2)\frac{1 - \exp\left(-\Delta y_\mu(t_i)\right)}{\Delta y_\mu(t_i)}, \tag{A.38}$$

$$\Delta\lambda(t_i) = \sum_{\mu=1}^{M} \Delta\lambda_\mu(t_i) = -\sum_{\mu=1}^{M} \left[1 - \exp\left(-\Delta y_\mu(t_i)\right)\right]\sigma_\mu(t_i). \tag{A.39}$$

Finally, the stress σ_μ at the end of the given interval depends solely on the stresses $\sigma_\mu(t_i)$ through the relation

$$\sigma_\mu(t_{i+1}) = \sigma_\mu(t_i)\exp\left(-\Delta y_\mu(t_i)\right) + \frac{\widehat{E}_\mu(t_i)}{\widehat{E}(t_i)}\left(\Delta\sigma(t_i) - \Delta\lambda(t_i)\right). \tag{A.40}$$

The above one-dimensional relations can be easily extended to general stress state by assuming that the material is isotropic and Poisson's ratio ν is the time-independent constant. Then it suffices to replace the instantaneous Young's modulus $\widehat{E}(t_i)$ by the instantaneous material stiffness matrix $[\mathsf{L}(t_i)]$ derived from time-dependent modulus $\widehat{E}(t_i)$ and time-independent Poisson's ratio ν by means of Eq. (A.22). Then, the incremental

solution can be written in the form [13, 21, 193]

$$\{\Delta\sigma(t_i)\} = \left[\mathsf{L}(\widehat{E}(t_i),\nu)\right]\{\Delta\varepsilon(t_i)\} + \{\Delta\lambda(t_i)\}, \tag{A.41}$$

with $\widehat{E}(t_i)$ given by Eq. (A.38) and remaining terms attain the form

$$\{\Delta\lambda(t_i)\} = \sum_{\mu=1}^{M}\{\Delta\lambda_\mu(t_i)\} = -\sum_{\mu=1}^{M}\left[1-\exp\left(-\Delta y_\mu(t_i)\right)\right]\{\sigma_\mu(t_i)\}, \tag{A.42}$$

$$\{\sigma_\mu(t_{i+1})\} = \{\sigma_\mu(t_i)\}\exp\left(-\Delta y_\mu(t_i)\right) + \frac{\widehat{E}_\mu(t_i)}{\widehat{E}(t_i)}\left(\{\Delta\sigma(t_i)\} - \{\Delta\lambda(t_i)\}\right). \tag{A.43}$$

A.4 Non-linear viscoelasticity

It is an experimentally confirmed fact that, to a good approximation, polymers show negligible volume deformation during plastic flow. Combing the Eyring flow model [129] for the plastic component of the shear strain rate

$$\frac{\mathrm{d}e_p}{\mathrm{d}t} = \frac{1}{A}\sinh\frac{\tau}{\tau_0}, \tag{A.44}$$

with the elastic shear strain rate $\mathrm{d}e_e/\,\mathrm{d}t$ yield the one-dimensional Leonov constitutive model [142]

$$\frac{\mathrm{d}e}{\mathrm{d}t} = \frac{\mathrm{d}e_e}{\mathrm{d}t} + \frac{\mathrm{d}e_p}{\mathrm{d}t} = \frac{\mathrm{d}e_e}{\mathrm{d}t} + \frac{\tau}{\eta(\,\mathrm{d}e_p/\,\mathrm{d}t)}, \tag{A.45}$$

where the shear-dependent viscosity η is provided by

$$\eta(\,\mathrm{d}e_p/\,\mathrm{d}t) = \frac{\eta_0\tau}{\tau_0\sinh(\tau/\tau_0)} = \eta_0 a_\sigma(\tau). \tag{A.46}$$

In Eq. (A.44), A and τ_0 are material parameters; a_σ appearing in Eq. (A.46) is the stress shift function with respect to the zero shear viscosity η_0 (viscosity corresponding to an elastic response). Clearly, the phenomenological representation of Eq. (A.45) is the Maxwell model with the variable viscosity η.

To describe multi-dimensional behavior of the material, the *generalized compressible Leonov model*, equivalent to the generalized Maxwell chain model, can be used [254, 270]. The viscosity term corresponding to the μ-th chain then can be written in the form

$$\eta_\mu = \eta_{0,\mu}a_\sigma(\tau_{\mathrm{eq}}), \tag{A.47}$$

where the equivalent shear stress τ_{eq} is provided by

$$\tau_{\mathrm{eq}} = \sqrt{\frac{1}{2}s_{ij}s_{ij}}. \tag{A.48}$$

Limiting our attention to the vicinity of the yield point and assuming small strains and isotropic material, a set of constitutive equations defining the generalized compressible

Leonov model can be written in the form

$$\sigma_m = 3K \operatorname{Tr} \boldsymbol{\varepsilon}, \tag{A.49}$$

$$\frac{\mathrm{d}\boldsymbol{s}}{\mathrm{d}t} = \sum_{\mu=1}^{M} 2G_\mu \left(\frac{\mathrm{d}\boldsymbol{e}}{\mathrm{d}t} - \frac{\mathrm{d}\boldsymbol{e}_p}{\mathrm{d}t} \right), \tag{A.50}$$

$$\boldsymbol{s}_\mu = 2\eta_\mu \frac{\mathrm{d}\boldsymbol{e}_p}{\mathrm{d}t} = 2\eta_{0,\mu} a_\sigma(\tau_{\mathrm{eq}}) \frac{\mathrm{d}\boldsymbol{e}_p}{\mathrm{d}t}, \tag{A.51}$$

$$\boldsymbol{s} = \sum_{\mu=1}^{M} \boldsymbol{s}_\mu, \tag{A.52}$$

where $\sigma_m = \operatorname{Tr} \boldsymbol{\sigma}/3$ is the mean stress, K is the bulk modulus and G_μ is the shear modulus of the μ-th unit.

A.4.1 Generalized Maxwell-like model

Following viscoelastic procedure introduced in Section A.3.2, an explicit incremental scheme is used to integrate Eqs. (A.49)–(A.52). To that end, we again divide the time axis into equisized intervals of length Δt and assume that at the beginning of the i-th interval the deviatoric stresses in individual chains $\boldsymbol{s}_\mu(t_i), \mu = 1, 2, \ldots, M$, are known. Next, we suppose that the functions $G_\mu = G_\mu(t_i + \Delta t_i/2)$ and $\eta_\mu = \eta_\mu(t_i + \Delta t_i/2)$ remain constant on a given interval. Under these simplifying assumptions, the incremental form yields

$$\{\Delta\sigma(t_i)\} = \left[\mathsf{L}\left(K, \widehat{G}(t_i) \right) \right] \{\Delta\varepsilon(t_i)\} + \{\Delta\lambda(t_i)\}, \tag{A.53}$$

where the material stiffness matrix is obtained from the time-dependent shear modulus $\widehat{G}(t_i)$ and from the time-independent bulk modulus K, Eq. (A.23); the remaining parameters are as follows[1]

$$\widehat{G}(t_i) = \sum_{\mu=1}^{M} \widehat{G}_\mu(t_i) = \sum_{\mu=1}^{M} \frac{\eta_\mu(t_i)}{\Delta t} \left(1 - \exp\left(-\frac{G_\mu(t_i)\Delta t}{\eta_\mu(t_i)} \right) \right), \tag{A.54}$$

$$\{\Delta\lambda(t_i)\} = \sum_{\mu=1}^{M} \{\Delta\lambda_\mu(t_i)\} = -\sum_{\mu=1}^{M} \left(1 - \exp\left(-\frac{G_\mu(t_i)\Delta t}{\eta_\mu(t_i)} \right) \right) \{\mathsf{s}_\mu(t_i)\}, \tag{A.55}$$

$$\begin{aligned} \{\mathsf{s}_\mu(t_{i+1})\} &= \{\mathsf{s}_\mu(t_i)\} \exp\left(-\frac{G_\mu(t_i)\Delta t}{\eta_\mu(t_i)} \right) \\ &+ \frac{2\eta_\mu(t_i)}{\Delta t} \left(1 - \exp\left(-\frac{G_\mu(t_i)\Delta t}{\eta_\mu(t_i)} \right) \right) [\mathsf{Q}] \{\Delta\mathsf{e}(t_i)\}, \end{aligned} \tag{A.56}$$

$$\eta_\mu(t_i) = \eta_0 a_\sigma \left(\tau_{\mathrm{eq}}(\{\mathsf{s}(t_i)\}) \right), \tag{A.57}$$

$$[\mathsf{Q}] = \operatorname{diag}\left[1, 1, 1, \frac{1}{2}, \frac{1}{2}, \frac{1}{2} \right]. \tag{A.58}$$

[1] Note that setting setting $q_\mu = 1$ and $\Theta_\mu = \eta_\mu/G_\mu$ in the Dirichlet series expansion (A.33) and (A.34), the relations (A.53)–(A.58) basically follow from the linear viscoelastic model.

A.5 Hill's failure criterion

The Hill failure criterion is basically extension of the von Mises plasticity to general anisotropic materials in a multi-dimensional stress state. Assuming that coordinate system is aligned along three principal axes of anisotropy, this criterion is provided by the relation (see, e.g., [80, 88, 92] and references therein),

$$A(\sigma_{22}-\sigma_{33})^2 + B(\sigma_{33}-\sigma_{11})^2 + C(\sigma_{11}-\sigma_{22})^2 + 2D\sigma_{23}^2 + 2E\sigma_{13}^2 + 2F\sigma_{12}^2 = 1, \quad \text{(A.59)}$$

where the material constants A, B, C, D, E and F are defined as

$$\begin{aligned} 2A &= \frac{1}{Y_{22}^2} + \frac{1}{Y_{33}^2} - \frac{1}{Y_{11}^2}, \\ 2B &= \frac{1}{Y_{33}^2} + \frac{1}{Y_{11}^2} - \frac{1}{Y_{22}^2}, \\ 2C &= \frac{1}{Y_{11}^2} + \frac{1}{Y_{22}^2} - \frac{1}{Y_{33}^2}, \end{aligned}$$

and

$$2D = \frac{1}{Y_{23}^2},\ 2E = \frac{1}{Y_{13}^2},\ 2F = \frac{1}{Y_{12}^2}.$$

Note that the values Y_{ij} stand for the strength of a material with respect to a uni-axial stress state σ_{ij}.

Appendix B

THE FOURIER TRANSFORM, FUNDAMENTAL SOLUTIONS AND MICROSTRUCTURAL MATRICES

B.1 The Fourier transform

The d-dimensional Fourier transform of a function $f(\mathbf{x})$ is defined as (see, e.g., [123, Part 8], [218, Chapter 9])

$$\mathcal{F}\left(f(\mathbf{x})\right) = \widetilde{f}(\boldsymbol{\xi}) = \int_V f(\mathbf{x}) \mathrm{e}^{\mathrm{i}\boldsymbol{\xi}\cdot\mathbf{x}} \,\mathrm{d}\mathbf{x}, \tag{B.1}$$

where "i" is the imaginary unit. The operator $\mathcal{F}$ is called the Fourier transform operator. The inverse operator $\mathcal{F}^{-1}$ is obtained by changing the sign of i and normalizing by $(2\pi)^{-d}$. Hence, the inverse Fourier transform is given by

$$\mathcal{F}^{-1}\left(\widetilde{f}(\boldsymbol{\xi})\right) = f(\mathbf{x}) = \frac{1}{2\pi^d} \int_V f(\boldsymbol{\xi}) \mathrm{e}^{-\mathrm{i}\boldsymbol{\xi}\cdot\mathbf{x}} \,\mathrm{d}\boldsymbol{\xi}. \tag{B.2}$$

Simple algebra shows that the operator $\mathcal{F}$ satisfies the following equation

$$\mathcal{F}^{-1}\left(\mathcal{F}\left(f(\mathbf{x})\right)\right) = f(\mathbf{x}). \tag{B.3}$$

Further, provided that function $f(\mathbf{x})$ decays "sufficiently rapidly" to 0 for $|\mathbf{x}| \to \infty$ we have, by Green's theorem,

$$\widetilde{\left(\frac{\partial f}{\partial x_i}\right)}(\boldsymbol{\xi}) = \int_V \frac{\partial f}{\partial x_i} \mathrm{e}^{\mathrm{i}\boldsymbol{\xi}\cdot\mathbf{x}} \,\mathrm{d}\mathbf{x} = -\mathrm{i}\xi_i \int_V f(\mathbf{x}) \mathrm{e}^{\mathrm{i}\boldsymbol{\xi}\cdot\mathbf{x}} \,\mathrm{d}\mathbf{x} = -\mathrm{i}\xi_i \widetilde{f}(\boldsymbol{\xi}). \tag{B.4}$$

B.2 The discrete Fourier transform

The discrete Fourier Transform (DFT) often replaces its continuous counterpart when analyzing discrete systems such as digitized images of real microstructures. The complexity of their geometries usually calls for sampling large micrographs, recall Fig. 2.2. The actual microstructure is then approximated by the measured segment periodically extended outside the measured region. Such a representation invites an application of the DFT to carry out Fourier analysis if needed. Clearly, the discrete Fourier representation results in periodic representation in real space. Note that the spectrum of the discrete real space is also periodic.

Without loss of generality we now limit our attention to a one-dimensional problem and consider a discrete set of N points defined on the interval $0 \leq n \leq N-1$. Applying a discrete version of the Fourier series this set is given by

$$x(n) = \frac{1}{N} \sum_{k=0}^{N-1} \xi(k) \mathrm{e}^{-\mathrm{i}(2\pi/N)kn}, \tag{B.5}$$

where the coefficients $\xi(k)$ are provided by the Discrete Fourier Transform of $x(n)$

$$\xi(k) = \frac{1}{N} \sum_{n=0}^{N-1} x(n) \mathrm{e}^{\mathrm{i}(2\pi/N)kn}. \tag{B.6}$$

Extension to cover 2D and 3D problems is rather straightforward. Further discussion on this subject can be found in very readable form in, e.g., [28, 60, 203].

B.3 The convolution and correlation theorems

The *convolution* of two functions f and g is defined as

$$\int_V f(\mathbf{x} - \mathbf{x}') g(\mathbf{x}') \, \mathrm{d}\mathbf{x}'.$$

The convolution theorem states that the transform of the convolution equals the product of the transforms [123, 218]

$$\mathcal{F}\left(\int_V f(\mathbf{x} - \mathbf{x}') g(\mathbf{x}') \, \mathrm{d}\mathbf{x}' \right) = \mathcal{F}\left(f(\mathbf{x}) \right) \mathcal{F}\left(g(\mathbf{x}) \right). \tag{B.7}$$

Similarly, using Eq. (B.2) gives

$$\mathcal{F}^{-1}\left(\int_V \widetilde{f}(\boldsymbol{\xi} - \boldsymbol{\xi}') \widetilde{g}(\boldsymbol{\xi}') \, \mathrm{d}\boldsymbol{\xi}' \right) \;=\; (2\pi)^d f(\mathbf{x}) g(\mathbf{x}), \tag{B.8}$$

which implies that

$$\mathcal{F}\left(f(\mathbf{x}) g(\mathbf{x}) \right) \;=\; (2\pi)^{-d} \int_V \widetilde{f}(\boldsymbol{\xi} - \boldsymbol{\xi}') \widetilde{g}(\boldsymbol{\xi}') \, \mathrm{d}\boldsymbol{\xi}'. \tag{B.9}$$

Finally, the Fourier transform of the *correlation* integral

$$\int_V f(\mathbf{x} + \mathbf{x}') g(\mathbf{x}') \, \mathrm{d}\mathbf{x}',$$

where $g(\mathbf{x})$ is a real function is given by

$$\mathcal{F}\left(\int_V f(\mathbf{x} + \mathbf{x}') g(\mathbf{x}') \, \mathrm{d}\mathbf{x}' \right) = \mathcal{F}\left(f(\mathbf{x}) \right) \overline{\mathcal{F}\left(g(\mathbf{x}) \right)}, \tag{B.10}$$

where $\bar{\cdot}$ means complex conjugate and should not be mistaken with the ensemble average used before.

B.4 Fundamental solutions

Physically speaking, the *displacement* fundamental solution $(u_0^*)_{pi}$[1] represents the displacement in the i direction at point $\mathbf{x} \in V$ due to a unit point force applied at a point

[1] Note that index "0" is, in accordance with Chapter 4, used for denoting the homogeneous (reference) medium. Further, in this section we heavily use the comma notation for derivatives and Einstein's summation convention with respect to repeated indices (see Notation on page xiii for more details).

$\mathbf{x}'$ in the direction p. For a homogeneous medium with the stiffness tensor $\mathbf{L}_0$, it can be obtained from the solution of the Lamé equation (see, e.g, [21, 49, 131, 174])

$$(L_0)_{ijkl}(u_0^*)_{pk,lj}(\mathbf{x}-\mathbf{x}') + \delta_{pi}\delta(\mathbf{x}-\mathbf{x}') = 0, \tag{B.11}$$

where $\delta(\cdot)$ is the Dirac delta function. Similarly, the *strain* fundamental solution, provided by

$$(\epsilon_0^*)_{pij} = \frac{1}{2}((u_0^*)_{pi,j} + (u_0^*)_{pj,i}), \tag{B.12}$$

then corresponds to the strains at a point $\mathbf{x}$ due to a unit point force applied at a point $\mathbf{x}'$ in the p^{th} direction. A careful analysis reveals that this function can be used to express the fluctuating part of the strain tensor $\boldsymbol{\varepsilon}'$ as a function of polarization stress $\boldsymbol{\tau}$, (the relation needed in Eq. (4.16))[2]

$$\varepsilon'_{pq}(\mathbf{x}') = \int_V (\epsilon_0^*)_{ijpq}(\mathbf{x}-\mathbf{x}')\,(\tau_{ij}(\mathbf{x}) - \langle\tau_{ij}\rangle)\,\mathrm{d}\mathbf{x}, \tag{B.13}$$

where the fourth order tensor $(\epsilon_0^*)_{ijpq}$ is obtained as

$$(\epsilon_0^*)_{ijkl}(\mathbf{x}) = \frac{1}{2}\left((\varepsilon_0^*)_{ikl,j}(\mathbf{x}) + (\varepsilon_0^*)_{jkl,i}(\mathbf{x})\right). \tag{B.14}$$

Finally, the local strain thus follows from the superposition of oscillating part of strain $\boldsymbol{\varepsilon}'$ and the uniform strain $\boldsymbol{E}$

$$\varepsilon_{pq}(\mathbf{x}') = E_{pq} + \varepsilon'_{pq}(\mathbf{x}') = E_{pq} + \int_V (\epsilon_0^*)_{ijpq}(\mathbf{x}-\mathbf{x}')\,(\tau_{ij}(\mathbf{x}) - \langle\tau_{ij}\rangle)\,\mathrm{d}\mathbf{x}. \tag{B.15}$$

B.5 The Fourier transform of tensors ϵ_0^* and σ_0^*

In the previous section we introduced the fourth order tensor $(\epsilon_0^*)_{ijkl}$ related to the fundamental solution $(u_0^*)_{ij}$. Specific forms of these quantities for a homogeneous and isotropic material and certain special cases of anisotropic materials can be found, e.g., in [21, 174]. Their Fourier transforms, however, needed for evaluation of matrices $[\mathsf{A}_{\mathsf{rs}}]$ and $[\mathsf{B}_{\mathsf{rs}}]$ in Eqs. (4.26) and (4.51), deserve more attention.

First, consider the tensor $(\epsilon_0^*)_{ijkl}$. Introducing Eq. (B.12) into Eq. (B.14) yields

$$(\epsilon_0^*)_{ijkl}(\mathbf{x}) = \frac{1}{4}\left((u_0^*)_{ik,lj}(\mathbf{x}) + (u_0^*)_{il,kj}(\mathbf{x}) + (u_0^*)_{jk,li}(\mathbf{x}) + (u_0^*)_{jl,ki}(\mathbf{x})\right). \tag{B.16}$$

Hence, according to B.4, the Fourier transform of Eq. (B.16) can be written in the form

$$\widetilde{(\epsilon_0^*)}_{ijkl}(\boldsymbol{\xi}) = -\frac{1}{4}\left(\widetilde{(u_0^*)}_{ik}(\boldsymbol{\xi})\xi_l\xi_j + \widetilde{(u_0^*)}_{il}(\boldsymbol{\xi})\xi_k\xi_j + \widetilde{(u_0^*)}_{jk}(\boldsymbol{\xi})\xi_l\xi_i + \widetilde{(u_0^*)}_{jl}(\boldsymbol{\xi})\xi_k\xi_i\right). \tag{B.17}$$

Similarly, the Fourier transform of Eq. (B.11) reads

$$-(L_0)_{ijkl}\xi_i\xi_l\widetilde{(u_0^*)}_{jm}(\boldsymbol{\xi}) + \delta_{km} = 0, \tag{B.18}$$

[2] Loosely speaking, the term $\tau_{ij}(\mathbf{x}) - \langle\tau_{ij}\rangle$ oscillates about zero and by virtue of St. Venant's principle the boundary terms due to this polarization stresses are insignificant except for a layer close to ∂V. See, e.g., [134, 140, 285] and [271, Appendix A]) for more detailed discussion.

so that

$$\widetilde{(u_0^*)}_{jk}(\boldsymbol{\xi}) = \left((L_0)_{ijkl}\xi_i\xi_l\right)^{-1}. \tag{B.19}$$

For a homogeneous and isotropic material the above equation assumes the form

$$\widetilde{(u_0^*)}_{jk}(\boldsymbol{\xi}) = \frac{1}{|\boldsymbol{\xi}|^2\mu}\delta_{jk} - \frac{\lambda+\mu}{\mu(\lambda+2\mu)}\frac{\xi_j}{|\boldsymbol{\xi}|^2}\frac{\xi_k}{|\boldsymbol{\xi}|^2}, \tag{B.20}$$

where λ and μ are the Lamé parameters (see, e.g., [97, 174]). Finally, substituting Eq (B.20) into Eq (B.17) gives the Fourier transform of the tensor $(\epsilon_0^*)_{ijkl}$

$$\widetilde{(\epsilon_0^*)}_{ijkl} = -\frac{1}{|\boldsymbol{\xi}|^4\mu}\left\{\frac{|\boldsymbol{\xi}|^2}{4}\left(\xi_j\xi_l\delta_{ik} + \xi_i\xi_l\delta_{jk} + \xi_j\xi_k\delta_{il} + \xi_i\xi_k\delta_{jl}\right) - \frac{\lambda+\mu}{\mu(\lambda+2\mu)}\xi_i\xi_j\xi_k\xi_l\right\}. \tag{B.21}$$

To derive the Fourier transform of the tensor $(\sigma_0^*)_{ijkl}$ we begin with the constitutive law of isotropic material given by

$$\sigma_{ij}(\mathbf{x}) = \lambda u_{l,l}(\mathbf{x})\delta_{ij} + \mu(u_{i,j}(\mathbf{x}) + u_{j,i}(\mathbf{x})). \tag{B.22}$$

The above equation can be used to show that

$$(\sigma_0^*)_{ijkl}(\mathbf{x}) = \lambda(\sigma_0^*)_{mkl,m}\delta_{ij} + \mu((\sigma_0^*)_{ikl,j} + (\sigma_0^*)_{jkl,i}), \tag{B.23}$$

where

$$(\sigma_0^*)_{ijk}(\mathbf{x}) = \lambda(u_0^*)_{il,l}(\mathbf{x})\delta_{jk} + \mu((u_0^*)_{ij,k}(\mathbf{x}) + (u_0^*)_{ik,j}(\mathbf{x})). \tag{B.24}$$

Fourier transforming of Eq. (B.24) then provides

$$\widetilde{(\sigma_0^*)}_{ijkl}(\boldsymbol{\xi}) = -\mathrm{i}\lambda\widetilde{(\sigma_0^*)}_{mkl}(\boldsymbol{\xi})\xi_m\delta_{ij} - \mathrm{i}\mu(\widetilde{(\sigma_0^*)}_{ikl}(\boldsymbol{\xi})\xi_j + \widetilde{(\sigma_0^*)}_{jkl}(\boldsymbol{\xi})\xi_i), \tag{B.25}$$

where the Fourier transform of $(\sigma_0^*)_{ijk}$ is given by

$$\widetilde{(\sigma_0^*)}_{ijk}(\boldsymbol{\xi}) = -\mathrm{i}\lambda\widetilde{(u_0^*)}_{il}(\boldsymbol{\xi})\xi_l\delta_{jk} - \mathrm{i}\mu(\widetilde{(u_0^*)}_{ij}(\boldsymbol{\xi})\xi_k + \widetilde{(u_0^*)}_{ik}(\boldsymbol{\xi})\xi_j). \tag{B.26}$$

Therefore, after substituting the above equation into Eq. (B.26) we arrive at

$$\begin{aligned}\widetilde{(\sigma_0^*)}_{ijkl}(\boldsymbol{\xi}) &= -\lambda^2\widetilde{(u_0^*)}_{mn}(\boldsymbol{\xi})\xi_m\xi_n\delta_{ij}\delta_{kl} \\ &\quad -\lambda\mu\left(\widetilde{(u_0^*)}_{mk}(\boldsymbol{\xi})\xi_l\xi_m\delta_{ij} + \widetilde{(u_0^*)}_{ml}(\boldsymbol{\xi})\xi_k\xi_m\delta_{ij} + \widetilde{(u_0^*)}_{in}(\boldsymbol{\xi})\xi_n\xi_j\delta_{kl} + \widetilde{(u_0^*)}_{jn}(\boldsymbol{\xi})\xi_n\xi_i\delta_{kl}\right) \\ &\quad -\mu^2\left(\widetilde{(u_0^*)}_{ik}(\boldsymbol{\xi})\xi_l\xi_j + \widetilde{(u_0^*)}_{il}(\boldsymbol{\xi})\xi_k\xi_j + \widetilde{(u_0^*)}_{jk}(\boldsymbol{\xi})\xi_l\xi_i + \widetilde{(u_0^*)}_{jl}(\boldsymbol{\xi})\xi_k\xi_i\right).\end{aligned} \tag{B.27}$$

The last step requires substitution of Eq. (B.20) into Eq. (B.28). After some lengthy algebra we finally get the desired results in the form

$$\begin{aligned}\widetilde{(\sigma_0^*)}_{ijkl}(\boldsymbol{\xi}) &= -\frac{\lambda\mu}{|\boldsymbol{\xi}|^2(\lambda+2\mu)}\left\{2(\xi_i\xi_j\delta_{kl} + \xi_k\xi_l\delta_{ij}) - \frac{4(\lambda+\mu)}{|\boldsymbol{\xi}|^2}\xi_i\xi_j\xi_k\xi_l\right. \\ &\quad +(\lambda+2\mu)(\xi_k\xi_j\delta_{il} + \xi_l\xi_k\delta_{ij} + \xi_k\xi_i\delta_{jl} + \xi_l\xi_i\delta_{jk}) \\ &\quad \left.+\frac{|\boldsymbol{\xi}|^2}{\lambda\mu}\delta_{ij}\delta_{kl}\right\}.\end{aligned} \tag{B.28}$$

For a general anisotropic solid one may start from Eq. (B.17) and write the tensor $\widetilde{(\sigma_0^*)}_{ijkl}$ in the form

$$\widetilde{(\sigma_0^*)}_{ijkl} = -(L_0)_{ijpq}\widetilde{(\epsilon_0^*)}_{pqrs}(L_0)_{rskl}. \tag{B.29}$$

Also note that engineering form of tensors $\widetilde{(\epsilon_0^*)}_{ijkl}$ and $\widetilde{(\sigma_0^*)}_{ijkl}$ for the generalized plane strain assumptions (see Appendix A) are

$$\left[\widetilde{\epsilon_0^*}\right] = \begin{bmatrix} \widetilde{(\epsilon_0^*)}_{1111} & \widetilde{(\epsilon_0^*)}_{1122} & 2\widetilde{(\epsilon_0^*)}_{1112} & 0 \\ \widetilde{(\epsilon_0^*)}_{1122} & \widetilde{(\epsilon_0^*)}_{2222} & 2\widetilde{(\epsilon_0^*)}_{2212} & 0 \\ 2\widetilde{(\epsilon_0^*)}_{1112} & 2\widetilde{(\epsilon_0^*)}_{2212} & 4\widetilde{(\epsilon_0^*)}_{1212} & 0 \\ 0 & 0 & 0 & 0 \end{bmatrix}, \tag{B.30}$$

and

$$\left[\widetilde{\sigma_0^*}\right] = -\left[\mathsf{L_0}\right]\left[\widetilde{\epsilon_0^*}\right]\left[\mathsf{L_0}\right], \tag{B.31}$$

where the last row and column in matrix $\left[\widetilde{\epsilon_0^*}\right]$ were augmented by zeros to comply with the generalized plane strain assumption.

B.6 Evaluation of matrices $[\mathsf{A_{rs}}]$ *and* $[\mathsf{B_{rs}}]$

Consider Eq. (4.26) to write the microstructure-dependent matrices $[\mathsf{A_{rs}}]$ in the form

$$\begin{aligned} [\mathsf{A_{rs}}] &= \int_V [\epsilon_0^*]\,(\mathbf{x}-\mathbf{x}')\,(S_{rs}(\mathbf{x}-\mathbf{x}') - c_r c_s)\,\mathrm{d}\mathbf{x}' \\ &= \int_V [\epsilon_0^*]\,(\mathbf{x}-\mathbf{x}')S'_{rs}(\mathbf{x}-\mathbf{x}')\,\mathrm{d}\mathbf{x}' = \int_V [\epsilon_0^*]\,(\mathbf{x})S'_{rs}(\mathbf{x})\,\mathrm{d}\mathbf{x}, \end{aligned} \tag{B.32}$$

where S'_{rs} denotes the fluctuating part of S_{rs} under the no-long range orders hypothesis (2.18). Next, using Eq. (B.1), observe that the preceding formula can be written as

$$\begin{aligned} [\mathsf{A_{rs}}] &= \int_V [\epsilon_0^*]\,(\mathbf{x})S'_{rs}(\mathbf{x})\,\mathrm{d}\mathbf{x} \\ &= \left[\int_V [\epsilon_0^*]\,(\mathbf{x})S'_{rs}(\mathbf{x})\mathrm{e}^{\mathrm{i}\mathbf{x}\cdot\boldsymbol{\xi}}\,\mathrm{d}V(\mathbf{x})\right]_{\boldsymbol{\xi}=\mathbf{0}} = \mathcal{F}\left([\epsilon_0^*]\,(\mathbf{x})S'_{rs}(\mathbf{x})\right)_{\boldsymbol{\xi}=\mathbf{0}}. \end{aligned} \tag{B.33}$$

Then, recall Eq. (B.9) to get

$$[\mathsf{A_{rs}}] = \frac{1}{(2\pi)^d}\left[\int_V \widetilde{[\epsilon_0^*]}(\boldsymbol{\xi}-\boldsymbol{\xi}')\widetilde{S}'_{rs}(\boldsymbol{\xi}')\,\mathrm{d}\boldsymbol{\xi}'\right]_{\boldsymbol{\xi}=\mathbf{0}} = \frac{1}{(2\pi)^d}\int_V \widetilde{[\epsilon_0^*]}(-\boldsymbol{\xi}')\widetilde{S}'_{rs}(\boldsymbol{\xi}')\,\mathrm{d}\boldsymbol{\xi}' \tag{B.34}$$

Since $\widetilde{[\epsilon_0^*]}(-\boldsymbol{\xi}) = \widetilde{[\epsilon_0^*]}(\boldsymbol{\xi})$ we finally arrive at

$$[\mathsf{A_{rs}}] = \frac{1}{(2\pi)^d}\int_V \widetilde{[\epsilon_0^*]}(\boldsymbol{\xi}')\widetilde{S}'_{rs}(\boldsymbol{\xi}')\,\mathrm{d}\boldsymbol{\xi}'. \tag{B.35}$$

Similar procedure then provides

$$[\mathsf{B_{rs}}] = \frac{1}{(2\pi)^d}\int_V \widetilde{[\sigma_0^*]}(\boldsymbol{\xi}')\widetilde{S}'_{rs}(\boldsymbol{\xi}')\,\mathrm{d}\boldsymbol{\xi}'. \tag{B.36}$$

Note again that Fourier's transform $\widetilde{[\epsilon_0^*]}$ or $\widetilde{[\sigma_0^*]}$ can be obtained for any homogeneous anisotropic reference medium (see previous section for explicit formulae), which is not generally possible for function $[\epsilon_0^*]$ itself. Therefore, once we are able to compute the values of $\widetilde{S}'_{rs}$ we may evaluate integrals (B.35) and (B.36) by an appropriate numerical integration procedure.

We close this section by introducing certain universal connections for matrices $[\mathsf{A_{rs}}]$ and $[\mathsf{B_{rs}}]$ evaluated for the two-phase composite medium. In particular, recall Eq. (2.12) to write function S'_{rs} as

$$S'_{rs}(\mathbf{x},\mathbf{x}') = \overline{\chi_r(\mathbf{x},\alpha)(\chi_s(\mathbf{x}',\alpha) - S_s(\mathbf{x}'))} = \overline{(\chi_r(\mathbf{x},\alpha) - S_r(\mathbf{x}))\chi_s(\mathbf{x}',\alpha)}. \tag{B.37}$$

The above relation together with Eq. (2.9) imply that (dropping the dependence on $\mathbf{x}$ and α for simplicity)

$$\begin{aligned} S'_{mm} &= \overline{\chi_m(\chi_m - S_m)} = S_{mm} - S_m^2, \\ S'_{ff} &= \overline{\chi_f(\chi_f - S_f)} = \overline{(1-\chi_m)(1-S_f-\chi_m)} = S_{mm} - S_m^2 = S'_{mm}, \qquad \text{(B.38)} \\ S'_{fm} &= S'_{mf} = \overline{\chi_m(\chi_f - S_f)} = S_m^2 - S'_{mm} = -S'_{mm}. \qquad \text{(B.39)} \end{aligned}$$

Introducing relations (B.38) into Eq. (B.32) yields

$$\begin{aligned} [\mathsf{A_{mm}}] &= [\mathsf{A_{ff}}] = -[\mathsf{A_{mf}}], \\ [\mathsf{B_{mm}}] &= [\mathsf{B_{ff}}] = -[\mathsf{B_{mf}}]. \end{aligned} \tag{B.40}$$

It now becomes clear that only a single matrix, say $[\mathsf{A_{mm}}]$, needs to be evaluated numerically, which substantially decreases the computational effort. Introducing some auxiliary matrices

$$[\mathsf{A}] = [\mathsf{A_{mm}}], \qquad [\mathsf{B}] = c_m c_f [\mathsf{M_0}]^{-1} - [\mathsf{B_{mm}}] \tag{B.41}$$

$$[\mathsf{K_r}] = [\mathsf{L_r}] - [\mathsf{L_0}], \qquad [\mathsf{N_r}] = \left(([\mathsf{M_r}] - [\mathsf{M_0}])^{-1} + [\mathsf{M_0}]^{-1}\right)^{-1} \tag{B.42}$$

we can finally obtain, with the help of Eq. (B.40), the matrices $[\mathsf{T_{rs}}]$ and $[\mathsf{R_{rs}}]$ in the form

$$\begin{aligned} [\mathsf{T_{rs}}] &= [\mathsf{K_r}]\left(c_f[\mathsf{K_m}] + c_m[\mathsf{K_f}] - c_f c_m [\mathsf{A}]^{-1}\right)([\mathsf{K_f}] + [\mathsf{K_m}] - [\mathsf{K_r}] \\ &+ \delta_{rs}(1-c_r)[\mathsf{A}]^{-1}), \qquad \text{(B.43)} \\ [\mathsf{R_{rs}}] &= [\mathsf{N_r}]\left(c_f[\mathsf{N_m}] + c_m[\mathsf{N_f}] - c_f c_m [\mathsf{B}]^{-1}\right)([\mathsf{N_f}] + [\mathsf{N_m}] - [\mathsf{N_r}] \\ &+ \delta_{rs}(1-c_r)[\mathsf{B}]^{-1}). \qquad \text{(B.44)} \end{aligned}$$

Appendix C

JUSTIFICATION OF UNCOUPLED MULTI-SCALE MODELING

The purpose of this appendix is to present a rigorous justification of the uncoupled homogenization approach to modeling of linearly elastic composite materials subjected, in addition to mechanical loading, to an eigenstress distribution. The motivation of such a study is twofold: first, we would like to quantify the assumptions under which such an uncoupling is appropriate, the second is the analysis of the stress and strain controlled homogenization which follows quite naturally from the presented theory.

Put in more mathematical terms, our goal is to describe, in a suitable sense, the limit solution of a system of linear elasticity equations with coefficients rapidly oscillation on several length scales. The theory of multiscale convergence, introduced by Nguetseng for two scales [180], further extented by Allaire [5] and finally generalized to the multiscale case by Allaire and Briane [6], appears to be an elegant framework for the analysis of the present problem[1]. There are several reasons which make the multiscale convergence method an attractive tool of the homogenization theory: it efficiently explores the unit cell equation obtained by the method of asymptotic expansion [16, 222, 223] to directly obtain the convergence proof, it is reasonably simple to use, allows a clear interpretations of macroscopic, mesoscopic and microscopic variables and its ideas can be used as a stepping stone for multiscale computational inelasticity [252]. Finally remark that compared to, e.g., the general theory of H-convergence [175], which is free of any assumptions on problem geometry, the multiscale convergence theory relies on the microstructure periodicity. Although this assumption may seem to be restrictive from the theoretical point of view, it fits perfectly well into the scope of the present work.

An outline of this chapter is as follows. Section C.1 briefly overviews the used notation and states the basic results of the three-scale convergence theory. Then, the problem to be analyzed in defined in Section C.2 and the assumptions on the data are introduced. The homogenization result for the present problem is proven in Section C.3 using the multiscale convergence theory. Finally, relations between the obtained result and engineering approaches employed in Chapters 3 and 5 are discussed in Section C.4.

C.1 Multi-scale convergence

Let us begin this section with a brief introduction of notation and function spaces, used later in the text. The detailed discussion and explanation of individual terms can be

[1] See the overview [148] for more detailed discussion and generalization of this method as well as the inventory of applications to various physical and engineering problems. Further, an excellent discussion on engineerings aspects of the application of two-scale convergence to problems of nonlinear mechanics can be found in the recent article [252] which was a great source of inspiration for the work presented in this Chapter.

found, e.g., in [23, 97, 123, 208]; see also [117] for spaces of periodic functions. Recall that in this section, we employ the general notation introduced on page xiii.

Let $\Omega \subset \mathbb{R}^d$ be a bounded domain with a Lipschitz boundary. We denote the set of all symmetric second order tensors as $\mathbb{S}^d$ and the symbol $\mathbb{S}^{d\times d}$ is used for the set of symmetric fourth-order tensors with the norm on $\mathbb{S}^d$ denoted as $\|\boldsymbol{a}\|^2 = \boldsymbol{a} : \boldsymbol{a}$. The symbol $L^2(\Omega)$ is used, as usual, for the Hilbert space of (equivalence classes of) square Lebesgue integrable functions on Ω endowed with the scalar product

$$(u, v)_{L^2(\Omega)} = \int_\Omega uv \,\mathrm{d}\Omega. \tag{C.1}$$

By $L^2(\Omega; B)$ we will denote the set of all strongly measurable functions with values in a separable Banach space B (see, e.g., [197, Chapter 5] or [213, Section 1.4]) such that $\|u\|_{L^2(\Omega;B)} < \infty$, where

$$\|u\|^2_{L^2(\Omega;B)} = \int_\Omega \|u(\mathbf{x})\|^2_B \,\mathrm{d}\Omega. \tag{C.2}$$

Therefore, for example, $L^2(\Omega; \mathbb{R}^d)$ denotes the set of vector-valued functions equipped with the scalar product

$$(\mathbf{u}, \mathbf{v})_{L^2(\Omega;\mathbb{R}^d)} = \int_\Omega \mathbf{u} \cdot \mathbf{v} \,\mathrm{d}\Omega.$$

The Hilbert space of functions from $u \in L^2(\Omega)$ with their weak gradient $\mathbf{D}u$ in $L^2(\Omega; \mathbb{R}^d)$ equipped with scalar product

$$(u, v)_{W^{1,2}(\Omega)} = (u, v)_{L^2(\Omega)} + (\mathbf{D}u, \mathbf{D}v)_{L^2(\Omega;\mathbb{R}^d)} \tag{C.3}$$

will be denoted as $W^{1,2}(\Omega)$. The symbol $C_0^\infty(\Omega)$ stands for the set of real-valued infinitely differentiable functions with a compact support in Ω. The closure of the set $C_0^\infty(\Omega)$ with respect to the norm $\|\cdot\|_{W^{1,2}(\Omega)}$ is denoted as $W_0^{1,2}(\Omega)$. Similarly, the $C^\infty_{\mathrm{per}}(Y)$ is the space of infinitely differentiable Y-periodic functions. The symbol $W^{1,2}_{\mathrm{per}}(\Omega)$ will be reserved for the space of functions from the completion of $C^\infty_{\mathrm{per}}(Y)$ with respect to the $\|\cdot\|_{W^{1,2}(\Omega)}$ norm which posses the zero mean value. Finally, $\mathcal{D}(\Omega; C^\infty_{\mathrm{per}}(Y))$ is the space of measurable function of $\Omega \times \mathbb{R}^d$ such that $u(\mathbf{x}, \cdot) \in C^\infty_{\mathrm{per}}(Y)$ for any $\mathbf{x} \in \Omega$ and the map $\mathbf{x} \mapsto u(\mathbf{x}, \cdot) \in C^\infty_{\mathrm{per}}(Y)$ is indefinitely differentiable with a compact support in Ω.

Now, we briefly recall the necessary results related to the theory of multiscale convergence and refer an interested reader to [5, 6, 148] for complete proofs. With reference to Chapter 1, we will restrict our attention to problems with three length scales and denote by ℓ_0, ℓ_1 and ℓ_2 the characteristic "macroscale", "mesoscale" and "microscale" dimensions, respectively. We further assume that they are naturally ordered such that $\ell_0 > \ell_1 > \ell_2$. The unit cells corresponding to lenghtscales ℓ_1 and ℓ_2 will be referred to as Y_1 and Y_2, respectively. Again, we assume that Y_1 and Y_2 are open bounded sets with a Lispschitz boundary. Finally, we introduce ratios $\xi_1 = \ell_1/\ell_0$ and $\xi_2 = \ell_2/\ell_0$ and assume that they depend of a single parameter ξ.

Definition 1 (Three-scale convergence) *A sequence of function* $\{u_\xi(\mathbf{x})\}$ *in* $L^2(\Omega)$ *is said to* three-scale converge *to a limit* $u_0(\mathbf{x}, \mathbf{y}) \in L^2(\Omega \times Y_1 \times Y_2)$ *if, for any function* ψ

in $L^2(\Omega; C_{\mathrm{per}}(Y_1 \times Y_2))$*, we have*

$$\lim_{\xi\to 0}\int_\Omega u_\xi(\mathbf{x})\psi\left(\mathbf{x},\frac{\mathbf{x}}{\xi_1},\frac{\mathbf{x}}{\xi_2}\right)\,\mathrm{d}\Omega = \frac{1}{|Y_1|}\frac{1}{|Y_2|}\int_\Omega\int_{Y_1}\int_{Y_2} u_0(\mathbf{x},\mathbf{y}_1,\mathbf{y}_2)\psi(\mathbf{x},\mathbf{y}_1,\mathbf{y}_2)\,\mathrm{d}\Omega\,\mathrm{d}Y_1\,\mathrm{d}Y_2. \tag{C.4}$$

We denote this mode of convergence as $u_\xi(\mathbf{x}) \overset{3-s}{\longrightarrow} u_0(\mathbf{x},\mathbf{y}_1,\mathbf{y}_2)$.

We further assume that the individual length scales are not of a same order of magnitude, i.e., the hypothesis on *separation of scales*,

$$\lim_{\xi\to 0}\frac{\xi_2}{\xi_1} = 0, \tag{C.5}$$

is valid. Now we are ready to state the key results of the three scale convergence theory.

Theorem 1 ([6, Theorem 1.1]) *Let assumption* (C.5) *hold. Then, for each bounded sequence* $\{u_\xi(\mathbf{x})\}$ *in* $L^2(\Omega)$*, there exists a subsequence* $\{u_{\xi'}(\mathbf{x})\}$ *and* $u_0(\mathbf{x},\mathbf{y}_1,\mathbf{y}_2) \in L^2(\Omega\times Y_1\times Y_2)$ *such that* $u_{\xi'} \overset{3-s}{\longrightarrow} u_0$.

Theorem 2 ([6, Theorem 2.5]) *Let* $\{v_\xi(\mathbf{x})\}$ *be a sequence in* $L^2(\Omega)$ *which three-scale converges to* $v(\mathbf{x},\mathbf{y}_1,\mathbf{y}_2) \in L^2(\Omega\times Y_1\times Y_2)$ *and assume that*

$$\lim_{\xi\to 0}\|v_\xi\|_{L^2(\Omega)} = \|v\|_{L_2(\Omega\times Y_1\times Y_2)}. \tag{C.6}$$

Then, for any sequence $\{u_\xi(\mathbf{x})\}$ *in* $L^2(\Omega)$ *which three-scale converges to* $u(\mathbf{x},\mathbf{y}_1,\mathbf{y}_2)$*, one has*

$$u_\xi(\mathbf{x})v_\xi(\mathbf{x}) \rightharpoonup \frac{1}{|Y_1|}\frac{1}{|Y_2|}\int_{Y_1}\int_{Y_2} u(\mathbf{x},\mathbf{y}_1,\mathbf{y}_2)v(\mathbf{x},\mathbf{y}_1,\mathbf{y}_2)\,\mathrm{d}Y_1\,\mathrm{d}Y_2 \tag{C.7}$$

weakly in $L^1(\Omega)$.

The next theorem states that similar result holds for Sobolev spaces as well.

Theorem 3 ([6, Theorem 1.2]) *Let assumption* (C.5) *be satisfied and* $\{u_\xi(\mathbf{x})\}$ *be a sequence in* $W_0^{1,2}(\Omega)$ *such that*

$$u_\xi \rightharpoonup u \qquad \text{weakly in } W_0^{1,2}(\Omega). \tag{C.8}$$

Then $u_\xi \overset{3-s}{\longrightarrow} u$ *and there exits a subsequence* $\{u_{\xi'}\}$ *and functions* $u_1(\mathbf{x},\mathbf{y}_1) \in L^2(\Omega; W^{1,2}_{\mathrm{per}}(Y_1))$ *and* $u_2(\mathbf{x},\mathbf{y}_1,\mathbf{y}_2) \in L^2(\Omega\times Y_1; W^{1,2}_{\mathrm{per}}(Y_2))$ *such that*

$$\mathbf{D}u_\xi(\mathbf{x}) \overset{3-s}{\longrightarrow} \mathbf{D}_x u(\mathbf{x}) + \mathbf{D}_{y_1}u_1(\mathbf{x},\mathbf{y}_1) + \mathbf{D}_{y_2}(\mathbf{x},\mathbf{y}_1,\mathbf{y}_2). \tag{C.9}$$

C.2 Setting of the problem

Consider, for simplicity, a composite body Ω with prescribed zero displacements on the boundary Γ. The material stiffness tensor is a rapidly oscillating function in the form $\mathbf{L}_\xi(\mathbf{x}) = \mathbf{L}\,(\mathbf{x}, \mathbf{x}/\xi_1, \mathbf{x}/\xi_2)$, where $\mathbf{L}_\xi(\mathbf{x})$ is Y_k-periodic with respect to each variable $\mathbf{y}_k = \mathbf{x}/\xi_k, k = 1, 2$. In addition, the body Ω is subjected to Y_k-periodic distribution of eigenstresses $\boldsymbol{\lambda}_\xi(\mathbf{x}) = \boldsymbol{\lambda}\,(\mathbf{x}, \mathbf{x}/\xi_1, \mathbf{x}/\xi_2)$. We assume that there exist constants c_L, C_L and $C_\lambda \in \mathbb{R}_+$, independent of ξ, such that

$$c_L\boldsymbol{\zeta} : \boldsymbol{\zeta} \le \boldsymbol{\zeta} : \mathbf{L}_\xi(\mathbf{x}) : \boldsymbol{\zeta}, \qquad \|\mathbf{L}_\xi(\mathbf{x}) : \boldsymbol{\zeta}\| \le C_L\|\boldsymbol{\zeta}\|, \qquad \text{for any } \boldsymbol{\zeta} \in \mathbb{S}^d, \tag{C.10}$$

$$\|\boldsymbol{\lambda}_\xi(\mathbf{x}) : \boldsymbol{\zeta}\| \le C_\lambda\|\boldsymbol{\zeta}\|, \qquad \text{for any } \boldsymbol{\zeta} \in \mathbb{S}^d, \tag{C.11}$$

and that both $\mathbf{L}_\xi(\mathbf{x})$ and $\boldsymbol{\lambda}_\xi(\mathbf{x})$ are essentially bounded

$$\mathbf{L}_\xi(\mathbf{x}) \in L^\infty(\Omega; \mathbb{S}^{d\times d}), \qquad \boldsymbol{\lambda}_\xi(\mathbf{x}) \in L^\infty(\Omega; \mathbb{S}^d).$$

Finally, we impose the following, rather technical, assumptions on $\mathbf{L}_\xi(\mathbf{x})$ and $\boldsymbol{\lambda}_\xi(\mathbf{x})$

$$\mathbf{L}_\xi(\mathbf{x}) \xrightarrow{3-s} \mathbf{L}(\mathbf{x}, \mathbf{y}_1, \mathbf{y}_2), \qquad \boldsymbol{\lambda}_\xi(\mathbf{x}) \xrightarrow{3-s} \boldsymbol{\lambda}(\mathbf{x}, \mathbf{y}_1, \mathbf{y}_2). \tag{C.12}$$

$$\lim_{\xi\to 0} \|(L_\xi)_{ijkl}\|_{L^2(\Omega)} = \|L_{ijkl}\|_{L^2(\Omega\times Y_1\times Y_2)}, \tag{C.13}$$

Define the strain tensor $\boldsymbol{\varepsilon} \in L^2(\Omega; \mathbb{S}^d)$ related to a displacement $\mathbf{u} \in W^{1,2}(\Omega; \mathbb{R}^d)$ as

$$\boldsymbol{\varepsilon}(\mathbf{u}) = \frac{1}{2}\left(\mathbf{D}\mathbf{u}(\mathbf{x}) + (\mathbf{D}\mathbf{u}(\mathbf{x}))^{\mathsf{T}}\right),$$

while the symbol $\boldsymbol{\varepsilon}_{y_k}(\mathbf{u})$ used for $(\mathbf{D}_{y_k}\mathbf{u} + (\mathbf{D}_{y_k}\mathbf{u})^{\mathsf{T}})/2$. The weak form of elasticity equations (3.5)–(3.8) for a heterogenous body Ω can be now written as

$$\begin{cases} \text{Find } \mathbf{u}_\xi \in W_0^{1,2}(\Omega; \mathbb{R}^d) \text{ such that} \\ a_\xi(\mathbf{u}_\xi, \mathbf{v}) = b_\xi(\mathbf{v}) \text{ for every } \mathbf{v} \in W_0^{1,2}(\Omega; \mathbb{R}^d), \end{cases} \tag{C.14}$$

where the bilinear form $a_\xi : W_0^{1,2}(\Omega; \mathbb{R}^d) \times W_0^{1,2}(\Omega; \mathbb{R}^d) \to \mathbb{R}$ and the linear form $b_\xi : W_0^{1,2}(\Omega; \mathbb{R}^d) \to \mathbb{R}$ are defined by

$$a_\xi(\mathbf{u}, \mathbf{v}) = \int_\Omega \boldsymbol{\varepsilon}(\mathbf{u}) : \mathbf{L}_\xi(\mathbf{x}) : \boldsymbol{\varepsilon}(\mathbf{v})\,\mathrm{d}\Omega, \tag{C.15}$$

$$b_\xi(\mathbf{v}) = \int_\Omega (\mathbf{b}\cdot\mathbf{v} - \boldsymbol{\lambda}_\xi(\mathbf{x}) : \boldsymbol{\varepsilon}(\mathbf{v}))\,\mathrm{d}\Omega, \tag{C.16}$$

with the vector of body forces $\mathbf{b} \in L^2(\Omega; \mathbb{R}^d)$.

C.3 Homogenization result

The goal of this section is to prove the following theorem:

Theorem 4 *Let the assumptions* (C.5) *and* (C.10)–(C.13) *hold. Then, the sequence of solutions* $\{\mathbf{u}_\xi\}$ *of the problem* (C.14) *weakly converges to a function* $\mathbf{u}(\mathbf{x}) \in W_0^{1,2}(\Omega;\mathbb{R}^d)$ *and the corresponding sequence of strain tensors* $\{\boldsymbol{\varepsilon}(\mathbf{u}_\xi)\}$ *three-scale converges to the limit*

$$\boldsymbol{\varepsilon}(\mathbf{u}) + \boldsymbol{\varepsilon}_{y_1}(\mathbf{u}_1) + \boldsymbol{\varepsilon}_{y_2}(\mathbf{u}_2), \tag{C.17}$$

where $\mathbf{u}(\mathbf{x}), \mathbf{u}_1(\mathbf{x},\mathbf{y}_1)$ *and* $\mathbf{u}_2(\mathbf{x},\mathbf{y}_1,\mathbf{y}_2)$ *are the unique solutions in the product space*

$$H = W_0^{1,2}(\Omega;\mathbb{R}^d) \times L^2(\Omega; W^{1,2}_{\mathrm{per}}(Y_1,\mathbb{R}^d)) \times L^2(\Omega\times Y_1; W^{1,2}_{\mathrm{per}}(Y_2,\mathbb{R}^d)) \tag{C.18}$$

of the following problem

$$a\left((\mathbf{u},\mathbf{u}_1,\mathbf{u}_2),(\mathbf{v},\mathbf{v}_1,\mathbf{v}_2)\right) = b\left(\mathbf{v},\mathbf{v}_1,\mathbf{v}_2\right) \qquad \text{for all } (\mathbf{v},\mathbf{v}_1,\mathbf{v}_2) \in H \tag{C.19}$$

where the bilinear form $a : H \times H \to \mathbb{R}$ *is defined as*

$$\begin{aligned} a\left((\mathbf{u},\mathbf{u}_1,\mathbf{u}_2),(\mathbf{v},\mathbf{v}_1,\mathbf{v}_2)\right) = \frac{1}{|Y_1|}\frac{1}{|Y_2|}\int_\Omega\int_{Y_1}\int_{Y_2} &\left(\boldsymbol{\varepsilon}(\mathbf{u}) + \boldsymbol{\varepsilon}_{y_1}(\mathbf{u}_1) + \boldsymbol{\varepsilon}_{y_2}(\mathbf{u}_2)\right) \,:\, \mathbf{L}(\mathbf{x},\mathbf{y}_1,\mathbf{y}_2) \\ &:\, \left(\boldsymbol{\varepsilon}(\mathbf{v}) + \boldsymbol{\varepsilon}_{y_1}(\mathbf{v}_1) + \boldsymbol{\varepsilon}_{y_2}(\mathbf{v}_2)\right) \,\mathrm{d}\Omega\,\mathrm{d}Y_1\,\mathrm{d}Y_2 \end{aligned} \tag{C.20}$$

and the linear form $b : H \to \mathbb{R}$ *as*

$$\begin{aligned} b\left(\mathbf{v},\mathbf{v}_1,\mathbf{v}_2\right) &= \int_\Omega \mathbf{b}\cdot\mathbf{v}\,\mathrm{d}\Omega \\ &- \frac{1}{|Y_1|}\frac{1}{|Y_2|}\int_\Omega\int_{Y_1}\int_{Y_2} \boldsymbol{\lambda}(\mathbf{x},\mathbf{y}_1,\mathbf{y}_2) :\, \left(\boldsymbol{\varepsilon}(\mathbf{v}) + \boldsymbol{\varepsilon}_{y_1}(\mathbf{v}_1) + \boldsymbol{\varepsilon}_{y_2}(\mathbf{v}_2)\right)\,\mathrm{d}\Omega\,\mathrm{d}Y_1\,\mathrm{d}Y_2. \end{aligned} \tag{C.21}$$

Proof. For the sake of clarity we divide the proof into three steps.

Step #1 (A priori estimates) By the assumptions $(\mathrm{C.10})_1$ on the material stiffness tensor we can easily verify that the bilinear form $a_\xi(\cdot,\cdot)$ is bounded and coercive on the space $W_0^{1,2}(\Omega;\mathbb{R}^d)$. Indeed, using the Korn inequality $\sqrt{2}\|\boldsymbol{\varepsilon}(\mathbf{u})\|_{L^2(\Omega;\mathbb{S}^d)} \geq \|\mathbf{D}\mathbf{u}\|_{L^2(\Omega;\mathbb{R}^{d\times d})}$ (see, e.g., [23, 97]) and Friedrichs' inequality $\|\mathbf{D}\mathbf{u}\|_{L^2(\Omega;\mathbb{R}^{d\times d})} \geq C(\Omega)\|\mathbf{u}\|_{W_0^{1,2}(\Omega;\mathbb{R}^d)}$ [23, 97, 208] we get

$$\begin{aligned} a_\xi(\mathbf{u},\mathbf{u}) \quad &= \quad \int_\Omega \boldsymbol{\varepsilon}(\mathbf{u}) : \mathbf{L}_\xi(\mathbf{x}) : \boldsymbol{\varepsilon}(\mathbf{u})\,\mathrm{d}\Omega \overset{\text{by } (\mathrm{C.10})_1}{\geq} c_L\|\boldsymbol{\varepsilon}(\mathbf{u})\|^2_{L^2(\Omega;\mathbb{S}^d)} \overset{\text{Korn}}{\geq} \frac{c_L}{2}\|\boldsymbol{D}\mathbf{u}\|^2_{L^2(\Omega;\mathbb{R}^{d\times d})} \\ &\overset{\text{Friedrichs}}{\geq} \quad \frac{c_L C(\Omega)^2}{2}\|\mathbf{u}\|^2_{W_0^{1,2}(\Omega;\mathbb{R}^d)} \end{aligned}$$

and the boundedness of the form $a_\xi(\cdot,\cdot)$ follows from

$$\begin{aligned} |a_\xi(\mathbf{u},\mathbf{v})| \quad &= \quad |\int_\Omega \boldsymbol{\varepsilon}(\mathbf{u}) : \mathbf{L}_\xi(\mathbf{x}) : \boldsymbol{\varepsilon}(\mathbf{v})\,\mathrm{d}\Omega| \leq \int_\Omega \|\boldsymbol{\varepsilon}(\mathbf{u})\|\|\mathbf{L}_\xi(\mathbf{x}) : \boldsymbol{\varepsilon}(\mathbf{v})\|\,\mathrm{d}\Omega \\ &\overset{\text{by } (\mathrm{C.10})_2}{\leq} \quad C_L\|\mathbf{u}\|_{W_0^{1,2}(\Omega;\mathbb{R}^d)}\|\mathbf{v}\|_{W_0^{1,2}(\Omega;\mathbb{R}^d)}. \end{aligned}$$

Similarly, the boundedness of the linear form $b(\cdot)$ yields from the assumption (C.11),

$$|b_\xi(\mathbf{v})| = |\int_\Omega \left(\mathbf{b}\cdot\mathbf{v} - \boldsymbol{\lambda}_\xi(\mathbf{x}) : \boldsymbol{\varepsilon}(\mathbf{v})\right)\,\mathrm{d}\Omega| \overset{\text{by } (\mathrm{C.11})}{\leq} \left(C_\lambda + \|\mathbf{b}\|_{L^2(\Omega;\mathbb{R}^d)}\right)\|\mathbf{v}\|_{W_0^{1,2}(\Omega;\mathbb{R}^d)}.$$

Hence, the existence and uniqueness of the solution to the problem (C.14) follows from the Lax-Milgram lemma [23, 97, 208]. Moreover, the norm of the solution $\mathbf{u}_\xi$ can be bounded by a constant C independent of ξ,

$$\|\mathbf{u}_\xi\|_{W_0^{1,2}(\Omega;\mathbb{R}^d)} \leq C.$$

Finally, since the space $W_0^{1,2}(\Omega;\mathbb{R}^d)$ is reflexive hence weakly compact, we can extract from the sequence of solutions $\{\mathbf{u}_\xi\}$ a weakly converging subsequence $\{\mathbf{u}_{\xi'}\}$,

$$\mathbf{u}_{\xi'} \rightharpoonup \mathbf{u} \qquad \text{weakly in } W_0^{1,2}(\Omega;\mathbb{R}^d).$$

Step #2 (Limit passage) From Theorem 3 it follows that there exists a subsequence of solutions $\{\mathbf{u}_{\xi''}\}$ and functions $\mathbf{u}_1 \in L^2(\Omega; W^{1,2}_{\text{per}}(Y_1,\mathbb{R}^d))$ and $\mathbf{u}_2 \in L^2(\Omega\times Y_1; W^{1,2}_{\text{per}}(Y_2,\mathbb{R}^d))$ such that

$$\boldsymbol{\varepsilon}(\mathbf{u}_{\xi''}) \overset{3-s}{\longrightarrow} \boldsymbol{\varepsilon}(\mathbf{u}) + \boldsymbol{\varepsilon}_{y_1}(\mathbf{u}_1) + \boldsymbol{\varepsilon}_{y_2}(\mathbf{u}_2). \tag{C.22}$$

Consider a smooth test function $\mathbf{w}_\xi$ of the form

$$\mathbf{w}_\xi(\mathbf{x}) = \mathbf{w}(\mathbf{x}) + \xi_1\mathbf{w}_1(\mathbf{x},\mathbf{x}/\xi_1) + \xi_2\mathbf{w}_2(\mathbf{x},\mathbf{x}/\xi_1,\mathbf{x}/\xi_2), \tag{C.23}$$

where $\mathbf{w} \in C_0^\infty(\Omega;\mathbb{R}^d)$, $\mathbf{w}_1 \in \mathcal{D}(\Omega; C^\infty_{\text{per}}(Y_1,\mathbb{R}^d))$ and $\mathbf{w}_2 \in \mathcal{D}(\Omega\times Y_1; C^\infty_{\text{per}}(Y_2,\mathbb{R}^d))$. The corresponding strain tensor is given by[2]

$$\boldsymbol{\varepsilon}(\mathbf{w}_\xi) = \boldsymbol{\varepsilon}(\mathbf{w}) + \xi_1\boldsymbol{\varepsilon}(\mathbf{w}_1) + \boldsymbol{\varepsilon}_{y_1}(\mathbf{w}_1) + \xi_2\boldsymbol{\varepsilon}_{y_2}(\mathbf{w}_2) + \frac{\xi_2}{\xi_1}\boldsymbol{\varepsilon}_{y_1}(\mathbf{w}_2) + \boldsymbol{\varepsilon}_{y_2}(\mathbf{w}_2).$$

The assumptions $(\text{C.12})_1$ and (C.13) authorize us to use the product $\mathbf{L}_{\xi''}(\mathbf{x}) : \boldsymbol{\varepsilon}(\mathbf{w}_\xi)$ as the function v_ξ appearing in Theorem 2. Moreover, by the condition of scale separation (C.5), we get[3]

$$\mathbf{L}_{\xi''} : \boldsymbol{\varepsilon}(\mathbf{w}_\xi) \overset{3-s}{\longrightarrow} \mathbf{L}(\mathbf{x},\mathbf{y}_1,\mathbf{y}_2) : \left(\boldsymbol{\varepsilon}(\mathbf{w}) + \boldsymbol{\varepsilon}_{y_1}(\mathbf{w}_1) + \boldsymbol{\varepsilon}_{y_2}(\mathbf{w}_2)\right) \tag{C.24}$$

Hence

$$\begin{aligned} a_\xi(\mathbf{u}_{\xi''},\mathbf{w}_\xi) \quad &= \quad \int_\Omega \boldsymbol{\varepsilon}(\mathbf{u}_{\xi''}) : \mathbf{L}_{\xi''}(\mathbf{x}) : \boldsymbol{\varepsilon}(\mathbf{w}_\xi)\,\mathrm{d}\Omega \\ &\overset{\text{Theorem 2}}{\longrightarrow} \quad \frac{1}{|Y_1|}\frac{1}{|Y_2|}\int_\Omega\int_{Y_1}\int_{Y_2} \left(\boldsymbol{\varepsilon}(\mathbf{u}) + \boldsymbol{\varepsilon}_{y_1}(\mathbf{u}_1) + \boldsymbol{\varepsilon}_{y_2}(\mathbf{u}_2)\right) : \mathbf{L}(\mathbf{x},\mathbf{y}_1,\mathbf{y}_2) \\ &\qquad\qquad : \left(\boldsymbol{\varepsilon}(\mathbf{w}) + \boldsymbol{\varepsilon}_{y_1}(\mathbf{w}_1) + \boldsymbol{\varepsilon}_{y_2}(\mathbf{w}_2)\right)\,\mathrm{d}\Omega\,\mathrm{d}Y_1\,\mathrm{d}Y_2 \\ &= \quad a\left((\mathbf{u},\mathbf{u}_1,\mathbf{u}_2),(\mathbf{w},\mathbf{w}_1,\mathbf{w}_2)\right). \end{aligned}$$

By density of the test functions (C.23), this result holds for any $(\mathbf{v},\mathbf{v}_1,\mathbf{v}_2) \in V$. Similar procedure can be employed to pass to the limit in the term $b(\cdot)$. Choosing the test function

[2] Recall that $\mathbf{y}_1 = \mathbf{x}/\xi_1$ and $\mathbf{y}_2 = \mathbf{x}/\xi_2$.

[3] Note that we have used the fact that for any oscillating function $\varphi \in L^2(\Omega; C_{\text{per}}(Y_1\times Y_2))$ the following convergence result holds (see, e.g., [6] and [148, Theorem 3])

$$\int_\Omega \varphi(\mathbf{x},\mathbf{x}/\xi_1,\mathbf{x}/\xi_2)^2\,\mathrm{d}\Omega \to \frac{1}{|Y_1|}\frac{1}{|Y_2|}\int_\Omega\int_{Y_1}\int_{Y_2}\varphi(\mathbf{x},\mathbf{y}_1,\mathbf{y}_2)^2\,\mathrm{d}\Omega\,\mathrm{d}Y_1\,\mathrm{d}Y_2.$$

$\mathbf{w}_\xi$ in the same form we get

$$\int_\Omega \boldsymbol{\lambda}_{\xi''}(\mathbf{x}) : \boldsymbol{\varepsilon}(\mathbf{w}_\xi)\,\mathrm{d}\Omega \overset{\text{by (C.12)}_2 \text{ and Theorem 2}}{\longrightarrow} \frac{1}{|Y_1|}\frac{1}{|Y_2|}\int_\Omega\int_{Y_1}\int_{Y_2} \boldsymbol{\lambda}(\mathbf{x},\mathbf{y}_1,\mathbf{y}_2) :\ (\boldsymbol{\varepsilon}(\mathbf{w}) + \boldsymbol{\varepsilon}_{y_1}(\mathbf{w}_1) + \boldsymbol{\varepsilon}_{y_2}(\mathbf{w}_2))\ \mathrm{d}\Omega\,\mathrm{d}Y_1\,\mathrm{d}Y_2$$

and

$$\int_\Omega \mathbf{b}\cdot\mathbf{w}_\xi\,\mathrm{d}\Omega \longrightarrow \int_\Omega \mathbf{b}\cdot\mathbf{w}\,\mathrm{d}\Omega$$

Thus, we have just shown that

$$b_{\xi''}(\mathbf{w}_\xi) \to b(\mathbf{w},\mathbf{w}_1,\mathbf{w}_2) \tag{C.25}$$

for any smooth test function $\mathbf{w}_\xi$ and, by density, for any $(\mathbf{v},\mathbf{v}_1,\mathbf{v}_2)\in V$.

Step #3 (Uniqueness of the solution) Let us endow the Hilbert space H, defined in (C.18), with the norm

$$\|\mathbf{U}\|_H^2 = \|\mathbf{D}\mathbf{u}\|^2_{L^2(\Omega;\mathbb{R}^d\times\mathbb{R}^d)} + \|\mathbf{D}_{y_1}\mathbf{u}_1\|^2_{L^2(\Omega\times Y_1;\mathbb{R}^d\times\mathbb{R}^d)} + \|\mathbf{D}_{y_2}\mathbf{u}_2\|^2_{L^2(\Omega\times Y_1\times Y_2;\mathbb{R}^d\times\mathbb{R}^d)}, \tag{C.26}$$

where, for the notational simplicity, we introduced $\mathbf{U}=(\mathbf{u},\mathbf{u}_1,\mathbf{u}_2)$. Before proceeding with the "homogenization" proof, we will state the following result:

Lemma 1 *The norm $\|\cdot\|_H$ and the norm $\|\cdot\|_W$ defined by*

$$\|\mathbf{U}\|_W^2 = \|\mathbf{u}\|^2_{W_0^{1,2}(\Omega;\mathbb{R}^d)} + \|\mathbf{u}_1\|^2_{L^2(\Omega;W^{1,2}_{\mathrm{per}}(Y_1,\mathbb{R}^d))} + \|\mathbf{u}_2\|^2_{L^2(\Omega\times Y_1;W^{1,2}_{\mathrm{per}}(Y_2,\mathbb{R}^d))} \tag{C.27}$$

are equivalent on H.

Proof. Recall that two norms $\|\cdot\|_H$ and $\|\cdot\|_W$ on H are equivalent if there exist two positive constants C_1 and C_2 such that, for every $\mathbf{U}\in H$,

$$C_1\|\mathbf{U}\|_H \le \|\mathbf{U}\|_W \le C_2\|\mathbf{U}\|_H.$$

Writing the individual terms in the definition of the $\|\cdot\|_W$ in more details using relations (C.2) and (C.3), we arrive at

$$\begin{aligned}
\|\mathbf{U}\|_W^2 &= \overbrace{\|\mathbf{u}\|^2_{L^2(\Omega;\mathbb{R}^d)}}^{\geq 0} + \|\mathbf{D}\mathbf{u}\|^2_{L^2(\Omega,\mathbb{R}^{d\times d})} \\
&+ \int_\Omega \Big(\overbrace{\|\mathbf{u}_1\|^2_{L^2(Y_1,\mathbb{R}^d)}}^{\geq 0} + \|\mathbf{D}_{\mathbf{y}_1}\mathbf{u}_1\|^2_{L^2(Y_1,\mathbb{R}^{d\times d})}\Big)\,\mathrm{d}\Omega \\
&+ \int_\Omega\int_{Y_1} \Big(\overbrace{\|\mathbf{u}_2\|^2_{L^2(Y_2,\mathbb{R}^d)}}^{\geq 0} + \|\mathbf{D}_{\mathbf{y}_2}\mathbf{u}_2\|^2_{L^2(Y_2,\mathbb{R}^{d\times d})}\Big)\,\mathrm{d}Y_1\,\mathrm{d}\Omega \\
&\geq \|\mathbf{D}\mathbf{u}\|^2_{L^2(\Omega;\mathbb{R}^d\times\mathbb{R}^d)} + \|\mathbf{D}_{y_1}\mathbf{u}_1\|^2_{L^2(\Omega\times Y_1;\mathbb{R}^d\times\mathbb{R}^d)} + \|\mathbf{D}_{y_2}\mathbf{u}_2\|^2_{L^2(\Omega\times Y_1\times Y_2;\mathbb{R}^d\times\mathbb{R}^d)} \\
&= \|\mathbf{U}\|_H^2,
\end{aligned}$$

which proves the first inequality. To show the validity of the opposite inequality, recall that by the Friedrichs inequality [117, 208], $\int_\Omega u^2\,\mathrm{d}\Omega \le C\int_\Omega \|\mathbf{D}u\|^2\,\mathrm{d}\Omega$ for any bounded set Ω and $u \in W_0^{1,2}(\Omega)$ while, thanks to the Poincaré inequality [117, 208], $\int_\Omega u^2\,\mathrm{d}\Omega \le C\{\big(\int_\Omega u\,\mathrm{d}\Omega\big)^2 + \int_\Omega \|\mathbf{D}u\|^2\,\mathrm{d}\Omega\}$, for any Lipschitz set Ω and $u \in W^{1,2}(\Omega) \supset W^{1,2}_{\mathrm{per}}(\Omega)$. Note that, thanks to the definition of the $W^{1,2}_{\mathrm{per}}(\Omega)$, $\int_\Omega u\,\mathrm{d}\Omega = 0$ for any $u \in W^{1,2}_{\mathrm{per}}(\Omega)$. Hence,

$$
\begin{aligned}
\|\mathbf{U}\|_W^2 &= \overbrace{\|\mathbf{u}\|^2_{L^2(\Omega;\mathbb{R}^d)}}^{\le C\|\mathbf{Du}\|^2_{L^2(\Omega,\mathbb{R}^{d\times d})}\text{(Friedrichs)}} + \|\mathbf{Du}\|^2_{L^2(\Omega,\mathbb{R}^{d\times d})} \\
&+ \int_\Omega \Big(\overbrace{\|\mathbf{u}_1\|^2_{L^2(Y_1,\mathbb{R}^d)}}^{\le C\left\|\mathbf{D}_{\mathbf{y_1}}\mathbf{u}_1\right\|^2_{L^2(Y_1,\mathbb{R}^{d\times d})}\text{(Poincare)}} + \|\mathbf{D}_{\mathbf{y}_1}\mathbf{u}_1\|^2_{L^2(Y_1,\mathbb{R}^{d\times d})}\Big)\,\mathrm{d}\Omega \\
&+ \int_\Omega\int_{Y_1} \Big(\overbrace{\|\mathbf{u}_2\|^2_{L^2(Y_2,\mathbb{R}^d)}}^{\le C\left\|\mathbf{D}_{\mathbf{y}_2}\mathbf{u}_2\right\|^2_{L^2(Y_2,\mathbb{R}^{d\times d})}\text{(Poincare)}} + \|\mathbf{D}_{\mathbf{y}_2}\mathbf{u}_2\|^2_{L^2(Y_2,\mathbb{R}^{d\times d})}\Big)\,\mathrm{d}Y_1\,\mathrm{d}\Omega \\
&\le C\big(\|\mathbf{Du}\|^2_{L^2(\Omega;\mathbb{R}^d\times\mathbb{R}^d)} + \|\mathbf{D}_{y_1}\mathbf{u}_1\|^2_{L^2(\Omega\times Y_1;\mathbb{R}^d\times\mathbb{R}^d)} + \|\mathbf{D}_{y_2}\mathbf{u}_2\|^2_{L^2(\Omega\times Y_1\times Y_2;\mathbb{R}^d\times\mathbb{R}^d)}\big) \\
&= C\|\mathbf{U}\|_H^2.
\end{aligned}
$$

□

Now, if we prove that the bilinear form $a(\cdot,\cdot)$ (C.20) is coercive and bounded on H, the uniqueness of the solution follows directly from the Lax-Milgram lemma. The verification of the ellipticity follows the procedure in Step 1,

$$
\begin{aligned}
a(\mathbf{U},\mathbf{U}) &= \frac{1}{|Y_1|}\frac{1}{|Y_2|}\int_\Omega\int_{Y_1}\int_{Y_2} (\boldsymbol{\varepsilon}(\mathbf{u}) + \boldsymbol{\varepsilon}_{y_1}(\mathbf{u}_1) + \boldsymbol{\varepsilon}_{y_2}(\mathbf{u}_2)) \,:\, \mathbf{L}(\mathbf{x},\mathbf{y}_1,\mathbf{y}_2) \\
&\qquad : (\boldsymbol{\varepsilon}(\mathbf{u}) + \boldsymbol{\varepsilon}_{y_1}(\mathbf{u}_1) + \boldsymbol{\varepsilon}_{y_2}(\mathbf{u}_2))\,\mathrm{d}\Omega\,\mathrm{d}Y_1\,\mathrm{d}Y_2 \\
&\overset{\text{by (C.10)}_1}{\ge} \frac{c_L}{|Y_1||Y_2|}\int_\Omega\int_{Y_1}\int_{Y_2} \|\boldsymbol{\varepsilon}(\mathbf{u}) + \boldsymbol{\varepsilon}_{y_1}(\mathbf{u}_1) + \boldsymbol{\varepsilon}_{y_2}(\mathbf{u}_2)\|^2\,\mathrm{d}\Omega\,\mathrm{d}Y_1\,\mathrm{d}Y_2 \\
&= \frac{c_L}{|Y_1||Y_2|}\int_\Omega\int_{Y_1}\int_{Y_2}\Big(\|\boldsymbol{\varepsilon}(\mathbf{u})\|^2_{L^2(\Omega;\mathbb{S}^d)} + \|\boldsymbol{\varepsilon}_{y_1}(\mathbf{u}_1)\|^2_{L^2(\Omega\times Y_1;\mathbb{S}^d)} \\
&\qquad + \|\boldsymbol{\varepsilon}_{y_2}(\mathbf{u}_2)\|^2_{L^2(\Omega\times Y_1\times Y_2;\mathbb{S}^d)}\Big)\,\mathrm{d}\Omega\,\mathrm{d}Y_1\,\mathrm{d}Y_2 \qquad \text{(C.28)} \\
&+ \frac{2c_L}{|Y_1||Y_2|}\int_\Omega\int_{Y_1}\int_{Y_2}\Big(\boldsymbol{\varepsilon}(\mathbf{u}) : \boldsymbol{\varepsilon}_{y_1}(\mathbf{u}_1) + \boldsymbol{\varepsilon}(\mathbf{u}) : \boldsymbol{\varepsilon}_{y_2}(\mathbf{u}_2) \\
&\qquad + \boldsymbol{\varepsilon}_{y_1}(\mathbf{u}_1) : \boldsymbol{\varepsilon}_{y_2}(\mathbf{u}_2)\Big)\,\mathrm{d}\Omega\,\mathrm{d}Y_1\,\mathrm{d}Y_2 \qquad \text{(C.29)}
\end{aligned}
$$

By the Korn inequality, the term (C.28) can be, similarly to the Step 1, estimated as

$$
\text{(C.28)} \ge \frac{c_L}{2|Y_1||Y_2|}\|\mathbf{U}\|_H^2,
$$

while (C.29) vanishes. To demonstrate this, consider the term

$$\begin{aligned}\int_\Omega \int_{Y_1} \boldsymbol{\varepsilon}(\mathbf{u}(\mathbf{x})) : \boldsymbol{\varepsilon}_{y_1}(\mathbf{u}_1(\mathbf{x},\mathbf{y}_1))\,\mathrm{d}\Omega\,\mathrm{d}Y_1 &\overset{\text{by Green's theorem}}{=} \underbrace{\int_\Omega \int_{\Gamma_1} \mathbf{n}(\mathbf{y}_1)\cdot\boldsymbol{\varepsilon}(\mathbf{x})\cdot\mathbf{u}_1(\mathbf{x},\mathbf{y}_1)\,\mathrm{d}\Omega\,\mathrm{d}\Gamma_1}_{=0 \text{ by } Y_1 \text{ periodicity of } \mathbf{u}_1} \\ &- \underbrace{\int_\Omega \int_{Y_1} \boldsymbol{\varepsilon}_{y_1}(\boldsymbol{\varepsilon}(\mathbf{u}(\mathbf{x})))\,\mathrm{d}\Omega\,\mathrm{d}Y_1}_{=0} \\ &= 0.\end{aligned}$$

Using analogous procedure, it can be easily seen that also the remaining terms in (C.29) are equal to zero.

Let us now check that $a(\cdot,\cdot)$ is bounded. The assumption $(\text{C.10})_2$ implies that

$$\begin{aligned}|a(\mathbf{U},\mathbf{V})| &= \frac{1}{|Y_1|}\frac{1}{|Y_2|}\Big|\int_\Omega\int_{Y_1}\int_{Y_2} (\boldsymbol{\varepsilon}(\mathbf{u})+\boldsymbol{\varepsilon}_{y_1}(\mathbf{u}_1)+\boldsymbol{\varepsilon}_{y_2}(\mathbf{u}_2)) : \mathbf{L}(\mathbf{x},\mathbf{y}_1,\mathbf{y}_2) \\ &\qquad : (\boldsymbol{\varepsilon}(\mathbf{v})+\boldsymbol{\varepsilon}_{y_1}(\mathbf{v}_1)+\boldsymbol{\varepsilon}_{y_2}(\mathbf{v}_2))\,\mathrm{d}\Omega\,\mathrm{d}Y_1\,\mathrm{d}Y_2\Big| \\ &\le \frac{1}{|Y_1|}\frac{1}{|Y_2|}\int_\Omega\int_{Y_1}\int_{Y_2} \|\boldsymbol{\varepsilon}(\mathbf{u})+\boldsymbol{\varepsilon}_{y_1}(\mathbf{u}_1)+\boldsymbol{\varepsilon}_{y_2}(\mathbf{u}_2)\| \\ &\qquad \|\mathbf{L}(\mathbf{x},\mathbf{y}_1,\mathbf{y}_2) : (\boldsymbol{\varepsilon}(\mathbf{v})+\boldsymbol{\varepsilon}_{y_1}(\mathbf{v}_1)+\boldsymbol{\varepsilon}_{y_2}(\mathbf{v}_2))\|\,\mathrm{d}\Omega\,\mathrm{d}Y_1\,\mathrm{d}Y_2 \\ &\overset{\text{by } (\text{C.10})_2}{\le} \frac{C_L}{|Y_1||Y_2|}\int_\Omega\int_{Y_1}\int_{Y_2} \|\boldsymbol{\varepsilon}(\mathbf{u})+\boldsymbol{\varepsilon}_{y_1}(\mathbf{u}_1)+\boldsymbol{\varepsilon}_{y_2}(\mathbf{u}_2)\| \\ &\qquad \|\boldsymbol{\varepsilon}(\mathbf{v})+\boldsymbol{\varepsilon}_{y_1}(\mathbf{v}_1)+\boldsymbol{\varepsilon}_{y_2}(\mathbf{v}_2)\|\,\mathrm{d}\Omega\,\mathrm{d}Y_1\,\mathrm{d}Y_2 \\ &\le \frac{C_L}{|Y_1||Y_2|}\|\mathbf{U}\|_H\|\mathbf{V}\|_H.\end{aligned}$$

Similarly, the assumption (C.11) ensures that the linear form $b(\cdot)$ is bounded on H.

Now, from the uniqueness of the solution $\mathbf{U}$, it follows that the whole sequences of solutions and corresponding strain tensors, not just subsequences $\{\mathbf{u}_{\xi'}\}$ and $\{\boldsymbol{\varepsilon}(\mathbf{u}_{\xi''})\}$, converge to their limits.

□

C.4 Strain and stress controlled homogenization

The convergence result obtained in the previous section can be used for the analysis of stress and strain controlled homogenization. To this end, exploring the independence of test functions $\mathbf{v}$, $\mathbf{v}_1$ and $\mathbf{v}_2$, we may reformulate the problem (C.20) in the form of *uncoupled* three scale homogenized system. Thus, we may separately investigate the *microscale*, *mesoscale* and *macroscale* levels with a connection to the strain and stress controlled homogenization.

Microscale problem (test function $\mathbf{v}_2$). We start with the microscale problem stated as: For the fixed coordinates $\mathbf{x}\in\Omega$ and $\mathbf{y}_1\in Y_1$ and a given overall microscale strain $\boldsymbol{E}_{\text{micro}}(\mathbf{x},\mathbf{y}_1)\in\mathbb{S}^d$ find the microscale fluctuating displacement field $\mathbf{u}_2(\mathbf{x},\mathbf{y}_1,\cdot)\in W^{1,2}_{\text{per}}(Y_2)$

such that

$$\int_{Y_2} \boldsymbol{\varepsilon}_{y_2}(\mathbf{v}_2) : \left(\mathbf{L}(\mathbf{x},\mathbf{y}_1,\mathbf{y}_2) : \left(\overbrace{\boldsymbol{\varepsilon}(\mathbf{u}) + \boldsymbol{\varepsilon}_{y_1}(\mathbf{u}_1)}^{\boldsymbol{E}_{\mathrm{micro}}(\mathbf{x},\mathbf{y}_1)} + \boldsymbol{\varepsilon}_{y_2}(\mathbf{u}_2) \right) + \boldsymbol{\lambda}(\mathbf{x},\mathbf{y}_1,\mathbf{y}_2) \right) \mathrm{d}Y_2 = 0 \quad \text{(C.30)}$$

holds for all $\mathbf{v}_2 \in W^{1,2}_{\mathrm{per}}(Y_2)$. Note that this variational formulation is actually identical to the strain controlled homogenization approach (3.20).

The linearity of the problem allows us to relate the microscale strain field $\boldsymbol{\varepsilon}_{y_2}(\mathbf{u}_2)$ to the overall strain $\boldsymbol{E}_{\mathrm{micro}}$ by means of solutions of the well-known unit cell problem [16, 117, 241]: Find displacement fields $\boldsymbol{\chi}^{kl}(\mathbf{x},\mathbf{y}_1,\cdot) \in W^{1,2}_{\mathrm{per}}(Y_2,\mathbb{R}^d), k = 1,\ldots,d, l = 1,\ldots,d$ such that, for all $\mathbf{v}_2 \in W^{1,2}_{\mathrm{per}}(Y_2,\mathbb{R}^d)$,

$$\int_{Y_2} \boldsymbol{\varepsilon}_{y_2}(\mathbf{v}_2) : \mathbf{L}(\mathbf{x},\mathbf{y}_1,\mathbf{y}_2) : \boldsymbol{\varepsilon}_{y_2}(\boldsymbol{\chi}^{kl}) \,\mathrm{d}Y_2 = -\int_{Y_2} \boldsymbol{\varepsilon}_{y_2}(\mathbf{v}_2) : \mathbf{L}(\mathbf{x},\mathbf{y}_1,\mathbf{y}_2) : \boldsymbol{I}^{kl} \,\mathrm{d}Y_2,$$

where the second-order tensor of "unit strain impulses" is provided by relation $(\boldsymbol{I}^{kl})_{ij} = (\delta_{ik}\delta_{jk} + \delta_{il}\delta_{jk})/2$. Further, denote as $\boldsymbol{\chi}^{\lambda}(\mathbf{x},\mathbf{y}_1,\cdot) \in W^{1,2}_{\mathrm{per}}(Y_2,\mathbb{R}^d)$ the solution of following variational problem[4]

$$\int_{Y_2} \boldsymbol{\varepsilon}_{y_2}(\mathbf{v}_2) : \mathbf{L}(\mathbf{x},\mathbf{y}_1,\mathbf{y}_2) : \boldsymbol{\varepsilon}_{y_2}(\boldsymbol{\chi}^{\lambda}) \,\mathrm{d}Y_2 = -\int_{Y_2} \boldsymbol{\varepsilon}_{y_2}(\mathbf{v}_2) : \boldsymbol{\lambda}(\mathbf{x},\mathbf{y}_1,\mathbf{y}_2) \,\mathrm{d}Y_2.$$

The microscale stresses now can be expressed by means of microscale strain $\boldsymbol{E}_{\mathrm{micro}}$,

$$\boldsymbol{\sigma}(\mathbf{x},\mathbf{y}_1,\mathbf{y}_2) = \mathbf{L}(\mathbf{x},\mathbf{y}_1,\mathbf{y}_2) : \left(\mathbf{B}(\mathbf{x},\mathbf{y}_1,\mathbf{y}_2) : \boldsymbol{E}_{\mathrm{micro}}(\mathbf{x},\mathbf{y}_1) - \boldsymbol{\varepsilon}_{y_2}\left(\boldsymbol{\chi}^{\lambda}(\mathbf{x},\mathbf{y}_1,\mathbf{y}_2)\right) \right), \quad \text{(C.31)}$$

where the fourth-order strain concentration tensor $\mathbf{B}$ is defined as

$$B_{ijkl} = I_{ijkl} + \left(\varepsilon_{y_2}(\boldsymbol{\chi}^{kh})\right)_{ij}.$$

Finally, averaging the stress tensor with respect to the microscale unit cell Y_2 yields

$$\begin{aligned} \boldsymbol{\Sigma}_{\mathrm{micro}}(\mathbf{x},\mathbf{y}_1) &= \frac{1}{|Y_2|}\int_{Y_2} \mathbf{L}(\mathbf{x},\mathbf{y}_1,\mathbf{y}_2) : \left(\mathbf{B}(\mathbf{x},\mathbf{y}_1,\mathbf{y}_2) : \boldsymbol{E}_{\mathrm{micro}}(\mathbf{x},\mathbf{y}_1) - \boldsymbol{\varepsilon}_{y_2}\left(\boldsymbol{\chi}^{\lambda}(\mathbf{x},\mathbf{y}_1,\mathbf{y}_2)\right) \right) \mathrm{d}Y_2 \\ &= \mathbf{L}^{\mathrm{hom}}_{\mathrm{micro}}(\mathbf{x},\mathbf{y}_1) : \boldsymbol{E}_{\mathrm{micro}}(\mathbf{x},\mathbf{y}_1) + \boldsymbol{\Lambda}^{\mathrm{hom}}_{\mathrm{micro}}(\mathbf{x},\mathbf{y}_1). \end{aligned} \quad \text{(C.32)}$$

Note that the procedure of determination of effective material behavior is actually identical to the engineering approach used in Section 3.2.

Mesoscale problem (test function $\mathbf{v}_1$) Having solved the microscale problem, we can move one level up and consider a mesoscale problem stated as follows: For a fixed

[4] A concrete example of function $\boldsymbol{\chi}^{12}$ for a hexagonal unit cell can be seen in Figs. 3.11a–c, while the individual components of the field $\boldsymbol{\varepsilon}_{y_2}(\boldsymbol{\chi}^{\lambda})$ are shown in Figs. 3.11d–f. See also Fig. 5.10 for the mesoscale level.

coordinate $\mathbf{x} \in \Omega$ and mesoscale overall strain tensor $\boldsymbol{E}_{\text{meso}}(\mathbf{x}) \in \mathbb{S}^d$ find the mesoscale fluctuating displacement $\mathbf{u}_1(\mathbf{x}, \cdot) \in W^{1,2}_{\text{per}}(Y_1)$ such that, for any $\mathbf{v}_1 \in W^{1,2}_{\text{per}}(Y_1)$,

$$\int_{Y_1} \boldsymbol{\varepsilon}_{y_1}(\mathbf{v}_1) : \underbrace{\frac{1}{|Y_2|}\left(\int_{Y_2} \mathsf{L}(\mathbf{x}, \mathbf{y}_1, \mathbf{y}_2) : \left(\overbrace{\boldsymbol{\varepsilon}(\mathbf{u})}^{=\boldsymbol{E}_{\text{meso}}(\mathbf{x})} + \boldsymbol{\varepsilon}_{y_1}(\mathbf{u}_1) + \boldsymbol{\varepsilon}_{y_2}(\mathbf{u}_2)\right) + \boldsymbol{\lambda}(\mathbf{x}, \mathbf{y}_1, \mathbf{y}_2)\, \mathrm{d}Y_2\right)}_{=\boldsymbol{\Sigma}_{\text{micro}}(\mathbf{x}, \mathbf{y}_1)} \mathrm{d}Y_1 = 0. \quad \text{(C.33)}$$

Observe that the underbraced term is nothing else that the overall microscale stress tensor $\boldsymbol{\Sigma}_{\text{micro}}$ defined by Eq. (C.32). Therefore, the mesoscale problem can be reformulated as the variational problem

$$\int_{Y_1} \boldsymbol{\varepsilon}_{y_1}(\mathbf{v}_1) : \mathsf{L}^{\text{hom}}_{\text{micro}}(\mathbf{x}, \mathbf{y}_1) : (\boldsymbol{\varepsilon}(\mathbf{u}) + \boldsymbol{\varepsilon}_{y_1}(\mathbf{v}_1))\, \mathrm{d}Y_1 = -\int_{Y_1} \boldsymbol{\varepsilon}_{y_1}(\mathbf{v}_1) : \boldsymbol{\Lambda}^{\text{hom}}_{\text{micro}}(\mathbf{x}, \mathbf{y}_1)\, \mathrm{d}Y_1. \quad \text{(C.34)}$$

Repeating in verbatim the procedure described for the microscale problem, the mesoscopic constitutive stress-strain relationship can be put in the form

$$\boldsymbol{\Sigma}_{\text{meso}}(\mathbf{x}) = \frac{1}{|Y_1|}\int_{Y_1} \boldsymbol{\Sigma}_{\text{micro}}(\mathbf{x}, \mathbf{y}_1)\, \mathrm{d}Y_1 = \mathsf{L}^{\text{hom}}_{\text{meso}}(\mathbf{x}) : \boldsymbol{E}_{\text{meso}}(\mathbf{x}) + \boldsymbol{\Lambda}^{\text{hom}}_{\text{meso}}(\mathbf{x}), \quad \text{(C.35)}$$

which is, again, fully consistent with procedure introduced in Chapter 5.

Macroscale problem (test function v). Finally, we are left with only unresolved macroscopic scale. To that end, we solve the macroscopic problem

$$\int_\Omega \boldsymbol{\varepsilon}(\mathbf{v}) : \overbrace{\left(\frac{1}{|Y_1|}\int_{Y_1}\frac{1}{|Y_2|}\int_{Y_2} \mathsf{L}(\mathbf{x}, \mathbf{y}_1, \mathbf{y}_2) : (\boldsymbol{\varepsilon}(\mathbf{u}) + \boldsymbol{\varepsilon}_{y_1}(\mathbf{u}_1) + \boldsymbol{\varepsilon}_{y_2}(\mathbf{u}_2)) + \boldsymbol{\lambda}(\mathbf{x}, \mathbf{y}_1, \mathbf{y}_2)\, \mathrm{d}Y_2\, \mathrm{d}Y_1\right)}^{=\boldsymbol{\Sigma}_{\text{meso}}(\mathbf{x})} \mathrm{d}\Omega = \int_\Omega \mathbf{g} \cdot \mathbf{v}\, \mathrm{d}\Omega, \quad \text{(C.36)}$$

i.e., we have to find the microscopic displacement field $\mathbf{u} \in W^{1,2}_0(\Omega; \mathbb{R}^d)$, such that

$$\int_\Omega \boldsymbol{\varepsilon}(\mathbf{v}) : \mathsf{L}^{\text{hom}}_{\text{meso}}(\mathbf{x}) : \boldsymbol{\varepsilon}(\mathbf{u})\, \mathrm{d}\Omega = \int_\Omega \left(\mathbf{b} \cdot \mathbf{v} - \boldsymbol{\varepsilon}(\mathbf{v}) : \boldsymbol{\Lambda}^{\text{hom}}_{\text{meso}}(\mathbf{x})\right) \mathrm{d}\Omega \quad \text{(C.37)}$$

holds for all $\mathbf{v} \in W^{1,2}_0(\Omega; \mathbb{R}^d)$.

Stress controlled homogenization. To recover stress-controlled homogenization formula, we take into account that for this particular loading conditions, overall strains on individual levels, $\boldsymbol{E}_{\text{micro}}$ and $\boldsymbol{E}_{\text{meso}}$ are now unknown variables. The definitions of overall stresses $\boldsymbol{\Sigma}_{\text{micro}}$ and $\boldsymbol{\Sigma}_{\text{meso}}$, introduced in Eqs. (C.33) and (C.36), however, can be directly used to obtain a well-posed problem.

Indeed, consider the microscale problem which now reads as: For the fixed coordinates $\mathbf{x} \in \Omega$ and $\mathbf{y}_1 \in Y_1$ and a given overall microscale stress $\boldsymbol{\Sigma}_{\text{micro}}(\mathbf{x}, \mathbf{y}_1) \in \mathbb{S}^d$ find the

microscale fluctuating displacement field $\mathbf{u}_2(\mathbf{x},\mathbf{y}_1,\cdot)\in W^{1,2}_{\mathrm{per}}(Y_2)$ and overall microscopic strain $\boldsymbol{E}_{\mathrm{micro}}(\mathbf{x},\mathbf{y}_1)\in\mathbb{S}^d$, such that, for all $\mathbf{v}_2\in W^{1,2}_{\mathrm{per}}(Y_2)$,

$$\begin{cases} \dfrac{1}{|Y_2|}\displaystyle\int_{Y_2}\mathsf{L}(\mathbf{x},\mathbf{y}_1,\mathbf{y}_2):\ (\boldsymbol{E}_{\mathrm{micro}}(\mathbf{x},\mathbf{y}_1)+\boldsymbol{\varepsilon}_{y_2}(\mathbf{u}_2))\ \mathrm{d}Y_2=\boldsymbol{\Sigma}_{\mathrm{micro}}(\mathbf{x},\mathbf{y}_1) \\ \qquad\qquad -\dfrac{1}{|Y_2|}\displaystyle\int_{Y_2}\boldsymbol{\lambda}(\mathbf{x},\mathbf{y}_1,\mathbf{y}_2)\,\mathrm{d}Y_2, \\ \displaystyle\int_{Y_2}\boldsymbol{\varepsilon}_{y_2}(\mathbf{v}_2):\mathsf{L}(\mathbf{x},\mathbf{y}_1,\mathbf{y}_2):(\boldsymbol{E}_{\mathrm{micro}}(\mathbf{x},\mathbf{y}_1)+\boldsymbol{\varepsilon}_{y_2}(\mathbf{u}_2))\,\mathrm{d}Y_2=-\int_{Y_2}\boldsymbol{\varepsilon}_{y_2}(\mathbf{v}_2):\boldsymbol{\lambda}(\mathbf{x},\mathbf{y}_1,\mathbf{y}_2)\,\mathrm{d}Y_2. \end{cases}$$

i.e., we acquire exactly the same formulation as in Section 3.2.3. Similarly, using the definition of microscale homogenized properties, we can easily arrive at the system of mesoscale equations in the form

$$\begin{cases} \dfrac{1}{|Y_1|}\displaystyle\int_{Y_1}\mathsf{L}^{\mathrm{hom}}_{\mathrm{micro}}(\mathbf{x},\mathbf{y}_1):\ (\boldsymbol{E}_{\mathrm{meso}}(\mathbf{x})+\boldsymbol{\varepsilon}_{y_1}(\mathbf{u}_1))\ \mathrm{d}Y_1=\boldsymbol{\Sigma}_{\mathrm{meso}}(\mathbf{x}) \\ \qquad\qquad -\dfrac{1}{|Y_1|}\displaystyle\int_{Y_1}\boldsymbol{\Lambda}^{\mathrm{hom}}_{\mathrm{micro}}(\mathbf{x},\mathbf{y}_1)\,\mathrm{d}Y_1, \\ \displaystyle\int_{Y_1}\boldsymbol{\varepsilon}_{y_1}(\mathbf{v}_1):\mathsf{L}^{\mathrm{hom}}_{\mathrm{micro}}(\mathbf{x},\mathbf{y}_1):(\boldsymbol{E}_{\mathrm{meso}}(\mathbf{x})+\boldsymbol{\varepsilon}_{y_1}(\mathbf{u}_1))\,\mathrm{d}Y_1=-\int_{Y_1}\boldsymbol{\varepsilon}_{y_1}(\mathbf{v}_1):\boldsymbol{\Lambda}^{\mathrm{hom}}_{\mathrm{micro}}(\mathbf{x},\mathbf{y}_1)\,\mathrm{d}Y_1. \end{cases}$$

Finally, we solve the following problem on the mesoscale level

$$\int_\Omega\boldsymbol{\varepsilon}(\mathbf{v}):\boldsymbol{\Sigma}_{\mathrm{meso}}(\mathbf{x})\,\mathrm{d}\Omega=\int_\Omega\mathbf{v}\cdot\mathbf{b}\,\mathrm{d}\Omega,\quad\text{for any}\quad\mathbf{v}\in W^{1,2}_0(\Omega;\mathbb{R}^d).$$

We conclude this section by a brief discussion on practical aspects following from results of the presented theory. First, it should be stresses that the solution of homogenized system is only a *limit solution* as $\xi\to 0$. In the practical problems, however, this ratio is actually given and cannot be arbitrary changed; on the other hand, it is typically so small that direct numerical investigation is not possible. The two scale problem with periodic microstructure but with a *fixed* ratio ξ was first addressed by Babuška [9], further extended by Morgan and Babuška [171, 170]; the results of these analyses have been recently incorporated into the framework of generalized Finite Element methods in [155, 156]. In the general multiscale case, to author's best knowledge, such an analysis is still lacking. It is, however, a widely accepted heuristic that the homogenized system is appropriate for simulation of real composite materials as long as the lengthscales ξ_1 and ξ_2 are reasonably small with respect to typical macrostructural dimension and wavelengths of imposed loads.

The assumptions on material data, Eqs. (C.10)–(C.12), appear to be sufficiently general to be satisfied in vast majority of problems of practical interest. The assumption (C.13), however, is seemingly purely technical and rather restrictive. Fortunately, this condition is known to hold in several important cases [6, Remark 2.13]; in particular, it is satisfied if the individual entries of material stiffness tensor $\mathsf{L}(\mathbf{x},\mathbf{y}_1,\mathbf{y}_2)$ are finite sums of products of the type

$$\varphi(\mathbf{x})\varphi_1(\mathbf{y}_1)\varphi_2(\mathbf{y}_2)\quad\text{with}\quad\varphi(\mathbf{x})\in L^\infty(\Omega),\varphi_1(\mathbf{y}_1)\in L^\infty_{\mathrm{per}}(Y_1),\varphi_2(\mathbf{y}_2)\in L^\infty_{\mathrm{per}}(Y_2).$$

This condition is sufficiently general to present no practical obstacles.